THÈSE

Présentée à

Université Lille 1 — Sciences et Technologies

Ecole doctorale des Sciences de la Matière, du Rayonnement et de l'Environnement

Par

Cheng CHEN

Pour obtenir le grade de

Docteur de l' Université de Lille 1

Spécialité:

Optique, Lasers, Physico-chimie, Atmosphère

Retrieving global sources of aerosol emissions from satellite observations

---

Soutenance prévue le 31 janvier 2018 devant le jury composé de:

Mian CHIN	Senior Scientist, NASA Goddard Space Flight Center	Rapporteuse
Gregory L. SCHUSTER	Senior Scientist, NASA Langley Research Center	Rapporteur
Lorraine A. REMER	Professor, University of Maryland, Baltimore	Exminatrice
Oliver BOUCHER	Directeur de recherche CNRS, Institut Pierre-Simon Laplace	Examinateur
Daven K. HENZE	Associate Professor, University of Colorado, Boulder	Examinateur
Didier TANRÉ	Directeur de recherche CNRS, CNRS/Université Lille1	Examinateur
Oleg DUBOVIK	Directeur de recherche CNRS, CNRS/Université Lille1	Directeur de thèse

Laboratoire d'Optique Atmosphérique

U.F.R. de Physique Fondamentale

Université Lille1 Sciences et Technologies

59655 Villeneuve D'ASCQ, France

Abstract

Understanding of the role that atmospheric aerosol play in the Earth-atmosphere system is limited by uncertainties in aerosol distribution, composition and sources. Thus, accurate chemical transport model simulation systems are crucial needed to analyse and predict atmospheric aerosols and their impacts on climate change and environment. Satellite observations have ability to provide an extensive spatial coverage and accurate aerosol products, however, are constrained by clear-sky condition, global coverage orbit cycle and information content. One of the most promising approaches is to reduce model uncertainty by improving the aerosol emission fields (i.e., model input) by means of inverse modeling relying on satellite observations as a constrain. In this study, we designed a method of simultaneous retrievals of desert dust, black carbon and organic carbon aerosol emission sources using aerosol data obtained from GRASP algorithm applied to POLDER/PARASOL satellite observations, and relying on the GEOS-Chem inverse modeling framework. Then, a satellite-based global aerosol emission database (2006-2011) has been developed. This aerosol emission database has been further evaluated by utilization in GEOS-Chem and GEOS-5/GOCART models. The model posterior simulation of aerosol properties employing the retrieved emissions shows a better agreement than the model prior simulation; it is true for not only fitted PARASOL products, but also for completely independent measurements from ground-based AERONET and satellites aerosol products (e.g., MODIS, MISR, OMI). The results suggest that the satellite-based aerosol emission database improves overall global aerosol modeling.

Keywords: aerosol emissions; PARASOL/GRASP; adjoint GEOS-Chem; inverse modeling; desert dust; black carbon; organic carbon.

Résumé

La compréhension du rôle des aérosols atmosphériques dans le fonctionnement du système terre-atmosphère est limitée par les incertitudes sur leur répartition spatiale, leur composition et leurs sources. Si leurs impacts sur le changement climatique et l'environnement peuvent être évalués grâce aux modèles de chimie-transport, ces incertitudes en limitent la précision. Les observations satellitaires ont la capacité de fournir à l'échelle globale des informations précises sur un certain nombre de paramètres « aérosols » mais elles sont limitées par les conditions nuageuses, la périodicité des orbites et par le contenu en information, c'est-à-dire le type de paramètres que l'on peut retrouver suivant la nature de ces observations. Une approche prometteuse consiste à améliorer les champs d'émission des modèles en utilisant le principe de la modélisation inverse. Dans cette étude, nous avons conçu une méthode de restitution simultanée des sources d'émission de poussières désertiques, de carbone suie et de carbone organique à partir des produits satellitaires (POLDER/PARASOL) dérivés en utilisant l'algorithme GRASP, conjointement à une modélisation inverse du modèle GEOS-Chem. Cela nous a permis de créer une base de données d'émissions globales d'aérosols sur la période 2006–2011. Des simulations réalisées avec les modèles directs GEOS-Chem et GEOS-5/GOCART utilisant cette base de données montrent bien entendu un bon accord avec des observations POLDER mais aussi une nette amélioration de la modélisation de l'aérosol à l'échelle globale lorsque l'on compare les sorties à des mesures indépendantes du réseau AERONET ou à d'autres mesures spatiales (MODIS, MISR, OMI).

Mots clés: émissions d'aérosols; PARASOL/GRASP; adjoint GEOS-Chem; modélisation inverse; poussière du désert; carbone noir; carbone organique.

Acknowledgements

I would like to express my sincere gratitude to many people without whom this thesis would not have been possible. Foremost, I would also particular thank my supervisor, Dr. Oleg Duvovik. He gave me a framework insight to start this scientific research and led me to appreciate the pleasure of doing research step by step. I have been very fortunate to have an excellent advisor to guide me thought my PhD. Oleg is an advisor who is really supportive not only to the scientific work but also the academic career of his students. He always encouraged and motivated me, providing me the effective point view from time to time, and correcting opportunely my mistakes. Thanks to Oleg for encouraging and supporting me to attend many conferences to present my studies and to get connected to the peers and scientists in my research fields. I sincerely appreciate the genuine support and investment Oleg has shown in my academic career.

Special thanks to my thesis committee members: Dr. Mian Chin, Dr. Gregory L. Schuster, Dr. Lorraine A. Remer, Dr. Oliver Boucher, Dr. Daven K. Henze and Dr. Didier Tanré. I thank them to their careful reviews, invaluable advices and comments that helped to improve this manuscript and would be of great benefit for my future research. Daven guided me to develop the PARASOL/GRASP module on the GEOS-Chem adjoint modeling, and providing constructive suggestions on my manuscript and help thought my PhD. Mian encourage me to implement the retrieved aerosol emission data on other CTMs, which is the desirable goal of this thesis.

I would also like to thank Tatyana Lapyonak for her continuous help of the development of the inversion model, and carefully answering my questions regarding the adjoint method used in this study. I also wish to thank her patient for revising this manuscript. I would like to acknowledge all the great help I received from people in Laboratoire d'Optique Atmosphérique. I thank Fabrice Ducos, François Thieuleux and Romain De Filippi for help in using LOA sever. I also thank Philippe Goloub, Yevgeny Derimian, Jankowiak Isabelle, Anne Priem, Marie-Lyse Liévin, Lucia Deaconu, Laura Rivellini, Ioana Popovici and Forin Unga for providing the helps not only in scientific research but also the logistics in France.

I'm highly thankful all my friends in GRASP group, including Pavel Litvinov, Benjamin Torres, David Fuertes, Anton Lopatin, Xin Huang, Qiaoyun Hu and Lei Li. I'm really lucky and enjoyable for working with you. Without supports from them, much of this work would not have been completed.

Finally, to my father Guocheng Zhang, my mother Meilan Yan, my wonderful wife Fan Yang, and my nice mother-in-law Hong Li and father-in-law Bensong Yang. This work is dedicated to them.

Dedication

To

my father Guocheng Zhang (张国成), my mother Meilan Yan (颜美兰), my wonderful wife Fan Yang (杨帆), and my nice mother-in-law Hong Li (李红) and father-in-law Bensong Yang (杨本松) for their constant support and unconditional love.

Table of Contents

List of Figures

List of Tables

Chapter 1

General introduction

> Even though the future seems far away, it is actually beginning right now.
>
> Mattie Stepanek

The atmospheric aerosol is a complex and dynamic mixture of solid and liquid particles from natural and anthropogenic sources. The amount and properties of aerosols are extremely variable in space and time. The aerosol characteristics of high interest are the size distribution, chemical composition, and shape of the particles. It is useful to classify aerosols in different categories according to these properties. There are several possible classifications.

Natural and Anthropogenic Aerosols

Aerosols are produced from natural processes and anthropogenic activities. The natural sources include windborne dust, sea spray, volcanic activities and biomass burning etc., while emissions attributable to the anthropogenic activities arise primarily from fuel combustion, industrial processes, nonindustrial fugitive sources (e.g. construction work), and transportation sources (e.g. vehicles, ships). Natural aerosols are 4 to 5 times larger in amount than anthropogenic ones on a global scale, but regional variation in man-made pollution may change this ratio significantly in certain area, particularly in the industrialized Northern Hemisphere.

Primary and Secondary Aerosols

Aerosols also can be divided into two classes, namely primary and secondary aerosols, according to the mechanisms of their origination. Primary aerosol particles

are emitted into the air directly. This is the case of aerosols produced by the effect of the wind friction on an oceanic or terrestrial surface and aerosols produced during an incomplete combustion. While secondary aerosol particles designate those particles that have not been emitted directly in the particulate phase but formed in the atmosphere by gas-particle conversion such as nucleation, condensation, heterogeneous and multiphase chemical reactions. Anthropogenic aerosols include primary (directly emitted) particles and secondary particles that are formed in the atmosphere from aerosol precursor gases.

Fine and Coarse Mode Aerosols

The Nuclei Mode (particle diameter < 0.1μm) consists primarily of combustion particles emitted directly into the atmosphere and particles formed in the atmosphere by gas-to-particle conversion. They are usually found near highways and other sources of combustion. Because of their high number concentration, especially near their sources, these small particles coagulate rapidly. Consequently, nuclei particles have relatively short lifetimes in the atmosphere and end up in the accumulation mode.

The Accumulation Mode (0.1μm < particle diameter < 2.0μm or 2.5μm) includes combustion particles, smoke particles and coagulated nuclei mode particles. Particles in this mode are small but they coagulated too slowly to reach the coarse mode. Hence, they have a relatively long lifetime in the atmosphere and they account for most the visibility effects of atmosphere. In general, the nuclei and accumulation modes together constitute “Fine Mode” aerosols.

The Coarse Mode (particle diameter > 2.0μm or 2.5μm) consists of windblown dust, large sea salt particles from sea spray and mechanically generated anthropogenic particles such as those from agriculture and surface mining. Because of their large size, the coarse particles readily settle out or impact on surface, so their lifetime in the atmosphere is short. (http://aerosol.ees.ufl.edu/atmos_aerosol/section04-1.html)

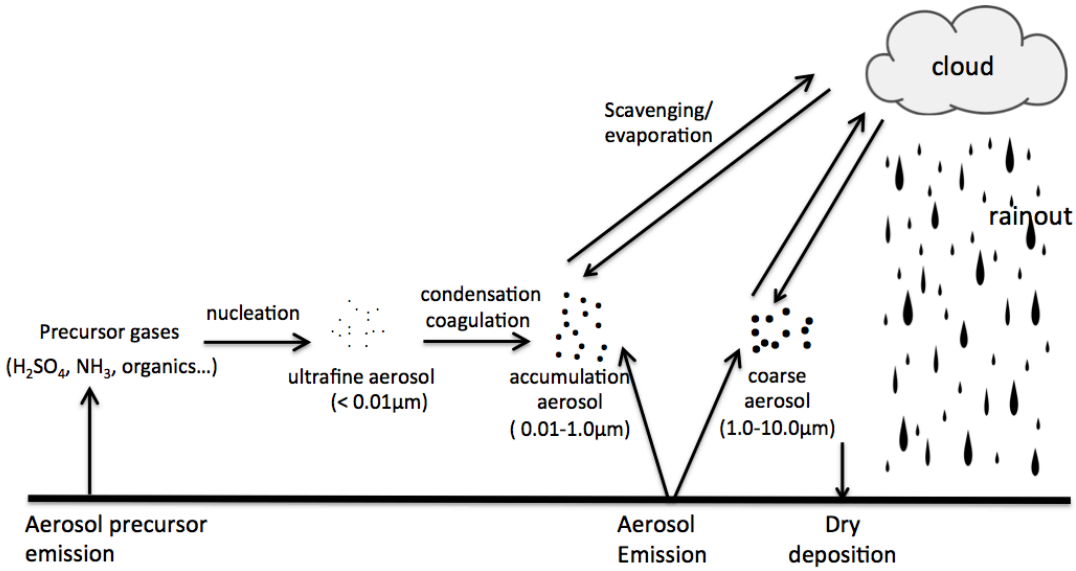

Figure 1.1: Illustration of emission, growth and removal of atmospheric aerosols, referred to Jacob, (1999).

Table 1.1: Estimated source strengths, lifetimes, and optical depth of major aerosol types. Statistics are based on results from 16 models examined by the Aerosol Comparisons between Observations and Models (AeroCom) projects (Kinne et al., 2006; Textor et al., 2006).

Aerosol Type	Total Emission (Tg/yr)	Optical Depth (550nm)	Life Time (day)
Sulfate	190 (100-230)	0.034 (0.015-0.051)	4.1 (2.6-5.4)
Black Carbon	11 (8-20)	0.004 (0.002-0.009)	6.5 (5.3-15)
Organic Matter	100 (50-140)	0.019 (0.006-0.030)	6.2 (4.3-11)
Desert Dust	1600 (700-4000)	0.032 (0.012-0.054)	4.0 (0.03-7)
Sea Salt	6000 (2000-120000)	0.030 (0.020-0.067)	0.4 (0.03-1.1)

Tg (teragram)=10^{12} gram or 1 million metric tons

The sulfate aerosol source is mainly SO_2 oxidation plus a small fraction of direct emission. The organic matter source includes direct emission and hydrocarbon oxidation

Figure 1.1 illustrates the different processes involved in the aerosol emission, growth and eventual removal of different type and size of atmospheric aerosol particles. Aerosol simulation community commonly uses a discrimination of aerosol in five components: sulfate (SU), black carbon (BC), organic matter (OM), desert dust (DD) and sea salt (SS) for a better characterization of aerosol optical and microphysical properties. SS and DD contributions dominate the coarse size mode, while the fine mode is accumulated by SU, BC and OM. In addition, DD and OM

particles absorb most strongly in the UV and short wave visible channels, while BC particles are absorbing more ubiquitously (Kinne et al., 2006; Textor et al., 2006). Table 1.1 reproduced from Chin et al. (2009), presents the emissions, optical depth and life time of these five aerosol components, as represented by current aerosol transport models.

1.1 Importance of atmospheric aerosols

Atmospheric aerosols play a key role in many important environmental aspects including climate change, stratospheric ozone depletion and tropospheric air pollution. Atmospheric aerosols affect climate through three primary mechanisms (King et al., 1999). First, direct radiative forcing results when radiation is scattered or absorbed by the aerosol itself. Scattering of shortwave radiation enhances the radiation reflected back to space, therefore increasing the reflectance (albedo) of the earth and cooling the climate system. Absorption of solar and long wave radiation alters the atmospheric heating rate, which in turn may result into changes to the atmospheric circulation. Second, indirect radiative forcing results to enhance concentrations of aerosol particles and modify cloud properties, resulting in more cloud droplets, albeit smaller in size, that generally increase the albedo of clouds in the earth's atmosphere. The indirect effect could be subdivided in two different groups: Twomey effect (Twomey, 1974, 1977) and Albreicht effect (Albrecht, 1989). In Twomey effect, aerosol influences cloud formation by providing additional nuclei for droplet of ice crystals growth (Boucher, 1999). While in Albreicht effect, aerosol effects change cloud lifetime and other cloud properties like liquid water content and cloud top height. Finally, aerosol particles could modify the atmospheric temperature profile by absorbing aerosols, and then affecting the presence of clouds. Detailed description of definition of aerosol three climate effects can be found in Haywood and Boucher, (2000).

The radiative forcing (RF) is one of the ways to quantify how aerosol contributes to climate change. Aerosol radiative forcing is the net change in the energy balance of the earth system due to the presence of atmospheric aerosols. It is usually expressed in watts per square meter (w/m^2) averaged over a particular period of time and quantifies the energy imbalance that occurs when the imposed change take place. In the Intergovernmental Panel on Climate Change (IPCC) reports, there are RF of aerosol-radiation interaction (direct effect), RF of the aerosol-cloud interaction

(indirect and semi-direct effect) and the impact of BC particles on snow and ice surface albedo. According to the latest IPCC (2013), the total aerosol-radiation and aerosol-cloud interaction (excluding BC on snow and ice) is estimated with a 5% to 95% uncertainty between -1.9 and -0.1 w/m^2 with the best estimate value of -0.9 w/m^2 (medium confidence). Table 1.2 lists the best estimates of RF due to aerosol-radiation interaction for various aerosol components taken from four versions of IPCC reports. Because absorption by ice is very weak at visible and ultraviolet wavelengths, BC in snow makes the snow darker and increases absorption. The anthropogenic BC on snow/ice is assessed to have a positive global and annual mean RF of +0.04 w/m^2, with a 5% to 95% uncertainty from +0.02 to +0.09 w/m^2 (IPCC, 2013). Overall, aerosol RF can be compared in magnitude to a radiative forcing for well-mixed greenhouse gases, however the aerosol effects continue to represent one of the largest uncertainties in the detection and prediction of climate change study.

Table 1.2: Summary of aerosol radiative forcing (w/m^2) due to aerosol-radiation interaction of seven aerosol components and comparisons between four versions of IPCC assessment reports, taken from (IPCC), (2013).

	Global Mean Aerosol Radiative Forcing (w/m^2)			
	IPCC (1995)	**IPCC (2001)**	**IPCC (2007)**	**IPCC (2013)**
Sulfate	-0.4(-0.80 to -0.20)	-0.4(-0.60 to -0.20)	-0.4(-0.60 to -0.20)	-0.4(-0.60 to -0.20)
Anthropogenic BC	+0.10(+0.03 to +0.30)	+0.20(+0.10 to +0.40)	+0.20(+0.05 to +0.35)	+0.40(+0.05 to +0.8(
Anthropogenic OC	Not estimated	-0.10(-0.30 to -0.03)	-0.05(0.00 to -0.10)	-0.09(-0.16 to -0.03)
Biomass burning	-0.20(-0.60 to -0.07)	-0.20(-0.60 to -0.07)	+0.03(-0.09 to +0.15)	-0.0(-0.20 to +0.20)
SOA	Not estimated	Not estimated	Not estimated	-0.03(-0.27 to +0.20)
Nitrate	Not estimated	Not estimated	-0.10(-0.20 to 0.00)	-0.11(-0.30 to -0.03)
Dust	Not estimated	-0.60 to +0.40	-0.10(-0.30 to +0.10)	-0.10(-0.30 to +0.10)
Total	Not estimated	Not estimated	-0.50(-0.90 to -0.10)	-0.35(-0.85 to +0.15)

In the short term and regional scale, aerosol particles can degrade visibility and damage aviation and transport. The World Health Organization (WHO, 2016) has reported country estimates of air pollution exposure and its health impact, which suggests that 6.5 millions deaths (11.6% of all global deaths per year) may be associated with air pollution, and 92% of the world's population lives in places where air quality levels do not meet the WHO ambient air quality guideline of an annual mean $PM_{2.5}$ (particulate matter with a diameter of less than 2.5 microns) concentration of less than 10 $\mu g/m^3$. From this environment standpoint, aerosols still constitute an

important policy issue in air quality, and it is probably the most pressing issue in air quality regulation worldwide. Thus, knowledge of the global distribution of atmospheric aerosols is important for studying the effects of aerosols on global climate and air pollution. Thus, reliable observation and simulation systems are needed to be established to understand the role atmospheric aerosols play in earth-atmosphere system (Bellouin et al., 2005).

1.2 Challenges and opportunities

At present, there are many well-established Global Circulation Models (GCMs) that simulate the global aerosol distributions by generating their own meteorology (e.g. models by Koch, 2001; Koch et al., 1999; Roeckner et al., 1996, 2003; Stevens et al., 2013; Tegen et al., 2000) and Chemical Transport Models (CTMs) that incorporate meteorological data from external sources into the model physics (e.g. models by Balkanski et al., 1993; Chin et al., 2000; Takemura et al., 2000; Ginoux et al., 2001; Bessagnet et al., 2004; Grell et al., 2005; Spracklen et al., 2005; Mann et al., 2010). However, the CTMs simulation is limited by uncertainties in knowledge of aerosol emission source characteristics, knowledge of atmospheric processes and the meteorological field data used. The large model diversity in compositional aerosol emissions, shown in Table 1.1, affects the simulation of aerosol properties. As a result, even the most recent models are mainly expected to capture only the principal global features of aerosol. For example, among different models, quantitative estimates of average regional aerosol properties often disagree by amounts exceeding the uncertainty of remote sensing of aerosol observations (Chin et al., 2002, 2014, Kinne et al., 2003, 2006; Textor et al., 2006). Therefore, there are diverse and continuing efforts to harmonize and improve aerosol modeling by refining the meteorology, atmospheric process representations, emissions and other components (e.g. aerosol aging scheme, particle mixing state etc.) (Watson et al., 2002; Dabberdt et al., 2004; Generoso et al., 2007; Ghan et al., 2007; He et al., 2016; Wang et al., 2014a, 2016).

Current aerosol emission estimation is largely based on the “bottom-up” method that integrates diverse information such as population, fuel consumption in various industries and corresponding measurements of emission rates for different species (Streets et al., 2003), economic growth, and the statistics of the land use and fire burned area (van der Werf et al., 2006). While significant progress has been made

(Streets et al., 2006), the "bottom-up" approach still has a number of limitations (Xu et al., 2013):

(i) The bottom-up emission inventory usually has a temporal lag of at least 2 to 3 years, because time is needed to aggregate information from different sources and format them into the emission inventories that are suitable for use in climate models.

(ii) The temporal resolution of the current bottom-up aerosol emission inventories is usually on monthly to annual scale, which is not sufficient to capture the daily or diurnal variation of aerosol distributions.

(iii) The spatial resolutions of the bottom-up emission inventories are usually limited by the availability of the external information, which often lack the spatial coverage for emission estimation in a uniformly fine resolution for regional modeling of aerosol transport.

(iv) The bottom-up emission inventories may miss important emission sources that are not well documented including emission from wild fires, volcanic eruptions, and agricultural activities.

All these limitations can be amplified in the chemical transport model simulation, because the uncertainty of aerosol emission can translate into a high uncertainty of aerosol simulation and a significant high uncertainty of aerosol climate effect evaluation.

Space-borne remote sensing instruments offer an integrated atmospheric column measurement of the amount of light scattering by aerosols through modification of diffuse and direct solar radiation. Numerous satellite observations of the spatial and temporal distribution of aerosols have been conducted in the last two decades (King et al., 1999; Kaufman et al., 2002; Lenoble et al., 2013). The satellite retrievals of Aerosol Optical Depth (AOD) and Aerosol Absorption Optical Depth (AAOD) are directly related to light extinction and absorption due to the presence of aerosol particles. AOD is a basic optical property derived from many earth-observation satellite sensors, such as AVHRR (Advanced Very High Resolution Radiometer), MODIS (Moderate Resolution Imaging Spectroradiometer), MISR (Multi-angular Imaging SpectroRadiometer) and POLDER (Polarization and Directionality of the Earth's Reflectances) (Goloub et al., 1999; Geogdzhayev et al., 2002; Kahn et al., 2009; Tanré et al., 2011; Levy et al., 2013). AAOD is another valuable product to quantify the solar absorption potential of aerosol, however only a few satellite sensors

can provide retrieval of AAOD, and only with limited accuracy, for example OMI (Ozone Monitoring Instrument) on the Aura satellite (Torres et al., 2007; Veihelmann et al., 2007) and POLDER on PARASOL (Polarization & Anisotropy of Reflectances for Atmospheric Sciences coupled with Observations from a Lidar), because only ultraviolet (UV) and shortwave visible channels and polarimetric measurements are sensitive to aerosol absorption.

Despite their ability to provide a high-degree of spatial coverage, satellite measurements alone are not sufficient for answering question regarding the distributions, magnitudes, and fates of aerosols in the atmosphere. These aspects can be studied using CTMs. Combination of aerosol satellite remote sensing and aerosol model simulation can be applied for interpretation of observed spatial distributions, as observed from the satellite, and vice verse. One of the most promising approaches for reducing model uncertainty is to improve the aerosol emission fields (that is input for the models) by inverse modeling, i.e. fitting satellite observations and model estimates and by adjusting aerosol emissions. For example, Dubovik et al. (2008) developed an algorithm for inverting MODIS data and implemented the approach to retrieve distributions of aerosol emissions. The algorithm was used to implement the first formal retrieval of global emission distributions of fine mode aerosol from the MODIS fine mode AOD data. Wang et al. (2012) and Xu et al. (2013) use MODIS radiances to constrain aerosol sources over China. Huneeus et al. (2012, 2013) optimize global aerosol emission source from MODIS AOD with a simplified aerosol model (Huneeus et al., 2009). However, as discussed in works such as Dubovik et al. (2008) and Meland et al. (2013), MODIS AOD (as well as currently available aerosol satellite data) contains only limited information to evaluate aerosol types, properties, or speciated emissions. Further, inconsistencies between representations of aerosol microphysics between the CTM and the aerosol retrieval algorithm can have significant influences on inverse modeling of aerosol sources (e.g. Drury et al., 2010; Wang et al., 2010). Therefore, the retrieval of aerosol emission sources from satellite observations remains very challenging.

The recently generated PARASOL/GRASP (General Retrieval of Atmosphere and Surface Properties) spectral AOD and AAOD data (Dubovik et al., 2011, 2014; data available from ICARE data distribution portal: http://www.icare.univ-lille1.fr/) present new opportunities for constraining DD, BC and OC sources because their optical properties vary dramatically in the spectrum of short wave visible to near

infrared (VIS-NIR) viewed by PARASOL. Polarimetric remote sensing measurements such as those from PARASOL have been postulated to provide much greater constraints on speciated aerosol emissions and microphysical properties (Meland et al., 2013). DD aerosols are dominated by coarse mode particles, and their AOD varies slightly in the VIS-NIR spectral range; in contrast, the AOD of fine mode dominated BC and OC aerosols decrease sharply in this spectral range. In addition, DD and OC particles absorb most strongly in the UV and short wave visible channels, such as 443 nm, while BC particles are absorbing more ubiquitously (Sato et al., 2003). The GRASP retrieval overcomes the difficulty of deriving aerosol over bright surfaces in the shortwave visible wavelengths, which should help improve constraints of DD emissions over source regions, rather than having to rely on downwind observations (e.g., Wang et al., 2012).

1.3 Research goals and thesis outline

The main research goal of this PhD work is to explore the possibility of the retrieval of aerosol emission sources from recent aerosol data retrieved from the polarimetric POLDER/PARASOL produced with the GRASP algorithm. To achieve the objective, GEOS-Chem model (Bey et al., 2001) has been chosen for this study because it is the community model (http://acmg.seas.harvard.edu/geos/) with constantly maintained and improved adjoint module. The adjoint operator of GEOS-Chem model is realized by Henze et al. (2007). However, the current aerosol emission retrievals are limited by the information from satellite observations. The approach proposed in this work is aimed to take advantage from aerosol spectral AOD and AAOD from PARASOL/GRASP to retrieve emissions of the major aerosol types by inverting GEOS-Chem model. In order to achieve this objective, several developments were realized. First, the modeling of AOD and AAOD consistent with PARASOL/GRASP forward model was implemented in adjoint GEOS-Chem model. Second, the retrieval procedure of aerosol emissions has been set up. The procedure was designed as simultaneous fitting of spectral aerosol extinction and absorption information by adjusting the emission of the aerosol. The study was relaying on the positive heritage of inverse modeling in the previous studies (Dubovik et al., 2008; Henze et al., 2007, 2009).

This PhD thesis is structured into six logical parts, each describing a milestone in the aerosol emission retrieval method development. First chapter provides an

overview of the challenges and opportunities in the field of study followed by the description of research goals and structural outline of this study. Second chapter is dedicated to the atmospheric aerosols and their properties, as well as to the aerosol remote sensing techniques both from ground base and satellites and the introduction of aerosol simulation system. Third chapter contains detailed description of the proposed retrieval methods. The retrieval method was rigorously tested by a series of sensitivity experiments, for two scenarios when the retrieval is implemented over Africa and over entire Globe. Fourth chapter is an application of designed retrieval method over Africa. It contains the detailed description of the method application over Africa, the evaluation of input PARASOL/GRASP aerosol products over Africa, and the description of retrieved one-year DD, BC and organic carbon (OC) aerosol emission. Also, the results are also validated with independent measurements. Fifth chapter discusses the efforts on applying the developed method for the generation of a six-years (2006-2011) of global dataset of aerosol emission of DD, primary BC and OC. It contains the evaluation of this PARASOL/GRASP based aerosol emission dataset and analysis of the obtained datasets compare to the existent emission datasets. Specifically, the obtained emissions were implemented in GEOS-Chem and GEOS-5/GOCART (Goddard Chemistry Aerosol Radiation and Transport) chemical transport models (Chin et al., 2002, 2009, 2014; Colarco et al., 2010) and the simulated aerosol properties are validated against independent measurements from ground-based AERONET and space-borne MODIS, MISR and OMI. Sixth chapter contains the conclusions and the discussions of algorithm potential and limitations.

Chapter 2

Remote sensing and modeling of atmospheric aerosols

> Research is to see what everybody else has seen, and to think what nobody else has thought.
>
> Albert Szent-Gyorgyi

2.1 Aerosol optical and microphysical properties

Aerosol particles can be described and characterized by optical and microphysical properties. The main optical and microphysical properties of aerosols required for determining their radiation effects include the aerosol optical depth, aerosol absorption optical depth, Ångström exponent (spectral dependence of optical depth), single scattering albedo, phase matrix, complex refractive index and particle size distribution. In this section, we will describe the different aerosol properties that are used in our study.

2.1.1 Aerosol Optical Depth (AOD)

The Aerosol Optical Depth (AOD or τ) (also called aerosol optical thickness, AOT, in the literature) is the measure of aerosols distributed within an integrated

atmospheric column from the Earth's surface to the top of atmosphere, and is an extensive state parameter associated with aerosol column amount. In general, most remote sensing methods retrieve AOD. According to the Bouguer-Lambert-Beer law, the sunlight traverses atmosphere by scattering and absorption:

$$I(\lambda) = I_0(\lambda)\exp\left[-m \cdot \tau^{atm}(\lambda)\right] \quad (2.1)$$

where λ stands for wavelength, I_0 is the intensity of sunlight at the upper limit of the atmosphere, m is the optical air mass that can be approximated as $m = 1/[cos\theta_s + 0.50572 \cdot (96.07995 - \theta_s)^{-1.6364}]$, here θ_s represents solar zenith angle (Kasten and Young, 1989). τ^{atm} describes the total column optical depth and is the sum of aerosol and molecular (Rayleigh) optical depth under the cloud-free conditions:

$$\tau^{atm}(\lambda) = \tau^{aer}(\lambda) + \tau^{ray}(\lambda) \quad (2.2)$$

Meanwhile, optical depth of aerosols in the light path is referred to AOD and is also sum of depth of optical scattering and absorption.

$$\tau(\lambda) = \tau_a(\lambda) + \tau_s(\lambda) \quad (2.3)$$

where τ represents optical depth of aerosols, τ_a is optical depth due to aerosol absorption (also called aerosol absorption optical depth), and τ_s stands for aerosol scattering optical depth.

2.1.2 Single Scattering Albedo (SSA)

Aerosol scattering albedo (SSA or ω_0) is a measure of the fraction of aerosol total light extinction due to scattering, which also provides information about the absorption properties of the aerosols, and therefore it is of critical importance for quantifying the impact of aerosols on climate. The aerosol single scattering albedo is defined as the fraction of the aerosol light scattering in the total extinction:

$$\omega_0 = \tau_s/\tau = {}^{\sigma_s}/_{(\sigma_s + \sigma_a)} \quad (2.4)$$

where τ_s and τ represent aerosol scattering optical depth and aerosol optical depth respectively; σ_s and σ_a are the aerosol scattering and absorption coefficients, respectively. SSA is one of the most relevant optical properties of aerosols, since their direct radiative effect is very sensitive to it. Values of SSA range from 0.0 for totally absorbing (dark) particles to 1.0 for purely scattering particles; in nature, SSA is rarely lower than about 0.70.

2.1.3 Ångström exponent (AExp)

Ångström exponent (AExp or α) is a measure of differences of AOD at different wavelengths, which is also used to describe the dependency of the AOD, or aerosol extinction coefficient with wavelength. The AOD at two different wavelengths allows determination of Ångström exponent as follows (Ångström, (1929)):

$$\alpha = -\ln [\tau(\lambda_1)/\tau(\lambda_2)]/\ln (\lambda_1/\lambda_2) \quad (2.5)$$

Ångström exponent relates to the sizes of aerosol particles. Namely, α tends to be inversely dependent on particle size; larger values are generally associated with smaller aerosol particles. Basically, the values of α less than 0.6 indicate large particles like desert dust and the values greater than 1.0 indicate small particles like sulfate, black and organic carbon particles (Eck et al., 1999; Schuster et al., 2006). Ångström exponent with combination with other parameters such as AOD and SSA are widely used for aerosol classifications in various studies (e.g. Toledano et al., 2007; Penning de Vries et al., 2015).

2.1.4 Aerosol Absorption Optical Depth (AAOD)

The aerosol absorption optical depth (AAOD or τ_a) is defined as integration of the aerosol absorption coefficient of the layers $\sigma_a(z)$ over a vertical path of a light beam from the ground to the top of the atmosphere (TOA):

$$\tau_a = \int_0^{TOA} \sigma_a(z)dz \quad (2.6)$$

The aerosol absorption properties are directly related to its composition, for example, most of the absorption in aerosol compound is due to presence of black carbon, absorbing mineral dust and organic/brown carbon, whereas other species (sea salt and sulfate) are predominantly non-absorbing aerosols. However, the spectral range allows discrimination between absorbing species that absorb most strongly in the UV and short visible region, such as organic/brown carbon and mineral dust, and the more ubiquitously absorbing black carbon (Sato et al., 2003).

2.1.5 Aerosol complex refractive index

The real part of complex refractive index is the ratio of light velocity in a vacuum to light velocity in this substance, which is related to light scattering. Meanwhile, the aerosol absorbing ability is determined by the imaginary part of the complex refractive index. The complex refractive index (m) is expressed as:

$$m = n + ik \tag{2.7}$$

where n and k represent real and imaginary parts of refractive index, respectively. The aerosol refractive index depends on the chemical composition and the source of pollution. For example, the DD and SS aerosol, there is high spectral dependency of imaginary part. BC aerosol is the most strongly absorbers of solar radiation, furthermore the imaginary part of the complex refractive index, which is about 2 orders of magnitude higher for BC aerosol than other aerosol species. For biomass burning aerosol, the real part is ranged from 1.47 to 1.52. The refractive index of hydrophilic aerosol also depends on relative humidity (RH) decreasing with its increase.

2.1.5 Aerosol size distribution

The distribution of aerosol particle size can be represented by differential radius number density distribution, which represents the number of particles with radius between r and $r + dr$ per unit volume. Hence, the total number of particles per unit volume, N_0, is given by

$$N_0 = \int_0^\infty n(r)dr \tag{2.8}$$

The particle size distribution can also be approximately described using a mathematical function, such as Junge power function distribution, gamma distribution, lognormal distribution etc. According to many studies (Deshler et al., 1993; Jäger and Hofmann, 1991), the lognormal size distribution can well characterize many observed real size distributions. Variation in the number of particles n as a function of the natural logarithm of the radius r can be written as

$$n(\ln r) = \frac{dN}{d\ln r} = \frac{N_0}{\sqrt{2\pi}} \frac{1}{\ln \sigma_0} \exp\left[-\frac{(\ln r - \ln r_0)^2}{2\ln^2 \sigma_0}\right] \tag{2.9}$$

where $n(\ln r)$ is the number of particles with radius between $\ln r$ and $\ln r + d\ln r$, r_0 is the mode radius, σ_0 is the standard deviation of the natural logarithm of the radius (the width of the distribution) and N_0 is the total number of particles.

Equivalent equation can be calculated for a log-normal volume density distribution, $v(\ln r)$, can be expressed as

$$v(\ln r) = \frac{dV}{d\ln r} = \frac{V_0}{\sqrt{2\pi}} \frac{1}{\ln \sigma_v} \exp\left[-\frac{(lnr - lnr_v)^2}{2ln^2 \sigma_v}\right] \tag{2.10}$$

where V_0 is the total aerosol volume per unit volume of atmosphere, r_v is the mode radius for the volume size distribution and σ_v is the geometric standard deviation.

A multi-mode distribution is simply described by a sum of several lognormal distributions. For example, the bi-modal lognormal size distribution is widely used in aerosol remote sensing and modeling. In addition, sometimes aerosol size distributions are complex superposition of more than two modes, and modern retrieval methods that allow for arbitrary shaped size distributions do retrieve distributions that would not fit a lognormal. For example, in the AERONET retrieval, volume size distribution was represented by 22 radius bins of equidistant in logarithmic scale, covering the size range from 0.05 to 15μm (Dubovik and King, 2000).

2.2 Aerosol remote sensing

The global distribution of aerosols can be detected by remote sensing techniques from ground-based instruments and space-borne satellites. One of the reasons for applying remote sensing techniques to derive distribution of aerosol characteristics is to provide strong observational constrains on model depictions of global aerosol distribution (Chung et al., 2012; Sato et al., 2003).

2.2.1 Ground-based remote sensing by AERONET

The AERONET (AErosol RObotic NETwork) is a global collection of ground-based sun photometers providing reliable and accurate aerosol measurements (Holben et al., 1998), and is federation of regional and national networks deployed in the 1990s by collaboration of the National Aeronautics and Space Administration (NASA) with PHOTONS (Laboratoire d'Optique Atmosphérique-LOA, University of Lille1) in the form of automatic stations for monitoring atmospheric aerosols. The automatic sun and sky scanning radiometers are returned annually to calibration center in GSFC (Goddard Space Flight Center) and LOA for calibration against Langley calibrated reference instrument of AOD (±0.01) and a referenced integrating sphere for sky radiances (>5% absolute accuracy).

For AERONET standard sun photometer (CIMEL 318), the direct sun measurements are made in several spectral channels (anywhere between 340nm and

1640nm; 440nm, 670nm, 870nm, 940nm and 1020nm are standard). Sky measurements are performed at 440nm, 670nm, 870nm and 1020nm. The latest AERONET inversion algorithm (Dubovik et al., 2006; Dubovik and King, 2000) provides improved aerosol retrievals by fitting the entire measured field of radiances (sun radiance and the angular distribution of sky radiances) at four wavelengths (440, 670, 870 and 1020nm) to a radiative transfer model. Currently, the radiances measured by the almucantar sequence are used to make aerosol information retrieval. The radiation field is driven by the wavelength dependent aerosol complex index of refraction and the particle size distribution (in the range: 0.05 $\mu m \leq r \leq 15\ \mu m$) in the total atmospheric column. Using such a general aerosol model in the retrieval algorithm allows us to derive the aerosol properties with minimal assumptions. Only spectral and size smoothness constrains are used, preventing unrealistic oscillations in either parameter. Recent studies try to include polarimetric measurements from new CIMEL 318DP sun photometer into inversion algorithm (Fedarenka et al., 2016; Li et al., 2009b; Xu et al., 2015; Xu and Wang, 2015).

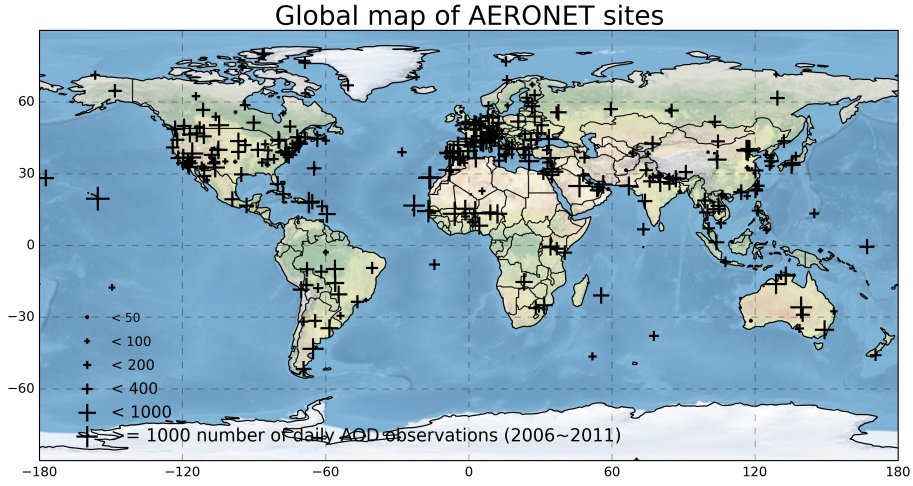

Figure 2.1: Global map of AERONET sites used in this study; the total number of daily AOD observations of a single site from 2006 to 2011 determines the size of each cross over plotted; according to the data from AERONET website: https://aeronet.gsfc.nasa.gov/

AERONET measures clear sky spectral AOD with an accuracy of ±0.02 at wavelength 440nm and ±0.01 at wavelengths ≥ 440nm (Eck et al., 1999). In addition, a number of other tendencies useful for improving retrieved aerosol properties accuracies were identified in Dubovik et al. (2000, 2002b, 2006) and Dubovik and

King, (2000). For example, the accuracy of SSA is ±0.03 when AOD>0.2. Because of consistent calibration, cloud screening and retrieval methods, uniformly acquired and processed data are available from all stations, some of which have operated for over 20 years. These data provide a high quality ground-based climatology and are suitable for long-term trend analysis over regions. For example, AERONET data have been widely used to evaluate satellite aerosol retrievals (Kahn et al., 2005; Levy et al., 2007; Remer et al., 2005). Figure 2.1 shows the global map of AERONET sites used in this study, the total number of daily AOD observations of a single site from 2006 to 2011 determines the size of each cross over plotted. Although AERONET measurements are of the highest quality to date and rapid development in last 2 decades, they are only point measurements lucking global coverage. Therefore, accurate monitoring of aerosols on a global scale still requires improving current satellite remote sensing techniques, as well as extending the surface network.

2.2.2 Space-borne satellite remote sensing

While all types of observations provide important information and help to constrain models, only satellite remote sensing has the ability to observe and quantify the aerosol distribution on a global scale. Monitoring aerosols from space has been performed for over two decades (Deuzé et al., 1999, 2001, Dubovik et al., 2011, 2014; Goloub et al., 1999; Herman et al., 2005; Higurashi et al., 1999; Hsu et al., 2004; Husar et al., 1997; Ignatov et al., 2000; Kahn et al., 2005, 2009, Levy et al., 2007, 2010, 2013, Martonchik et al., 1998, 2002, Mishchenko et al., 1999, 2007, Remer et al., 2002, 2005, Torres et al., 1998, 2007). A number of developed and launched space instruments provide global monitoring of aerosol properties. Table 2.1 summaries major passive satellite measurements available for the tropospheric aerosol characterization. The Figure 2.2 illustrates the constellation of satellites known as the “A-Train”, which are making nearly contiguous observations of many facets of the Earth system.

Table 2.1: Summary of major satellite measurements currently available for the aerosol products

Properties	Sensor	Parameters	Spatial coverage	Temporal	Resolution	Reference
Loading	AVHRR	AOD	Ocean	1981-present	110km	(Husar et al., 1997; Ignatov et al., 2000; Mishchenko et al., 1999)
	TOMS		Land and ocean	1979-2001	50km	(Torres et al., 1998)
	POLDER/PARASOL			1997-present	18.5km	(Deuzé et al., 1999, 2001; Goloub et al., 1999)
	MODIS			2000-present (Terra) 2002-present (Aqua)	10km	(Hsu et al., 2004; Levy et al., 2013; Remer et al., 2002, 2005)
	MISR		Land and ocean	2000-present	17.6km	(Martonchik et al., 1998, 2002)
	OMI		Land and ocean	2005-present	13x24km	(Torres et al., 2007)
Size, shape	AVHRR	AExp	Ocean	1981-present	110km	(Higurashi et al., 1999)
	POLDER/PARASOL	FMF, AExp, non-spherical fraction	Land and ocean	1997-present	18.5km	(Deuzé et al., 2001; Herman et al., 2005)
	MODIS	FMF AExp, Effective radius	Land and ocean Ocean	2000-present (Terra) 2002-present (Aqua)	10km	(Remer et al., 2002, 2005) (Hsu et al., 2004; Levy et al., 2013)
	MISR	AExp, small, medium, large fractions, non-spherical fraction	Land and ocean	2000-present	17.6km	(Martonchik et al., 1998, 2002)
Absorption	TOMS	AI, SSA, AAOD	Land and ocean	1979-2001	50km	(Torres et al., 1998)
	OMI			2005-present	13x24km	(Torres et al., 2007)
	MISR	SSA (2-4bins)		2000-present	17.6km	(Martonchik et al., 1998, 2002)
Loading **Size, shape** **Absorption**	PARASOL (GRASP algorithm)	AOD AExp Size distribution non-spherical fraction AAOD SSA	Land and ocean	2004-2013	6km	(Dubovik et al., 2011, 2014)

Satellite aerosol retrievals have become increasingly sophisticated over the past decade. Now, satellites measure the angular dependence of radiance and polarization at multiple wavelengths from UV to the infrared (IR) at fine spatial resolution. From these observations, aerosol retrieval algorithm attempts to determine not only AOD at one wavelength, but also some information about particle size properties (size over both ocean and land). The accuracy for AOD measurements from these sensors is about 0.05 or 20% of AOD (Remer et al., 2005; Kahn et al., 2005) and somewhat better over dark water, but that for aerosol microphysical properties, which is useful for distinguishing aerosol mass types, is generally low.

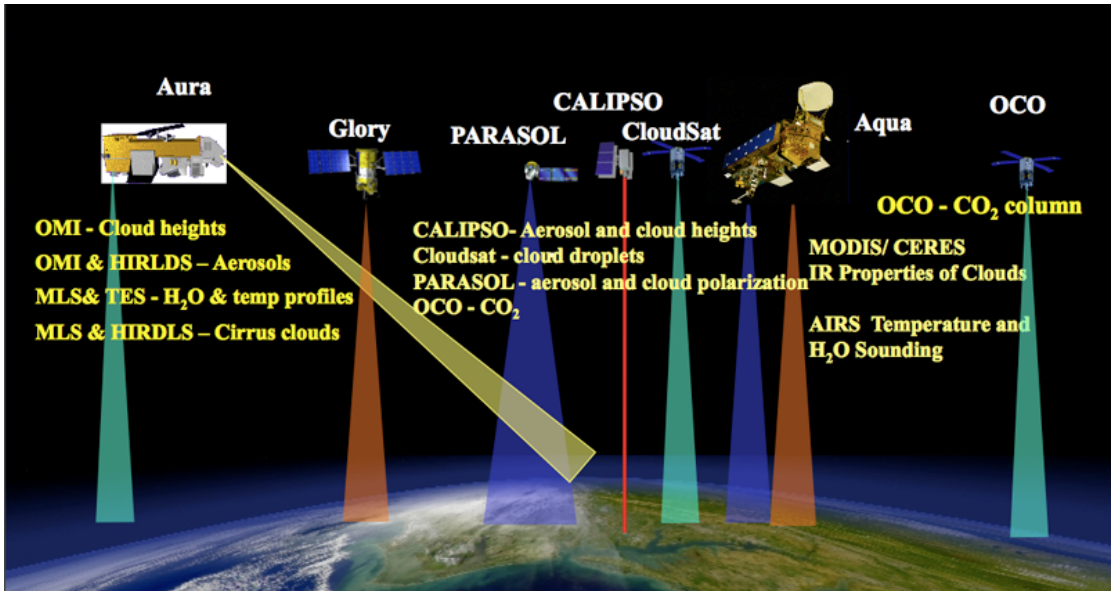

Figure 2.2: The Afternoon Constellation, so-called A-Train consists of five satellites with another two failed (Glory and OCO), of spacecraft that overfly the Equator at about 1:30PM local time; adapted from https://atrain.gsfc.nasa.gov/ScienceFormationFlying.php

The main satellites and passive sensors provide aerosol products including: Terra-MODIS, Terra-MISR, Aqua-MODIS, Aura-OMI and PARASOL-POLDER.

- MODIS

Each MODIS sensor obtains near global, daily observations of atmospheric aerosols with a swath width of 2330 km and 36 channels ranging from 410 to 15,000 nm. Eight channels, nominally, 410, 470, 550, 660, 870, 1,240, 1,630 and 2,130 nm are adopted to retrieve aerosol properties in cloud-free pixels with appropriate surface features (Hsu et al., 2006; Li et al., 2005; Martins et al., 2002; Remer et al., 2005). Because of the simplicity of the dark ocean surface, and wide spectral range, MODIS has the capability of retrieving AOD with a relative high accuracy of $\pm 0.03 \pm 0.05\tau$ according to evaluation with AERONET (Chu et al., 2002; Levy et al., 2010; Remer et al., 2002, 2005). The dark ocean surface conditions permit retrieval of information on particle size. Over vegetated land, the MODIS dark-target (DT) algorithm estimates surface reflectance in the blue and red channels based on an empirical relationship using the shortwave infrared (2,130 nm) radiance and retrieves AOD (Kaufman et al., 1997; Levy et al., 2007). AOD is retrieved at 550 nm with an accuracy of $\pm 0.05 \pm 0.15\tau$ and then extrapolated to 470 nm and 660 nm using the

selected aerosol model (Chu et al., 2002; Levy et al., 2010; Remer et al., 2005). Because of the complex spectral structure of the land surface (note that vegetation is bright, not dark in the near-IR), retrieval of aerosol information over bright surface (e.g. desert dust) is not possible.

The Deep Blue (DB) (Hsu et al., 2004) and the MultiAngle Implementation of Atmospheric Correction (MAIAC) (Lyapustin et al., 2011a, 2011b, 2012) aerosol algorithms have been developed and applied to MODIS measurements. The DB and the MAIAC algorithm offer complementary and alternative products to the original DT algorithm described above. The Deep Blue algorithm makes use of the much darker surface reflectance in the blue than at red wavelengths (Hsu et al., 2004). This is especially helpful for retrieving AOD over bright surfaces, although DB is not limited to desert dust regions. MAIAC retrieves aerosol information over land simultaneously with parameters of a surface bidirectional reflectance factor model using image-based processing applied to the time series of MODIS measurements at higher spatial resolution 1km in comparison to DT and DB 10km Level 2 aerosol products (Lyapustin et al., 2011a, 2011b, 2012).

- MISR

MISR, aboard the sun-synchronous polar orbiting Terra satellite, measures upwelling solar radiance in four spectral bands (at 446, 558, 672, and 866 nm) at each of nine view angles spread out in the forward and backward directions along the flight path (at nadir, ±70.5°, ±60.0°, ±45.6°, and ±26.1° of nadir) (Diner et al., 2002). It acquires global coverage about once per week, because a more narrow swath than MODIS, OMI and POLDER. Remote sensing of aerosol using a single view direction, as is common practice for the vast majority of satellite sensors, has limited information content even when a large number of spectral bands are available. MISR's wide range of along-track view angles makes it feasible to more accurately evaluate the surface contribution to the TOA radiances and hence retrieve aerosols over both ocean and land surfaces, including bright desert aerosol source regions and ocean regions that are contaminated by sun glint for mono-directional instruments (Diner et al., 1998, 2002, Kahn et al., 2005, 2010, Kalashnikova and Kahn, 2006, 2008, Martonchik et al., 1998, 2002). MISR limits on aerosol type to enhance MISR AOD accuracy compared to single-angle instruments in many circumstances. MISR

aerosol products provide particle type classification, based on particle size, shape and SSA constraints. These amount to distinguishing three-to-five particle size bins, two-to-four bins in SSA, and spherical vs. non-spherical particles, provided the mid-visible AOD exceeds 0.15 or 0.2, and the scene meets other basic retrieval-quality criteria (Kahn et al., 2001, 2010). More details about the MISR aerosol products are given in the references above and the MISR ATB (Algorithm Theoretical Basis) (https://eospso.gsfc.nasa.gov/atbd-category/45).

- OMI

OMI is aboard on the Aura satellite with a swath 2600 km that covers the Earth in one day. OMI is a hyper-spectral instrument that measures from 270 to 500 nm. The Aerosol Index (AI; sometimes referred to as the UV Aerosol Index, UVAI; or the Absorbing Aerosol Index, AAI) provides a measure of absorbing aerosol and a simple index to distinguish between absorbing and non-absorbing aerosols. AAI is calculated without assuming aerosol particle properties. It has been frequently used to characterize aerosol transport (Li et al., 2009a; Moulin and Chiapello, 2004; Yu et al., 2012, 2013).

There are two operational aerosol retrieval algorithms taking advantage of OMI measurements, the OMAERUV and OMAERO. The OMAERUV algorithm uses the measured radiances at 354 and 388 nm to derive AOD and AAOD at 388 nm (Torres et al., 2007). The algorithm is based on the deviation of observed radiances from expected values from Rayleigh scattering and is sensitive to AOD, aerosol absorption and height of the aerosol layer. With only two pieces of information from the two measured channels, OMAERUV cannot retrieve all three unknowns. The operational algorithm assumes aerosol layer height from climatology. The AOD is extrapolated to the visible regions using the selected aerosol spectral model (Torres et al., 2002, 2007). The OMAERO algorithm uses up to 19 channels in the spectral range of 330 nm to 500 nm to derive quantitative aerosol information. The oxygen absorption band at 477 nm is used to enhance the sensitivity to the aerosol layer height (Veihelmann et al., 2007) in a way similar to its use in the retrieval of cloud height (Acarreta et al., 2004), and becomes one of the retrieved parameters. The primary retrieved parameters are AOD and the best fitting aerosol model. Both OMAERUV and OMAERO retrieve quantitative AOD. This is AOD of the entire column, including the surface layer. Due to its spatial resolution, i.e., 13 x 24 km^2 at nadir, OMI AOD

retrievals are prone to sub-pixel cloud contamination. OMI AOD values are generally biased high with respect to MODIS measurements, likely as a result of a calibration offset and subpixel cloud contamination (Ahn et al., 2008). In comparison, OMI AAOD is less sensitive to the cloud contamination because of a partial cancellation of cloud contamination effects on AOD and SSA (Torres et al., 2007, 2013).

- POLDER/PARASOL

POLDER has multi-angular and polarimetric measurements. There have been three POLDER instruments launched into space ADEOS-POLDER (1996-1997), ADEOS2-POLDER (2003) and PARASOL-POLDER (2005–2013). The principle behind the use of polarization for the remote sensing of aerosol properties from space is the extreme sensitivity that polarization has to the microphysical properties of the aerosol particles. When used in combination with the total reflection function, either at one or multiple view angles, there is nearly a complete orthogonally in the simultaneous retrieval of extinction, absorption and particle size information, thereby leading to a much more accurate solution for both parameters. Further advantages of polarization include the fact that polarization radiance is less sensitive to surface reflection than total radiance alone (King et al., 1999). POLDER/PARASOL imager provides spectral information of angular distribution of both total and polarized components of solar radiation reflected to space. With the expectation of 3 gaseous absorption channels (763, 765 and 710 nm), the observations over each pixel include total radiance at 6 channels (443, 490, 565, 670, 865 and 1,020 nm) and linear polarization among 3 channels (490, 670 and 865 nm). The number of viewing angle is similar for all spectral channels and varies from 14 to 16 depending on solar zenith and geographical location. Meanwhile, PARASOL provides global coverage about every 2 days (Dubovik et al., 2011; Tanré et al., 2011).

The observed multi-angular polarized radiances can be exploited to better separate atmospheric from surface contributions over both land and ocean (Deuzé et al., 2001). Over ocean, the total and polarized radiances at 670 and 865 nm are used to retrieve total AOD (Deuzé et al., 1999), with a typical accuracy of $\pm 0.05 \pm 0.05\tau$ (Goloub et al., 1999). When the geometrical conditions are optimal (scattering angle ranging between 90°-160°), POLDER can derive the shape of coarse-mode particles (Herman et al., 2005). Over land, the operational aerosol retrieval is based on

measurements using only polarized light at the two wavelengths (Deuzé et al., 2001; Herman et al., 1997), to capitalize on the small and fairly spectrally neutral polarized reflectance typical of land surfaces.

Recently, advanced algorithms (GRASP, General Retrieval of Atmosphere and Surface Properties) has been developed to further exploit the aerosol information content of the POLDER measurements (Dubovik et al., 2011, 2014). The retrieval is designed as a statistically optimized multi-variable fitting of the complete PARASOL observation set: all wavelengths, all angles, and all states of polarization. The algorithm allows for a large number of unknown parameters and retrieves a set of parameters affecting measured radiation. The GRASP retrieval does not utilize precalculated look-up tables commonly used in satellite retrievals for fitting observations. Instead, GRASP retrievals searches in continuous space for the solutions and optimizes the statistical properties of the obtained retrieval. Comprehensive measurements (~144 independent measurements per pixel) from PARASOL allow GRASP to infer aerosol properties including spectral AOD and AAOD, the particle size distribution, single scattering albedo, spectral refractive index and the fraction of spherical particles (some description of the products can be found in papers of Kokhanovsky et al. (2015) and Popp et al. (2016)). Extensive information of aerosol distribution and their properties are contributed to look further into the aerosol types or compositions, which are vital to characterize the emissions from different aerosol species.

2.3 Aerosol modeling

Despite aerosol satellite remote sensing techniques having ability to provide a high-degree of spatial coverage aerosol products with a high accuracy, the drawbacks of the satellite observations is the lack of information on the chemical composition, the relatively large time span (usually more than 24 hours for polar orbiting satellites) between two successive overpasses over an area. In these regards, three dimensional (3D) chemical transport models are being developed that can describe the global speciated aerosol fields in a time continuous scale (e.g. models by Balkanski et al., 1993; Chin et al., 2000; Takemura et al., 2000; Ginoux et al., 2001; Bessagnet et al., 2004; Grell et al., 2005; Spracklen et al., 2005; Mann et al., 2010).

2.3.1 General description

Modeling of atmospheric aerosol is one useful way to understand the global distribution and transport of atmospheric aerosols. CTMs solve the continuity equation of the chemical species and each aerosol species for individual grid boxes defined in the Eulerian model (Seinfeld and Pandis, 2016). The major inputs needed for a CTM are the meteorological information and emission inventories of various species. These models generate aerosol from estimates of source emissions, then allow the particles to be transported by modeled meteorology, transformed from modeled chemical processes and removed from the atmosphere by modeled dry and wet deposition. A microphysics model is also needed to simulate the optical properties of aerosols. Hence, CTMs can simulate the temporal and spatial distribution of trace gases and aerosols (Jacob, 1999). A central goal of atmospheric modeling is to understand quantitatively how the concentrations or mass of species depend on controlling process: emissions, transport, chemistry and deposition.

- Emissions. Chemical species are emitted to atmosphere by a variety of sources. Some of these sources, such as fossil fuel combustion, originate from human activity and are called anthropogenic. Others, such as photosynthesis of oxygen, originate from natural functions of biological organisms and are called biogenic. Still others, such as volcanoes, originate from bon-biogenic natural process. In general, the CTMs deal with the aerosol species emissions according to the wind speed, soil type, etc., such as mineral dust, sea salt; or obtain the emissions from emission inventories, such as carbonaceous aerosols.
- Chemistry. Reactions in the atmosphere can lead to the formation and removal of species.
- Transport. Winds transport atmospheric species away from their point of origin.
- Deposition. All material in the atmosphere is eventually deposited back to the Earth's surface. Escape from the atmosphere to outer space is negligible because of the Earth's gravitational pull. Deposition takes two forms: "dry deposition" involving direct reaction or absorption at the Earth's surface, such as the uptake of CO_2 by photosynthesis; and "wet deposition" involving scavenging by precipitation.

Here we describe one simplest type of model used in atmospheric modeling research, one-box model. A one-box model for an atmospheric species X (e.g. sulfate aerosols) is show in Figure 2.3. Transport is treated as a flow of X into the box (F_{in}) and out of the box (F_{out}). If the box is the global atmosphere then $F_{in} = F_{out} = 0$. The production and loss rates of X inside the box may include contributions from emissions (E), chemical production (P), chemical loss (L) and deposition (D). The terms F_{in}, E and P are sources of X in the box; the terms F_{out}, L and D are sinks of X in the box.

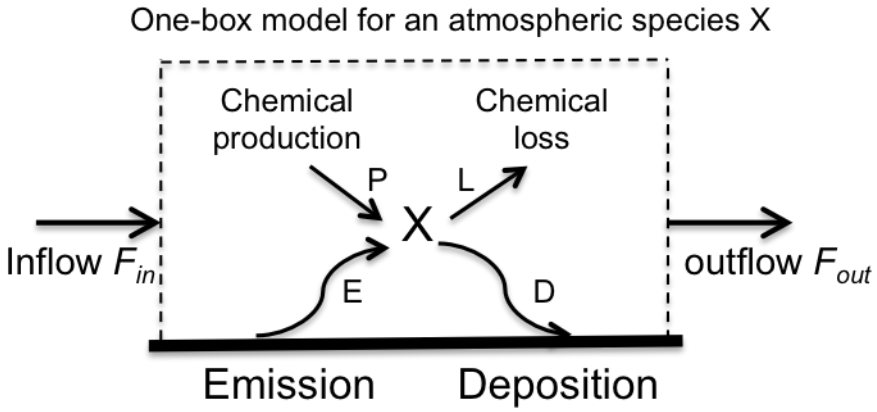

Figure 2.3: One-box model for an atmospheric species X, refer to Jacob, (1999)

By mass balance, the change with time in abundance of species X inside the box must be equal to the difference between sources and sinks:

$$\frac{dm}{dt} = \sum sources - \sum sinks = F_{in} + E + P - F_{out} - L - D \quad (2.11)$$

This formula provides the foundation for all atmospheric modeling research. In real 3D earth system simulation, the spatial and temporal behavior of atmospheric species is simulated in CTMs by solving the continuity equation (Brasseur and Jacob, 2017; Brasseur et al., 1999; Jacob, 1999):

$$\frac{\partial m}{\partial t} = -\nabla \cdot m\boldsymbol{U} + S - \boldsymbol{R} \quad (2.12)$$

where $\nabla = (\partial/\partial x, \partial/\partial y, \partial/\partial z)$ is the gradient vector, $\boldsymbol{U}$ is the transport velocity vector, m is mass. S and R stand for source and loss terms, respectively. The characteristics $\boldsymbol{U}$, m, S and R in Eq. (2.12) are explicit functions of time t and spatial coordinates $\boldsymbol{x} = (x, y, z)$. Thus, the continuity equation is a first-order differential equation in space and time that relates the mass field of a species in the atmosphere to its sources and sinks and to the wind field.

The continuity equation is usually solved numerically using discrete analogues. Consider the problem of calculating $m(\boldsymbol{x}, t_0 + \Delta t)$ from knowledge of $m(\boldsymbol{x}, t_0)$. The first step involves separation of the different terms in Eq. (2.12):

$$\frac{\partial m}{\partial t} = (\frac{\partial m}{\partial t})_{advection} + (\frac{\partial m}{\partial t})_{convection} - \left(\frac{\partial m}{\partial t}\right)_{deposition} + S \qquad (2.13)$$

Each term in Eq. (2.13) is integrated independently from others over finite time step Δt using an advection operator A, a convection operator C, and a deposition operator D. The formulation then can be expressed as

$$\begin{aligned} m(\boldsymbol{x}, t_0 + \Delta t) &= S + m(\boldsymbol{x}, t_0) \\ &+ \int_{t_0}^{t_0+\Delta t} \left(\frac{\partial m}{\partial t}\right)_{advection} dt \\ &+ \int_{t_0}^{t_0+\Delta t} \left(\frac{\partial m}{\partial t}\right)_{convection} dt \\ &+ \int_{t_0}^{t_0+\Delta t} \left(\frac{\partial m}{\partial t}\right)_{deposition} dt \\ &= \mathrm{S} + A \cdot C \cdot D \cdot m(\boldsymbol{x}, t_0) \end{aligned} \qquad (2.14)$$

This approach is called operator splitting. Separating the operators over large time steps makes the calculation tractable, but it is based on the assumption that advection, convection and deposition operators are independent of each other over the time step. To carry out the integration involved in each operator, one can discretize the spatial domain over a 3D grid (Figure 2.4). The continuous mass function $m(\boldsymbol{x}, t)$ then can be expressed by the discrete function $m(i, j, k, t)$ where i, j, k are the indices of the grid elements in the 3D directions x, y, z respectively. The advection operator can be expressed algebraically:

$$\begin{aligned} m(i,j,k,t_0 + \Delta t) &= A \cdot m(i,j,k,t_0) = m(i,j,k,t_0) \\ &+ \frac{u(i-1,j,k,t_0)m(i-1,j,k,t_0) - u(i,j,k,t_0)m(i,j,k,t_0)}{\Delta x}\Delta t \\ &+ \frac{v(i,j-1,k,t_0)m(i,j-1,k,t_0) - v(i,j,k,t_0)m(i,j,k,t_0)}{\Delta y}\Delta t \\ &+ \frac{w(i,j,k-1,t_0)m(i,j,k-1,t_0) - w(i,j,k,t_0)m(i,j,k,t_0)}{\Delta z}\Delta t \end{aligned} \qquad (2.15)$$

$\boldsymbol{U} = (u, v, w)$ is the local wind velocity vector. The convection and deposition operators are applied on the discrete grid in the same way as advection operator.

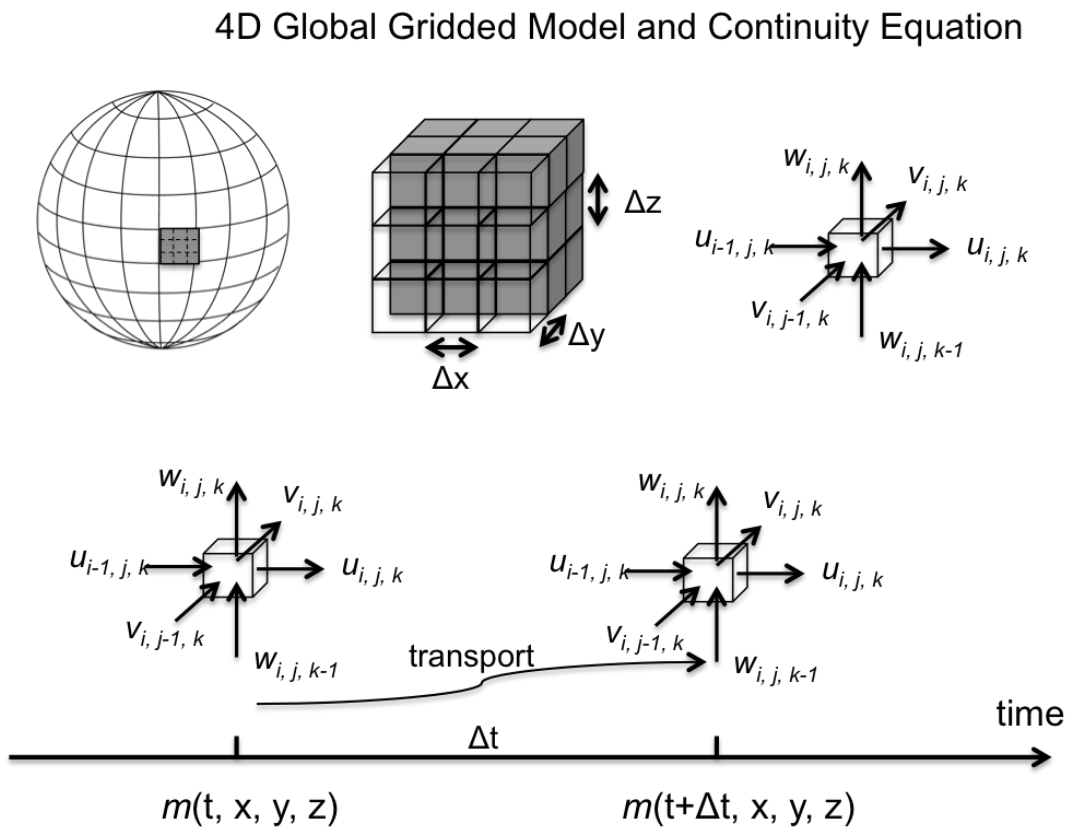

Figure 2.4: General concept illustration of spatial and temporal discretization of the continuity equation

Basically, we have arrived at a numerical solution of the continuity equation. Then, the quality of aerosol simulation depends on the grid resolution, the time step, the aerosol emission inventories or models adopted in CTMs, and the algorithms used for these transport operators.

GEOS-Chem model has been chosen for this study, because it is the community model (http://acmg.seas.harvard.edu/geos/) with constantly maintained and improved adjoint module. GEOS-Chem is a global 3D chemical transport model driven by assimilated meteorological data from the NASA Goddard Earth Observing System Data Assimilation System (GEOS-DAS) (Bey et al., 2001). We use the GEOS-Chem (v9-02) model for forward aerosol simulation with 47 layers vertical resolution and 2° (latitude) x 2.5° (longitude) horizontal resolution. The standard aerosol dry deposition in GEOS-Chem is described in (Wang et al., 1998; Wesely, 1989), and accounting for gravitational settling and turbulent mixing of particles to the surface (Pye et al., 2009; Zhang et al., 2001). Aerosol wet deposition is through wet scavenging in convective

updrafts as well as in- and below-cloud scavenging from convective and large scale precipitation (Liu et al., 2001).

2.3.2 Aerosol emission sources

Emissions of DD and SS aerosols are either prescribed in global models or interactively calculated as a function of wind speed, soil particle size distribution, vegetation cover, soil moisture and other local variables. For BC, OC and SU aerosols and/or their precursors, emissions are prescribed using global inventories exclusively based on bottom-up techniques, which integrate source information across different economical sectors.

I. Dust aerosol emission

In GEOS-Chem simulation, the DD aerosol emission is calculated from the mineral dust entrainment and deposition (DEAD) model (Zender et al., 2003) coupling with the GOCART dust source function (Ginoux et al., 2001), in order to have a good strength and spatial structure of DD emissions (Fairlie et al., 2007). The total horizontal saltation flux, Q_s, based on the theory of White (1979):

$$Q_s = C_z \frac{\rho_{air}}{g} U^{*3} \left(1 - \frac{U_t^*}{U^*}\right)\left(1 + \frac{U_t^*}{U^*}\right)^2 \quad (2.16)$$

where U^* is the friction velocity, U_t^* is the threshold friction velocity, ρ_{air} is the air density, g is the acceleration of gravity, and C_z is a global tuning factor. In reality, soil moisture, vegetation, rocks and stones, and snow cover inhibit dust mobilization by contribution to cohesion, and then impact the soil moisture and increase threshold friction U_t^* (Zender et al., 2003) (Here, we adopt $g = 9.80616\, m/s^2$; $C_z = 0.00049$).

The total vertical DD flux is combined the entrainment scheme in DEAD with the source function, S, in GOCART model.

$$F = (1 - A_s) S \alpha Q_s \quad (2.17)$$

where the sandblasting mass efficiency, α, depends on the fraction M_{clay} of clay in the soil; A_s is the snow- covered fractional area, $(1 - A_s)$ retains suppression due to snow cover; S stands for source function, which restricts dust emissions to persistent desert and semi-desert regions. Figure 2.5 compares the GOCART source function (Figure 2.5a) and the GEOS-Chem annual total DD emission (Figure 2.6b), and the similarity between the source distribution and the annual dust emission shows the

importance of the source function. However, the limitation of the usage of source function is the DD aerosol generation is constrained in the place where the source function *S* is nonzero.

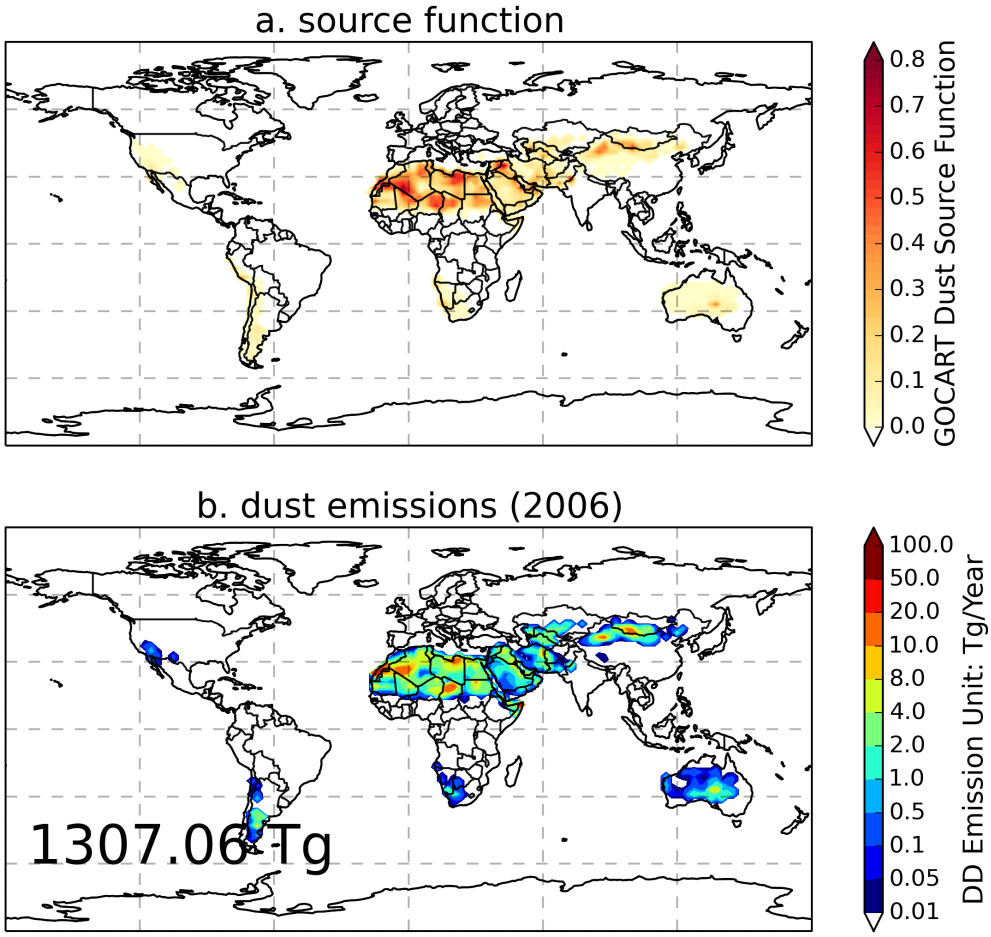

Figure 2.5: Comparison between (a) the GOCART 2°x2.5° dust source function used in GEOS-Chem dust mobilization and (b) the GEOS-Chem annual total dust emission in 2006; Note 0.1 to 6.0μm (radius) dust particles are taken into account.

II. Sea-salt aerosol emission

The SS aerosols module in GEOS-Chem model was first implemented by (Alexander et al., 2005) using the source function described by (Monahan et al., 1986). And then it was updated to the formulation of Gong (2003), which improved the simulation of dry radius smaller than 0.1μm (Jaeglé et al., 2011). The main mechanism leading to SS emission is by air bubbles bursting at the surface of the ocean as a result of wind stress (Blanchard, 1985; Monahan et al., 1986). The expression of density function $\mathrm{d}F/\mathrm{dr}_{80}$ (in units of particles $m^{-2}s^{-1}\mu m^{-1}$):

$$\frac{dF}{\mathrm{dr}_{80}} = 1.373 u_{10m}^{3.41} r_{80}^{-A} (1 + 0.057 r_{80}^{3.45}) \cdot 10^{1.607 e^{-B^2}} \quad (2.18)$$

where $A = 4.7(1 + \Theta_{r_{80}})^{-0.017 r_{80}^{-1.44}}$, $B = [0.433 - \log_{10}(r_{80})]/0.433$, r_{80} is the particle radius at RH $= 80\%$ (with $r_{80} \sim 2 r_{dry}$), and u_{10m} is the 10-meter wind speed. The parameter $\Theta_{r_{80}}$ is an adjustable parameter, which controls the shape of the size distribution of submicron aerosols, which is recommended to $\Theta_{r_{80}} = 30$ in Gong, (2003).

In the GEOS-Chem simulation, the sea salt aerosol is distributed in two modes, with radius varying from 0.1 to 0.5μm in fine mode, and 0.5 to 4.0μm for coarse mode. In each mode, the radius is divided into size bins by interval of 0.05μm. Figure 2.6a shows an example of annual sea salt aerosol emissions for year 2006.

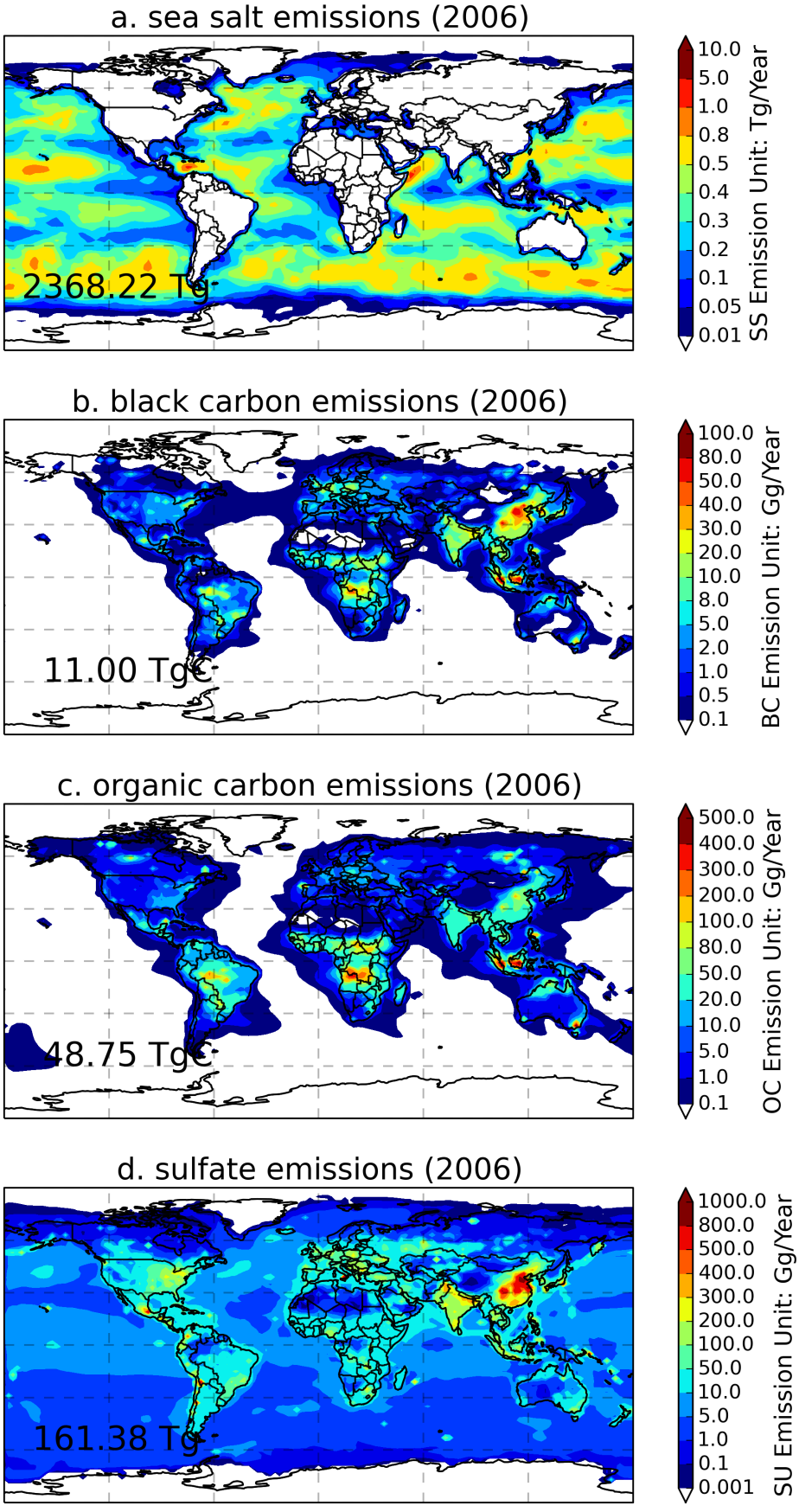

Figure 2.6: GEOS-Chem model annual aerosol emission sources in 2006, a. sea salt, b. black carbon, c. organic carbon, d. sulfate-nitrate-ammonium; note emissions of sea salt particles for radius from 0.1 to 4.0μm are calculated. Gg (gigagram)=10^9 gram.

III. Carbonaceous aerosol emission

Carbonaceous aerosol is one of the least understood components of fine mode aerosols. It is usually divided in two fractions, BC and OC. BC is the dominant component of the light-absorbing aerosol; meanwhile OC is one of the major abundant components of the aerosol over the globe. BC is a primary aerosol component emitted directly to the atmosphere by incomplete combustion process. The emission sources include fossil fuel combustion and biomass burning. OC aerosol can be emitted directly to the atmosphere (primary OC) and formed in situ by condensation of low-volatility products of the photo-oxidation of hydrocarbons (secondary OC). The major emission sources of OC include combustion of fossil fuels, biofuels and biomass.

The model acquires the carbonaceous aerosol emission from bottom-up inventories. Figure 2.6b and Figure 2.6c shows the examples of GEOS-Chem BC and OC total annual emissions in 2006 respectively. Here, the carbonaceous aerosol emission inventory is combined Bond monthly anthropogenic inventory and version 3 of daily global fire emissions database (GFED3). In our simulation of GEOS-Chem, the model resolves BC and OC, with a hydrophobic and a hydrophilic fraction for four aerosol types. The model assumes that 80% of black carbon and 50% of organic carbon from primary sources are hydrophobic. All secondary OC is assumed to be hydrophilic (Park et al., 2003). And we adopt BC aging process by assuming a fixed *e*-folding time of 1.2 days for the hydrophobic-to-hydrophilic BC conversion in the forms (Park et al., 2003).

IV. Sulfate-nitrate-ammonium aerosol emission

Sulfate aerosols are formed mainly by chemical reactions of SO_2 and dimethylsulfide (DMS). DMS is emitted mainly from the oceanic phytoplankton and react with hydroxyl (OH) radical, so it is converted into SO_2 and sulfate through intermediates. SO_2, which is emitted from fossil fuel consumption and volcanic activities, is mainly oxidized by hydroxyl radical in the gas phase and H_2O_2 and O_3 in

liquid phase, so it is converted into sulfate. Sources ammonium aerosols include biomass burning, biofuel, animals, fertilizers, human bodies, industry, fossil fuels, oceans, crops, soils and wild animals (Bouwman et al., 1997; Park et al., 2004). Meanwhile, the total inorganic nitrate aerosol in the model is computed from ozone-NO_x-hydrocarbon chemical mechanism. Details on their sources are described in Bey et al. (2001) and Martin et al. (2002). Figure 2.7d shows an example of GEOS-Chem total annual sulfate- nitrate-ammonium aerosol emissions in 2006.

2.3.4 Conversion of aerosol mass to optical properties

The CTMs are simulating the aerosol mass or concentration distribution. In order to obtain the distribution of AOD and AAOD, we need to assume the aerosol optical properties to convert the aerosol mass to AOD and AAOD. The GEOS-Chem model assumes external mixing for all aerosol components with lognormal size distributions. The modal diameter and width for each dry aerosol species and their optical properties is specified. The extinction and scattering coefficients are calculated from size distribution and refractive index with spherical particle shape assumption. Different aerosol species are considered to have different degree of hydroscopic growth rate with ambient relative humidity. The simulated aerosol mass are then converted to AOD (τ) and AAOD (τ_a) through the general relationship between aerosol optical depth and aerosol mass (Tegen and Lacis, 1996):

$$\tau(\lambda) = \sum_{i=1}^{n} \frac{3Q_{ext,i}(\lambda)}{4\rho_i r_{e,i}} m_i \tag{2.19}$$

$$\tau_a(\lambda) = \sum_{i=1}^{n} \frac{3Q_{abs,i}(\lambda)}{4\rho_i r_{e,i}} m_i \tag{2.20}$$

where n is the total number of aerosol components, i represents individual aerosol component, m is the aerosol mass, λ is wavelength, ρ is aerosol particle density, r_e is the particle effective radius, and $Q_{ext}(\lambda)$ and $Q_{abs}(\lambda)$ are the aerosol particle extinction and absorption coefficients, respectively. The size distribution and the spectral aerosol refractive index used to calculate $Q_{ext}(\lambda)$ and $Q_{abs}(\lambda)$ are assumed based on Global Aerosol Data Set (Koepke et al., 1997), with modifications for dust particles by including a spectral dependence for the imaginary part based on analysis of AERONET measurements (Dubovik et al., 2002b). Further, the particle optical

properties $Q_{ext}(\lambda)$ and $Q_{abs}(\lambda)$ are calculated according to AERONET Kernel (Dubovik et al., 2002a). The particle density and hydroscopic growth rate are described in Chin et al. (2002) and Martin et al. (2003). Table 2.2 lists the detailed aerosol properties used in this study. Here we consider two cases of BC refractive index. Figure 2.7a demonstrates the relative humidity dependence of these two cases of BC aerosols extinction ($Q_{ext}(\lambda)/r_e$) at 565nm, and Figure 2.7b presents the wavelength dependence of single scattering albedo (SSA) for these two cases. The Case 1 BC refractive index is based on Chin et al. (2002) and Martin et al. (2003). More recent studies have recommended a BC refractive index of 1.95-0.79i (Schuster et al., 2005; Bond and Bergstrom, 2006; Koch et al., 2009; Arola et al., 2011), which has higher absorption and scattering ability than Case 1. Figure 2.7a shows that the extinctions calculated from AERONET Kernel for Case 2 BC particle are about a factor 1.5 higher than for Case 1. The difference of SSA is small (Case 2 is about 2% higher at 565nm when RH=0%), however the difference increases when RH=95%, for which Case 2 is about 18% lower at 565nm. Since the particle absorption efficiency $Q_{abs} = (1 - SSA) \cdot Q_{ext}$, the Case 2 BC particle shows a higher absorbing ability than Case 1. Sensitivity tests are conducted to evaluate how these two BC refractive indexes influence the total BC emissions retrieval in Section 3.3.1.

Table 2.2: Aerosol refractive index, size distribution and particle density for DD, BC, OC, SU, SS and host water employed in this study

Aerosol	Complex refractive index			Size distribution (μm)			Density
	n	k(440/670/870/1020)		r_{mean}	r_{eff}	sigm	(g/cm^3)
DD	1.56	0.0029/0.0013/0.0001/0.0001	DST1	0.0421	0.14	2.0	2.5
			DST2	0.0722	0.24	2.0	2.5
			DST3	0.1354	0.45	2.0	2.5
			DST4	0.2407	0.80	2.0	2.5
			DST5	0.4212	1.40	2.0	2.65
			DST6	0.7220	2.40	2.0	2.65
			DST7	1.3540	4.50	2.0	2.65
BC (Case 1)	1.75	0.45		0.0118	0.039	2.0	1.0
BC (Case 2)	1.95	0.79		0.0118	0.039	2.0	1.0
OC	1.53	0.005		0.0212	0.087	2.2	1.8
SU	1.43	1.0e-8		0.0695	0.156	2.03	1.7
SS	1.5	1.55e-8	SSa	0.0855	0.129	1.5	2.2
			SSc	0.4010	0.952	1.8	2.2
Water	1.33	1.0e-8					1.0

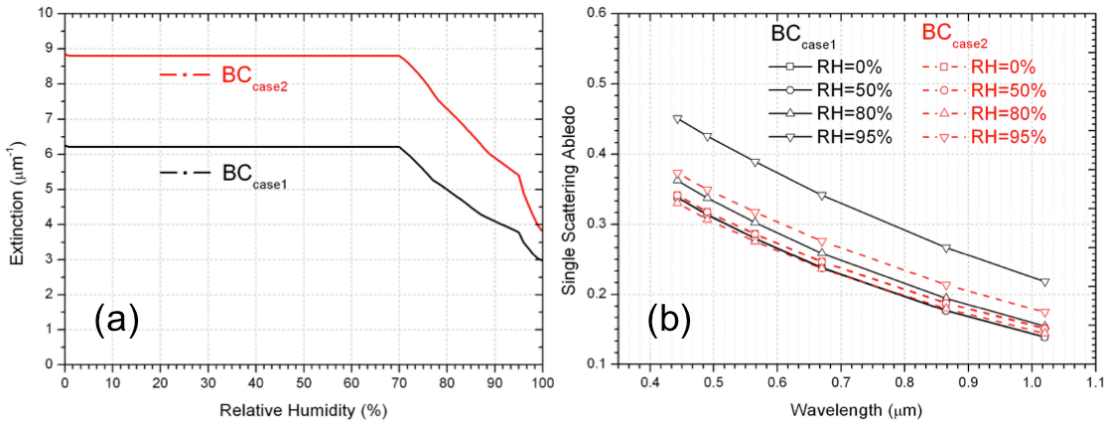

Figure 2.7: (a) The relative humidity dependence of BC particle extinction at 565nm; (b) Wavelength dependence of BC particle single scattering albedo at six PARASOL wavelengths

Figure 2.8 shows an example of GEOS-Chem model simulated annual mean (2006) global AOD and AAOD at 550nm, and aerosol species-specified (DD, BC, OC, SU and SS) AOD and AAOD. Figure 2.9 shows a simple analysis of global aerosol types according to each component's relative contribution to the annual total AOD and AAOD at 550nm. Figure 2.9a presents the 1st contributor to the total AOD, and Figure 2.9b shows the relative contribution of the 1st contributor to total AOD. Statistically, among the global 13,104 grid boxes, 6627 (51%) grid boxes are dominant by SS aerosol, 3574 (27%) grid boxes are dominant by SU, 1909 (15%) grid boxes are dominant by DD aerosol, 994 (7%) grid boxes are dominant by OC aerosol and 0 grid box is dominant by BC particle. In addition, Figure 2.9c presents the 1st contributor to the total AAOD, and Figure 2.9d shows the relative contribution of the 1st contributor to total AAOD. In terms of aerosol absorption, all the grid boxes are dominant by BC and DD aerosol particles, 11886 (91%) gird boxes are dominant by BC and 1218 (9%) grid boxes are dominant by DD particles.

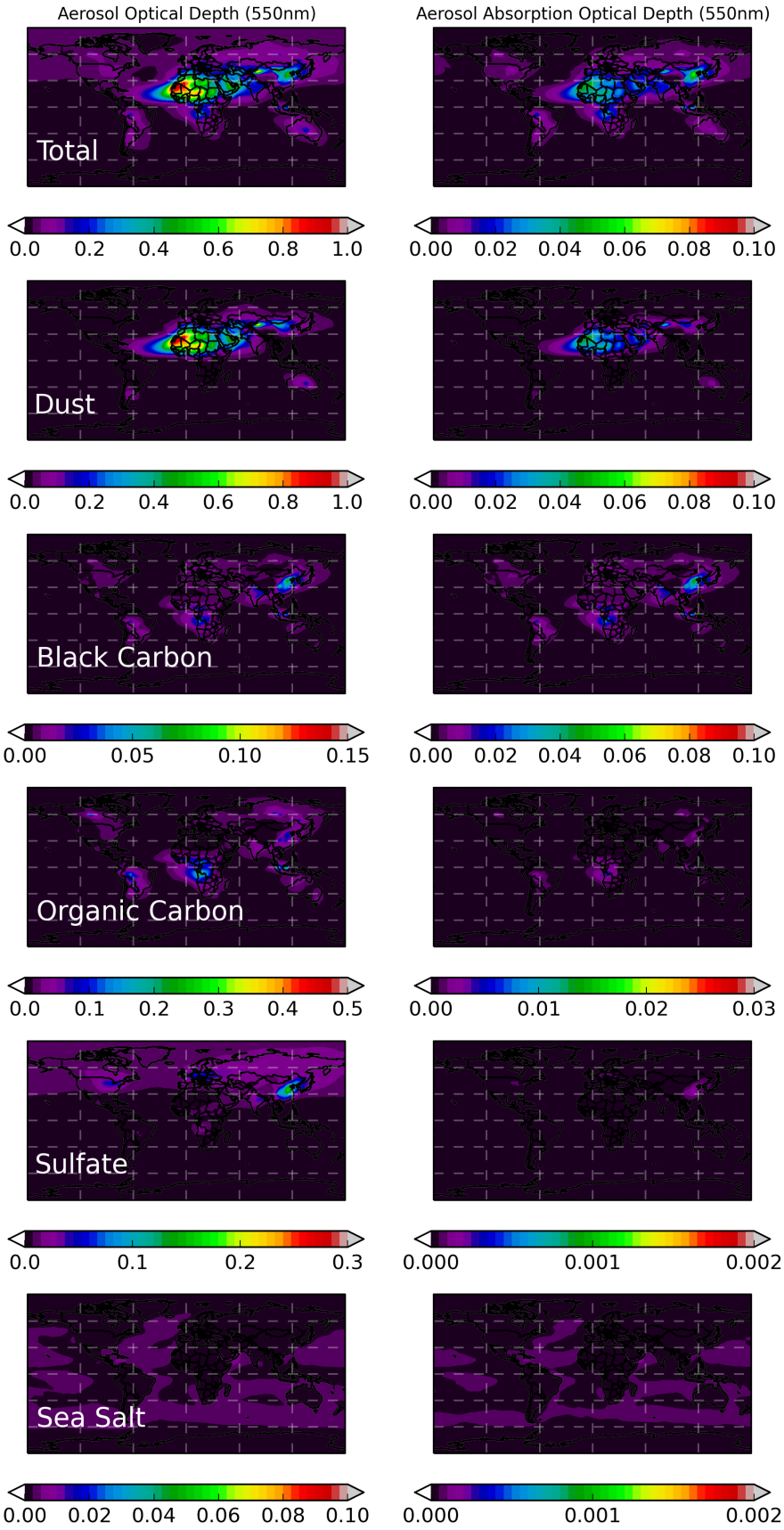

Figure 2.8: Global distribution of column integrated aerosol optical depth and aerosol absorption optical depth simulated by GEOS-Chem model at 550nm for 2006.

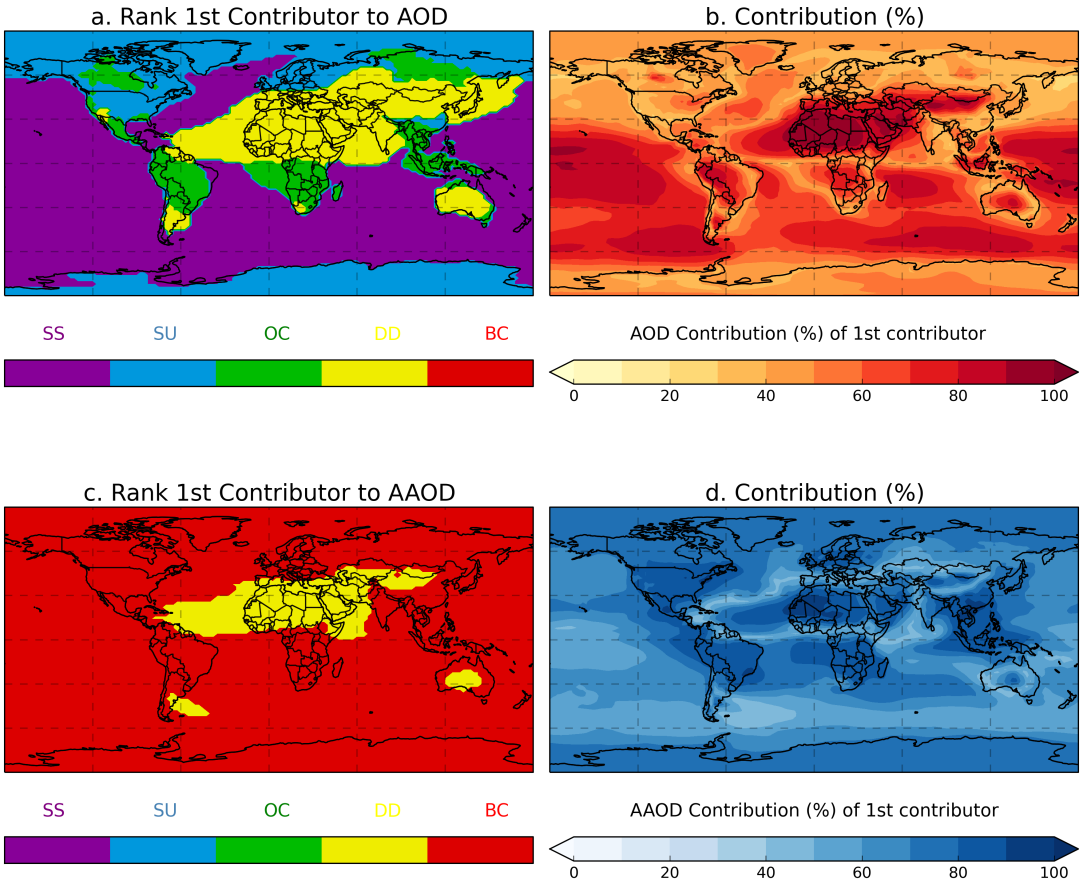

Figure 2.9: Simply classify the global aerosol type according to each component relative contribution to the total AOD and AAOD at 550nm. a. Rank 1st contributor to total AOD; b. the relative contribution of the 1st contributor to total AOD; c. rank 1st contributor to total AAOD; d. the relative contribution of the 1st contributor to total AAOD.

Chapter 3

Inverse modeling and numerical tests

> Everything is theoretically impossible,
> until it is done.
>
> Robert A. Heinlein

3.1 General concept of inverse modeling

Inverse modeling is an elaborated tool for combining observations of atmospheric composition with knowledge of atmospheric processes (transport chemistry) to derive quantitative estimates on emissions to the atmosphere. A chemical transport model (CTM), known as the forward model for inversion, solves the continuity equation to predict concentrations as a function of emissions. The inverse model then optimizes the emission estimates by fitting the CTM to the observed concentrations. This chapter explores the possibility of deriving aerosol emission distribution and strength from satellite observations by inverting GEOS-Chem model. Figure 3.1 illustrates the general concept of aerosol emission inverse modeling.

Retrieval of aerosol emission source from satellite observations requires three distinct parts of efforts. First, enough information of observed atmospheric aerosols, is an essential component of the inverse modeling. As discussed in works such as

Dubovik et al. (2008) and Meland et al. (2013), AOD at one wavelength (as well as currently available aerosol satellite data) contains only limited information to evaluate aerosol types, properties, or speciated emissions. The second important component is a chemical transport model that has the capability to simulate the aerosol distribution according the input emission sources by modeling transport, chemistry, removal processes. Third, an inversion algorithm based on adjoint chemical transport model is necessary to allow to optimize *a priori* aerosol emission sources in the transport model and to improve the agreement between model simulations and observations.

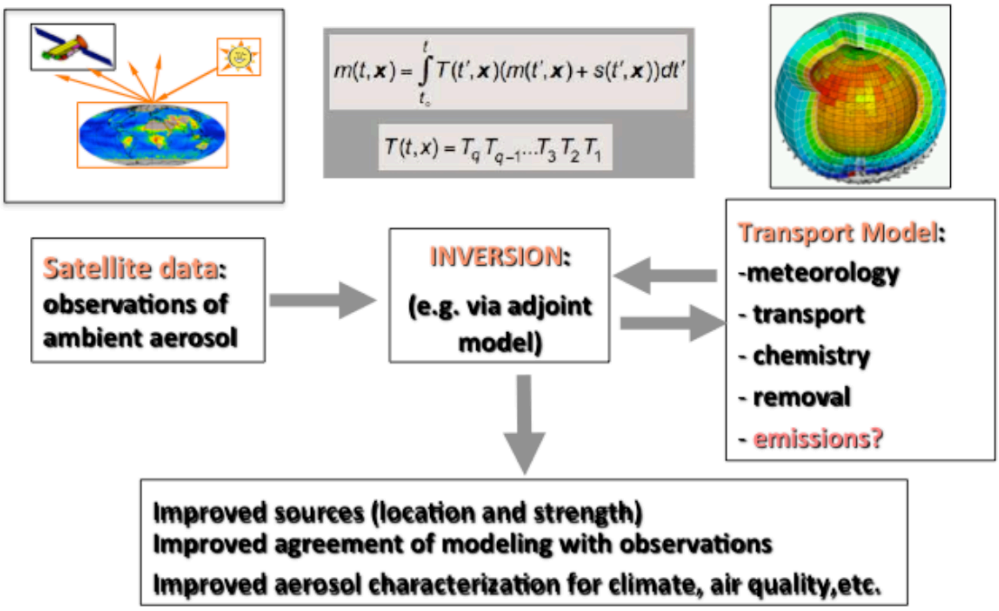

Figure 3.1: Flowchart of the general concept of inverse modeling

Method proposed in this work is to develop GEOS-Chem based inverse modeling algorithm for simultaneous fitting spectral AOD and AAOD data from the polarimetric POLDER/PARASOL produced with the GRASP algorithm, and optimizing the speciated aerosol emissions. The PARASOL/GRASP AOD and AAOD are available at all six wavelengths (443, 490, 565, 670, 865 and 1020nm) in the spectrum of short wave visible to near infrared (VIS-NIR). Our method explores to determine DD, BC and OC sources simultaneously, because DD, BC and OC aerosol optical properties vary dramatically in the spectrum of VIS-NIR. For example, DD aerosols are dominated by coarse mode particles, and their AOD varies slightly in the VIS-NIR spectral range; in contrast, the AOD of fine mode dominated BC and OC aerosols decrease sharply in this spectral range. In addition, DD and OC particles

absorb most strongly in the UV and short wave visible channels, such as 443 nm, while BC particles are absorbing more ubiquitously (Sato et al., 2003).

3.2 The methodology of inverse modeling

3.2.1 Inversion using adjoint method

In CTM system, the spatial and temporal behavior of aerosol is simulated by solving the continuity equation Eq. (2.12). The continuity equation does not yield general analytical solution and is usually solved numerically using discrete analogues, seen in Eq. (2.15). Each component process in numerical equivalent of Eq. (2.12) is isolated and treated sequentially at each time step Δt:

$$m(t+\Delta t) = T(t,\boldsymbol{x})\big(m(t,\boldsymbol{x}) + s(t,\boldsymbol{x})\big)\Delta t \tag{3.1}$$

where $m(t,\boldsymbol{x})$ is aerosol mass, $s(t,\boldsymbol{x})$ represents aerosol emission, $T(t,\boldsymbol{x})$ represents transport operators, that can be approximated as:

$$T(t,\boldsymbol{x}) = T_i T_{i-1} \dots T_3 T_2 T_1 \tag{3.2}$$

and T_k $(k = 1, \dots, i)$ represents operators for isolated transport process such as advection, diffusion, convection and deposition (see in Eq. 2.14). Thus, the aerosol mass at any given time t can be expressed to numerical integration of transport and source functions:

$$m(t,\boldsymbol{x}) = \int_{t_0}^{t} T(t',\boldsymbol{x})\big(m(t',\boldsymbol{x}) + s(t',\boldsymbol{x})\big)dt' \tag{3.3}$$

If the transport operator is linear, Eq. (3.1) can also be written in matrix form for a single time step:

$$\boldsymbol{M}_n = \mathbf{T}_{n-1}(\boldsymbol{M}_{n-1} + \boldsymbol{S}_{n-1}) \tag{3.4}$$

where the subscripts $n-1$ and n are associated with time step t_{n-1} and $t_n = t_{n-1} + \Delta t$, for the time steps $t_0, t_1, t_2, \dots, t_n$, the aerosol mass vector $\boldsymbol{M}_n$ can be expressed as:

$$\boldsymbol{M}_n = \left(\prod_{i=0}^{i=n-1} \mathbf{T}_i\right)\boldsymbol{M}_0 + \sum_{k=0}^{k=n-1}\Big(\prod_{i=k}^{i=n-1} \mathbf{T}_i\Big)\boldsymbol{S}_k$$

thus, Eq. (3.3) can be equivalently written in matrix form as:

$$\boldsymbol{M} = \mathbf{T}\boldsymbol{S} + \mathbf{T}_0\boldsymbol{M}_0 \tag{3.5}$$

where $\boldsymbol{M}_0$ donates a vector of aerosol mass at all locations at time t_0, $\boldsymbol{M}$ and $\boldsymbol{S}$ are the vectors of mass and emission at all locations and considered times $t_0, t_1, t_2, \dots, t_n$ (i.e.

these vectors represents the 4D aerosol mass and emission variability), **T** is the coefficient matrix define the mass transport to each locations $\boldsymbol{x}$. Thus, the source vector $\boldsymbol{S}$ can be derived by solving the matrix equation, if the aerosol mass observations are available $\Delta\boldsymbol{M} = \boldsymbol{M}_{obs} - \boldsymbol{M}$.

However, in a real global 4D chemical transport model simulation, the vectors $\boldsymbol{M}$, $\boldsymbol{S}$ and matrix **T** have extremely large dimensions; thus, direct implement of matrix operations can be very difficult. Therefore, emission estimation is achieved using 4D-Variational (4D-Var) data assimilation adjoint techniques (Le Dimet and Talagrand, 1986; Elbern et al., 2000; Elbern and Schmidt, 2001; Enting, 2002; Errico, 1997; Menut, 2003; Talagrand and Courtier, 1987; Vukićević and Hess, 2000).

An adjoint model is a set of equations auxiliary to a forward model that are used to efficiently calculate the gradient of a scalar model response function with respect to all model parameters simultaneously. Adjoint methods were initially suggested as approaches to source analysis of atmospheric tracers several decades ago (Lions, 1971; Marchuk, 1974). By the late 1990s, the method was applied to chemical transport models of the stratosphere (Fisher and Lary, 1995) and troposphere (Elbern et al., 1997). The method was used to constrain emissions in an Eulerian air quality model of chemically active species in the troposphere by Elbern et al. (2000). Subsequent investigations of emissions have been explored with adjoints of chemical transport models such as CHIMERE (Menut, 2003; Vautard et al., 2000), Polair (Quélo et al., 2005), the CIT model (Martien et al., 2006; Philip T. Martien and Harley, 2006), STEM (Hakami et al., 2005; Sandu et al., 2005), DRAIS (Nester and Panitz, 2006), CMAQ (Hakami et al., 2007), IMAGES (Müller and Stavrakou, 2005), and GOCART (Dubovik, 2004; Dubovik et al., 2008).

In this work, adjoint GEOS-Chem (v35i) is used in the inversion. The adjoint GEOS-Chem model was developed specifically for inverse modeling of aerosols or their precursors and gas emissions (Henze et al., 2007, 2009), with code updates following the relevant parts of the GEOS-Chem forward model. In the adjoint GEOS-Chem framework, the inverse algorithm iteratively seeks the corrections that minimize the differences between observations and simulations; in general, the cost function J is given by:

$$J(\boldsymbol{S}) = \frac{1}{2}\sum_{\boldsymbol{M}\in\Omega}(\boldsymbol{M}(\boldsymbol{S}) - \boldsymbol{M}_{obs})^{\mathrm{T}}\mathbf{C}_{obs}^{-1}(\boldsymbol{M}(\boldsymbol{S}) - \boldsymbol{M}_{obs}) \qquad (3.6)$$

where $\boldsymbol{M}$ is the vector of simulated aerosol mass in 4D spatial and temporal space Ω with emission sources $\boldsymbol{S}$; $\boldsymbol{M}_{obs}$ is the vector of observed aerosol mass; $\mathbf{C}_{obs}^{-1}$ is the error covariance matrix of $\boldsymbol{M}_{obs}$.

The adjoint model offers a computationally efficient approach to calculate the sensitivity of a model scalar (e.g. aerosol mass concentration) with respect to model input parameters (e.g. emissions in all grid boxes) in a single time backward adjoint model run. In this study, the adjoint model computes the gradients of cost function with respect to aerosol emission corrections $\Delta \boldsymbol{S}^p(\boldsymbol{x}) = \nabla J^p(t, \boldsymbol{x})$ (see derivations by Dubovik et al. (2008)):

$$\nabla J^p(t, \boldsymbol{x}) = \int_t^{t_0} T^{\#}(t', \boldsymbol{x})(\nabla J^p(t', \boldsymbol{x}) + C_{obs}^{-1} \Delta m^{\boldsymbol{p}}(t', \boldsymbol{x}))(-\mathrm{d}t') \qquad (3.7)$$

where $C_{obs}^{-1}\Delta m^{\boldsymbol{p}}$ is the continuous analogue of the covariance matrix $\mathbf{C}_{obs}^{-1}\Delta \boldsymbol{M}^p$, $T^{\#}(t', \boldsymbol{x})$ is the transport adjoint operator $T(t, \boldsymbol{x})$, and is composed of adjoints $T_k^{\#}(t, \boldsymbol{x})$ of the component processes $T_k(t, \boldsymbol{x})$:

$$T^{\#}(t, \boldsymbol{x}) = T_1^{\#} T_2^{\#} T_3^{\#} \ldots T_{i-1}^{\#} T_i^{\#} \qquad (3.8)$$

If the observation errors are uncorrelated, i.e. the covariance matrix of measurements $\mathbf{C}_{obs}$ is diagonal with the elements on diagonal equal to $\sigma^2(t, \boldsymbol{x})$, the element $C_{obs}^{-1}\Delta m^{\boldsymbol{p}}$ relate to the continuous function $\sigma^{-2}(t, \boldsymbol{x})\Delta m^{\boldsymbol{p}}(t, \boldsymbol{x})$ in a straightforward way. Then the Eq. (3.7) can be written as:

$$\nabla J^p(t, \boldsymbol{x}) = \int_t^{t_0} T^{\#}(t', \boldsymbol{x})(\nabla J^p(t', \boldsymbol{x}) + \sigma^{-2}(t', \boldsymbol{x}) \Delta m^{\boldsymbol{p}}(t', \boldsymbol{x}))(-\mathrm{d}t') \qquad (3.9)$$

where $\Delta m^{\boldsymbol{p}}(t, \boldsymbol{x})$ can be expressed according to Eq. (3.3):

$$\Delta m^{\boldsymbol{p}}(t, \boldsymbol{x}) = m_{obs}(t, \boldsymbol{x}) - \int_{t_0}^{t} T(t', \boldsymbol{x})\big(m(t', \boldsymbol{x}) + s^p(t', \boldsymbol{x})\big)\,\mathrm{d}t' \qquad (3.10)$$

The symbols $s^p(t, \boldsymbol{x})$, $\Delta m^{\boldsymbol{p}}(t, \boldsymbol{x})$ and $\sigma^{-2}(t, \boldsymbol{x})$ denote function equivalents of vectors $\boldsymbol{S}^p$, $\Delta \boldsymbol{M}^p$ and matrix $\mathbf{C}_{obs}^{-1}$, respectively. Thus, the steepest descent iterative solution can be also written in matrix expression:

$$\nabla J^p(\boldsymbol{S}^p) = \mathbf{T}^{\mathrm{T}} \mathbf{C}_{obs}^{-1} \Delta \boldsymbol{M}^p \qquad (3.11)$$

This method uses the fact that the gradient $\nabla J(\boldsymbol{S})$ points in the direction of maximal local changes of the cost function $J(\boldsymbol{S})$, and this direction can always be used to correct $\boldsymbol{S}^p$, so it moves toward the solution $\boldsymbol{S}'$ that minimize the cost function $J(\boldsymbol{S})$.

3.2.2 Implement a priori constrain on inversion

Previous equations describe an approach to invert transport model based on the measurements of aerosol mass $\boldsymbol{M}_{obs}$, which is the direct simulation parameter in the chemical transport model. In practice, satellite observations do not provide the same aerosol quantities, coverage, and sampling as model simulation. Accordingly, the inverse algorithm, as well as some aspects of inversion concept, need to be adjusted when invert real observations. Figure 3.2 show that aerosol emission sources have very high spatial and temporal variability. Although PARASOL/GRASP provides aerosol extinction and absorption information in spectrum VIS-NIR, it is still insufficient for unique retrieval of all parameters describing emissions. The problem is still ill-posed. Therefore, two methods are proposed to adjust inverse method, (i) implement *a priori* constrain on inversion; (ii) assume aerosol emission correction is constant in a time window to reduce the unknown parameters (see discussion in Section 3.3).

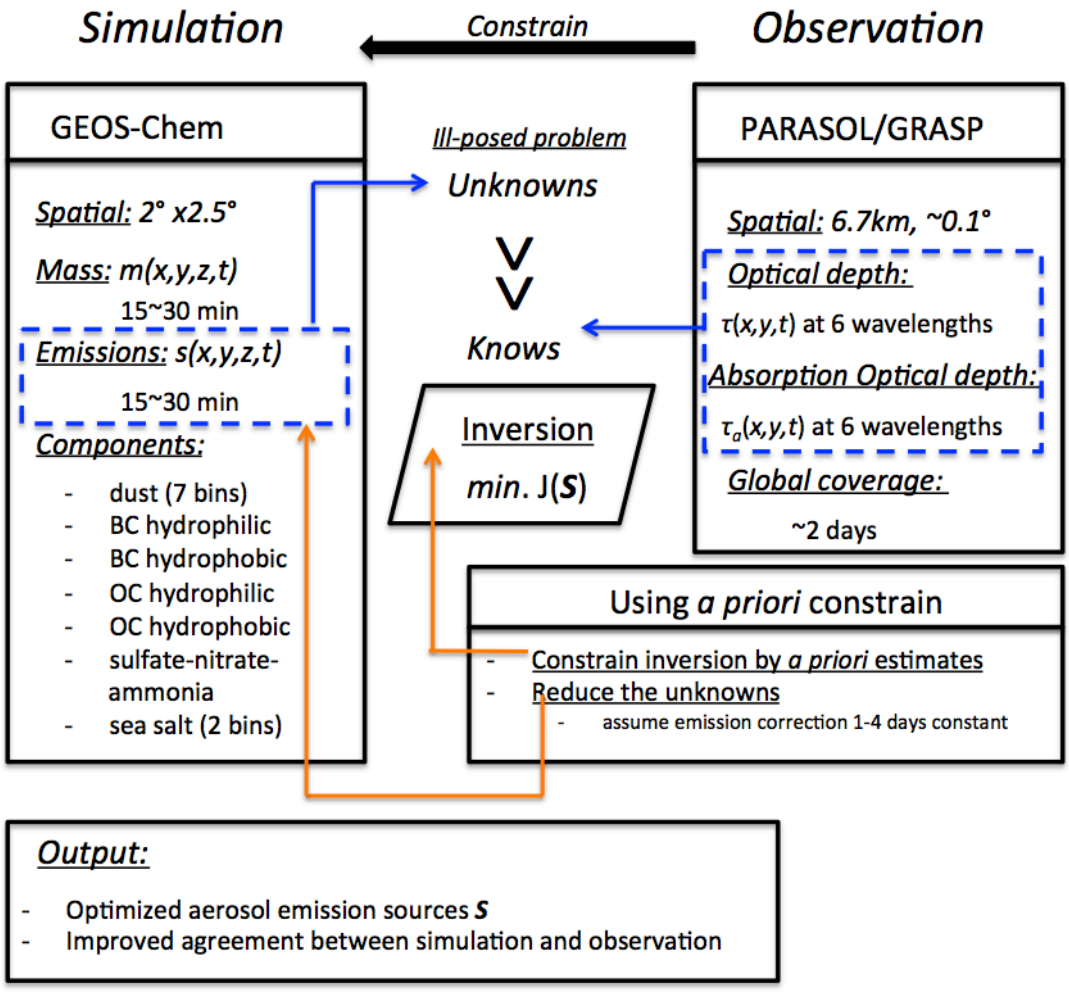

Figure 3.2: The concepts of constraining aerosol emission retrievals from satellite observations

In real observations, the aerosol data fields may be available only in the form of optical depth and absorption optical depth from the satellite measurements:

$$\boldsymbol{f} = \boldsymbol{\tau}(t, \boldsymbol{x}) = F(m(t, \boldsymbol{x}), \lambda, Q_{ext}, Q_{abs}, \dots) \quad (3.12)$$

where $F(\dots)$ is a function converting aerosol mass $m(t, \boldsymbol{x})$ to AOD and AAOD based on spectral characteristics λ, aerosol extinction Q_{ext} and absorption Q_{abs} coefficients, etc, see in Eq (2.19-2.20). Here, $\boldsymbol{\tau}$ represents PARASOL/GRASP spectral AOD and AAOD. Next, we will discuss about using *a priori* information to constrain the aerosol emission inversion from observed AOD and AAOD. In most applications "prior model" emission from bottom-up inventories $\boldsymbol{S}_a$ (i.e. standard model emissions) are used as *a priori* estimates of fundamentally unknown emissions. In such chases, instead of quadratic form of Eq. (3.6) the inversion minimizes the sum of following quadratic form:

$$J_{obs}(\boldsymbol{S}) + J_{a\ priori}(\boldsymbol{S}) =$$
$$\frac{1}{2}\sum(\boldsymbol{f}(\boldsymbol{S}) - \boldsymbol{f}_{obs})^{\mathrm{T}}\mathbf{C}_{obs}^{-1}(\boldsymbol{f}(\boldsymbol{S}) - \boldsymbol{f}_{obs}) + \frac{1}{2}\gamma_r(\boldsymbol{S} - \boldsymbol{S}_a)^{\mathrm{T}}\mathbf{C}_a^{-1}(\boldsymbol{S}^p - \boldsymbol{S}_a) \quad (3.13)$$

Here, the first term characterizes the fitting of observation, where the vector $\boldsymbol{f}_{obs}$ represent observations used for inversion (e.g. spectral AOD and AAOD) and the vector $\boldsymbol{f}(\boldsymbol{S})$ is simulated based on emission sources $\boldsymbol{S}$, while vectors $\boldsymbol{S}$ and $\boldsymbol{S}_a$ describes generally 4D distribution of emissions. $\mathbf{C}_{obs}^{-1}$ is the error covariance matrix of $\boldsymbol{f}_{obs}$. The second term is introduced to constrain retrieval and it indicates the agreement with *a priori* estimates $\boldsymbol{S}_a$ of the emissions. $\mathbf{C}_a^{-1}$ is the error covariance estimate of *a priori* emissions. γ_r is a regularization parameter.

The minimization of the quadratic form given by Eq. (3.13) can be obtained by steepest decent iterations:

$$\boldsymbol{S}^{p+1} = \boldsymbol{S}^p + \Delta\boldsymbol{S}^p,$$
$$\Delta\boldsymbol{S}^p = \nabla J_{obs}(\boldsymbol{S}^p) + \nabla J_{a\ priori}(\boldsymbol{S}^p) = \mathbf{K}_{obs}^T\mathbf{C}_{obs}^{-1}\Delta f^p + \gamma\mathbf{C}_a^{-1}(\boldsymbol{S}^p - \boldsymbol{S}_a), \quad (3.14)$$

where $\mathbf{K}_{obs}^T$ denotes matrix of Jacobeans of observation characteristics $\boldsymbol{f}$. Equations (3.13) and (3.14) are written using vectors and matrices, describing 4D geophysical fields that are generally are very large. However, in practice neither transport models nor inverse modeling algorithms (if emissions retrieved at high resolution) explicitly

utilize matrix and vectors. The transport models are generally organized as routines calculating continuous (i.e. with relatively small time step) time series of the geo characteristic resulted from time integration. For example, calculations of corrections $\Delta \boldsymbol{S}^p$ are obtained by running adjoint model that directly produces the product of $\mathbf{K}_{obs}^T \mathbf{C}_{obs}^{-1} \Delta\tau^p$ without explicit calculation of Jacobeans.

In this study, $\boldsymbol{f}(\boldsymbol{S})$ is the vector of model simulated AOD and AAOD with emission sources $\boldsymbol{S}$; Thus, the differences can be written as:

$$\Delta\boldsymbol{\tau} = \boldsymbol{f}(\boldsymbol{S}) - \boldsymbol{f}_{obs} = \boldsymbol{\tau} - \boldsymbol{\tau}_{obs} \tag{3.15}$$

The correction $\Delta \boldsymbol{S}^p(\boldsymbol{x}) = \nabla J^p(t, \boldsymbol{x})$ minimizing the form of Eq. (3.13) that relates to fitting of AOD and AAOD under *a priori* constraints can be defined as:

$$\nabla J^p(t, \boldsymbol{x}) = \int_t^{t_0} T^{\#}(t', \boldsymbol{x}) F^{\#}(t', \boldsymbol{x}) (\nabla J^p(t', \boldsymbol{x}) + C_{obs}^{-1} \Delta\tau^{\boldsymbol{p}}(t', \boldsymbol{x}))(-\mathrm{d}t') + \gamma_r C_a^{-1}(s^p - s_a) \tag{3.16}$$

here $F^{\#}(t', \boldsymbol{x})$ is adjoint operator corresponding to matrix operation $\mathbf{F}^T$, where matrix $\mathbf{F}$ contains first derivatives $d\tau/dm$. It should be noted that GEOS-Chem adjoint model is developed for inversion of mass (or AOD at single wavelength), therefore the operator $F^{\#}(t', \boldsymbol{x})$ for inversion spectral AOD and AAOD was developed as a part of this work. The symbols s^p, $\Delta\tau^{\boldsymbol{p}}(t, \boldsymbol{x})$, C_{obs}^{-1} and C_a^{-1} denote function equivalents of vectors $\boldsymbol{S}^p$, $\Delta\boldsymbol{\tau}^p$, matrix $\mathbf{C}_{obs}^{-1}$ and $\mathbf{C}_a^{-1}$ respectively. Thus, the iterative solution can be also written in matrix expression:

$$\nabla J^p(\boldsymbol{S}^p) = \mathbf{T}^{\mathrm{T}} \mathbf{F}^{\mathrm{T}} \mathbf{C}_{obs}^{-1} \Delta\boldsymbol{\tau}^p + \gamma_r \mathbf{C}_a^{-1}(\boldsymbol{S}_a - \boldsymbol{S}^p) \tag{3.17}$$

In principle, the methodology assumes that *a priori* information is available, i.e. before the inversion. However, in practice all available information is already accumulated in definitions of aerosol emissions used in the transport model. Therefore, usually the data sets that are adapted as "default" in the models are taken "a prior" emissions and as initial guess in iterative retrieval too. In present study we follow this strategy. Unfortunately the covariance matrix $\mathbf{C}_a$ of *a priori* emissions is not known accurately. As a result, this matrix is often assumed diagonal, where the elements of diagonal are equal or defined using rather straightforward strategy. Therefore, in order to address this fundamental lack of the knowledge of $\mathbf{C}_a$ the contribution of *a priori* term (second term) in Eq. (3.13) is weighted by a regulation parameter γ_r. This strategy is adapted for using GEOS-Chem adjoint. In addition,

GEOS-Chem setup of using gradient of Eq. (3.13) does not apply the gradient directly for adjusting emissions $\boldsymbol{S}$. Instead, the emission sources are adjusted using a vector of scaling factors $\boldsymbol{\sigma}$ ($\boldsymbol{S}^p = \boldsymbol{S}_0\boldsymbol{\sigma}^{p-1}$) that are scaling for initial emissions: $\boldsymbol{\sigma} = \boldsymbol{S}/\boldsymbol{S}_0$, where $\boldsymbol{S}$ and $\boldsymbol{S}_0$ are optimized and initial aerosol emissions respectively (Henze et al., 2007). This strategy was chosen probably to replace addition/subtraction correction of emission (that can generate negative unphysical values) by division/multiplication of initial positive and non-zero $\boldsymbol{S}$. Specifically, from the gradients of cost function with respect to aerosol emission scaling factors $\nabla_{\boldsymbol{\sigma}} J(t, \boldsymbol{x})$, the adjoint GEOS-Chem uses the L-BFGS-B optimization method (Byrd et al., 1995; Zhu et al., 1997), which affords bounded minimization of cost function, and ensuring positive values, to calculate the scaling factors for aerosol emissions. Figure 3.3 is the flowchart to illustrate the methodology.

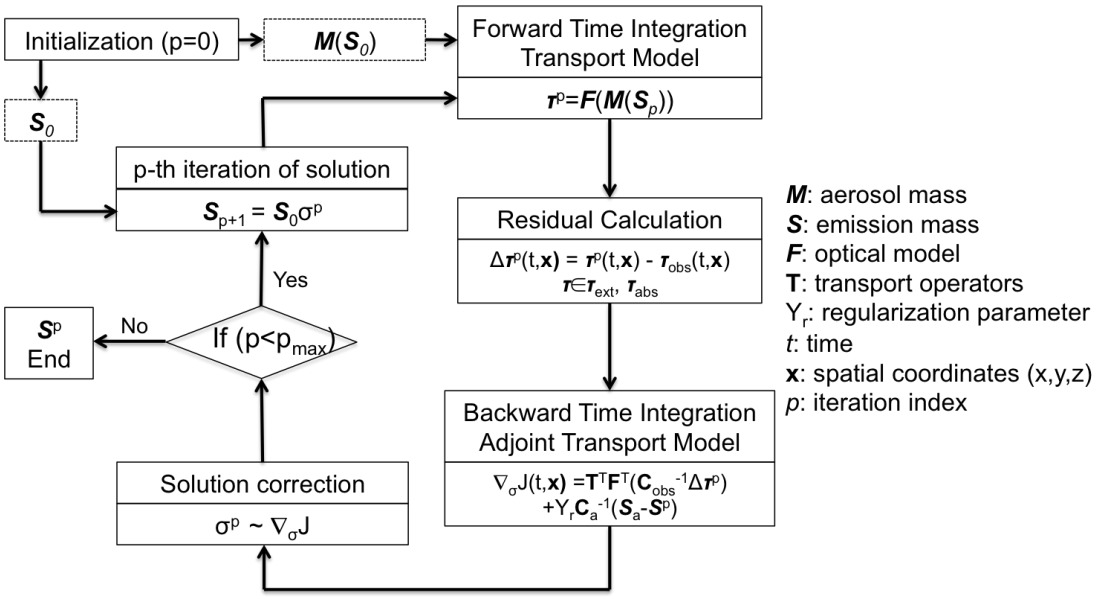

Figure 3.3: Diagram illustrating retrieval aerosol emission sources from satellite measurements

In order to optimize the specification of a priori constrains and initial guess, a number of synthetic tests were done in Section 3.2. It should be noted that using a priori estimate of emission S_0 is not the only way of adding a priori constraints in the inverse modeling. For example, Dubovik et al. (2008) demonstrated used of a priori knowledge on spatial and temporal variability of emissions, i.e. a priori limitation on derivative of corresponding functions (smoothness constraints). The potential advantage of smoothness constraints is that these limitations are milder than direct

assumptions about values of emissions and therefore they introduce less systematic errors in the retrieval. However, such constraints are not used in this study.

3.3 Numerical Test

In this section, a series of numerical tests was performed to verify and illustrate how the algorithm inverts the synthetic measurements, and tune the algorithm settings (e.g. initial guess, emission correction time resolution and BC refractive index). Two distinct experiments are conducted to test our retrieval over Africa (30°W-60°E, 40°S-40°N) and the globe. We first test our algorithm over Africa, because aerosol over Africa is relatively uncomplicated, dominant by desert dust in Sahara and seasonal biomass burning aerosols. This simplicity structure makes it the ideal study area to perform our retrieval algorithm preliminarily to define the setting for retrievals and evaluate its performance. Then, the globe experiment is conducted based on the knowledge of results over Africa. In order to retrieve aerosol emission over globe from PARASOL/GRASP observations, we further set the retrieval experiment in global scale to find a suitable way to perform retrievals.

3.3.1 Inverse algorithm test over Africa

We tested the possibility of retrieving DD, BC and OC aerosol emissions simultaneously from PARASOL-like remote sensing data that contains the spectral information of AOD and AAOD, lack information about vertical distribution and aerosol type. These tests are used for evaluating the effects of reducing the number of aerosol types and temporal variability of emissions.

Synthetic measurements are PARASOL-like spectral AOD and AAOD at six PARASOL wavelengths, simulated from 16 days of BC, OC and DD emissions, which, for simplicity, are specified to be constant over the 16 days, yet far from the prior model emissions in order to test the algorithm performance under the circumstances that a priori knowledge of the emission distribution is limited. Figure 3.4 shows the design of inversion test from synthetic measurements.

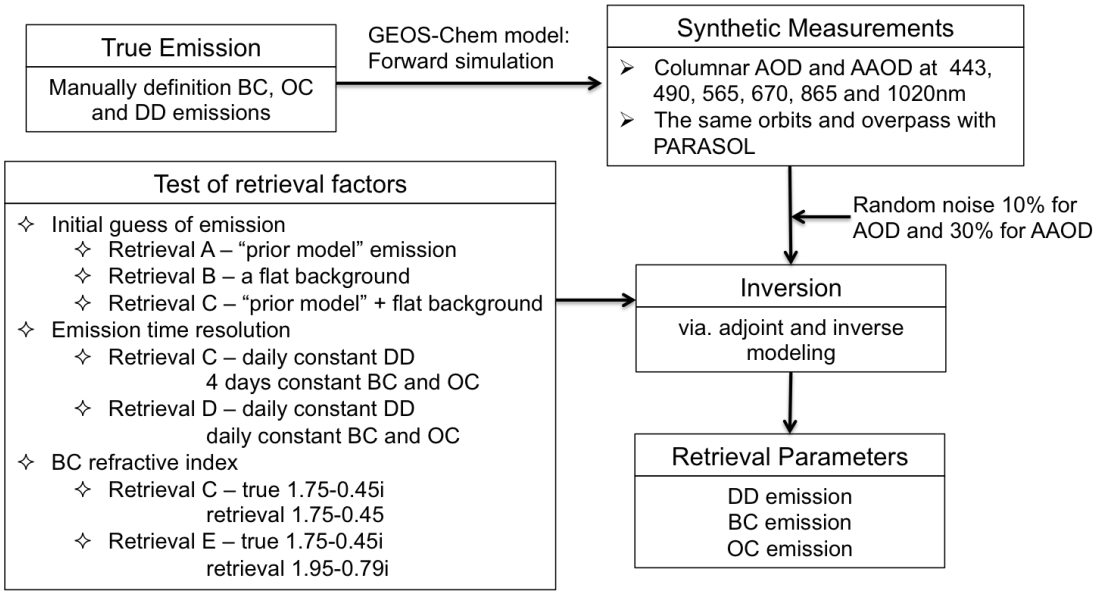

Figure 3.4: Diagram illustrating the inversion test from synthetic measurements

3.3.1.1 Spectrum weights

In our inversion framework, the observed aerosol parameters contain AOD and AAOD at six PARASOL wavelengths. In principle, the weighting of observations of AOD and AAOD at these different wavelengths should be defined by the observation error covariance matrix $\mathbf{C}_{obs}$. For example, usually AOD is about ten times higher than the AAOD at the same wavelength (SSA=1.0–AAOD/AOD) and therefore AAOD is expected to be retrieved and fitted more accurate on an absolute scale. However, at present knowledge of this matrix is uncertain, so we thus perform the following sets of tests to optimize the observational covariance weights. The spectral residual values are defined to characterize the quality of spectral AOD and AAOD fit:

$$R_{AOD}(\lambda) = \sqrt{\frac{1}{N_i} \sum_{i=1,\dots,N_i} [\tau_{i,obs}(\lambda) - \tau_{i,model}(\lambda)]^2} \tag{3.17}$$

$$R_{AAOD}(\lambda) = \sqrt{\frac{1}{N_i} \sum_{i=1,\dots,N_i} [\tau_{a,i,obs}(\lambda) - \tau_{a,i,model}(\lambda)]^2} \tag{3.18}$$

The values of the spectral residuals $R_{AOD}(\lambda)$ and $R_{AAOD}(\lambda)$ are calculated after each iteration. The following options were tested using well-known qualitative tendencies. In sensitivity test, two scenarios of spectrum weights are analysed. Since, we are fitting absolute value of AOD and AAOD, and the relative accuracy of

retrieved AOD and AAOD ($\Delta\tau/\tau$ and $\Delta\tau_a/\tau_a$) are expected the same. The spectrum weights are defined as follows:

Option A: Unify weights for AOD and AAOD at 6 wavelengths, for AOD $[1,1,1,1,1,1]^T$ and for AAOD $[1,1,1,1,1,1]^T$

Option B: Unify weights for AOD, while put more weights on AAOD, for AOD $[1,1,1,1,1,1]^T$ and for AAOD $[5,10,15,20,25,30]^T$

The retrievals are conducted with option A and option B respectively, with other settings held constant. Comparison of spectral residuals after 20 iterations are shown in Figure 6, which indicates Option B can have a better fit for AAOD by increasing the weights for AAOD, although spectral AOD can be fitted comparably well using either option.

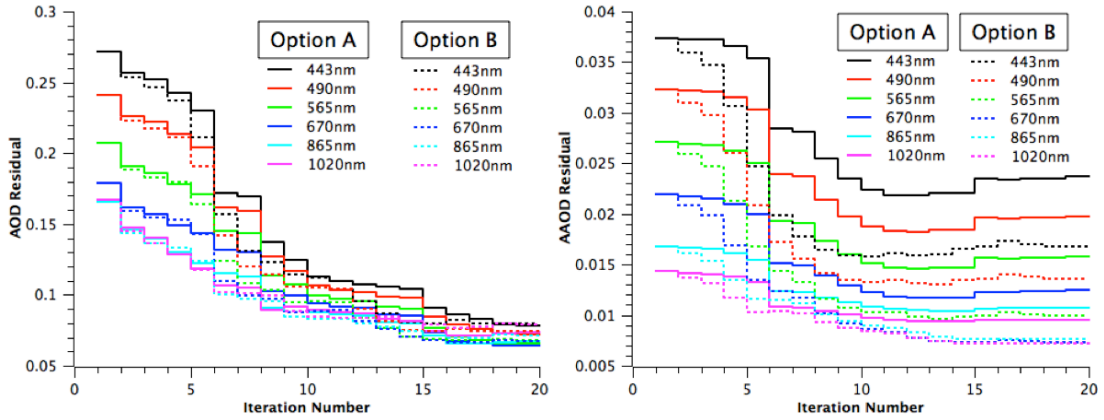

Figure 3.5: Comparison of spectral AOD and AAOD residual iteratively with two spectrum weight options

3.3.1.2 Effect of initial guess in emission retrieval

As mentioned in section 3.2, the emission retrieval is ill-posed problem and utilization of *a priori* constraints and initial guesses are essential factors for the retrieval. In our retrieval framework, the emissions are adjusted using scaling factors that scaling for initial guess of emissions, $\boldsymbol{S}=\boldsymbol{S}_0\boldsymbol{\sigma}$. In principle, if the inverse problem is well-constrained the solution should be independent of the initial guess. Therefore, we analyse the dependence on initial guess using different retrieval settings. The inversion is conducted with three different initial guess schemes that we describe in detail in the following sections. In each of these three schemes, the input synthetic measurements are 6 wavelengths AOD and AAOD, and the spectrum weights use the

"Option B" scenario, while the retrieved emission correction time variations are assumed to be daily constant for DD, and 4 day constant for BC and OC (note that we will separately test the assumption of emission correction time resolution in section 3.3.1.3). Figure 3.6 shows the "True emissions" of DD, BC and OC and also the difference between true and retrieved emissions from three different initial guess schemes (Retrieval A, Retrieval B and Retrieval C). Figure 3.8 shows the scatter plots between BC, OC and DD emissions retrieved from "Retrieval A, B, C" versus true values.

A. "Prior model": Initial guess is equal to "Prior model" emissions

In this method, the "prior model" emissions are directly used as initial guess, therefore the adjustments of emissions are limited to the pixels that prior model emissions $\boldsymbol{S}_0>0$. At the same time, the "True emissions" have difference with "prior model". The upper panel in Figure 3.6 is assumed true BC, OC and DD emission distributions (units: kg/day) respectively. And the second panel "Retrieval A - True" shows the differences between retrieved and true emissions from Retrieval A.

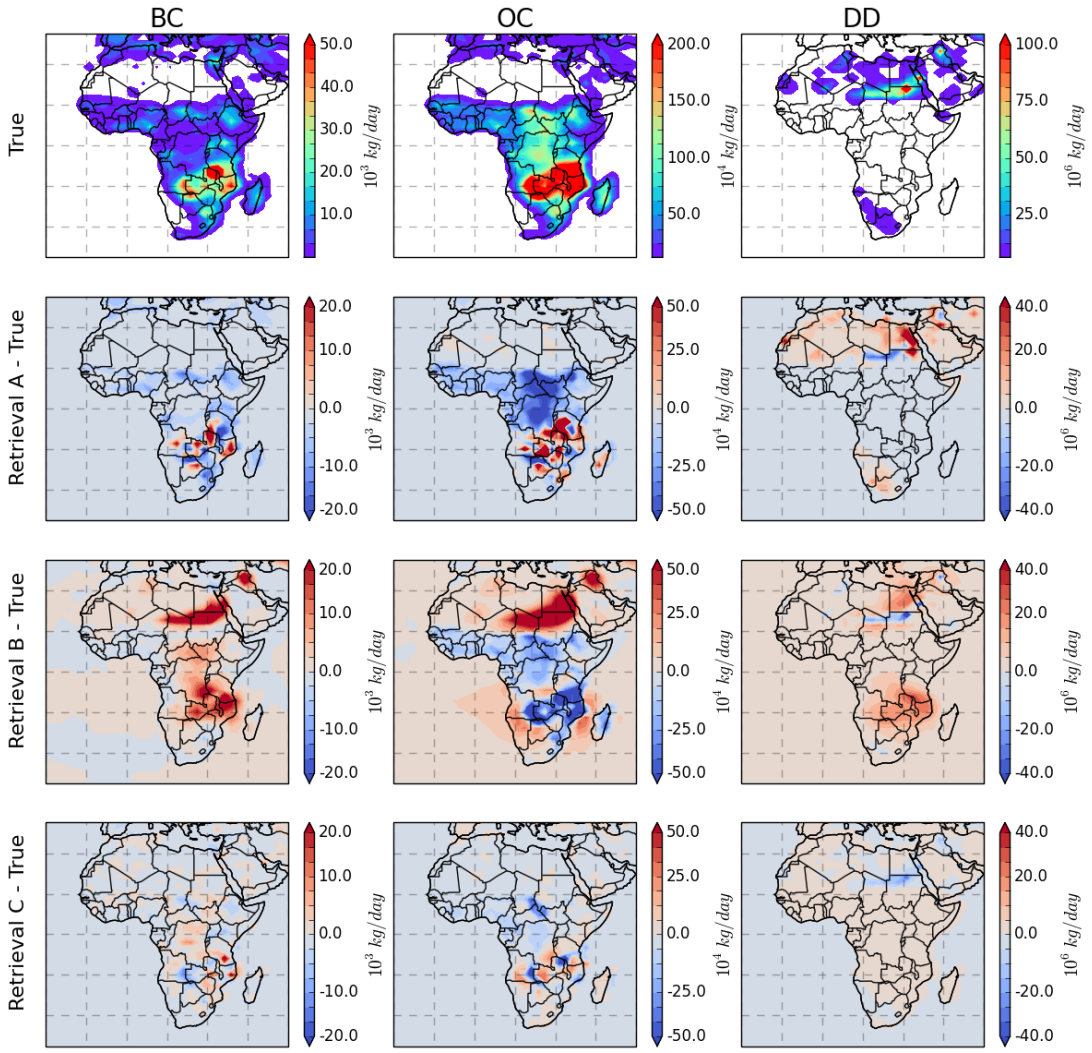

Figure 3.6: Inversion test for retrieving BC, OC and DD emissions from synthetic measurements with three different initial guess schemes: (A) "prior model" emissions – "Retrieval A"; (B) Spatially uniform – "Retrieval B"; (C) Prior emission with spatially uniform background – "Retrieval C";

For "Retrieval A", the retrieval highly relies on the accurate distribution of model prior emissions, because the retrieval only can adjust the emissions on the grid boxes that model prior emission is nonzero, and thus the retrieval couldn't create new sources. In our inversion test, the model prior emissions are different from the truth both for distribution and strength (Figure 3.8 shows the difference between the initial guess and assumed true emissions for BC, OC and DD). Therefore, as shown in Figure 3.6, the Retrieval A produces overestimations over the grid boxes that $\boldsymbol{S}_0$>0,

while $\boldsymbol{S}_{\text{true}}$=0, here $\boldsymbol{S}_{\text{true}}$ represent true emissions, however the underestimations occur over the grid boxes that $\boldsymbol{S}_0$=0, while $\boldsymbol{S}_{\text{true}}$>0.

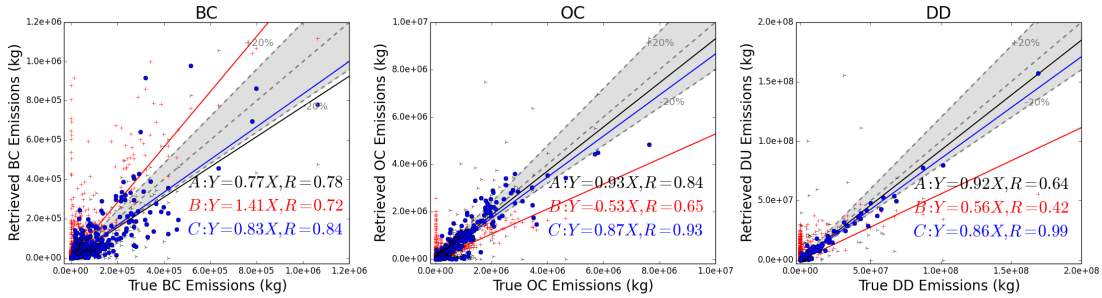

Figure 3.7: Scatter plots between BC, OC and DD emissions retrieved from "Retrieval A, B, C" versus true values

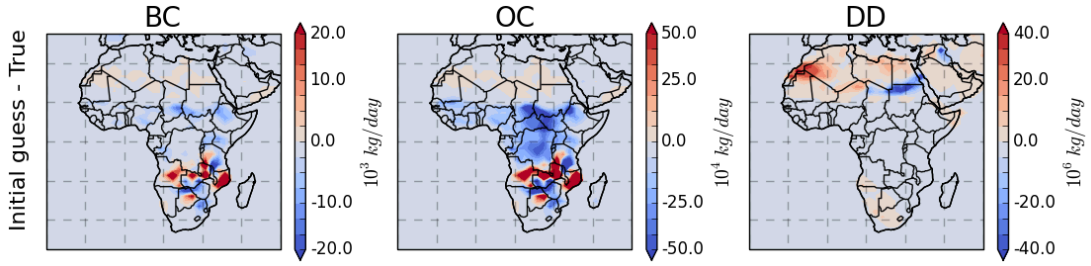

Figure 3.8: The differences between initial guess (from prior model) and assumed true BC, OC and DD emissions

B. Flat background everywhere

For Retrieval B, we investigate the use of spatially uniform initial guess for the emissions. With this initialization, we allow BC, OC and DD emission to be generated everywhere over land and ocean, which is equivalent to not using *a priori* knowledge of model aerosol emissions as an initial guess. From the Figure 3.6 panel "Retrieval B – True", the algorithm can determine the intensive aerosol emission grid boxes, where high aerosol loading is observed. However, the desert dust and carbonaceous aerosol sources were not correctly reproduced since a unify emission is used everywhere. The scatter plots between retrieved emissions from "Retrieval B" and true values are also shown in Figure 3.7. In this case, the retrieval could produce overestimations over some grid boxes where $\boldsymbol{S}_{\text{true}}$=0. Although, the uniform emission assumption gives the algorithm more freedom to find new sources, our tests indicate the retrieval could produce false sources in this assumption when the algorithm tries to determine BC, OC and DD emissions simultaneously. This misrepresentation

indicates that the spectral AOD and AAOD are not sufficient enough to identify BC, OC and DD emission without any *a priori* knowledge.

C. "Prior model" emission with flat background

In retrieval C, the retrieval was initiated using "prior model" emission but including a spatially uniform value over the land pixels where $\boldsymbol{S}_0$=0. In this study, flat value equals to 10^{-4} Tg/day/pixel for DD; 10^{-6} Tg/day/pixel for BC; $5*10^{-6}$ Tg/day/pixel for OC, the background value accounts for ~5% of the true emissions over entire area. This assumption allows retrieval of BC, OC and DD aerosol emissions everywhere over land (ship emissions over ocean are included in model prior emissions), and at the same time it uses prior emission constraints to prevent the false source generation. Figure 3.6 and 3.7 show that overall "Retrieval C" captures the emission distributions more accurately than "Retrieval A" and "Retrieval B". The averaged ratio of retrieved emission to truth ($\sum_{N_{pixels}} \frac{\mathbf{S}_{\text{retrieval}}}{\mathbf{S}_{\text{true}}} / N_{pixels}$) is 1.02 ± 1.05 for BC, 0.87 ± 1.42 for OC and 1.24 ± 1.80 for DD.

3.3.1.3 Assumption of emission correction temporal resolution

Aerosol sources are known to have high temporal and spatial variability. However, because PARASOL observations have limited temporal coverage (e.g. ~2 days global coverage, with observations once per day), the variability of aerosol emission at any given location can only be retrieved at a frequency no more than once per day. In order to investigate how assumptions regarding temporal variability of emission can affect the retrieval, we repeat the retrieval using two scenarios for emission correction: ET1, daily correction constant of DD, BC and OC emissions, and ET2, daily correction constant of DD emission and 4 days correction constant of BC and OC emissions. For each scenario, the input observations are 6 wavelengths of AOD and AAOD, and the retrieval is initialized by "prior model" emission with a uniform background emission (Retrieval C). Two scenarios are used. We test these two scenarios by conducting a 16-days retrieval, and Figure 3.9 shows the comparison between retrieved daily total DD, BC and OC emissions with the "True emissions". Note that the ET1 scenario uses the same settings with "Retrieval C" in section 3.3.1.2, and ET2 is named "Retrieval D".

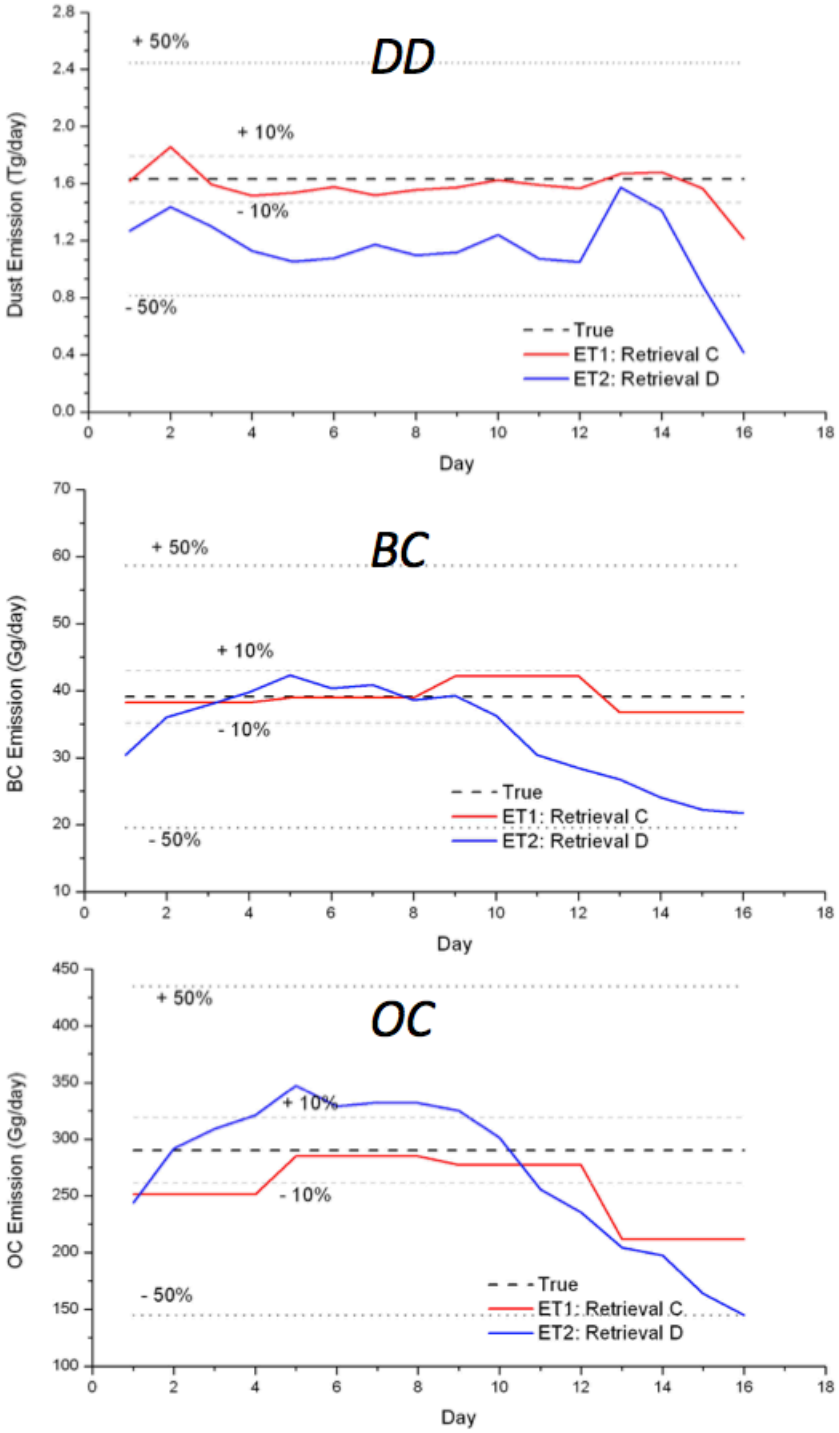

Figure 3.9: Sensitivity test for retrieving DD, BC and OC emissions over 16-days with two scenarios of assumption of emission correction temporal resolution

Figure 3.9 shows the retrieval maximum uncertainty for total daily DD emission over study area is within 25.8% for Retrieval C, however this value reaches more than 50% for Retrieval D. For BC, the maximum uncertainty is within 5.9% for total daily emission from Retrieval C, while up to 40.8% for Retrieval D. The uncertainty of

daily OC emission is within 26.9% for OC using Retrieval C, while about 38.6% for Retrieval D. Overall, from this sensitivity test, the "Retrieval C" shows a better capability to capture the spatial distribution of DD, BC and OC emissions than "Retrieval D", and it does not introduce false temporal variability.

3.3.1.4 Uncertainty in assumption of BC refractive index

Aerosol particles' light scattering and absorption efficiencies are determined by their complex refractive indices, expressed as m= n-ki, where n is the real part and k is the imaginary part. The real part of the complex refractive index defines the light scattering property of an aerosol species, whereas the imaginary part of the complex refractive index determines the absorbing ability. Black carbon aerosol is the strongest atmospheric absorber of solar radiation. Its imaginary refractive index is at least about two orders of magnitude higher than other aerosol species (see Table 2.2). To identify the impact of the uncertainties of BC refractive index in our results, we test another commonly used specification of 1.95-0.79i (Bond and Bergstrom, 2006) in our retrieval scheme (denoted as Retrieval E). Figure 10 compares the BC emission results from Retrieval E and Retrieval C (where the BC refractive index of 1.75-0.45i (Hess et al., 1998) was used), with the "true" BC emission.

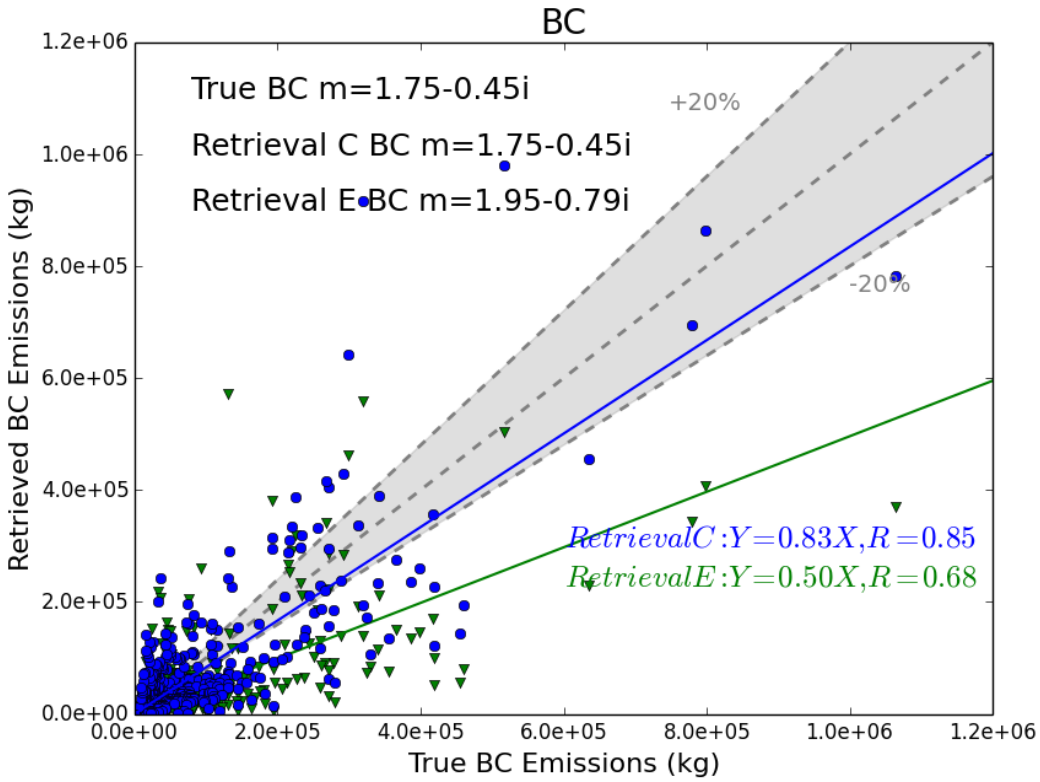

Figure 3.10: Test of BC particle refractive index influence on the retrieval of BC emissions

The synthetic measurements of AOD and AAOD are simulated with BC refractive index m=1.75-0.45i, and the scenario "Retrieval C" uses the retrieval with the same BC refractive index; the slope of linear regression between the resulting retrieved and true BC emissions is 0.83. In contrast, the "Retrieval E" scenario uses the retrieval with a higher BC absorption and scattering definition, m=1.95-0.79i, and as expected we get lower magnitudes of BC emissions (slope between retrieved and true BC emissions is about 0.5). This sensitivity test demonstrates that uncertainty in the BC refractive index can lead to a factor of about 1.6 in total BC emissions.

Overall, these sensitivity tests show that our inversion scheme is capable of determining the strength and spatial distribution of BC, OC and DD emissions simultaneously from the multispectral PARASPL/GRASP AOD and AAOD products in the following manner:

1. Six wavelengths (VIS-NIR) AOD and AAOD from PARASOL/GRASP are needed to retrieve BC, OC and DD emissions simultaneously.

2. The optimal spectral weighting factors for the PARASOL 6 wavelengths are $[1,1,1,1,1,1]^T$ for AOD and $[5,10,15,20,25,30]^T$ for AAOD, since it can provide a better fit of spectral AAOD.
3. The BC, OC and DD emissions are allowed everywhere over land. The retrieval is initialized by "prior model" emissions with a uniform background. The retrieval with this initialization could detect new sources and perform satisfactorily even when *a priori* knowledge of aerosol emission is not fully consistent with the assumed emissions.
4. The emission corrections are assumed daily constant for DD and 4 days constant for BC and OC. Owing to the limited observations available for assimilation, this assumption helps to make the retrieval more stable and accurate.
5. BC refractive index is sensitive to BC emission retrieval, which could produce a factor of 1.6 differences between the two sets of commonly used BC refractive index data for total BC emission. We will produce two BC emission datasets with two scenarios of BC refractive index, Case 1: m=1.75-0.45i and Case 2: m=1.95-0.79i.

3.3.2 Inverse algorithm test for global observations

In this section, we will discuss the inversion approach used in the retrieval of global desert dust and primary carbonaceous aerosol emissions from PARASOL/GRASP spectral AOD and AAOD. The application of this method will be presented in Chapter 5. Here we will focus on the method description and why we explore a new approach to retrieve over globe. We first do a similar experiment as in section 3.3.1. Synthetic measurements are global PARASOL-like spectral AOD and AAOD at PARASOL 6 wavelengths, simulated from manual definition of 28 days BC, OC and DD emissions ("True or Assumed emissions"), we keep the GEOS-Chem model prior SU and SS aerosol emissions (Jaeglé et al., 2011; Park et al., 2004) in simulation of synthetic measurements.

3.3.2.1 Effect of SU and SS on DD, BC and OC emission retrieval

In this study, we mainly focus on the aerosol emission of DD, BC and OC, while the retrieval of SU and SS aerosol emission is not included currently. In the sensitivity test over Africa, the test ignores the contribution of SU and SS. And in the retrieval of real data over Africa in Chapter 4, the algorithm optimizes DD, BC and OC aerosol emissions, while keep the standard SU and SS emissions as the GEOS-Chem model (Jaeglé et al., 2011; Park et al., 2004), because the SU and SS aerosol are not the major aerosol components over Africa, and the contribution to total AOD is less than 10%, (see the simulation in Figure 2.9). Thus, our retrieval ignores the uncertainty of SU and SS emission that could also contribute to the difference between of model simulation and satellite observation.

However, the SU aerosol is the leading component in the industry area, such as North America and East Asia. Figure 2.9 shows that the SU aerosol becomes the first contributor of total AOD in Southeast China and North America. Hence, the approach we did in the retrieval over Africa may be not applicable, since the uncertainty of SU emission can propagate to the retrieval of DD, BC and OC emissions.

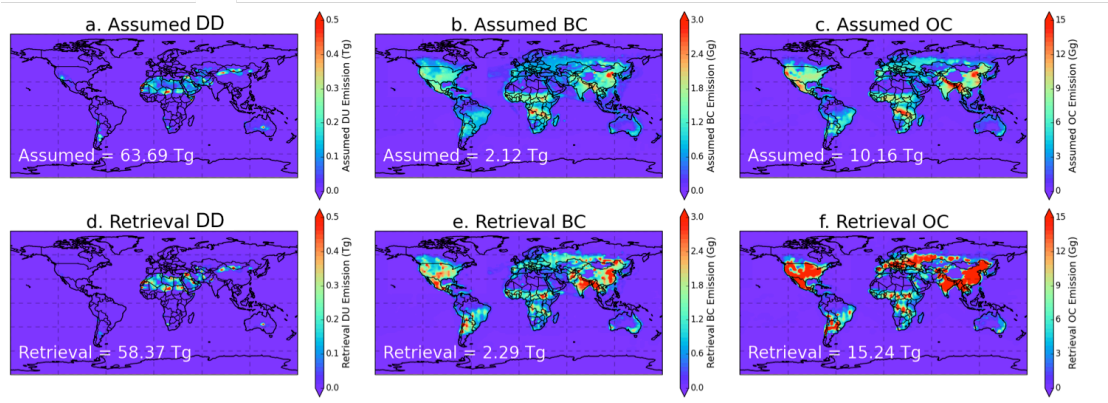

Figure 3.11: Inversion test for retrieving global BC, OC and DD emissions from synthetic measurements; (a) Assumed true dust emission; (b) Assumed true black carbon emission; (c) Assumed true organic carbon emission; (d-f) Retrieved global DD, BC and OC emissions if the retrieval ignore the contribution of sulfate and sea salt.

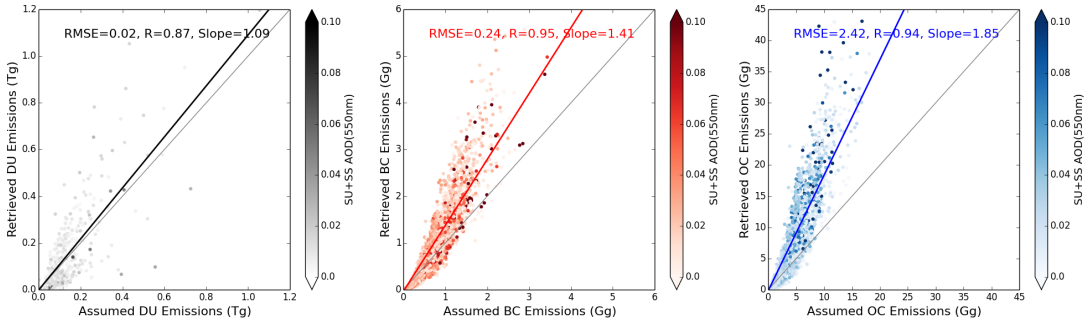

Figure 3.12: Scatter plots between retrieved global DD, BC and OC emissions versus true values, the color of the points present the assumed SU+SS AOD (550nm) of this grid box

First, we use the same approach (Retrieval C) to retrieve global DD, BC and OC emissions that ignoring the contribution of SU and SS contribution (equivalent to 100% underestimation of SU and SS emissions). Figure 3.11 shows the inversion test for retrieving global BC, OC and DD emissions from synthetic PARASOL-like measurements with the "Retrieval C" settings. Figure 3.11a-c shows the assumed true DD, BC and OC aerosol emissions respectively, and Figure 3.11d-c presents the retrieval results of DD, BC and OC aerosol emissions, respectively. Here the algorithm still shows the good capability to determine spatial distribution and strength of DD emission. However, the retrieved BC and OC emissions obviously show overestimation in Southeast China and North America, where the SU particles are dominant. The inversion algorithm will propagate the underestimation of SU and SS to overestimation of BC and OC emissions. Figure 3.11 shows the comparison of retrieved global DD, BC and OC emissions with assumed values, color-coded with SU+SS AOD (550nm). In this inversion test, 100% underestimation of SU and SS emission result in a factor of 1.1 (Normalized Mean Bias, NMB=+8.0%) and a factor of 1.5 (NMB=50%) overestimation of BC and OC emissions respectively, while the influences on DD emission are less than 10% (NMB=-8%).

3.3.2.2 Sequential approach

To resolve the effect of SU and SS emissions on the retrieval of DD, BC and OC emissions, or reduce this impact on inversion, we design a sequential approach. Figure 3.13 shows the structure of the sequential approach. The idea is to divide the retrieval into two steps using the fact that carbonaceous is usually fine mode dominant

and BC particles are absorbing more ubiquitously from UV to near infrared wavelengths; while DD aerosol is usually coarse mode dominant and is also a major component contribute to aerosol absorption, however, the DD particles absorb most strongly in the UV and short wave visible channels.

- ✓ Step 1: Using PARASOL/GRASP spectral AAOD to optimize the global BC and OC aerosol emissions, keeping the DD, SU and SS aerosol as prior model;
- ✓ Step 2: Select the PARASOL/GRASP retrievals where the AExp<1.0 as inputting observations to optimize global DD aerosol emissions, with optimized BC and OC aerosol emissions from Step 1 and prior model SS and SS emissions constant;

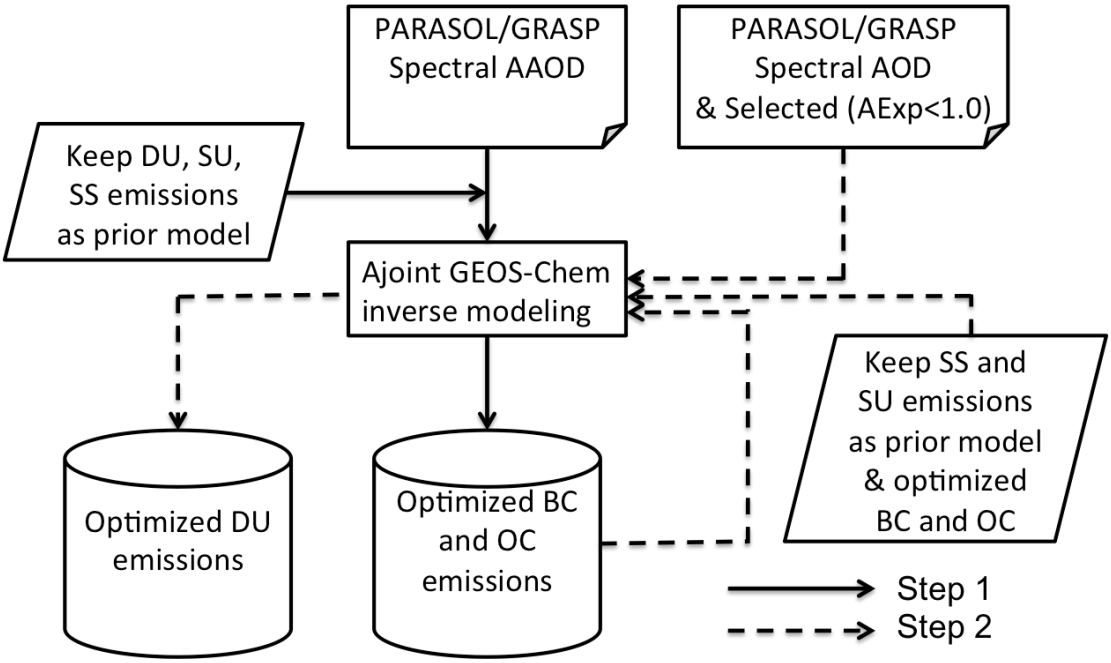

Figure 3.13: Design of a sequential approach to retrieve BC, OC and DD aerosol emission over globe; Step 1: Retrieval of BC and OC aerosol emissions from PARASOL/GRASP spectral AAOD; Step 2: Retrieval of DD aerosol emission from PARASOL/GRASP AOD (AExp<1.0) using optimized BC and OC emission from step 1 and SS and SU emission from prior model

Next, we will test and evaluate the inversion performance of this sequential approach. First, we compare the initial guess of the retrieval with the true values (see Figure 3.15). In order to test the inversion algorithm, the first initial guess cannot be

very close to the true value, otherwise, the inversion test will become inconclusive. In the globe emission retrieval, we keep the initial guess as we did over Africa, that a prior model emission with a spatially unified background over land. Thus, Figure 3.14 shows the comparison of AOD and AAOD simulated from initial guess with that simulated from assumed true values. Meanwhile, Figure 3.15 presents the assumed BC, OC and DD aerosol emission in comparison with that from the initial guess of the inversion.

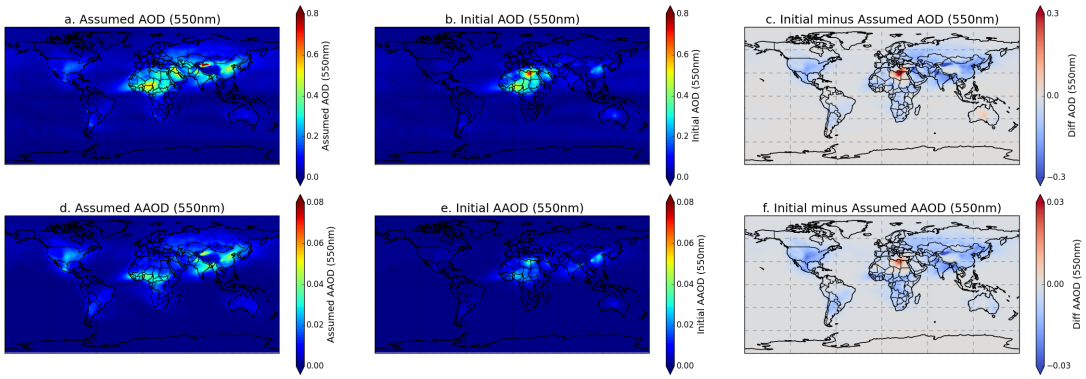

Figure 3.14: Distribution of assumed 28 days mean AOD and AAOD in comparison with AOD and AAOD at 550nm simulated from initial guess of aerosol emissions, and the differences of initial guess and assumption of AOD (c) and AAOD (f) are shown.

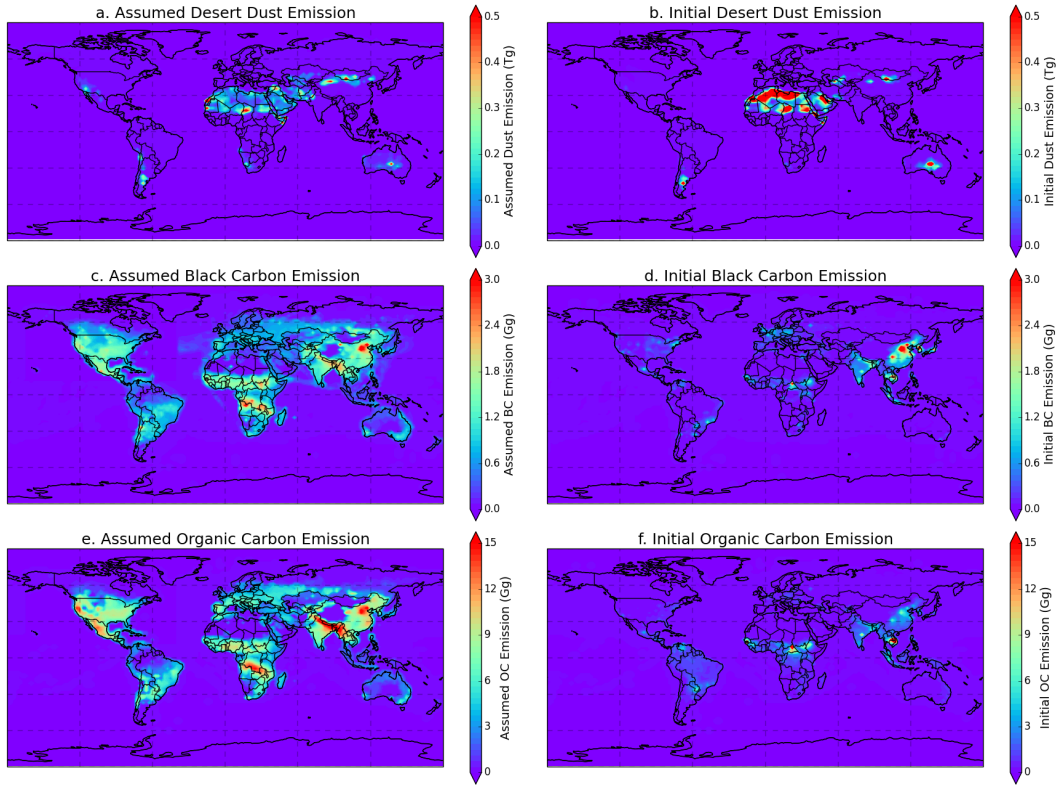

Figure 3.15: Distribution of assumed 28 days total DD, BC and OC aerosol emissions in comparison with the initial guess of DD, BC and OC emissions of our inversion

Figure 3.15a, 3.15c and 3.15e show the assumed true total DD, BC and OC aerosol emissions over entire 28 days, respectively. The distributions of AOD and AAOD at 550nm in Figure 3.14a and Figure 3.14d show the synthetic measurements of AOD and AAOD from assumed aerosol emissions (the SU and SS emission are adopted from prior GEOS-Chem simulation). Figure 3.15b, 3.15d and 3.15f show the initial guess of total DD, BC and OC aerosol emissions over 28 days; here the initial guess is adopted from the prior GEOS-Chem emission with a spatially unified background value. Figure 3.14d and Figure 3.14e present the initial guess of the AOD and AAOD; meanwhile the differences between initial guess and assumed AOD and AAOD are also shown in Figure 3.14c and 3.14f, respectively.

In order to test the inversion performance, the assumed true emission cannot be close to the initial guess of emissions. For example, the initial guess gives stronger DD emission in northwest Sahara where our assumption put a lower intensive value; in addition, the initial guess of global carbonaceous aerosol is broadly lower than our assumption and the spatial coverage has also some differences in particular areas, such as Northeast Asia, North America. However the spatial pattern is somewhat similar, because the emission assumption cannot be against our *a priori* knowledge of the distribution of industry, desert dust area.

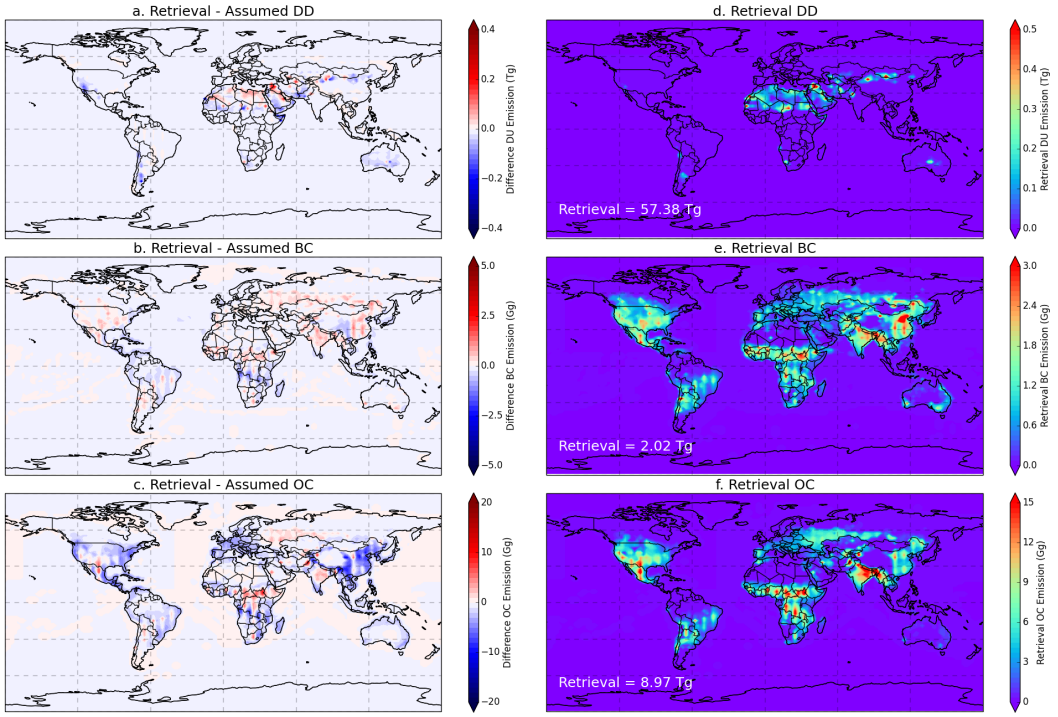

Figure 3.16: Inversion test of using sequential approach to retrieve global DD, BC and OC aerosol emissions; a. Spatial distribution of differences between retrieval and assumed DD emission; b. Spatial distribution of differences between retrieval and assumed BC emission; c. Spatial distribution of differences between retrieval and assumed OC emission; d. Retrieved DD emission; e. Retrieved BC emission; f. Retrieved OC emission over entire 28 days;

The spectrum weights and initial guess are used the same setting as we discussed in section 3.3. While we slight adjust the temporal resolution of emission corrections, we try to determine 2 days correction constant BC and OC aerosol emissions. Above all is the preparation of our inversion. Next the performance of our inversion will be analyzed. Figure 3.16d-f show the retrieval results of global distribution of DD, BC and OC aerosol emissions over 28 days from sequential approach; and the difference between retrieved emissions and assumed DD, BC and OC aerosol emissions are also shown in Figure 3.16a-c. The retrieval method can capture the spatial distribution and strength of global DD, BC and OC aerosol emissions. From the total global emission over entire 28 days, the retrieved DD emission is 57.38 Tg with the assumed value 63.69 Tg; retrieved BC emission is 2.02 Tg with assumed 2.12 Tg BC; retrieved OC 8.97 Tg with assumed 10.16 Tg OC emission. Hence, we diagnose for each component the normalized mean bias $\mathrm{NMB} = \sum(M_i - O_i)/\sum O_i$, where sums are

over the ensemble grid boxes i, and M_i and O_i are the retrieved and assumed values. NMB values are -9.9% for DD, -4.7% for BC, and -11.7% for OC.

Besides, the daily relative difference of the retrieval and assumed DD, BC and OC emissions are investigated and shown in Figure 3.17. The mean absolute bias (MAB $= \sum |M_i - O_i| / \sum O_i$) for retrieved daily global DD emission is 6.7%, and the maximum absolute bias is 48%; mean absolute bias for BC is 3.5% with the maximum to 18.3%; mean absolute bias for OC is 11.0% with the bias to 60.7%.

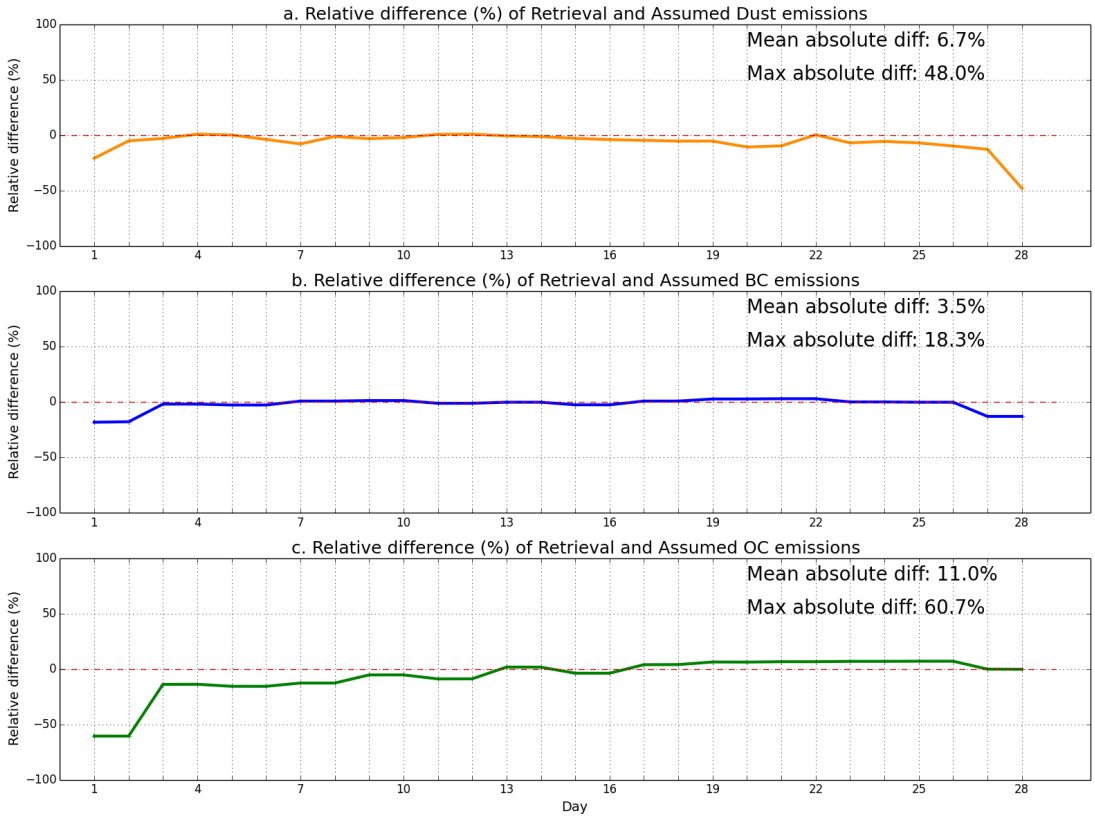

Figure 3.17: Relative difference (%) of retrieval and assumed daily total (a) DD, (b) BC and (c) OC emissions; The mean absolute difference and the max absolute difference during 28 days are also provided in the top right of each figures.

Another indicator of the inversion performance is the fitting of input observations. Figure 3.18 and 3.19 shows the fitting of input PARASOL-like six wavelengths AAOD and AOD, respectively. Meanwhile, the probability of the difference between fitted and assumed value at six wavelengths are also shown in Figures 3.18 and 3.19. From the fitting of spectral AAOD of Step 1 in Figure 3.18, the majority of the fitting differences of AAOD for all six wavelengths are located within ± 0.01, which indicates that the model posterior running with retrieved emissions can reproduce

spectral AAOD with a good agreement with input synthetic measurements. Meanwhile, the fitting differences of AOD are mainly in ±0.05 range, which also indicates that the retrieved emissions can reproduce spectral AOD with good agreement with measurements. The agreements of fitted spectral AOD and AAOD with input synthetic measurements suggest the convergence of the inversions.

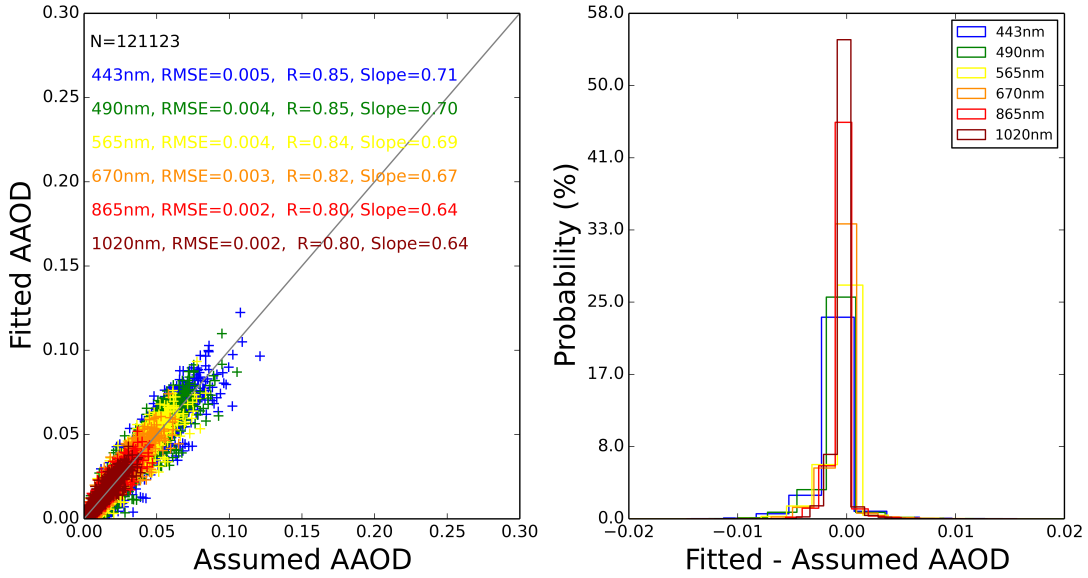

Figure 3.18: Illustration of fitting input PARASOL-like six wavelengths spectral AAOD of Step 1

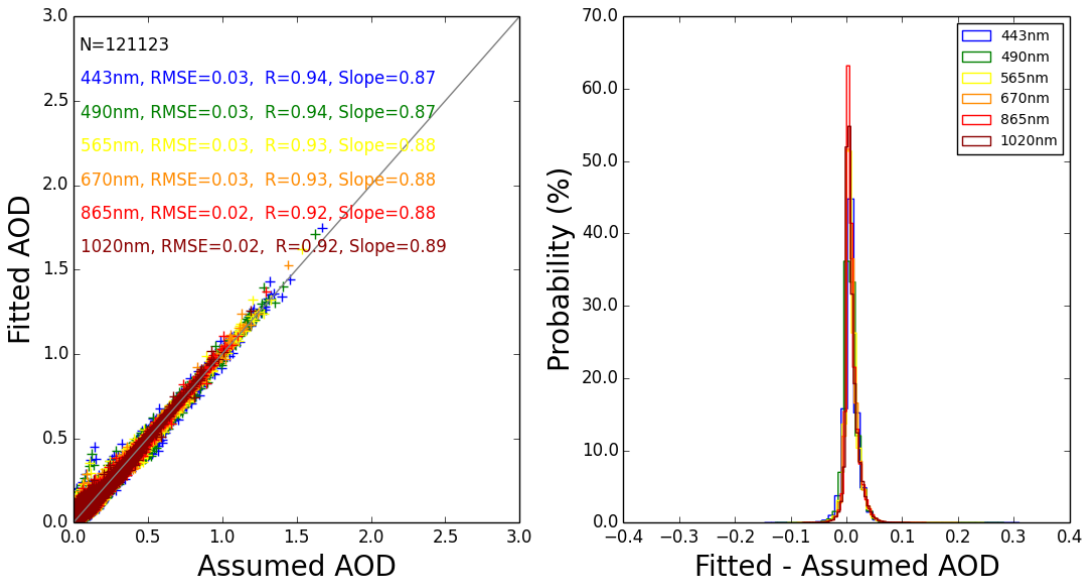

Figure 3.19: Illustration of fitting of input PARASOL-like six wavelengths spectral AOD of Step 2

In this chapter, we introduce the general concept of the methodology that using satellite observations to retrieve distribution and strength of aerosol emissions. Then the inverse model using adjoint method is discussed. In order to deal with the unbalance of the input known parameters and retrieved parameters, the implementation of *a priori* constrain of the inverse model is presented. Finally, we proposed two approaches to retrieve real PARASOL/GRASP observations over Africa and over globe, respectively. The inversion test using synthetic PARASOL-like measurements are performed; the performance of these two approaches are evaluated as well. Next, we will apply these two approaches to retrieve real PARASOL/GRASP aerosol data over Africa (Chapter 4) and over globe (Chapter 5).

Acknowledgements

I thank Daven K. Henze and Yanko Davila for providing continuous help of adjoint GEOS-Chem model and constructive suggestions on the inversion algorithm development. I also thank Tatyana Lapyonak and Anton Lopatin for revising this manuscript.

Chapter 4

Enhance/Optimized desert dust and carbonaceous aerosol emissions over Africa

I didn't fail the test, I just found 100 ways to do it wrong.

Benjamin Franklin

4.1 Introduction

Atmospheric aerosols have a variety of emission sources and complex chemical compositions. Desert dust (DD) aerosol is one of the most mass abundant types of aerosol emitted into atmosphere, while the range of global total dust emissions estimation spans a factor of about five (Huneeus et al., 2011). Primary carbonaceous aerosol, which consists of black carbon (BC) and organic carbon (OC) from combustion of fossil fuels, biofuels and biomass, has strong light absorbing that can affect the earth-atmosphere system energy balance. High uncertainty in carbonaceous aerosol emission sources (Bond et al., 2004) translates into a significant high uncertainty in evaluating their climate effects. The Intergovernmental Panel on Climate Change estimates the global mean radiative forcing due to carbonaceous aerosol of -0.1 w/m^2 in their 2001 report, in 2007 they raise it to 0.18 w/m^2, in the latest report (IPCC, 2013) the value comes to 0.31 w/m^2 (Myhre et al., 2013).

Furthermore, desert dust and carbonaceous aerosols can have deleterious impacts on regional air quality and public health (Chin et al., 2007; Monks et al., 2009; Li et al., 2013). Thus, reliable observation and simulation systems are needed to accurately evaluate their emissions that are crucial to understand the role atmospheric aerosols play in earth-atmosphere system (Bellouin et al., 2005).

In this chapter, I present the application of the aerosol emission inversion method for optimizing the desert dust and carbonaceous aerosol emissions over Africa. Section 4.2 describes the model and data used in this study. The aerosol model GEOS-Chem ajdoint of Henze et al. (2007) is fully conceptually consistent with the inversion developed by Dubovik et al. (2008) based on the GOCART model. The details of inverse modeling and performance evaluation of the inversion framework using numerical tests have been presented in the Section 3.2. In order to interpret the retrieval results and improve our understanding of aerosol emissions, we retrieve one-year of daily DD BC and OC emissions (see the Section 4.3). Evaluation of these inversion results using independent AERONET, MODIS and OMI observations, as well as implementation of the posterior emissions in the GEOS-5/GOCART model is presented in Section 4.4. Conclusions and discussion of the study's merits and limitations are considered in the Section 4.5.

4.2 Model and data description

4.2.1 Study Area

The study area (30°W-60°E, 40°S-40°N) is shown in Figure 4.1, which covers the whole of Africa and the Arabian Peninsula, comprising the largest dust source and biomass burning region of the globe. The spatial and temporal variability of DD, BC and OC aerosols in this area has drawn numerous research (Duncan et al., 2003; Prospero and Lamb, 2003; Engelstaedter et al., 2006; Liousse et al., 2010; Zhao et al., 2010; Ginoux et al., 2012; Ealo et al., 2016). The number of PARASOL/GRASP retrievals per 0.1° x 0.1° grid box over a year (December 2007 to November 2008) and 28 AERONET(Holben et al., 1998) sites (Table 4.1) used to evaluate GEOS-Chem model simulations and PARASOL/GRASP retrievals are shown in Figure 4.1. Note that the GRASP algorithm performs aerosol retrievals at PARASOL's native resolution of 6~7 km; each 0.1° grid box could thus have more than one GRASP

retrieval, so the number of PARASOL/GRASP retrievals exceeds the number of days in some grid boxes of Figure 1. The amount of GRASP algorithm (see in section 2.3) retrievals over Northern Africa Sahara and the Arabian Peninsula desert region is relatively high, whereas other regions have a reduced number of retrievals due to the presence of clouds.

Table 4.1: AERONET 28 sites used in this study for validation with model simulation and PARASOL/GRASP retrievals.

Site	Coordinates			Country
	Latitude	Longitude	Altitude	
Capo_Verde	16.72N	22.93W	60m	Sal Island
Dakar	14.38N	16.96W	0m	Senegal
Ascension_Island	7.98S	14.42W	30m	Ascension Island
Santa_Cruz_Tenerife	28.47N	16.25W	52m	Spain
Saada	31.63N	8.16W	420m	Morocco
IER_Cinzana	13.28N	5.93W	285m	Mali
Agoufou	15.35N	1.48W	305m	Mali
Granada	37.16N	3.61W	680m	Spain
Banizoumbou	13.54N	2.67E	250m	Niger
Blida	36.51N	2.87E	230m	Algeria
Ilorin	8.32N	4.34E	350m	Niger
Tamanrasset_INM	22.79N	5.53E	1377m	Algeria
Zinder_DMN	13.78N	8.98 E	460m	Niger
DMN_Maine_Soroa	13.22N	12.02E	350m	Niger
Messina	38.20N	15.57E	15m	Italy
IMAA_Potenza	40.60N	15.72E	820m	Italy
FORTH_CRETE	35.33N	25.28E	20m	Greece
Eilat	29.50N	34.92E	15m	Israel
IMS-METU-ERDEMLI	36.57N	34.26E	3m	Turkey
CRPSM_Malindi	3.00S	40.19E	12m	Kenya
Mezaira	23.15N	53.78E	204m	United Arab Emirates
Dhadnah	25.51N	56.33E	81m	United Arab Emirates
El_Arenosillo	37.11N	6.73W	0m	Spain
Lecce_University	40.34N	18.11E	30m	Italy
Nes_Ziona	31.92N	34.79E	40m	Israel
Nairobi	1.34S	36.87E	1650m	Kenya
REUNION_ST_DENIS	20.88S	55.48E	0m	Mauritius
Mongu	15.25S	23.15E	1107m	Zambia

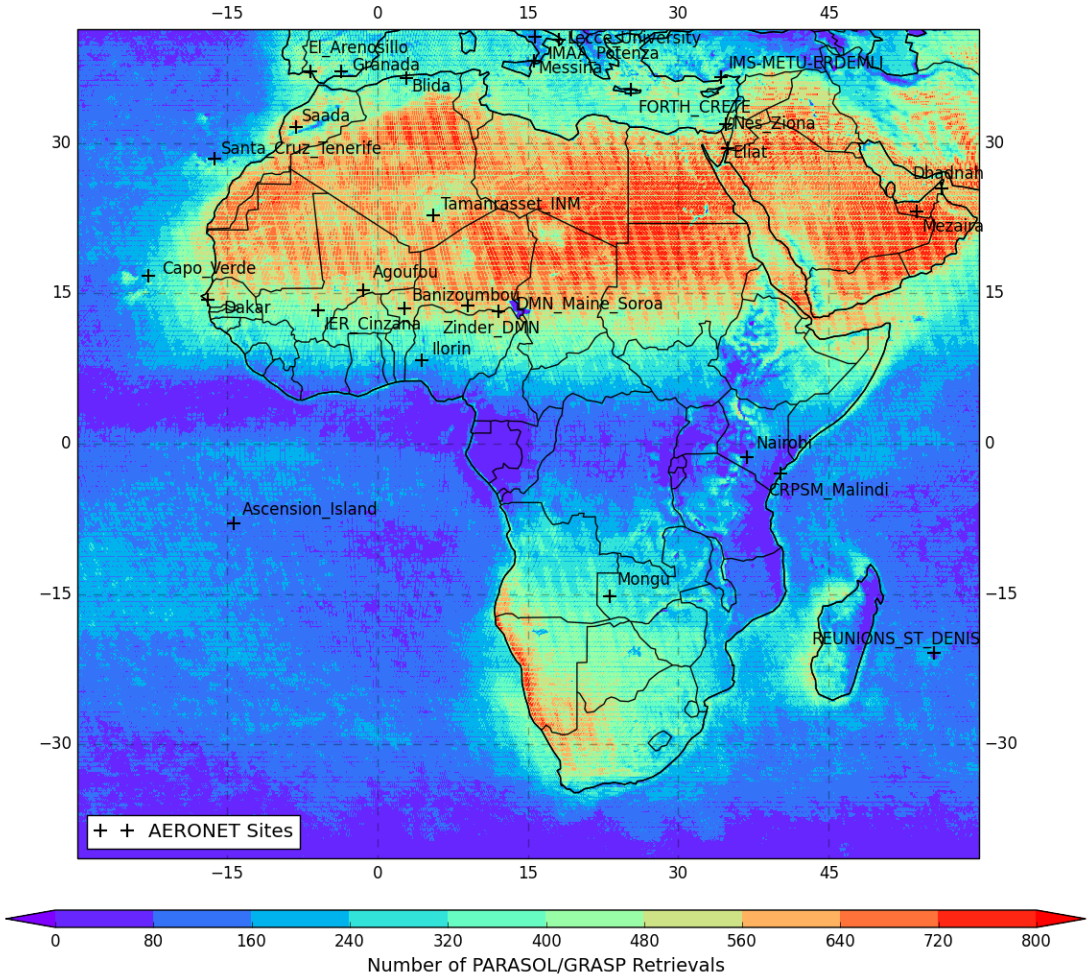

Figure 4.1: Distribution of PARASOL/GRASP AOD retrievals per 0.1° x 0.1° grid cell over a year (December 2007 to November 2008); the 28 AERONET sites used for validation are also shown with black cross.

4.2.2 GEOS-Chem model and its adjoint

GEOS-Chem is a global 3-dimensional chemical transport model driven by assimilated meteorological data from the NASA Goddard Earth Observing System Data Assimilation System (GEOS-DAS) (Bey et al., 2001). We use the GEOS-Chem (v9-02) model for forward aerosol simulation with 47 layers vertical resolution and 2° (latitude) x 2.5° (longitude) horizontal resolution. DD, BC and OC aerosols are simulated in our study, including 7 size bins for resolving dust (Fairle et al., 2007), and total aerosol mass of black and organic carbon (Park et al., 2003). Dust simulations in GEOS-Chem (Fairlie et al., 2007) consist of the mineral dust

entrainment and deposition (DEAD) model (Zender et al., 2003), which is coupled with the GOCART dust source function (Ginoux et al., 2001). The daily biomass burning sources are calculating from version 3 of Global Fire Emissions Database (GFED) inventory (van der Werf et al., 2006, 2010; Randerson et al., 2013). The monthly anthropogenic fossil fuel and biofuel BC and OC emissions are adpoted from Bond inventory with base year 2000 (Bond et al., 2007). The sulphate (SU) and sea salt (SS) aerosol simulation in GEOS-Chem is described in (Park et al., 2004; Jaeglé et al., 2011). The standard aerosol dry deposition in GEOS-Chem is described in (Wang et al., 1998; Wesely, 1989), and accounting for gravitational settling and turbulent mixing of particles to the surface (Pye et al., 2009; Zhang et al., 2001). Aerosol wet deposition is through wet scavenging in convective updrafts as well as in- and below-cloud scavenging from convective and large scale precipitation (Liu et al., 2001).

The GEOS-Chem model assumes external mixing for all aerosol components with lognormal size distributions. The modal diameter and width for each dry aerosol species and their optical properties is specified. The extinction and scattering coefficients are calculated from size distribution and refractive index with spherical particle shape assumption. Different aerosol species are considered to have different degree of hydroscopic growth rate with ambient relative humidity (RH). The simulated aerosol mass are then converted to AOD (τ) and AAOD (τ_a) through the general relationship between aerosol optical depth and aerosol mass (Tegen and Lacis, 1996) (see in section 2.3.4). The detailed aerosol properties used in this study show in Table 2.2.

The adjoint GEOS-Chem model was developed specifically for inverse modeling of aerosols or their precursors and gas emissions (Henze et al., 2007, 2009). The 4D-Variational data assimilation technique is used to optimize aerosol emissions by combining observations and model simulations. The adjoint of GEOS-Chem has been widely used to constrain emission sources. For example, Kopacz et al. (2009) utilized MOPITT measurements of carbon monoxide (CO) columns to optimize Asian CO sources. Zhu et al. (2013) constrain ammonia emissions over U.S. by the means of TES (Tropospheric Emission Spectrometer) measurements. Zhang et al. (2015) use OMI AAOD to constrain anthropogenic BC emissions over East Asia. However, these studies have focused on a single aerosol or gas species and kept others constant during the inversion, since the satellites or other available observations of aerosols

generally did not provide enough accurate information to estimate contributions from different species. The recent development of the PARASOL/GRASP retrieval, which retrieves more detailed and accurate aerosol information (see in section 4.2.3), thus presents a new opportunity for constraining emissions from different aerosol species simultaneously.

4.2.3 PARASOL/GRASP aerosol products evaluation

GRASP is a highly versatile and accurate aerosol retrieval algorithm that processes properties of aerosol and land surface reflectance. The algorithm is developed for enhanced characterization of aerosol properties from spectral, multi-angular polarimetric remote sensing observations (http://www.grasp-open.com/) (Dubovik et al., 2011, 2014; Lopatin et al., 2013). The POLDER/PARASOL imager provides spectral information of angular distribution of both total and polarized components of solar radiation reflected to space. With the expectation of 3 gaseous absorption channels (763, 765 and 710nm), the observations over each pixel include total radiance at 6 channels (443, 490, 565, 670, 865 and 1020nm) and linear polarization among 3 channels (490, 670 and 865nm). The number of viewing angle is similar for all spectral channels and varies from 14 to 16 depending on solar zenith and geographical location. Meanwhile, PARASOL provides global coverage about every 2 days. Comprehensive measurements (~144 independent measurements per pixel) from PARASOL allow GRASP to infer aerosol properties including spectral AOD and AAOD, the particle size distribution, single scattering albedo, spectral refractive index and the fraction of spherical particles (some description of GRASP aerosol products can be found in papers of Kokhanovsky et al. (2015) and Popp et al. (2016)). Extensive information of aerosol distribution and their properties provides a means to constrain specific aerosol types, which is vital to characterizing emissions from different aerosol species.

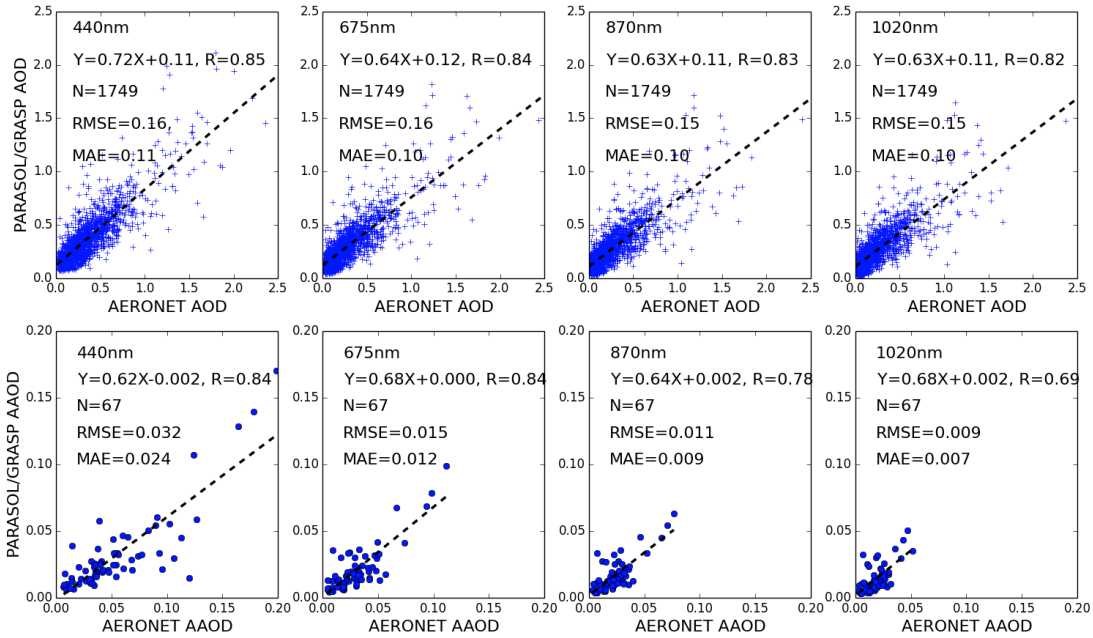

Figure 4.2: Validation of one-year PARASOL/GRASP spectral AOD and AAOD rescaled to 2.0° x 2.5° horizontal resolution with AERONET 28 sites measurements at 440, 675, 870 and 1020nm wavelengths over study area; The number of matched pairs (N), correlation coefficient (R), root mean square error (RMSE) and mean absolute error (MAE) are provided in the top left corner.

In this study, we adopt one-year (December 2007 to November 2008) PARASOL products of spectral AOD and AAOD from GRASP to retrieve DD, BC and OC emission sources over study area in Section 4.3. In order to evaluate the reliability of PARASOL aerosol products from GRASP, we compared PARASOL/GRASP retrievals with AERONET measured AOD and AAOD at 4 Sun photometer channels (440, 670, 870 and 1020nm) in Figure 4.2. Here, we use level 2 AERONET data, which are cloud screened and quality assured (Smirnov et al., 2000). From all one-year measurements collected from 28 sites, we extract data between 13:00PM and 14:00PM local time. This provides a 60 minutes window centered at the PARASOL overpassing time of ~13:30PM. The averaged AERONET sun-direct AOD and AAOD by inversion of almucantar measurements (Dubovik et al., 2000; Dubovik and King, 2000) over this 60 minutes window are averaged for comparison with PARASOL/GRASP retrievals. We aggregate the PARASOL/GRASP products into 2 ° latitude x 2.5° longitude horizontal resolution to match the spatial resolution used by GEOS-Chem; any 2° x 2.5° grid box with less than 500 available PARASOL/GRASP retrievals for averaging is omitted. Depending on geographical location, the number

of GRASP retrievals in a single 2° x 2.5° grid box ranges from 500 to 1600. Figure 4.2 presents the validation of retrieved PARASOL AOD and AAOD by GRASP algorithm against the AOD and AAOD measured by AERONET. There is a solid correlation between PARASOL/GRASP and AERONET for AOD as well as AAOD. For example, the correlation coefficients (R) are 0.85 and 0.84, and the root mean square errors (RMSE) are 0.16 and 0.032, and the mean absolute errors (MAE = $\frac{1}{N}\sum_{i=1}^{N}|(M_i - O_i)|$) are 0.11 and 0.024 for AOD and AAOD at 440nm respectively.

4.3 Results

In this section, we discuss retrieval of DD, BC and OC emission sources simultaneously from the actual PARASOL/GRASP spectral AOD and AAOD data from December 2007 to November 2008. The SU and SS aerosol simulations are kept as the prior model. PARASOL/GRASP retrievals were aggregated to the same horizontal resolution as the GEOS-Chem (2° x 2.5°) and averaged within the grid cells prior to assimilation. When iteratively minimizing Eq. (3.13), the maximum iteration number was chosen to be 40, which takes about 60 days to complete on a computer workstation with 32x3.3 GHz CPUs.

4.3.1 Fitting of Aerosol Optical Depth

One of the important indicators of our inversion performance is the fitting of PARASOL/GRASP spectral AOD and AAOD. We evaluate the GEOS-Chem simulated spectral AOD at 443, 490, 565, 670, 865 and 1020 nm using prior or posterior emissions against the corresponding PARASOL/GRASP retrieved AOD in Figure 4.3. The posterior GEOS-Chem spectral AOD are simulated using retrieved DD, BC and OC emissions, which will be presented in section 4.3.2. Figure 4.3a presents the annual average of the PARASOL spectral AOD from GRASP algorithm, whereas Figure 4.3b and 4.3c shows the same quantity from the GEOS-Chem simulations with prior and posterior emissions, respectively. Here we extract GEOS-Chem hourly AOD with the same PARASOL orbit partition at 13:00 p.m. local time, which is approximately the PARASOL overpass time of 13:30 p.m. Figure 4.3d and 4.3e display the grid-to-grid comparison between PARASOL/GRASP spectral AOD and prior and posterior GEOS-Chem simulation during one year, color-coded with the

PARASOL Ångström exponent $\alpha_{443-865} = {ln\,(\tau_{443}/\tau_{865})}\Big/{ln\,(865/443)}$. The Ångström exponent α is often used as a qualitative indicator of aerosol particle size; the higher the α, the larger the particle size. For example, the α values for "pure" dust aerosols are usually near zero, whereas that for smoke or pollution aerosols are generally greater than 1 (Eck et al., 1999; Schuster et al., 2006).

One of the major discrepancies between the prior GEOS-Chem simulation and PARASOL/GRASP observation is that the model produces the highest annual average AOD values over the major dust source region of Northern Africa; however, satellite data show the maxima AOD in Central and the Southern Africa, where carbonaceous aerosols usually dominate (although Central Africa may also be influenced by dust events). Hence, compared to PARASOL/GRASP observations, the prior GEOS-Chem AOD is overestimated in Northern Africa, while it is underestimated in the Southern Africa biomass burning and Arabian Peninsula regions. Some recent studies by Ridley et al. (2012, 2016) and Zhang et al. (2015) also indicate that the GEOS-Chem model overestimates dust AOD in Northern Africa. Meanwhile, Ridley et al. (2012) and Zhang et al. (2013) propose a new and realistic dust particle size distribution according to the measurements from Highwood et al. (2003), which can partially adjust the misrepresentation of dust near the source and over transport areas. This new particle size distribution has been adopted in our prior and posterior GEOS-Chem simulation. In addition, the underestimation of model simulated AOD in biomass burning regions with the GFED emission database was also shown in other modeling studies (Chin et al., 2009; Johnson et al., 2016). The model simulated spectral AOD with the posterior emissions agree with the PARASOL observations much better, in spite of slight systematic overestimations from 565nm to 1020nm (about 13% on an annual average). This overestimation indicates some disagreement in modeling of AOD for these bands that needs to be investigated and addressed in future studies.

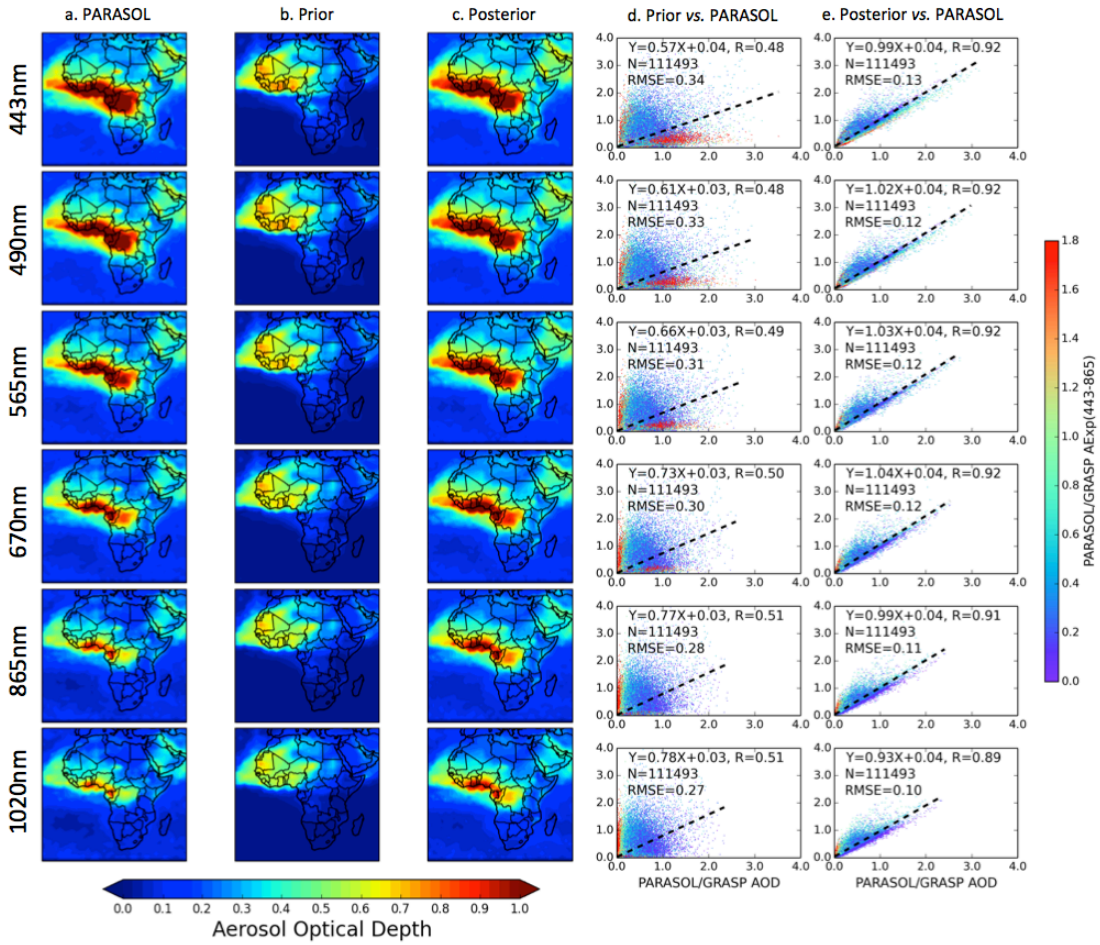

Figure 4.3: Comparison of the annual spatial distribution of prior (b) and posterior (c) GEOS-Chem simulated AOD at 443, 490, 565, 670 865 and 1020 nm with PARASOL/GRASP observations (a). The posterior spectral AOD are simulated using retrieved DD, BC and OC emissions. The scatter plots of grid-to-grid comparisons between PARASOL/GRASP spectral observations versus prior (d) and posterior (e) GEOS-Chem simulation during one year. The correlation coefficient (R) and root mean square error (RMSE) are provide in the top left corner.

Figure 4.3d and 4.3e show the statistics of prior and posterior GEOS-Chem simulated AOD versus PARASOL/GRASP observed AOD at 6 wavelengths during the entire year. The number of matched pairs is 111,493. For GEOS-Chem simulation with the posterior emissions, all the statistics parameters between model and observation are improved at all 6 wavelengths from the simulation with prior emissions. For example, the correlation coefficient has increased from 0.49-0.51 to 0.89-0.92 and the root mean square error has decreased from 0.27-0.34 to 0.10-0.13. Such improvements are expected as the posterior emissions are retrieved based on the

PARASOL/GRASP AOD data, so that a better agreement shown in Fig 4.3e does not represent an independent evaluation of improved emission sources. We will show further evaluations with other datasets in Section 4.4.

4.3.2 Fitting of Aerosol Absorption Optical Depth

Similar to the AOD analysis, here we evaluate the fitting of AAOD (Figure 4.4). From the annual-averaged spectral AAOD in Figure 4.4, the prior GEOS-Chem simulation (Figure 4.4b) shows significant underestimations of AAOD over the entire domain compared to PARASOL/GRASP observations (Figure 4.4a). On the other hand, the posterior GEOS-Chem simulation (Figure 4.4c) produces much better agreement with the PARASOL/GRASP data for all wavelengths, with a small overestimation of AAOD in the spectral range from 443nm to 565nm (about 6% on annual average) and a small underestimation at 865nm and 1020nm (about 9% on annual average). Linked with the ~13% overestimation of annual AOD from 565nm to 1020nm, this systematic phenomenon of fitting is likely due to the fact that the model relatively coarse resolution resulting to misrepresentations of DD, BC and OC emissions in some grid boxes.

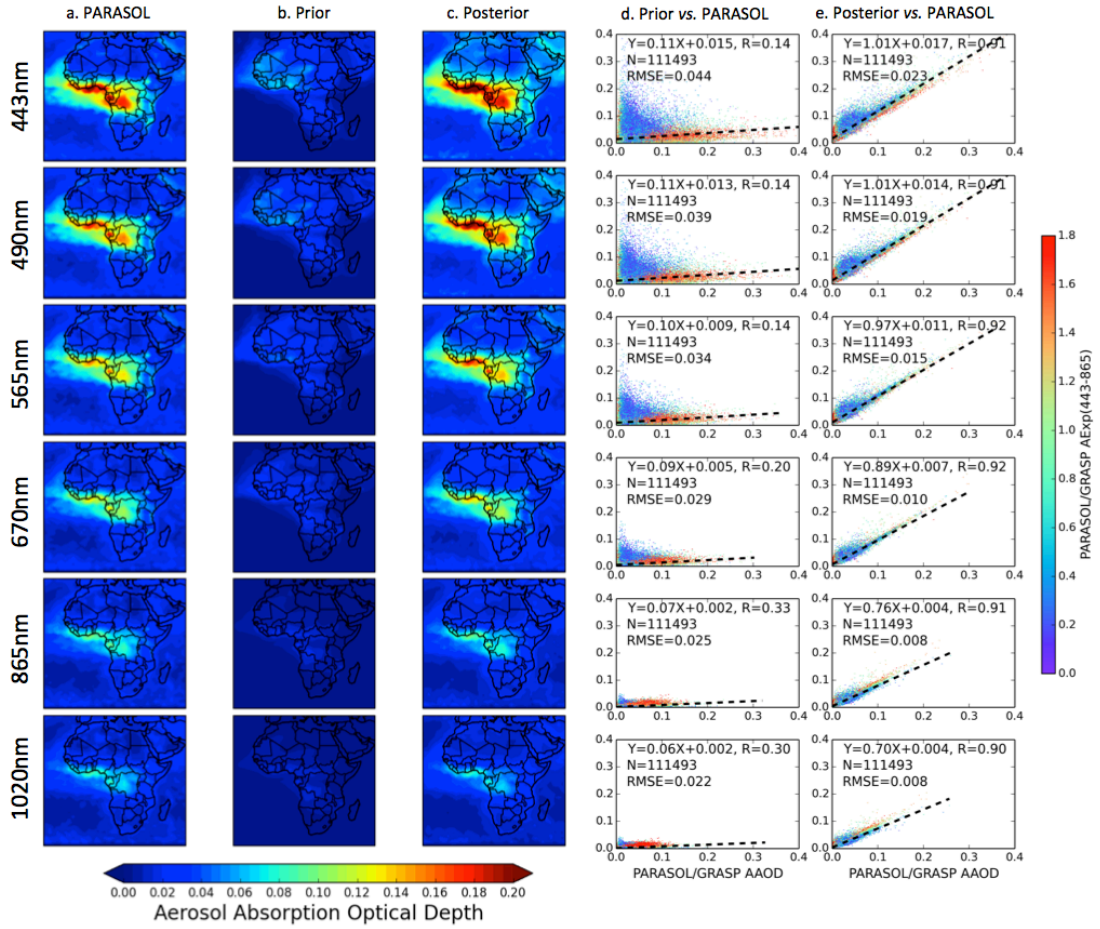

Figure 4.4: Same as Figure 4.3 but for AAOD.

Figures 4.4d and 4.4e show the comparisons of PARASOL/GRASP observed AAOD at 6 wavelengths with the corresponding GEOS-Chem simulated quantities using prior or posterior emissions. The very low linear regression slope between the model simulated AAOD using prior emissions with observations (less than 0.11 over all six wavelengths) indicates that the prior simulations significantly underestimate the AAOD. In contrast, model simulations with the posterior simulations improve the slope to 1.01 at 443 nm and 0.70 at 1020 nm. Similar to the case of AOD, the agreements between the PARASOL/GRASP AAOD data and the model simulations are much better using the posterior emissions than using the prior emissions, with the correlation coefficients increased from 0.14-0.33 to 0.90-0.92 and the root mean square error decreased from 0.022-0.044 to 0.008-0.023.

4.3.3 Emission sources

The retrieved and prior monthly total DD, BC and OC emission variations over the study area are shown in Figure 4.5.

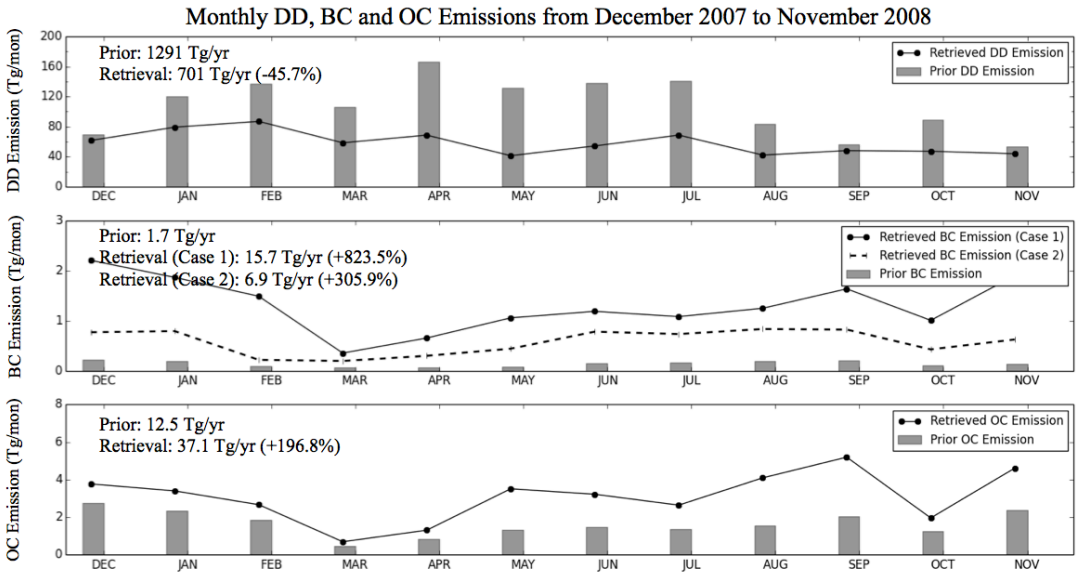

Figure 4.5: Comparison of monthly total DD, BC and OC emissions (unit: Tg mon^{-1}) over study area between prior model (GFED3 and Bond inventories for BC and OC, DEAD model for DD) and retrieved emissions, the annual values (unit: Tg yr^{-1}) are provided in the top left corner.

4.3.3.1 DD emissions

Figure 4.5 shows that the retrieved annual total DD emission in the study area is 701 Tg/yr (particle radius ranging from 0.1 to 6.0 microns, exclude super coarse mode dust particles), which is 45.7% smaller than the prior emissions of 1291 Tg/yr. Moreover, the retrieved total DD emissions show reduced emission amount from the prior values in every month, varying from 11.6% reduction in December to 68.5% in May. Figure 4.6 shows the comparison of the spatial distribution of seasonal DD emissions between the prior emissions (Figure 4.6a) and our retrievals (Figure 4.6b). As shown in Figure 4.6, the prior and the retrieved emissions show similar spatial and seasonal patterns; for example, the Bodélé Depression is the most active dust source area in DJF and SON and the Arabian Desert becomes active in MAM and JJA. One major discrepancy between the model and the retrieval is that the model has a much

stronger DD sources over Algeria and Morocco in MAM and JJA, which is even stronger than the Bodélé Depression and the Arabian Desert. However, the retrieval still shows the dust emissions there, while the strength reduces a factor of 5-6.

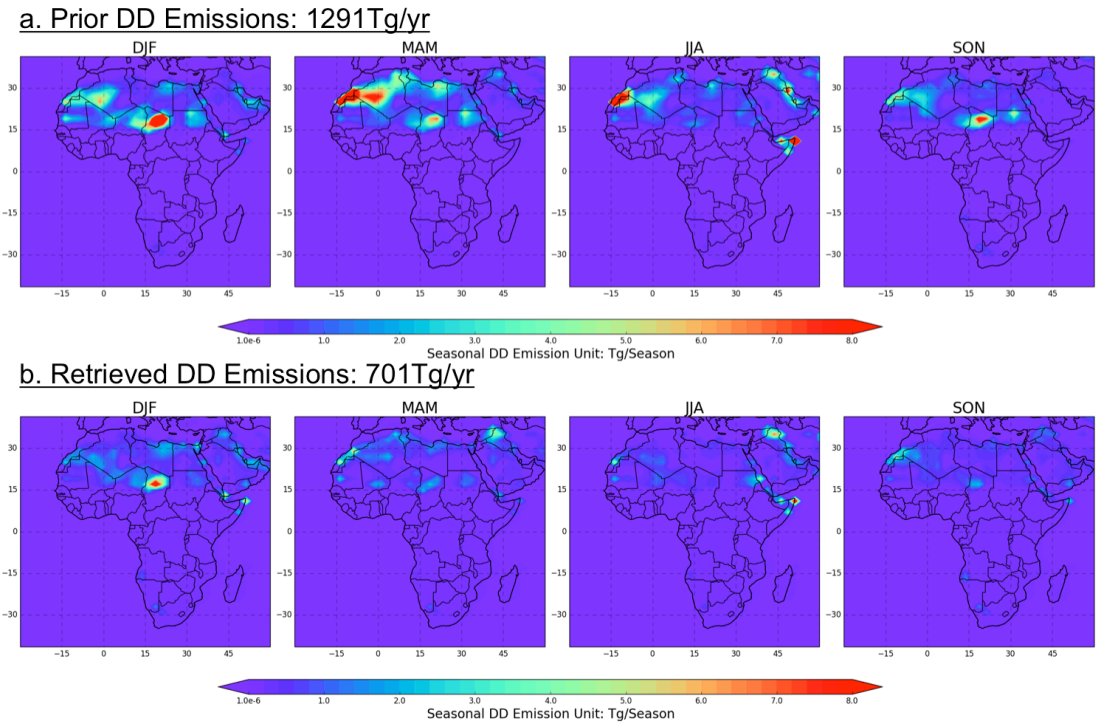

Figure 4.6: Spatial distribution of seasonal desert dust aerosol emission sources: (a) "prior model" DD emissions from DEAD model and (b) retrieved DD emissions.

4.3.3.2 BC emissions

As mentioned earlier, we considered two cases of BC aerosol refractive index to perform the retrieval (Case 1: m=1.75-0.45i; Case 2: m=1.95-0.79i), since the retrieved total BC emissions is very sensitive to the BC refractive index (our sensitivity test shows a factor of ~1.8 differences between Case 1 and Case 2, see section 3.3.1.4). Figure 4.5 shows the retrievals increase BC emissions for every month from the prior emissions by factors ranging from 5.9 in March to 14.4 in November with an annual averaged increase of a factor of ~8 in Case 1. For Case 2, the retrieved BC emissions have similar monthly variation as in Case 1 with a smaller magnitude of increase from the prior emissions, from a factor of 3.3 in March to 4.7 in November with an annual averaged increase of ~3.

The spatial comparison of seasonal BC emission is summarized in Figure 4.7. We plot model prior BC emission from GFED3 and Bond anthropogenic inventories in

Figure 4.7a, retrieved BC emissions from Case 1 in Figure 4.7b, and Case 2 retrieved BC emissions in Figure 4.7c. Note that the color bar range in Figure 4.7b is 2.5 times larger than that of Figure 4.7a and Figure 4.7c. Not surprisingly, the patterns of model prior emission, Case 1 and Case 2 retrievals are similar, with the highest BC emission source areas located in biomass burning regions, such as Central Africa during DJF and Southern Africa JJA. The large increases in the BC emissions in the retrieval relative to the prior suggests that the current model simulated AAOD is much too low, which is consistent with the PARASOL/GRASP observations in Section 4.3.2. Retrieval Case 2 shows a large increase over the Arabian Peninsula, indicating there is an emission source ~5 times higher than the prior model in DJF, MAM and SON, where the latter shows only a small amount of carbonaceous fine particles. AERONET ground-based measurements indicate a moderate absorption phenomenon there (Seasonal AAOD at 550nm about ~0.05, see Figure 21), which corroborates the retrieved values from the inversion.

4.3.3.3 OC emissions

The annual total OC emissions in Figure 4.5 shows that the retrieved annual OC emissions are higher than the prior model by a factor of ~2, with a minimum monthly increase found in March (1.54) and a maximum in May (5.71). Combined with BC emission, the retrieved total carbonaceous aerosol emissions are 52.8Tg/yr (with Case 1 BC) and 44.0Tg/yr (with Case 2 BC), which is 271.8% (Case 1) ~ 209.8% (Case 2) higher than prior model (14.2 Tg/yr). We compare the seasonal distribution of prior OC emissions with retrieved emissions in Figure 4.8. Both the retrieved and prior emissions have highest OC emission sources in Southern Africa in JJA and in Central Africa in DJF.

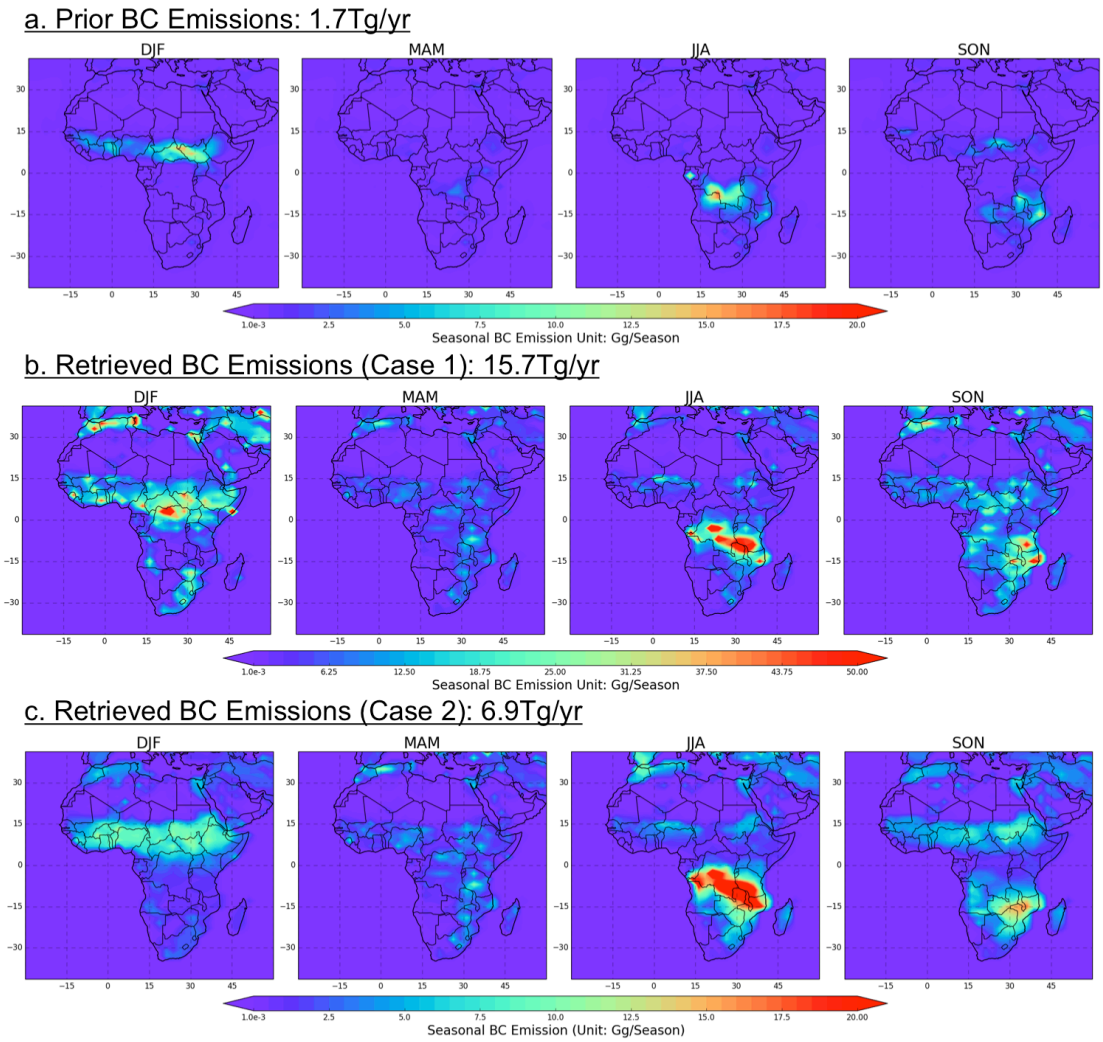

Figure 4.7: Spatial distribution of seasonal BC emissions: (a) prior model BC emissions from GFED3 and Bond inventories; (b) Case 1 retrieved BC emissions; (c) Case 2 retrieved BC emissions. Note that the color scale for (b) is different from (a) and (c) for better resolving the spatial contrasts.

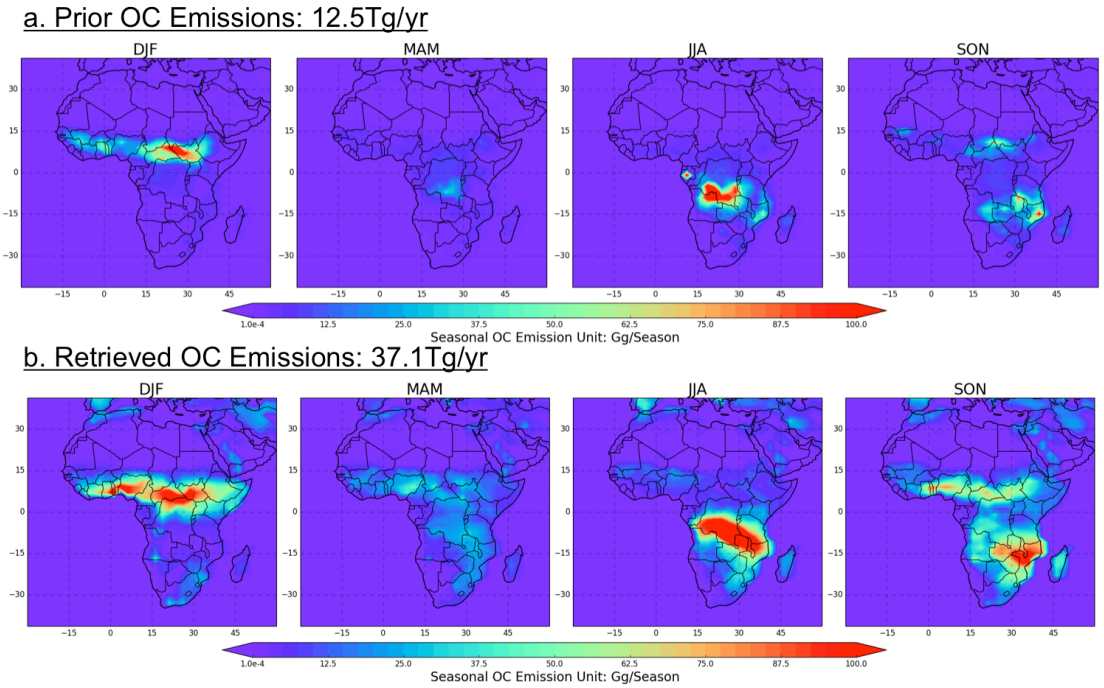

Figure 4.8: Spatial distribution of seasonal OC emissions: (a) prior model OC emissions using GFED3 and Bond inventories and (b) retrieved OC emissions.

4.3.3.4 Summary of retrieved emissions

Comparison of retrieved DD, BC and OC aerosol emissions over the study area with GEOS-Chem prior model emission inventories show basically a consistent of spatial and temporal variation. However, the significant differences are in the emission strength. The PARASOL/GRASP based retrieval reduces the GEOS-Chem annual DD emission to 701 Tg/yr over study area. Recent study by Escribano et al. (2017) estimated the mineral dust flux for particle size less than 6.0 microns over northern Africa and the Arabian Peninsula is between 630 and 845 Tg/yr. Some other studies also show similar dust emission flux over Africa (Werner et al., 2002; Miller et al., 2004; Escribano et al., 2016, 2017). However, the overestimation of the prior model dust emission could also result from the error in particle size distribution, which is shown to biased toward smaller particle sizes compared to the observation in the atmosphere (Kok et al., 2017). Meanwhile, the retrieval increases the model annual carbonaceous aerosol emission by about 2.5 times. This value is close to the recommendation given in Bond et al. (2013) that increasing global BC absorption by a factor of 3 to fit the observation of columnar aerosol absorption. In addition, there

are many other efforts to improve the simulation of AAOD, e.g. treating hydrophilic BC as internal with other soluble hygroscopic aerosol species (Wang et al., 2016); including the light absorbing brown carbon in the simulation (Wang et al., 2014b). These studies are all crucial to improve current CTMs aerosol simulation, which should be adopted in our aerosol emission inversion framework in the future.

4.4 Evaluation

4.4.1 Evaluation with AERONET

In order to objectively evaluate our retrieved aerosol emissions based on PARASOL/GRASP spectral AOD and AAOD, we made a series of evaluations using independent datasets and models not used by our inversion. First, the posterior simulated one-year AOD and AAOD are compared with the sun photometer measured AOD and AAOD at 28 AERONET sites (shown in Figure 4.1).

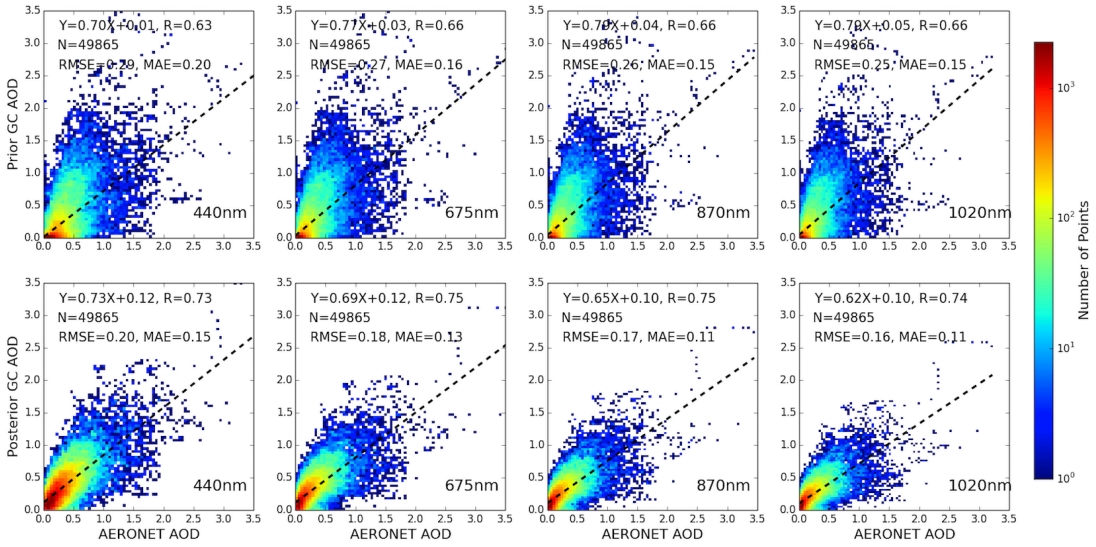

Figure 4.9: Density scatter plots of one-year GEOS-Chem simulated AOD using the prior emissions (top row) or the posterior emissions (bottom row) versus AERONET measured AOD at 440, 675, 870 and 1020 nm at 28 sites. The number of matched pairs (N), correlation coefficient (R), root mean square error (RMSE) and mean absolute error (MAE) are shown on each panel.

Figure 4.9 and 4.10 show the comparison of GEOS-Chem simulations using prior and posterior emissions with AERONET measurements of AOD and AAOD, respectively. The evaluation was conducted at 4 wavelengths (440, 675, 870 and 1020

nm) and GEOS-Chem hourly spectral AOD and AAOD are interpolated based on the Ångström exponent. AERONET AOD and AAOD averaged ±30 minutes centered by model output time are used to compare with the model simulations over the grid box containing the AERONET sites. Density scatter plots of 49,865 matched pairs of AOD are shown in Figure 4.9. The correlation coefficients between GEOS-Chem simulations with prior emissions and AERONET data (shown in upper four panels) are 0.62, 0.67, 0.66 and 0.66 for the four wavelengths respectively, and the corresponding root mean square errors are 0.28, 0.25, 0.24 and 0.24. Yet, the correlation coefficients are increased to 0.73, 0.75, 0.75 and 0.74 when the posterior emissions are used in GEOS-Chem simulation (shown in lower four panels), and meanwhile the root mean square errors are decreased to 0.20, 0.18 0.17 and 0.16, respectively. Meanwhile, the mean absolute errors are also decreased from prior (0.20, 0.16, 0.15 and 0.15) to posterior (0.15, 0.13, 0.11 and 0.11).

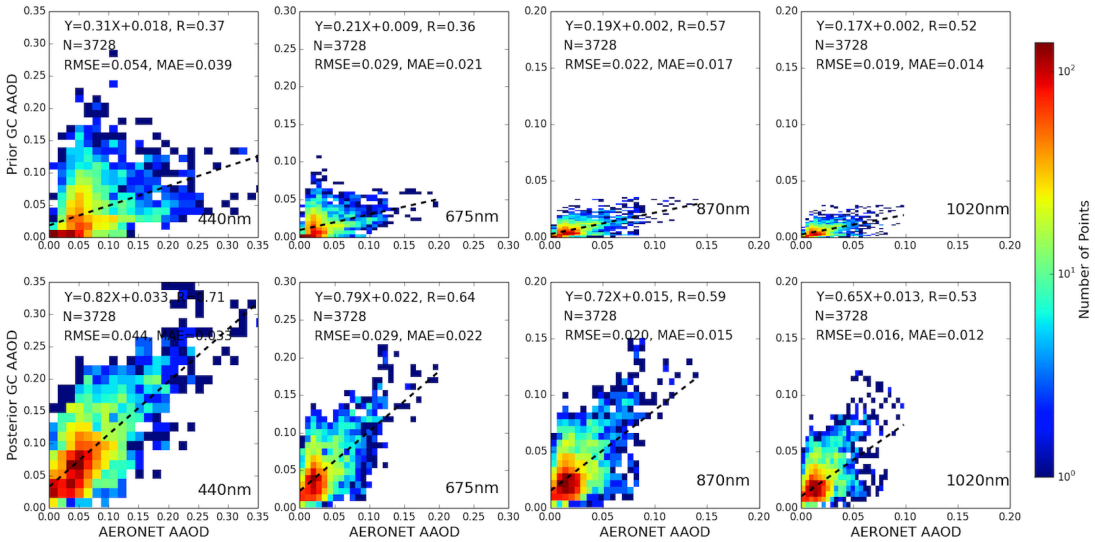

Figure 4.10: Same as Figure 4.9 but for AAOD.

Figure 4.10 shows the density scatter plots of comparison of AAOD. However, unlike sun direct measurement of AOD, AERONET AAOD is inverted from almucantar measurements. To select sufficiently accurate retrievals, we applied quality-screening criteria (e.g. Dubovik et al., (2002b) and Holben et al., (2006)). Therefore, there are fewer AERONET AAOD that matched with GEOS-Chem simulations than for AOD. The number of matched pairs is 3,728. The low slope of the linear regression between prior model AAOD and AERONET (shown in upper four panels) indicates that the prior model significantly underestimates AAOD. The

posterior GEOS-Chem simulations using retrieved emissions (shown in the lower four panels) shows the improvements validating with AERONET, with the correlation coefficients come to 0.71, 0.64, 0.59 and 0.53. In addition, the root mean square errors are also improved for posterior simulations.

Comparison between time series of AOD and AAOD at 440 nm from AERONET, PARASOL/GRASP, prior and posterior GEOS-Chem simulations, from December 2007 to November 2008, are made in two AERONET sites (Mongu and Ilorin), and the results are shown in Figure 4.11 and Figure 4.12. The geo-locations of these two sites are already apparent in Table 4.1 and Figure 4.1. Ilorin is located close to the active dust sources in the Northern Africa, where are also influenced by seasonal biomass burning events, especially from November to February. Mongu is located close to the Southern Africa seasonal biomass burning sources. The posterior simulations better capture the time series variations and magnitude of AOD and AAOD from AERONET measurements. For example, in Mongu, the prior simulation underestimates AOD and AAOD significantly. In September, the underestimations are about 3 times (a bias of -0.56 for monthly average) for AOD and 4 times for AAOD (a bias -0.09). Such bias is significantly reduced to -0.22 for AOD and +0.01 for AAOD in posterior simulation with retrieved emission sources. In terms of correlation coefficients, the prior GEOS-Chem simulation shows a solid correlation with measurements in Mongu, while the slope of linear regression (K) between prior simulation and AERONET (0.24 for AOD; 0.22 for AAOD) indicates that the model significantly underestimates the aerosol loading in Mongu. Furthermore, prior GEOS-Chem simulation can capture the variation and magnitude of AOD (R=0.79 and K=0.79) in Ilorin. However, for AAOD, the simulation shows underestimation with slope K=0.40, which is an indicator of the model underestimation of the aerosol absorption species, such as BC. Overall, the posterior GEOS-Chem simulation with retrieved emission sources can better capture the time serial variation and magnitude of AOD and AAOD in both Mongu and Ilorin.

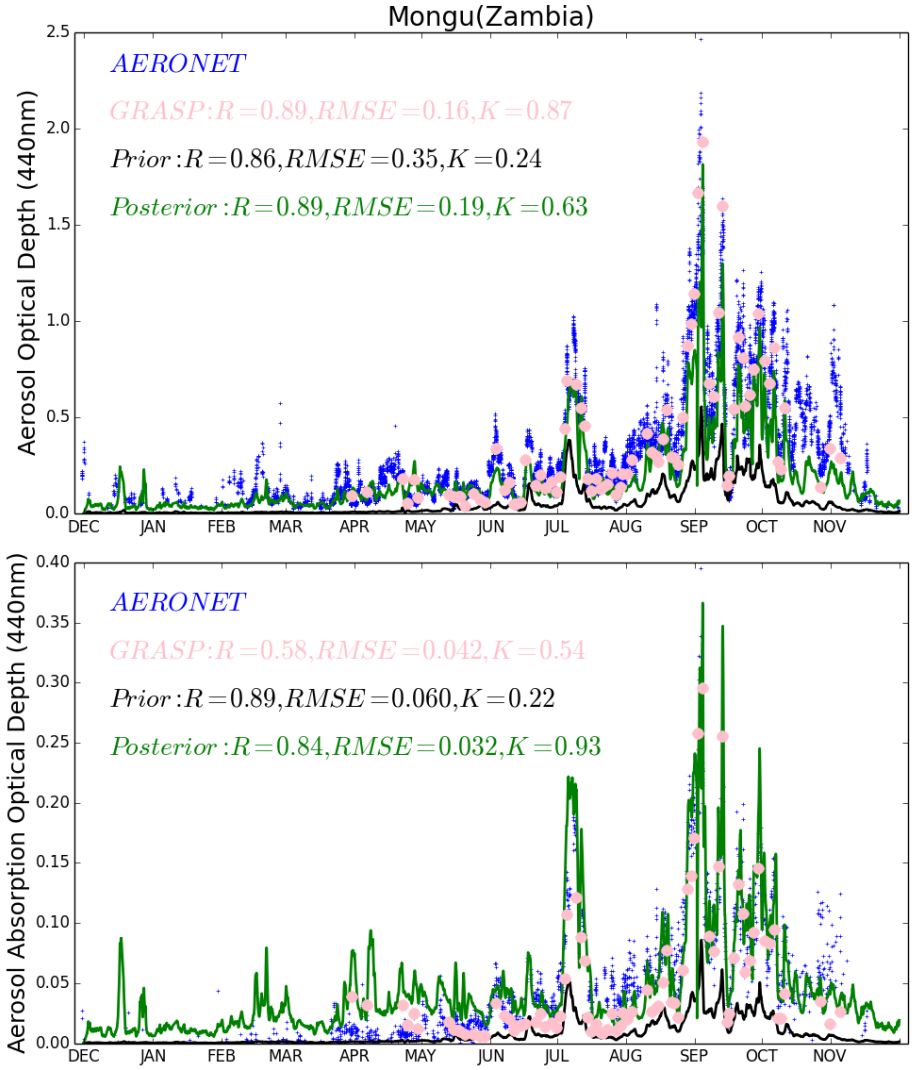

Figure 4.11: Time serial AOD (upper panel) and AAOD (lower pannel) from AERONET (blue crosses), PARASOL/GRASP (pink circles), Prior GEOS-Chem (black line) and Posterior (green line) GEOS-Chem simulations at Mongu (Zambia) site whose locations are given in Table 4.1. The statistic parameters between PARASPOL/GRASP, prior and posterior GEOS-Chem simulations with AERONET are also shown in the figure.

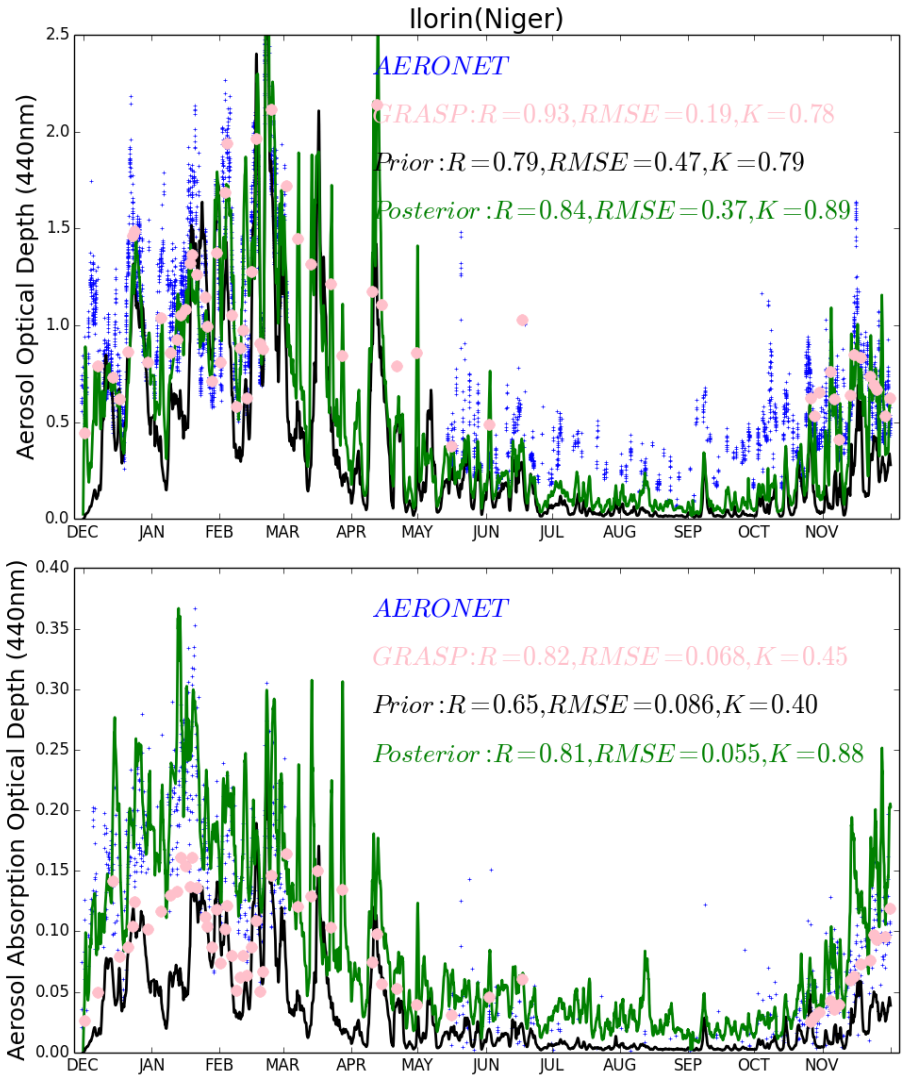

Figure 4.12: Time serial AOD (upper panel) and AAOD (lower pannel) from AERONET (blue crosses), PARASOL/GRASP (pink circles), Prior GEOS-Chem (black line) and Posterior (green line) GEOS-Chem simulations at Ilorin (Niger) site whose locations are given in Table 4.1. The statistic parameters between PARASPOL/GRASP, prior and posterior GEOS-Chem simulations with AERONET are also shown in the figure.

4.4.2 Testing retrieved emission in the GEOS-5/GOCART model

All the evaluations considered thus far are a based on simulations in the GEOS-Chem model. To evaluate how such results may be impacted by model biases owing to factors other than BC, OC and DD emissions, here we ask - can aerosol emissions retrieved from the GEOS-Chem based inversion improve the aerosol simulation for another chemical transport model? To investigate this, we implement our

PARASOL/GRASP based aerosol emission database into the GEOS-5/GOCART model (Chin et al., 2002, 2009, 2014; Colarco et al., 2010). The prior and posterior GEOS-5/GOCART model simulated seasonal AOD are compared with MODIS observations in Figure 4.13. GEOS-5/GOCART uses similar meteorological fields as GEOS-Chem, with the prior anthropogenic emissions from the Hemispheric Transport of Atmospheric Pollution (HTAP) Phase 2, biomass burning emissions from the Fire Energetics and Emission Research (FEER) database (Ichoku and Ellison, 2014), dust emission calculated as a function of 10-m winds and surface characteristics (Ginoux et al., 2001), and volcanic emissions from OMI-based estimates (Carn et al., 2015). The PARASOL/GRASP retrieved DD, BC, and OC emissions over the study domain are used in the "posterior" simulations while other sources remain unchanged. On an annual average, the DD, BC, and OC posterior/prior emission ratios in the study area are 0.53, 5.3, and 1.2, respectively.

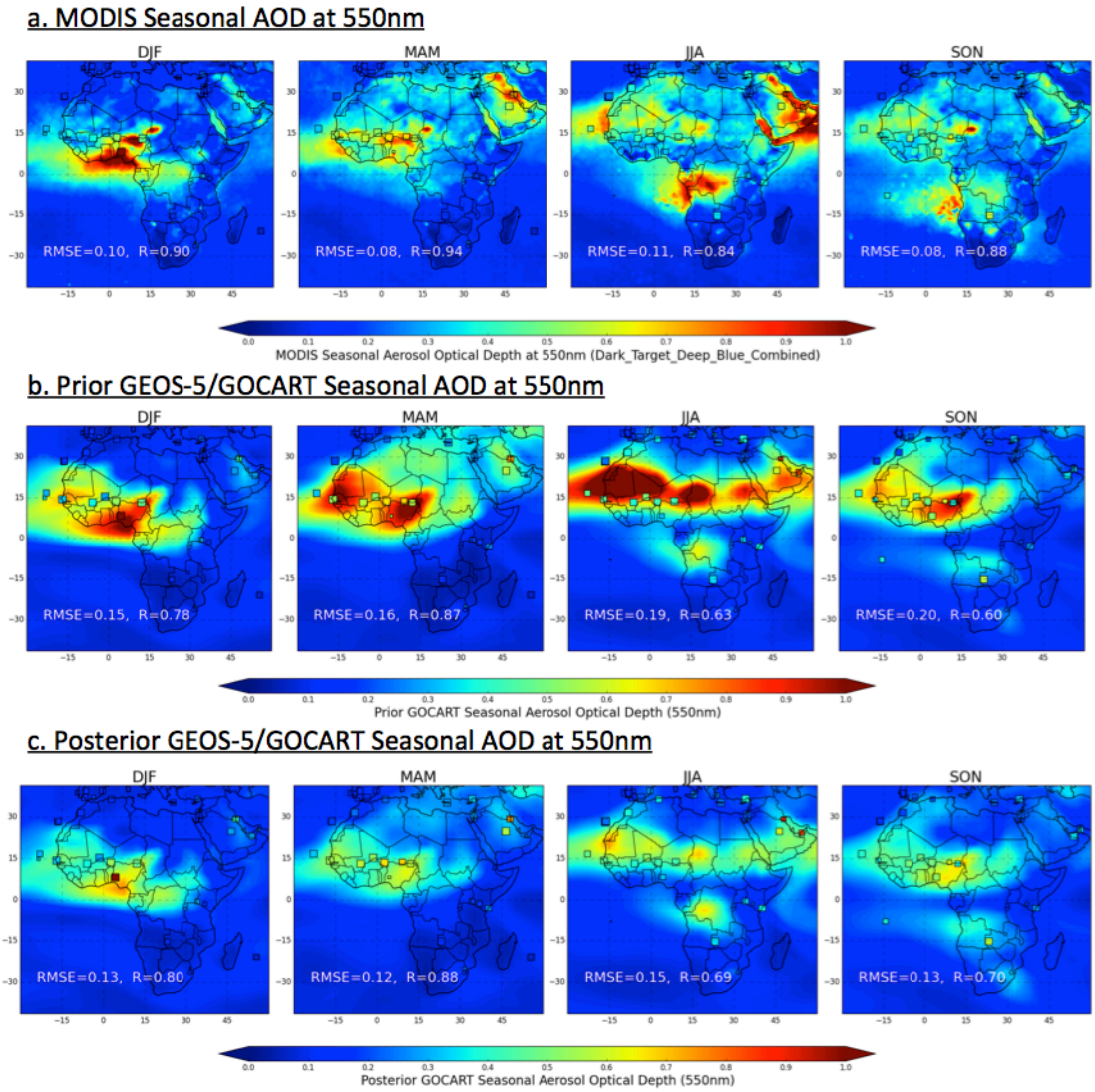

Figure 4.13: Comparison of the seasonal spatial distribution of prior (b) and posterior (c) GEOS-5/GOCART simulated AOD at 550 nm with MODIS observations (a). The ground-based measurements from AERONET (squares) are over plotted over figures a-c. The MODIS and GEOS-5/GOCART versus AERONET correlation coefficient (R) and root mean square error (RMSE) are provided in figures a-c.

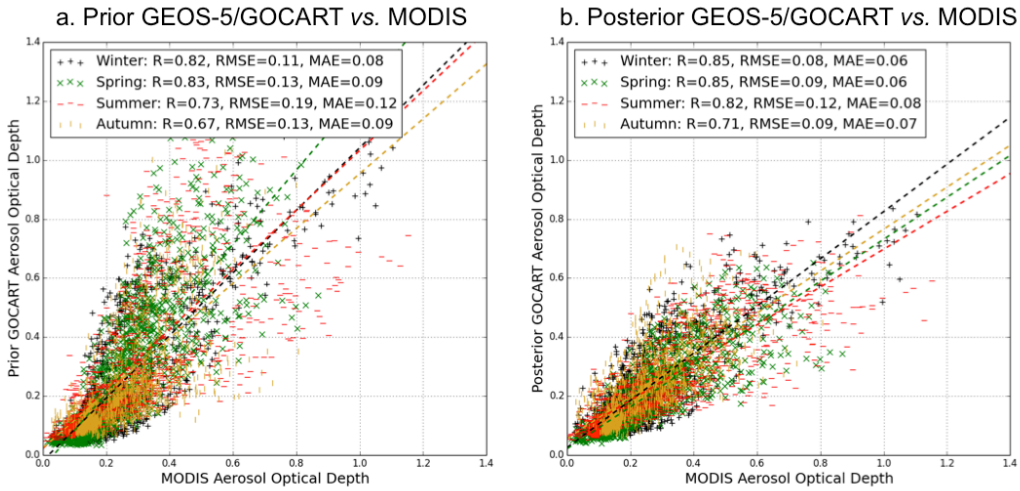

Figure 4.14: The scatter plots of grid-to-grid comparison between MODIS and prior GEOS-5/GOCART AOD (a) and posterior GEOS-5/GOCART AOD (b) are also shown. Meanwhile, the GEOS-5/GOCART versus MODIS R, RMSE and MAE are also provided in figures (a-b).

Figure 4.13a shows the MODIS seasonal AOD at 550nm. In order to have a better coverage, we take MODIS collection 6 combined dark target and deep blue AOD products at the spatial resolution of 1° x 1° (Hsu et al., 2004; Levy et al., 2013). Figure 4.13b presents prior GEOS-5/GOCART simulated seasonal AOD, and Figure 4.13c shows the posterior GEOS-5/GOCART simulation from our retrieved emissions (using Case 2 BC emission). In Figure 4.15a and 4.15b, we plot the grid-to-grid comparison between GEOS-5/GOCART prior and GEOS-5/GOCART posterior AOD with MODIS respectively; here the different color represents different seasons. In order to carry out this grid-to-grid comparison, MODIS 1° x 1° AOD is re-grided to the resolution 2.0° x 2.5°. The prior GEOS-5/GOCART simulate optical depth is comparable to MODIS observations with similar spatial pattern and correlation coefficient with MODIS R=~0.75 over a year. In addition, the simulation is better in DJF and MAM than in JJA and SON. The correlation coefficient with MODIS is about 0.82 and the root mean square error is about 0.12 in DJF and MAM, and it's

relative low correlation in JJA and SON (~0.7), meanwhile the RMSE becomes high (~0.16). The prior GEOS-5/GOCART simulation somewhat overestimated observations over the Northern Africa dust region over 4 seasons, while it is underestimated in the southern Africa biomass burning area, especially in biomass burning seasons (JJA and SON), which can also be inferred from the validation with AERONET measurements (squares) over plotted in Figure 4.13a-c. With the posterior emissions, GEOS-5/GOCART simulation show improvements compared with AERONET and MODIS observations, with higher correlation coefficient and lower root mean square error in all 4 seasons than the prior GEOS-5/GOCART simulation. The posterior GEOS-5/GOCART simulated AOD is a little lower than MODIS on average 13% (Normalized Mean Bias, NMB=-13%, NMB=$\sum(M_i - O_i)/\sum O_i$, where sums are over the ensemble of all data i, and M_i and O_i are the modeled and observed values), likely associated with that the MODIS AOD is observed at noon, however the GEOS-5/GOCART AOD is average over 24 hours during a day.

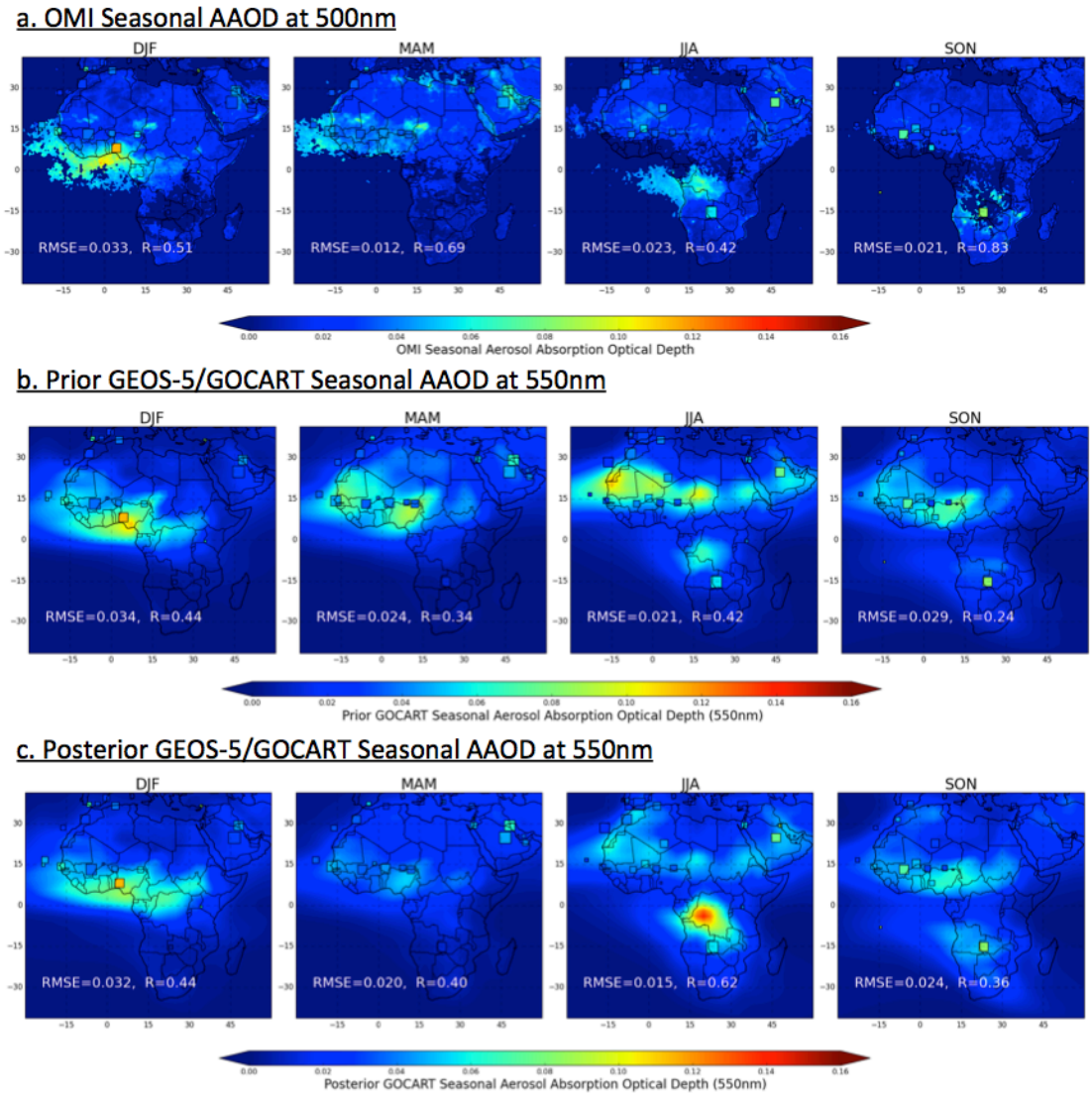

Figure 4.15: Comparison of the seasonal spatial distribution of prior (b) and posterior (c) GEOS-5/GOCART simulated AAOD at 550 nm with OMI observations (a). The ground-based measurements from AERONET (squares) are over plotted over figures a-c. The OMI and GEOS-5/GOCART versus AERONET correlation coefficient (R) and root mean square error (RMSE) are provided in figures a-c.

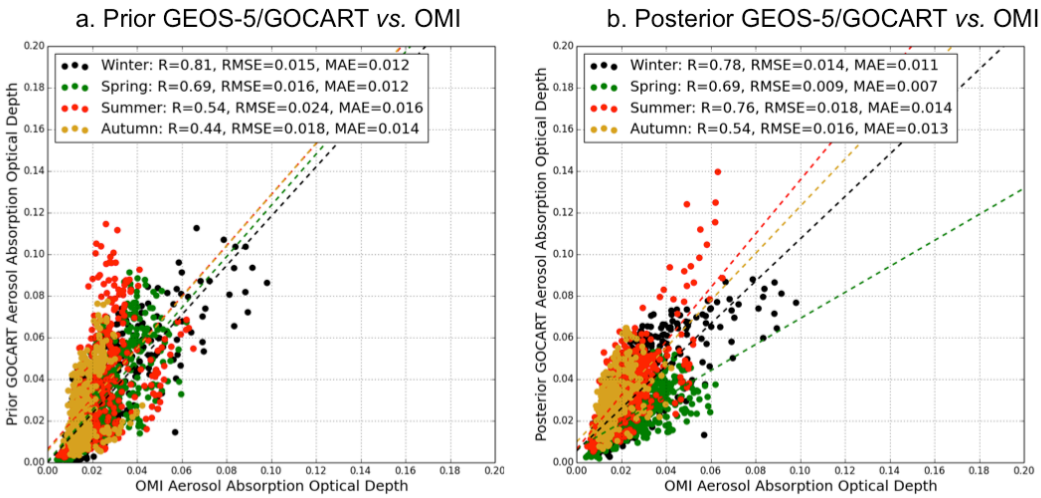

Figure 4.16: The scatter plots of grid-to-grid comparison between OMI and prior GEOS-5/GOCART AAOD (a) and posterior GEOS-5/GOCART AAOD (b) are also shown. Meanwhile, the GEOS-5/GOCART versus OMI R, RMSE and MAE are also provided in figures (a-b).

Because only ultraviolet and shortwave visible channels and polarimeter measurements are sensitive to aerosol absorption properties, long-term records of AAOD are limited to AERONET, PARASOL/GRASP and OMI. We use the latest OMI aerosol products (OMAERUV version 1.7.4) (Torres et al., 2007, 2013) to evaluate the GEOS-5/GOCART model simulated AAOD from prior aerosol emission inventories and our retrieved aerosol emission database. Meanwhile, collocated AERONET data over study area are also employed to the evaluation. Figure 4.15 shows the validation results. Figure 4.15a presents the OMI seasonal mean AAOD with original OMAERUV version 1.7.4 spatial resolution 0.5° x 0.5°. We plot grid-to-grid comparison between OMI and GEOS-5/GOCART AAOD in Figure 4.16a-b, here OMI AAOD are re-scaled to the same resolution with model simulation 2.0° x 2.5°. Any 2.0° x 2.5° grid box with less than 10 OMI original AAODs (~50% coverage) for averaging is abandoned. This evaluation highlights the following major findings:

1. The major discrepancy between OMI seasonal AAOD (Figure 4.15a) and the prior GEOS-5/GOCART simulated AAOD is that the simulated AAOD is higher than OMI values in the Northern Africa dust regions over all seasons, which can be attributed to the overestimation of dust particle absorption (Chin et al., 2009) and/or the total dust emissions. The posterior GEOS-5/GOCART

simulated AAOD shows similar spatial distribution and magnitude with OMI values over dust regions with reduced differences, although the model is still overall higher than OMI especially over the Southern Africa biomass regions in JJA.

2. As shown in Figure 4.15a, the correlation coefficients of OMI seasonal AAOD with AERONET vary from 0.42 in JJA to 0.83 in SON, meanwhile the root mean square error is smallest in MAM ~0.012 and largest in DJF ~0.033. Detailed assessments of OMI aerosol products are described in publications (Torres et al., 2013; Ahn et al., 2014; Jethva et al., 2014). The preliminary evaluation shows posterior GEOS-5/GOCART simulated seasonal AAOD (Figure 4.15c) have a slightly better correlation with AERONET comparing with prior GEOS-5/GOCART simulation (Figure 4.15b), the mean correlation coefficient over entire year improves from ~0.36 to ~0.46, and mean RMSE decreases from ~0.027 to ~0.023.
3. From the scatter plot of GEOS-5/GOCART simulated AAOD versus OMI AAOD in Figure 4.16a-b, the significant increase of correlation coefficient from prior to posterior simulations shows in summer (Prior: 0.54; Posterior: 0.76) and the decrease of RMSE and MAE (Prior: RMSE=0.024, MAE=0.016; Posterior: RMSE=0.018, MAE=0.014), suggesting the reliability of posterior aerosol emission at high biomass burning aerosol loading season.

4.5 Conclusion

In this study, we designed a method to retrieve BC, OC and DD aerosol emission sources simultaneously from satellite observed spectral AOD and AAOD based on the PARASOL/GRASP retrievals and the adjoint of GEOS-Chem chemical transport model. This method uses prior BC, OC and DD emissions as weak constraint in the inversion by initializing the retrieval with prior emissions and uniform background values. A series of numerical tests were performed which show this assumption can provide a better fit to observations, meanwhile it allows the retrieval to produce rather good results even if a priori knowledge of emissions is poor. Admittedly, the satellite observations are sparse due to several factors, e.g., the clear-sky condition, global coverage orbit cycle. Nevertheless, the PARASOL 6 wavelengths AOD and AAOD from GRASP algorithm are shown to be sufficient to characterize the distribution and magnitude of BC, OC and DD aerosol emission sources simultaneously under the

assumption of DD emissions correction constant over 24h and 4 days correction constant carbonaceous aerosol emissions. The inversion test of synthetic PARASOL-like measurements have shown about 25.8% uncertainty for daily total DD emission, 5.9% for daily total BC emission and 26.9% for daily total OC emissions. In addition, it was shown that using two different assumptions for BC refractive indexes (Case 1: m=1.75-0.45i; Case 2: 1.95-0.79i) could lead to an additional factor of 1.8 differences in total BC emissions.

We evaluated the GRASP retrieved one-year PARASOL spectral AOD and AAOD with AERONET ground-based observations/retrievals at 28 sites across study area (30°W-60°E, 40°S-40°N). Good agreements were found even using rescaling of the retrievals to the spatial resolution 2.0° x 2.5°. Derimian et al. (2016) and Popp et al. (2016) show similar validation results of PARASOL/GRASP with AERONET. Therefore, we used PARASOL/GRASP retrieved spectral AOD and AAOD to optimize BC, OC and DD aerosol emission sources in a year (December 2007 to November 2008) over the study area with horizontal resolution of 2.0° x 2.5° in order to match the adjoint GEOS-Chem spatial resolution. The retrieved emission sources are publically available at http://csuchencheng.wixsite.com/chencheng/research-blog; this dataset will be available soon at GEOS-Chem inventory finding website (http://wiki.seas.harvard.edu/geos-chem/index.php/Inventory_Findings).

Our analysis of the retrieved aerosol emissions indicates that the prior GEOS-Chem model overestimates annual desert dust aerosol emissions by a factor of about 1.8 (with the DEAD scheme) over the study area, similar to other previous modeling studies (Huneeus et al., 2012; Johnson et al., 2012; Ridley et al., 2012, 2016). The retrieved annual BC and OC emissions show a consistent seasonal variation with emission inventories (GFED3 for biomass burning and Bond for anthropogenic fossil fuel and biofuel combustions). However, we find these BC and OC emissions to have broad underestimations throughout the study area. For example, emissions from the emission inventories for BC are significant lower than our retrieved values up to 823.5% (Case 1) and 305.9% (Case 2), and for OC they are about 196.8% lower. These results are reflected in the model bias of AOD and AAOD from the prior GEOS-Chem simulation, e.g. significant low bias over the biomass burning regions and high bias over the Sahara desert region. Underestimation of BC and OC emissions in chemical transport models have been suggested previously (Sato et al., 2003; Zhang et al., 2015). However, we cannot rule-out the possibility that

differences between model and observations could also be attributed to the errors in removal processes and aerosol microphysical properties, in addition to the deficiencies in emissions (Bond et al., 2013). Nevertheless, the fidelity of our results is confirmed by comparison of posterior simulations with measurements from AERONET that are completely independent from and more temporally frequent than PARASOL observations. Specifically, to analyze the PARASOL/GRASP based aerosol emission database further, we implemented these emissions in the GEOS-5/GOCART model and compared the resulting simulations of AOD and AAOD with independent MODIS and OMI observations. The comparisons show better agreements between model and observations with the posterior GEOS-5/GOCART results (lower biases and higher correlation coefficients) than prior simulations. In the future, we plan to apply our approach to longer records and global domain of observations and to further investigate the inter-annual variability of aerosol emissions on global scale and to test our retrieved emission database in other models.

Acknowledgements

I thank the entire AERONET team, and especially the principal investigators and site mangers of the 28 AERONET stations that we acquired data from. I am also grateful for the MODIS and OMI aerosol team (O. Torres and H. Jethva) for providing the data used in this investigation, and Mian Chin, Huisheng Bian and Tom Kucsera for incorporating the PARASOL/GRASP emissions into the GEOS-5 model and provide the GEOS-5/GOCART simulation results.

Chapter 5

Global desert dust and primary carbonaceous aerosol emission database (v1.0, 2006-2011) retrieved from satellite

> The environmental crisis is a global problem, and only global action will resolve it.
>
> Barry Commoner

5.1 Introduction

Atmospheric aerosols are related to the climate system intricately by scattering and absorbing solar and terrestrial radiation and by altering cloud properties and lifetimes (Kaufman et al., 2002). They are also known to cause extreme weather, air pollution events and adverse public health effects (e.g., Li et al., 2011; Ramanathan et al., 2001; Zhang et al., 2017). Aerosol radiative forcing of climate over the industrial period remains the largest forcing uncertainty through the Intergovernmental Panel on Climate Change (IPCC) assessments since 1996. Reliable assessments of aerosol

effects on climate changing and public health depend on the development of global models.

One of the most important factors affecting the aerosol model simulation is adopted data for aerosol emissions (Kinne et al., 2003). Different climate models use differing aerosol emission databases or inventories, whose distribution and magnitude vary markedly from one model to next. Despite the general agreement in total AOD, there are significant model diversities at the individual component level for aerosol (Kinne et al., 2006). This indicates that uncertainties in assessing aerosol climate forcing are still large, because the aerosol climate forcing evaluation depends on not only total AOD but also on aerosol absorption (AAOD) and particle size (Ångström Exponent, AExp), which are determined by aerosol type and optical properties (Textor et al., 2006).

To further reduce the impact of differences in aerosol emissions on aerosol distribution simulation, the availability of aerosol remote sensing products, especially global aerosol fields provided by space-borne satellite observations, is of critical importance for constrain and optimize the aerosol emission. In the last decade, many efforts have been made to use satellite observations to constrain or optimize aerosol emissions in climate model (Dubovik et al., 2008; Huneeus et al., 2012, 2013; Wang et al., 2012; Xu et al., 2013; Zhang et al., 2015; Escribano et al., 2016, 2017). However, these studies are mostly focused on the regional scale, or retrieving a single aerosol or gas species and keeping others constant, or to aggregating adjustments made to emissions to several pre-defined regions. The objective of these treatments is to reduce the number of unknown parameters describing the retrieved emissions. As discussed in works such as Dubovik et al. (2008) and Meland et al. (2013), AOD at one wavelength contains only limited information to evaluate aerosol types, properties, or speciated emissions. Thus, a long record of global aerosol emission based on satellite observations still remains a very challenging and underdeveloped task.

In this chapter, we first develop a long record of desert dust and primary carbonaceous (including black and organic carbon) aerosol emissions using the advanced PARASOL/GRASP aerosol data (the data available from ICARE data distribution portal) and the GEOS-Chem inverse modeling framework. The methodology of the inversion has been discussed in Chapter 3. Here, we first present the evaluation of atmospheric aerosol properties from the free-running model (prior simulation) and PARASOL/GRASP with ground-based observations from

AERONET (section 5.2). After that in section 5.3, we describe the newly developed satellite-based aerosol emission database for 2006 to 2011, considering the emissions magnitude, distribution, trends and the comparison with other studies. The posterior atmospheric aerosol simulations (section 5.4) are evaluated using independent measurements from ground and space. In section 5.5, we test the satellite based aerosol emission database in the GEOS-5/GOCART model to evaluate how much results may be impacted by model bias owing to factors other than BC, OC and DD emissions.

5.2 Prior GEOS-Chem simulation of atmospheric aerosols

We evaluate the atmospheric aerosol properties from prior (free-running) GEOS-Chem model simulation on daily and annual mean scale, respectively. Table 5.1 shows a summary of physical processes, emission models and inventories used for the prior GEOS-Chem model simulation. The detailed aerosol properties used in this study are shown in Table 2.2. The global distribution of columnar AOD, AAOD, SSA and AExp are adopted from GEOS-Chem model simulation for evaluation. Global distributed ground-based AERONET (Holben et al., 1998) measurements of aerosol provide an opportunity to evaluate the model simulation of atmospheric aerosols. More than 400 AERONET sits (shown in Figure 2.1) are used for our evaluation. Here, we use level 2 AERONET data, which are cloud screened and quality assured (Smirnov et al., 2000). AERONET annual mean aerosol data is averaged based on their monthly aerosol products. Any site with less than 6 monthly values is omitted.

Figure 5.1 shows the comparison of prior GEOS-Chem annual mean AOD, AAOD, SSA at 550 nm and AExp (440-870) with collocated AERONET observations between 2006 and 2011. There are ~450 grid boxes with AERONET annul AOD data covering ~3.5% of the 13,104 grid boxes in the global 2°x2.5° model domain. The prior GEOS-Chem annual mean AExp (Figure 5.1d) has a solid agreement with AERONET (R=0.74). Meanwhile, the prior AOD (Figure 5.1a) and AAOD (Figure 5.1b) at 550 nm show correlation with AERONET measurements (AOD: R=0.42; AAOD: R=0.40), however the prior SSA (Figure 5.1c) has the lowest correlation coefficient with AERONET (R=0.21).

Table 5.1: A summary of physical processes, emission models and inventories used in free-running GEOS-Chem simulation

	Description	References
Emissions		
Anthropogenic	Global: BOND monthly inventory for base year 2000	(Bond et al., 2007)
Biomass burning	Version 3 Global Fire Emission Database (GFED3), daily	(van der Werf et al., 2006, 2010; Randerson et al., 2013)
Dust	The mineral dust entrainment and deposition (DEAD) model coupled with the GOCART dust source function	(Fairlie et al., 2007; Ginoux et al., 2001; Zender et al., 2003)
Sea salt	Sea salt emissions include both wind speed and sea surface temperature (SST) dependence.	(Gong, 2003; Jaeglé et al., 2011; Monahan et al., 1986)
Sulfate	Natural Sulfur: DMS from oceanic phytoplankton; SO2 from volcanoes; SO2 from biomass burning Anthropogenic SO2: Gridded monthly aircraft emissions and biofuel use Ammonia: 1° x 1° GEIA inventory based on year 1990	(Bouwman et al., 1997; Andres and Kasgnoc, 1998; Duncan et al., 2003; Kettle et al., 1999; Chin et al., 2000; Park et al., 2004)
Physical processes		
Wet deposition	Parameterization for scavenging in convective updrafts as well as in- and below-cloud scavenging from convective and large scale precipitation for soluble gases and aerosols	(Liu et al., 2001; Wang et al., 2011)
Dry deposition	Accounting for gravitational settling	(Wang et al., 1998; Wesely, 1989)
PBL mixing	Non-local PBL mixing scheme	(Lin and McElroy, 2010)

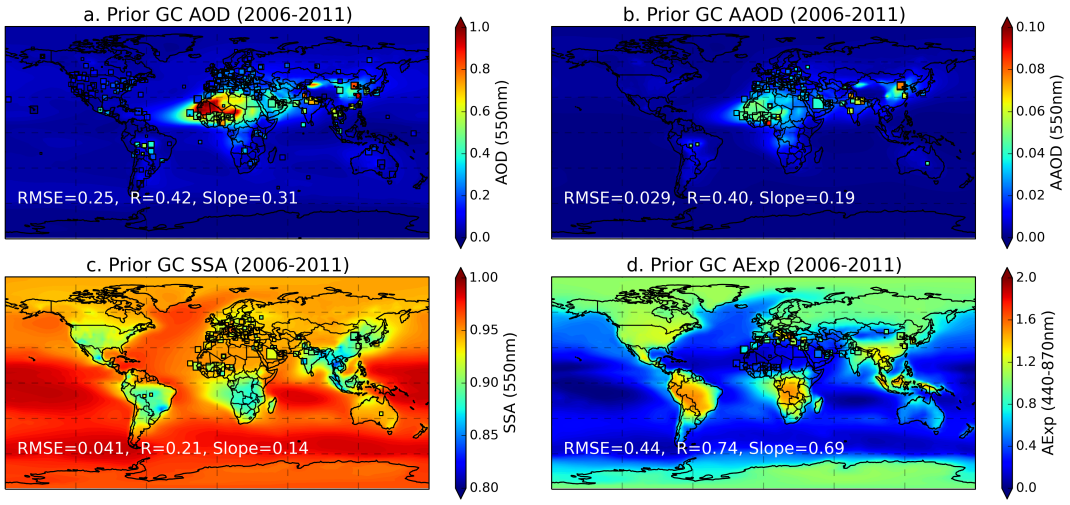

Figure 5.1: Spatial distribution of AOD (a), AAOD (b), SSA (c) and AExp (d) simulated from the prior GEOS-Chem model; the ground-based measurements from AERONET (squares) are plotted over figures a-d. The root mean square error (RMSE), correlation coefficient (R) and slope of linear regression (Slope) versus AERONET are provided in figures.

Space-borne satellites offer a direct measure of the amount of light scattering or even polarized light through the integrated atmospheric column modifying the diffuse and direct solar radiation by the presence of atmospheric aerosols. The GRASP algorithm is developed for enhanced characterization of aerosol properties from spectral, multi-angular polarimetric measurements, such as PARASOL (Dubovik et al., 2011, 2014; data available from ICARE data distribution portal: http://www.icare.univ-lille1.fr/). The global PARASOL/GRASP daily aerosol products (AOD, AAOD, SSA and AExp) from 2006 to 2011 are also evaluated with AERONET daily dataset. In this validation, PARASOL/GRASP original retrievals (~0.1°) are aggregated to the same resolution as the GEOS-Chem model (2°x2.5°); any grid box with less than 500 available PARASOL/GRASP retrievals (fitting residual < 10%) for averaging is omitted. Depending on geographical location, the number of GRASP retrievals in a single 2° x 2.5° grid box ranges from 500 to 1600. This 2°x2.5° PARASOL/GRASP aerosol dataset will then be used to retrieve global aerosol emissions.

Figure 5.2 shows the comparisons of PARASOL/GRASP 2° x 2.5° aerosol products with the corresponding AERONET daily aerosol products. PARASOL/GRASP AOD, AAOD and AExp show solid correlation with AERONET measurements. The correlation coefficient for SSA is somewhat lower (R=0.41), though the dynamic range of SSA is narrow (mainly located in 0.7 to 1.0). For each aerosol parameter, we calculate the mean bias (MB $= \frac{1}{N}\sum_{i=1}^{N}(M_i - O_i)$). MB values are -0.03 for AOD, -0.013 for AAOD, 0.011 for SSA, and -0.11 for AExp. Underestimations of PARASOL/GRASP AOD, AAOD and AExp are likely associated with the aggregation of GRASP retrievals from 6 x 6 km pixels in one 2° x 2.5° grid box. PARASOL/GRASP AExp shows solid correlation with AERONET measurements (R=0.79, MAE=0.27), which indicates the reliability of using PARASOL/GRASP 2°x2.5° spectral AOD. Note that we carried out the comparison of AAOD and SSA following the AERONET standard quality-screening criteria (Dubovik et al., 2002b; Holben et al., 2006) that AOD≥0.4, meanwhile the comparison of AExp was done with AOD≥0.2. The objective is to select sufficiently accurate retrievals for reference in the evaluation.

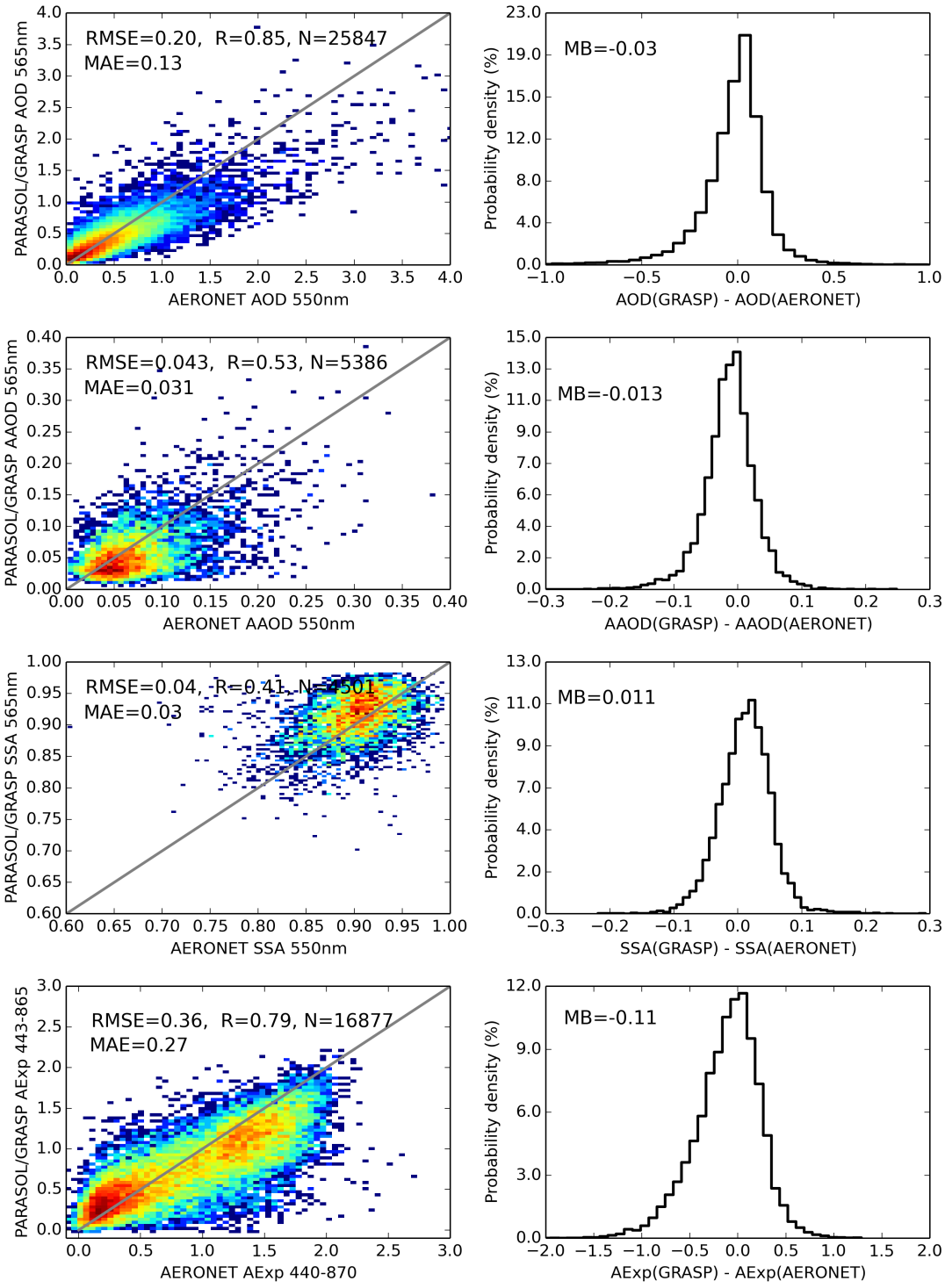

Figure 5.2: Density scatterplot (left panel) of daily PARASOL/GRASP 2°x2.5° aerosol products (AOD, AAOD, SSA and AExp) in comparison with AERONET; the correlation coefficient (R) and root mean square errors (RMSE), mean absolute error (MAE) are provided in the figures. The differences probability plots (right panel) are shown in the right column. The mean bias (MB) is provided in the top left of the figures.

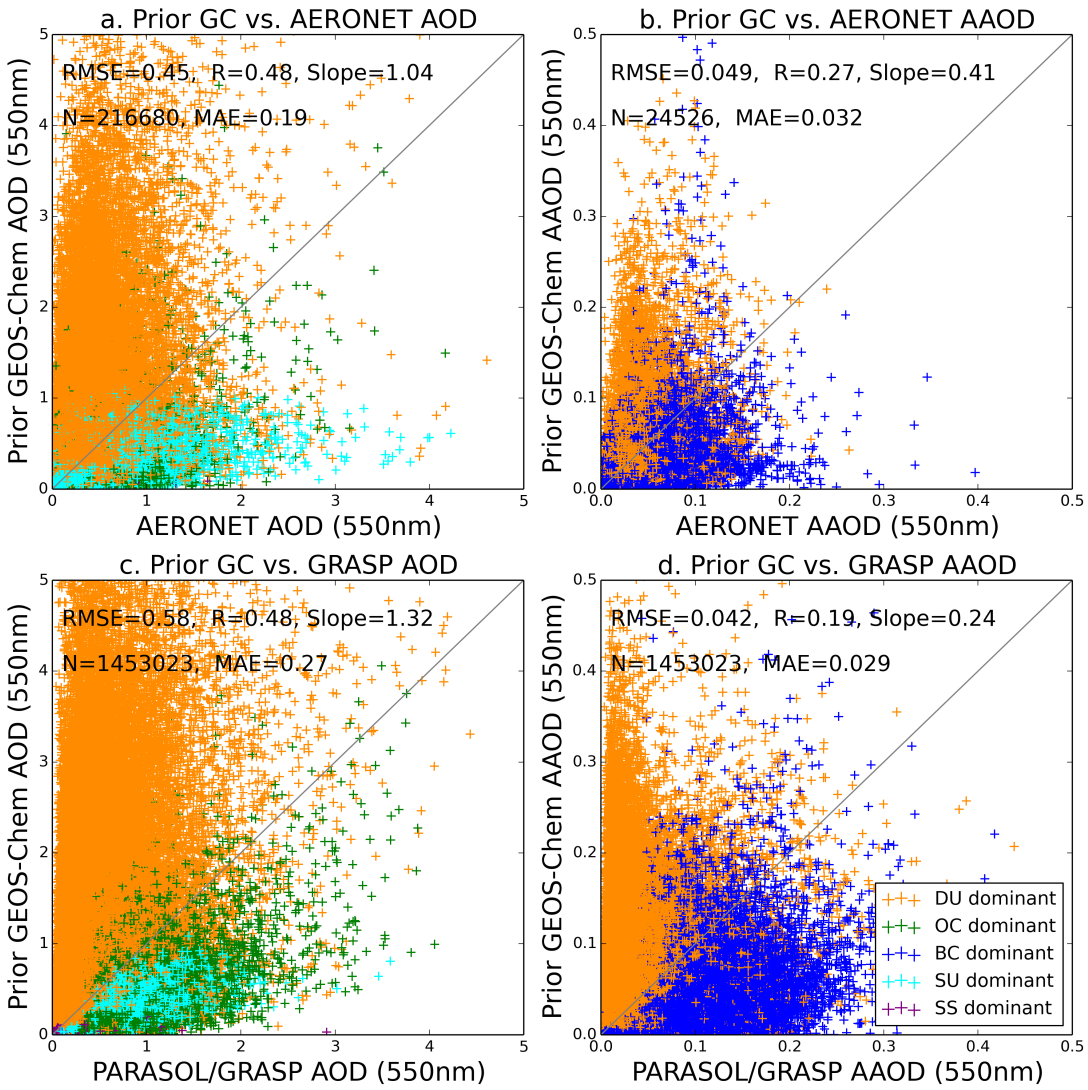

Figure 5.3: Comparison of prior GEOS-Chem (GC) daily AOD with collocated AERONET (a) and PARASOL/GRASP (c) AOD at 550nm; and prior GEOS-Chem daily AAOD versus AERONET (b) and PARASOL/GRASP (d) AAOD at 550nm. The discriminated different aerosol types determined by the first contributor to the total AOD and AAOD are shown with color code (yellow – DD; green – OC; blue – BC; cyan – SU; purple – SS).

In addition, the prior GEOS-Chem daily AOD and AAOD (averaged from 24 hourly data) at 550nm are validated against collocated AERONET Level 2.0 and space-borne PARASOL/GRASP aerosol products. In order to quantify further the simulation of aerosol properties at the individual component level, each independent grid box aerosol type is determined by the first contributor of its total AOD and AAOD, respectively (the same method as shown in Figure 2.9). Note that the aerosol type for each independent grid box could be different in different days, and the aerosol type for one grid box at a particular day could be different from the aspects of

AOD and AAOD, respectively. For statistics, in terms of global daily AOD from 2006 to 2011, all grid boxes can be divided into 49.4% DD, 0.0% BC, 13.5% OC, 14.5% SU and 22.6% SS. For AAOD, there are 38.6% DD, 60.8% BC, 0.0% OC, 0.0% SU and 0.6% SS.

The GEOS-Chem daily AOD from 2006 to 2011 is evaluated against AERONET (Figure 5.3a) and PARASOL/GRASP (Figure 5.3c). AOD in about 50.0% of the grid boxes is dominated by DD particles. However, the prior GEOS-Chem AODs over DD dominant (dusty) grid boxes are explicitly overestimated in comparison with both AERONET and PARASOL/GRASP (yellow crosses in Figure 5.3a and 5.3c). The comparison of GEOS-Chem daily AAOD with AERONET and PARASOL/GRASP are also shown in Figure 5.3b and Figure 5.3d, respectively. 99.4% grid boxes AAOD, with the exception 0.6% over oceans, are dominated by DD and BC particles. The DD AAOD dominant grid boxes consistently exhibit overestimation of total AAOD (yellow crosses in Figure 5.3b and 5.3d). However, BC dominant grid boxes generally underestimate total AAOD compared with both AERONET and PARASOL/GRASP (blue crosses in Figure 5.3b and 5.3d). Overall, the prior GEOS-Chem AAOD is broadly underestimated in comparison with measurements, with a linear regression slope of ~0.41 versus AERONET and ~0.24 versus PARASOL/GRASP. However, the simulation of aerosol total extinction and absorption over dusty areas are higher than observations.

Satellite remote sensing of atmospheric aerosols show an extensive spatial coverage as well as good agreement with ground-based measurements (Bréon et al., 2011; Kahn et al., 2005; Kleidman et al., 2005; Popp et al., 2016; Remer et al., 2002, 2005; Smirnov et al., 2011; Torres et al., 2002). However, the satellite observations alone are not sufficient to fully constrain the emission, transport, removal and distribution of aerosols, since satellite observations are sparse and limited due to several factors, e.g., the clear-sky condition, and global coverage orbit cycle. There are limitations for chemical transport models that driven by modeling the physical and chemistry processes of atmospheric aerosols. Hence, combination of observation and simulation is crucial to understand the role of atmospheric aerosols play in earth-atmosphere system.

5.3 Satellite-based emission database of BC, OC and DD

5.3.1 Database description

Since PARSOL/GRASP aerosol products provide an extensive and accurate record of information about aerosols, we use spectral AOD and AAOD from PARASOL/GRASP at 6 wavelengths (443, 490, 565, 670, 865 and 1020nm) to optimize global DD, BC and OC aerosol emissions using the GEOS-Chem based inversing modeling. Compared to previous studies discussing global emission retrievals (e.g. Dubovik et al., 2008), the present study is more advanced in the following ways: (i) we use the PARASOL/GRASP aerosol product, which is the first long-time record aerosol dataset retrieved from space-borne observation, providing wavelength dependence (VIS-NIR) aerosol scattering and absorption properties. (ii) different from many previous studies (Cohen and Wang, 2014; Escribano et al., 2016, 2017; Huneeus et al., 2012), we estimate grid-box level BC, OC and DD contributions by spectral dependence of aerosol scattering and absorption. (iii) The present study uniquely uses observational information to determine speciated aerosol emissions and produce a global aerosol emission database, which provides the potential to improve the model simulation of aerosol properties simultaneously, i.e. AOD, AAOD, AExp. The main limitation of this study is that all the difference of modeled aerosols are attributed to emissions, however some of the difference could be coming from poorly modeled transport processes and aerosol microphysical properties assumed in the model instead of emissions.

Figure 5.4a-c shows the global map of 2006-2011 retrieved annual BC, OC and DD aerosol emissions. The daily emissions are freely accessible from our website. The database includes primary carbonaceous (BC and OC) and DD aerosol emissions. However, due to the limited information content of satellite observation, the database does not currently distinguish between natural and anthropogenic aerosol sources. For DD emission, 0.1~6.0μm (particle radius) particles are considered, and super coarse DD particles are excluded. Figure 5.5a-c shows the monthly cycle of retrieved global BC, OC and DD aerosol emissions in contrast with the GEOS-Chem emission acquired from prior emission inventories. The prior GEOS-Chem DD emission module (Fairlie et al., 2007) is originated from the mineral dust entrainment and deposition (DEAD) model (Zender et al., 2003), which is coupled with the GOCART dust source function (Ginoux et al., 2001). The daily biomass burning sources are

calculating from version 3 of Global Fire Emissions Database (GFED) inventory (van der Werf et al., 2006, 2010; Randerson et al., 2013). The monthly anthropogenic fossil fuel and biofuel BC and OC emissions are adopted from Bond inventory with base year 2000 (Bond et al., 2007).

I. Black Carbon

Satellite-based aerosol emission database shows the annual global BC aerosol emission is 27.59 Tg/yr with an increasing trend +0.20 Tg/yr from 2006 to 2011 (Figure 5.4a and 5.5a). It is 2.58 times higher than the GEOS-Chem BC emission inventory, in which the value is 10.71 Tg/yr. Furthermore the annual trend in the prior inventory (-0.10 Tg/yr) is the reverse of our database. Satellite-based BC emission (27.59 Tg/yr) is close to the upper limit (29.0 Tg/yr) given by Bond et al. (2013) using bottom-up methods for the base year 2000. Thus, findings suggest that there is more absorption BC aerosols emitted than has generally been realized, and the total aerosol absorbing due to BC will be enhanced 2~3 times using satellite-based BC emission database.

II. Organic Carbon

The seasonal cycle of satellite-based OC aerosol emission is shown in Figure 5.5b as the comparison between satellite-based emission database and prior GEOS-Chem emission. The annual OC emission (Figure 5.4b) in our database is 132.51 Tg/yr, which is 2.94 times higher than that of GEOS-Chem (45.09 Tg/yr). Meanwhile, the annual trend of OC emission from 2006 to 2011 is reversed from -0.70 Tg/yr in GEOS-Chem to +0.67 Tg/yr in satellite-based OC emission database.

III. Desert Dust

In addition to global 0.1~6.0μm DD aerosol emission (Figure 5.4c and 5.5c), satellite-based emission database (831 Tg/yr) indicates a reduction about 41% to the GEOS-Chem dust model (1409 Tg/yr). GEOS-Chem dust model shows a decreasing trend of annual dust emission -40.56 Tg/yr from 2006 to 2011, while satellite-based DD emission indicates an increasing trend about 1.62 Tg/yr.

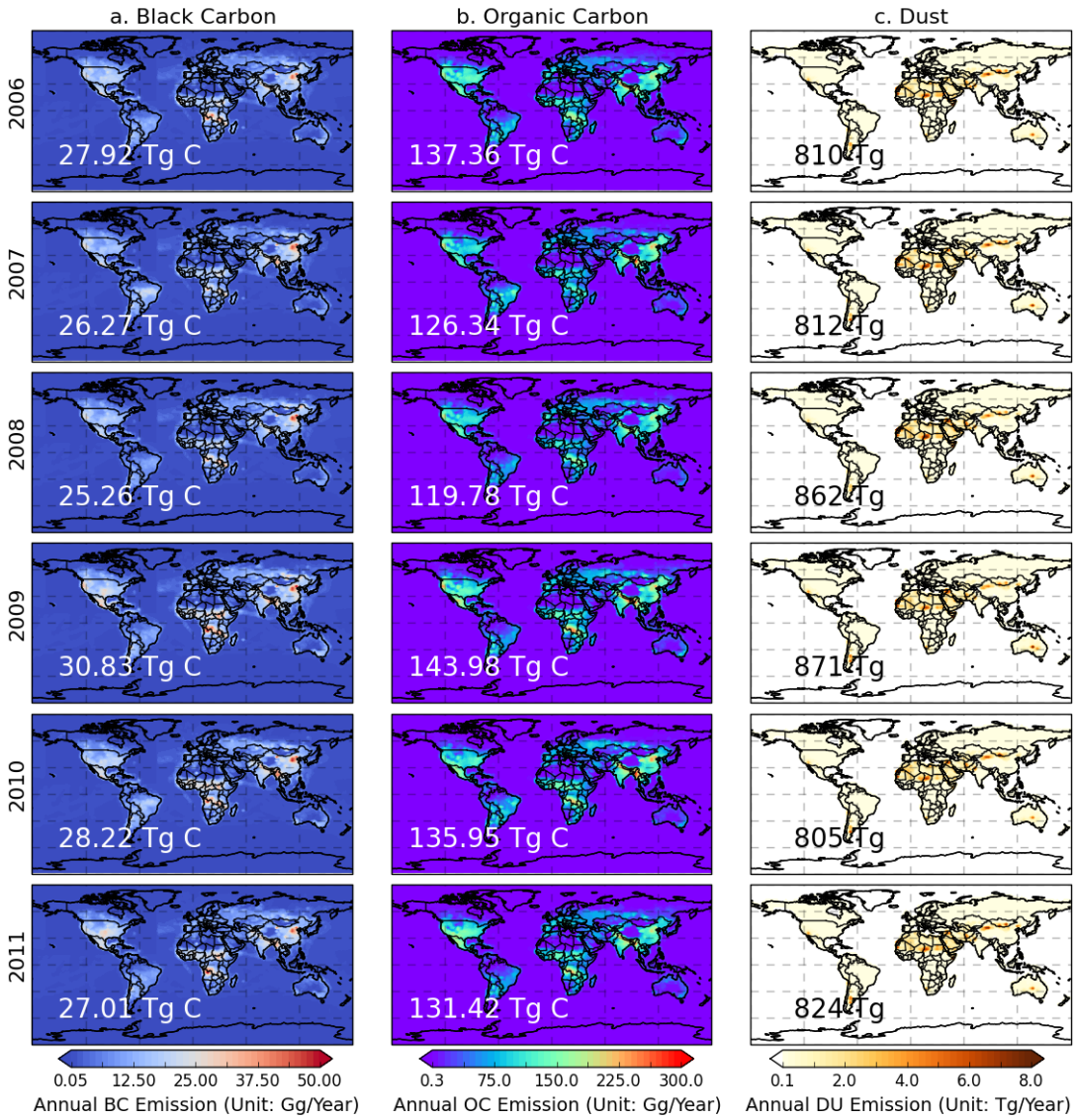

Figure 5.4: Satellite-based global distribution aerosol emission database from 2006 to 2011, (a) black carbon, (b) organic carbon, and (c) desert dust; the annual BC, OC and DD aerosol emissions are also provided in the figure.

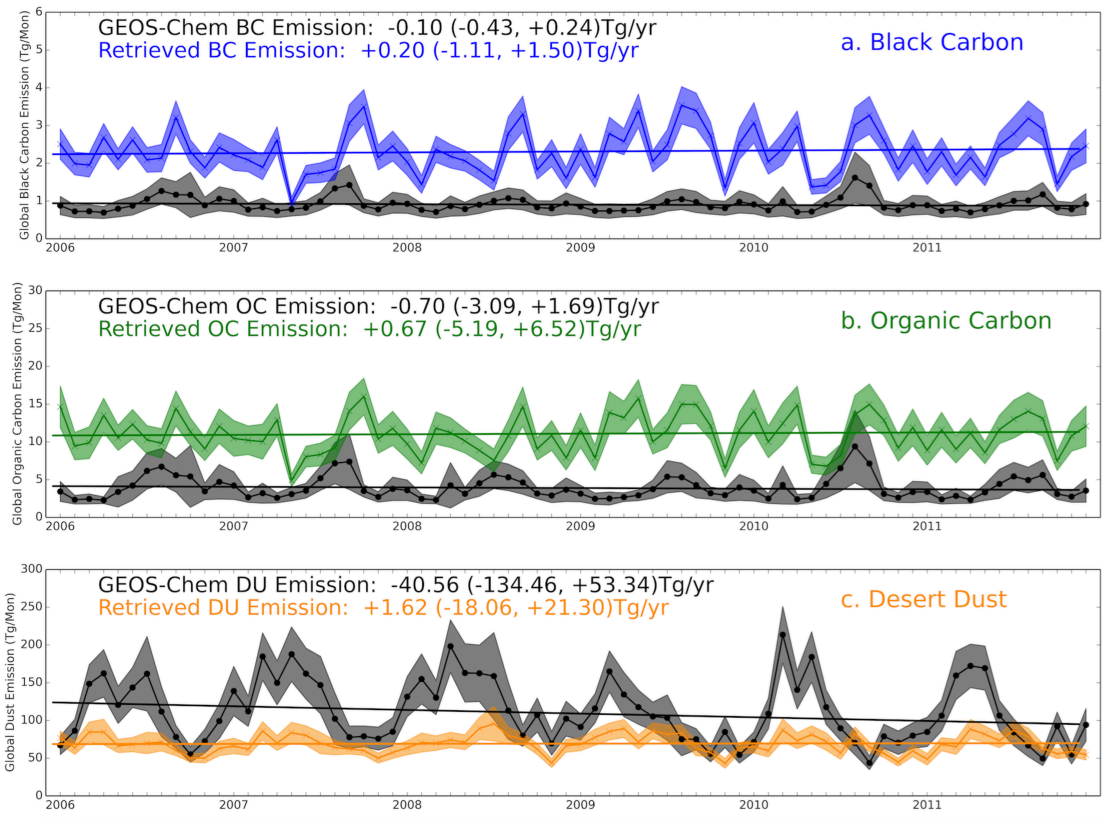

Figure 5.5: Monthly cycle of global BC (a), OC (b) and DD (c) aerosol emission from satellite-based emission database in contrast with the GEOS-Chem prior emission database; the annual trends of emissions are provided in top left of figure a-c.

5.3.2 Database evaluation

In this section, results of satellite-based aerosol emission database of DD, BC and OC are also compared to the bottom-up emission inventories and top-down retrievals from literatures. Table 5.2 shows a summary of the estimates of global annual DD, BC and OC emission flux from previous studies in comparison with those from this study. The emission of this study is averaged from 2006 to 2011. For the estimates from the IPCC (2013) report, we simply account 10% of biomass burning emission for BC and 90% for OC. Meanwhile, the value from the GEOS-Chem and GEOS-5/GOCART models is also averaged from 2006 to 2011, and only 0.1~6.0μm dust particle emissions are considered.

The IPCC report (IPCC, 2013) estimates DD emission from 1000 to 4000 Tg/yr, spanning a factor of 4. The annual mean DD emission in this study is 831 Tg/yr. The super coarse dust particles are not included, because the observed spectral AOD in the VIR-NIR wavelengths are not sensitive to super coarse particles. In addition, the

super coarse bin contributes about 721 Tg/yr emission flux in GEOS-5/GOCART model.

The global BC emissions inferred from IPCC (2013) report, using an assumption that 10% BB emission accounting for BC, is 6.5 to 14.5 Tg/yr. Meanwhile, the estimation of OC emission is 30.6 to 87.7 Tg/yr. The bottom-up carbonaceous aerosol emission inventories (Bond et al., 2004; Chin et al., 2009; Cooke and Wilson, 1996; Kim et al., 2008; Liousse et al., 1996; Penner et al., 1993; Takemura et al., 2005) are estimated indirectly, the highest value is 24.0 Tg/yr, given by Penner et al. (1993) using measured ambient concentration ratio of BC and SO_2 at locations throughout the world. The most common value used in current climate models is the central estimats of 8.0 Tg/yr by Bond et al. (2004). Meanwhile, the total uncertainties are at the order of factor 2, with uncertainty ranging from 4.3 to 22 Tg/yr. In addition, Bond et al. (2013) recommend to increase global absorption by a factor of 3 to match the observations of columar aerosol absorption. The top-down estimations from Cohen and Wang (2014) and Huneeus et al. (2012) give higher global BC emission than bottom-up methods. Cohen and Wang (2014) estimates global BC emissions using a top-down Kalman Filter approach from column AAOD from ground-based 112 AERONET stations and 26 surface BC concertration measurement stations, with an optimized range from 14.6 Tg/yr to 22.2 Tg/yr. Huneeus et al. (2012) assimilated daily total AOD and Fine mode AOD at 550nm from MODIS to constrain global aerosol emissions, and the optimized BC emission is 15.0 Tg/yr. However, Cohen and Wang (2014) and Huneeus et al. (2012) all adopt simiplied models with predefined regions; thus, the emission correction over a predefined region is constant. In this study, we try to retrieve global grid box level BC emission, and our estimation of global annual BC emission is 27.6 Tg/yr. This result is esitimated based on space-borne measurement of columar total aerosol absorption, which provides an opportunity to harmonize and improve the simulation of AAOD. However, satellite-based BC emission database should be improved in future by considering the BC particles absorption enhancement by particle mixing state(Liu et al., 2017), treating hydrophilic BC as internal with other soluble hygroscopic aerosol species (Wang et al., 2016); including the light absorbing brown carbon in the simulation (Wang et al., 2014b).

Similar to the BC emission, the satellite-based OC emissions show a global annual flux of 132.5 Tg/yr. This value is close to the top-down estimate from

Huneeus et al. (2012) of 119.0 Tg/yr. Our value is still higher than other estimations based on bottom-up methods (Bond et al., 2004; Chin et al., 2009; IPCC, 2013; Kim et al., 2008; Liousse et al., 1996; Takemura et al., 2005).

Table 5.2: A summary of the global annual DD, BC and OC aerosol emission flux from previous studies and that from this study. The unit is Tg/yr. Note that the value adopt from GEOS-Chem and GOCART model is also annual average from 2006-2011, and the dust particle size is considered from 0.1~6.0μm for GEOS-Chem and GOCART model.

DD		**BC**		**OC**	
IPCC (2013)	1000-4000	IPCC (2013)$^{+}$	6.5-14.5	IPCC (2013)$^{+}$	30.6-87.7
Dentener et al. (2006)	1678	Bond et al. (2004)	8.0	Bond et al. (2004)	33.0
Tanaka and Chiba (2006)	1877	Penner et al. (1993)	12.6-24.0		
Miller et al. (2004)	1019	Liousse et al. (1996)	12.0	Liousse et al. (1996)	73.0
Ginoux et al. (2004)	2073	Chin et al. (2009)	10.2	Chin et al. (2009)	61.8
Zender et al. (2003)	1490	Takemura et al. (2005)	15.98	Takemura et al. (2005)	105.7
Luo et al. (2003)	1654	Kim et al. (2008)	14.4	Kim et al. (2008)	54.4
Werner et al. (2002)	1060	Cooke and Wilson (1996)	14.0		
Huneeus et al. (2012)	1383	Huneeus et al. (2012)	15.0	Huneeus et al. (2012)	119.0
		Cohen and Wang (2014)	14.6-22.2		
GEOS-Chem	1409	GEOS-Chem	10.7	GEOS-Chem	45.1
GOCART	2077	GOCART	9.3	GOCART	54.7
This study*	831	This study*	27.6	This study*	132.5

** The emission of this study is averaged from 2006 to 2011. + We simply account 10% biomass burning (BB) emission for BC and 90% BB emission for OC.*

5.4 Consistency with observations

5.4.1 Evaluation of posterior GEOS-Chem model simulation

The satellite-based aerosol emission database is firstly analyzed by evaluating output of posterior GEOS-Chem simulations obtained using satellite-based emission database. We evaluate the posterior GEOS-Chem AOD, AAOD, SSA and AExp with not only fitted observations of PARASOL/GRASP, but also against the completely independent and more time frequent measurements from (than those from PARASOL) ground-based AERONET. Figure 5.6 shows the comparison of posterior GEOS-Chem simulated annual mean (2006-2011) AOD, AAOD, SSA, AExp with collocated AERONET measurements (similar to Figure 5.1 but for posterior simulation). Posterior GEOS-Chem AOD have a better correlation (R=0.75), smaller root mean square error (RMSE=0.12) than the counterparts in Figure 5.1a using prior emissions

(R=0.42, RMSE=0.25); Posterior AAOD also shows a better agreement with AERONET; the correlation coefficient improves from R=0.40 (prior) to R=0.65 (posterior), and the RMSE decreases from 0.029 (prior) to 0.018 (posterior). In addition, the improvements also show for SSA (Prior: R=0.21, RMSE=0.041; Posterior: R=0.63, RMSE=0.027) and AExp (Prior: R=0.74, RMSE=0.44; Posterior: R=0.80, RMSE=0.23). However, the posterior AAOD over North America in Figure 5.6b is slightly higher than AERONET results, which lead to a smaller SSA than AERONET in Figure 5.6c. The overestimation of posterior AAOD over North America is likely associated with the high PARASOL/GRASP retrieval uncertainties there resulting from relative low absolute values. This overestimation needs to be investigated in the future by using slow version of PARASOL/GRASP aerosol products. Overall, the posterior GEOS-Chem aerosol simulation using satellite-based emission database shows a better agreement with ground-based AERONET measurements for annual mean AOD, AAOD, SSA and AExp.

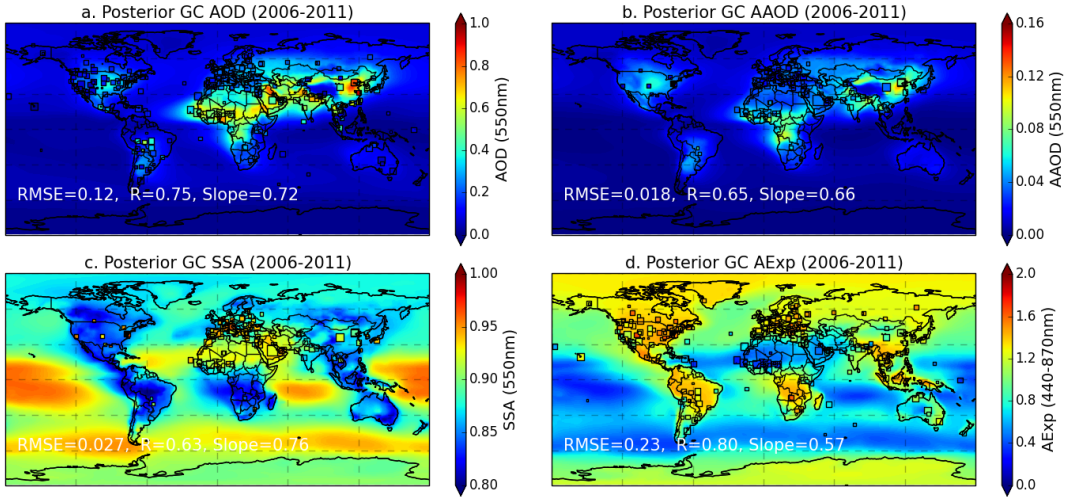

Figure 5.6: Comparison of annual mean AOD, AAOD, SSA and AExp from the posterior GEOS-Chem model with AERONET between 2006 and 2011 (similar to Figure 5.1, but for posterior GEOS-Chem simulation using satellite-based aerosol emission database);

Figure 5.7 shows the improvement of the posterior GEOS-Chem model simulation using satellite-based aerosol emission database is further reflected in comparison of posterior daily AOD and AAOD with ground-based collocated AERONET measurements and PARASOL/GRASP retrievals. Similar to Figure 5.3, aerosol in each corresponding grid box is classified into five component groups. In comparison with the prior simulation (Figure 5.3), the improvements of agreement

with PARASOL/GRAP AOD and AAOD are not surprising, because the inverse model iteratively seeks the correction of aerosol emissions that minimizes the differences between the PARASOL/GRASP spectral AOD and AAOD with that from model simulation. Furthermore, the improved agreements found with AERONET aerosol data (AOD and AAOD) that are completely independent and more temporal frequent than PARASOL observations.

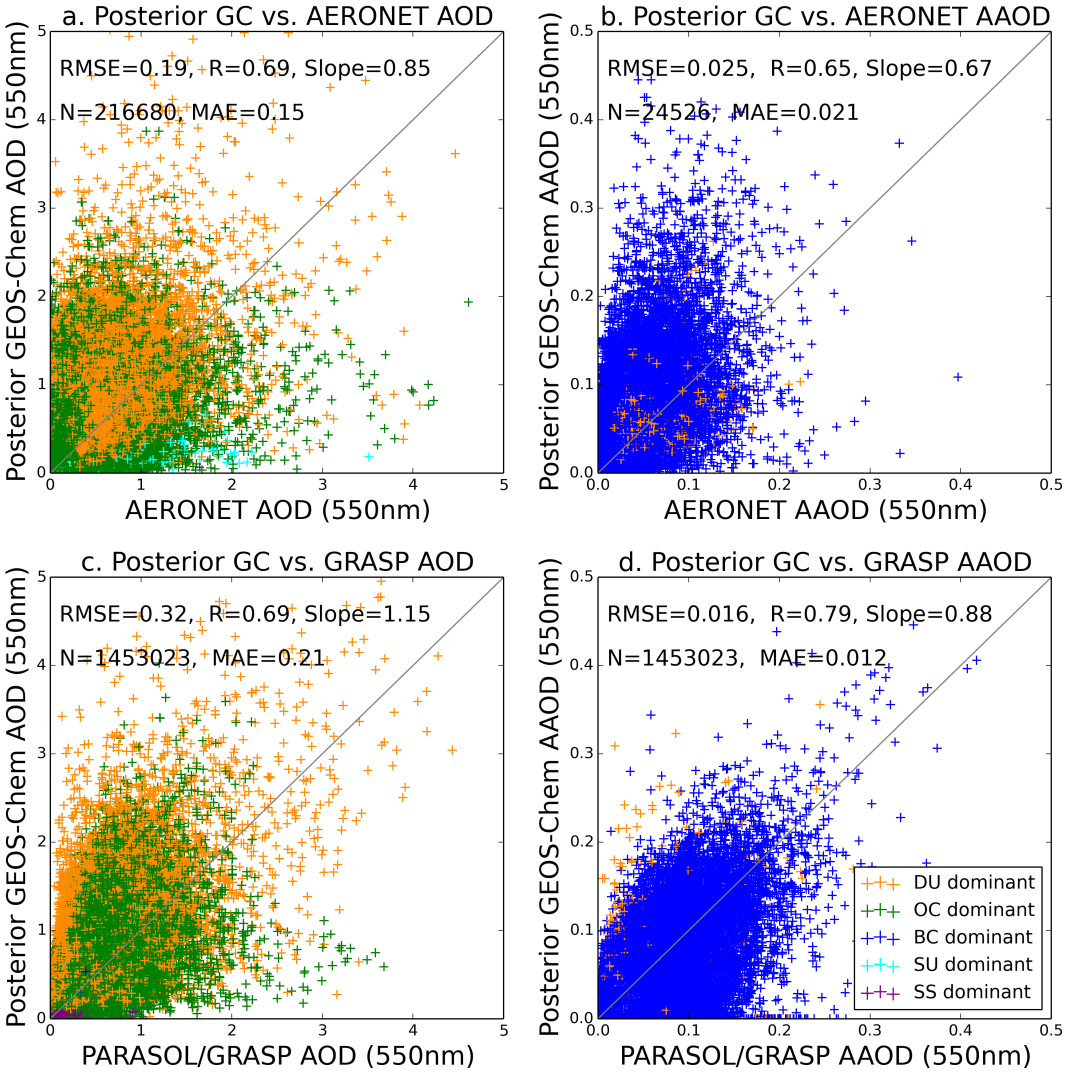

Figure 5.7: Comparison of posterior GEOS-Chem daily AOD and AAOD with collocated AERONET and PARASOL/GRASP at 550nm (similar to Figure 5.2, but for posterior GEOS-Chem simulation using satellite-based aerosol emission database).

5.4.2 Modeling applications

All the evaluations considered above are a based on simulations in the GEOS-Chem model. In order to evaluate how such results may be impacted by model biases owing to factors other than BC, OC and DD emissions, here we implement our satellite –based aerosol emission database into the GEOS-5/GOCART model (Chin et al., 2002, 2009, 2014; Colarco et al., 2010). The prior and posterior GEOS-5/GOCART model AOD and AAOD are compared with independent space-borne MODIS, MISR and OMI operational aerosol products (https://disc.gsfc.nasa.gov/). Here we take MODIS collection 6 combined dark target and deep blue Level 3 AOD products at the spatial resolution of 1° x 1° (Hsu et al., 2004; Levy et al., 2013), MISR Level 3 AOD products at the spatial resolution 0.5° x 0.5° (Diner et al., 2005; Kahn et al., 2005) and the latest OMI Level 3 (OMAERUV version 1.7.4) (Torres et al., 2007, 2013) AAOD products at the spatial resolution 0.5° x 0.5°. These satellite aerosol retrievals are aggregated to the same model resolution of 2.0° x 2.5°, and any grid box with less than 50% coverage for averaging is omitted. GEOS-5/GOCART uses similar meteorological fields as GEOS-Chem, with the prior anthropogenic emissions from the Hemispheric Transport of Atmospheric Pollution (HTAP) Phase 2, biomass burning emissions from the Fire Energetics and Emission Research (FEER) database (Ichoku and Ellison, 2014), dust emission calculated as a function of 10-m winds and surface characteristics (Ginoux et al., 2001), and volcanic emissions from OMI-based estimates (Carn et al., 2015). The global satellite-based DD, BC, and OC emissions are used in the "posterior" simulations while other sources remain unchanged. On an annual average, the DD, BC, and OC posterior/prior emission ratios over globe are 0.40, 3.0, and 2.4, respectively.

Figure 5.8 shows the comparison between the annual mean (2006-2011) AOD from prior and posterior GEOS-5/GOCART simulations with MODIS and MISR AOD products. Figures 5.8a and 5.8b present the spatial distribution of AOD difference between prior GEO-5/GOCART simulation and MODIS, MISR AOD, respectively. One of the major discrepancies between the prior model AOD and satellite observations is that the prior model AOD over desert dust regions (e.g. Sahara, Arabian Peninsula, Taklimakan etc.) is higher than that of satellite AOD products, which is likely associated with the overestimation of DD emissions. The posterior GEOS-5/GOCART simulation of AOD reduce this overestimation by

reducing global DD emission ~60%. However, this reduction of DD emission leads to slight underestimation of posterior GEOS-5/GOCART AOD (~0.1 at 550nm) over desert dust regions in comparison with MODIS and MISR, which is likely associated with the disagreement in modeling of DD AOD that needs to be investigated and addressed in future studies.

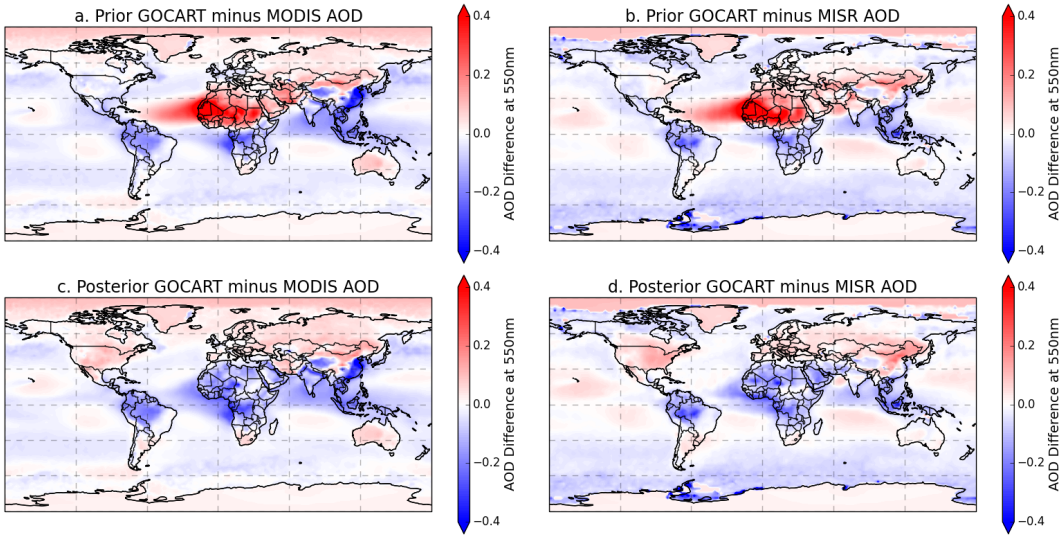

Figure 5.8: Comparison of prior and posterior GEOS-5/GOCART annual mean (2006-2011) AOD at 550nm with AOD products from MODIS and MISR; (a) Prior GOCART minus MODIS AOD; (b) Prior GOCART minus MISR AOD; (c) Posterior GOCART minus MODIS AOD; (d) Posterior GOCART minus MISR AOD;

Figure 5.9 shows the comparison of the collocated seasonal mean AOD at 550nm between prior and posterior GEOS-5/GOCART (red scatters) simulations and AOD from MODIS and MISR observations. The correlation coefficients between GEOS-5/GOCART simulation with prior emissions and observation data (shown in upper two panels) are 0.65 and 0.71 for MODIS and MISR respectively, the corresponding root mean square errors are 0.11 and 0.10, and the corresponding mean absolute errors are 0.07 and 0.06. The correlation coefficients are increased to 0.79 and 0.80 when the satellite-based emission database is used in the posterior GEOS-5/GOCART (shown in lower two panels), and meanwhile the root mean square errors are decreased to 0.08 and 0.07, and the absolute errors are also decreased to 0.05 and 0.04 respectively. However, the posterior GEOS-5/GOCART AOD is explicitly lower than MODIS and MISR observations, with linear regression slopes equal to 0.55 and 0.66 against MODIS and MISR respectively, and the corresponding mean biases are -0.03 and -0.02. The underestimation of posterior AOD is likely associated with the fact

that MODIS and MISR AOD is observed at noon, however the GEOS-5/GOCART AOD is average over 24 hours during a day and some disagreements in modeling of aerosol particles that needs to be investigated in future studies.

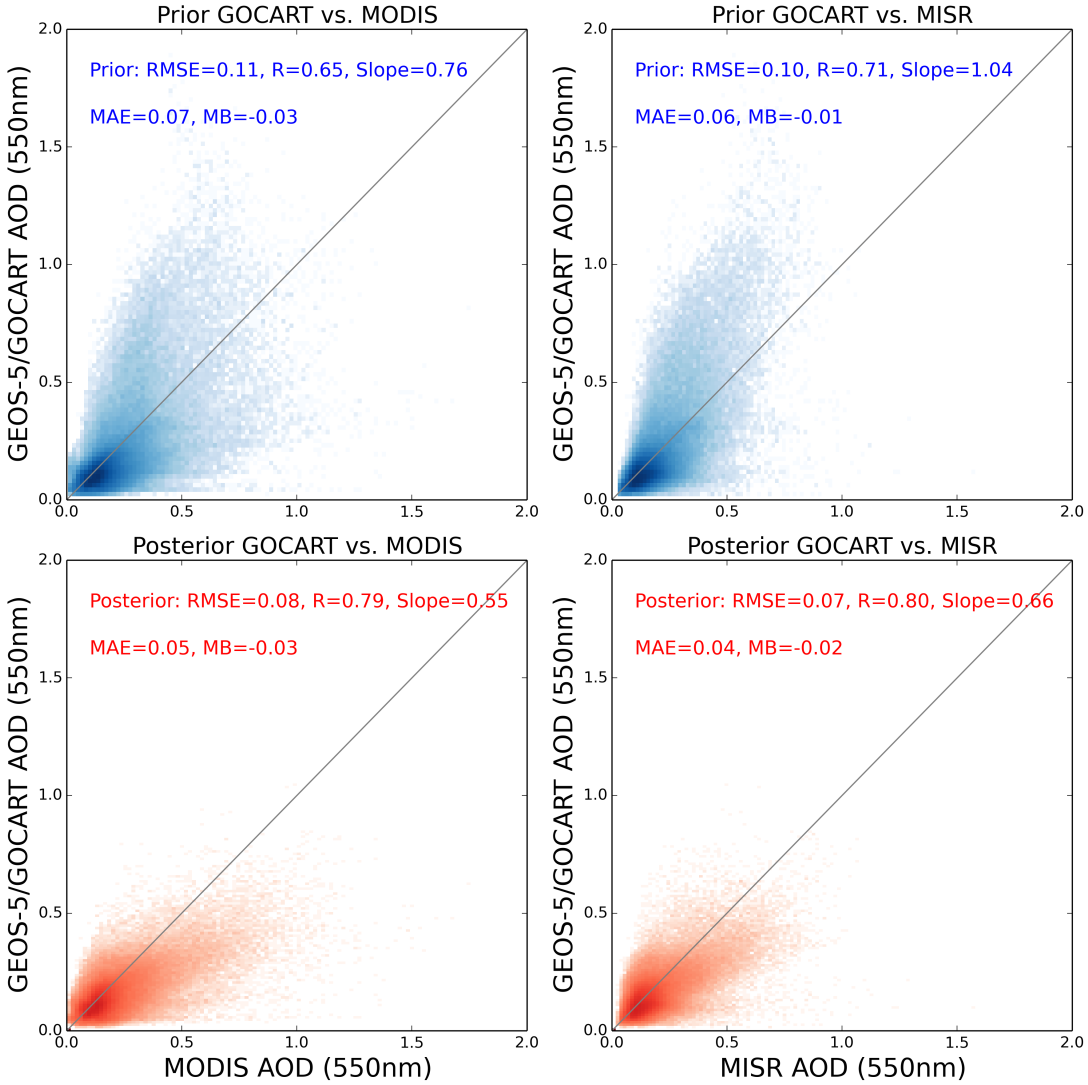

Figure 5.9: Scatter plots of prior/posterior GEOS-5/GOCART simulated AOD at 550nm in comparison with AOD from MODIS and MISR. The correlation coefficient (R), root mean square errors (RMSE), slope of linear regression (Slope), mean absolute error (MAE) and mean bias (MB) are provided in the top left of the figures.

Because there are only ultraviolet and shortwave visible channels and polarimeter measurements that are sensitive to aerosol absorption properties, long-term records of global coverage AAOD are limited to PARASOL/GRASP and OMI. We use the latest OMI aerosol products (OMAERUV version 1.7.4) (Torres et al., 2007, 2013) to evaluate the prior and posterior GEOS-5/GOCART model simulation of AAOD at 550nm. Figure 5.10a-b show the spatial distribution of AAOD differences between

prior and posterior GEO-5/GOCART AAOD and OMI AAOD. Figure 5.10c-d show the scatterplots of grid box level evaluation of prior/posterior GEOS-5/GOCART AAOD against OMI observations. The correlation coefficient between GEOS-5/GOCART simulation with prior emissions and OMI data is 0.57 (shown in Figure 5.10c), and the root mean square error is 0.016, and the corresponding mean absolute error is 0.11. Yet, the correlation coefficient is increased to 0.64 when the satellite-based emission database is used in the posterior GEOS-5/GOCART simulation (shown in Figure 5.10d), and meanwhile the root mean square error is decreased to 0.012, and the absolute error is also decreased to 0.008. However, the mean bias is increased from 0.001 (prior) to 0.003 (posterior). And the posterior GEOS-5/GOCART AAOD shows overestimation of both AOD and AAOD over North America, reflecting overestimation of posterior carbonaceous aerosol emission in this area, which we need to be investigated in the future.

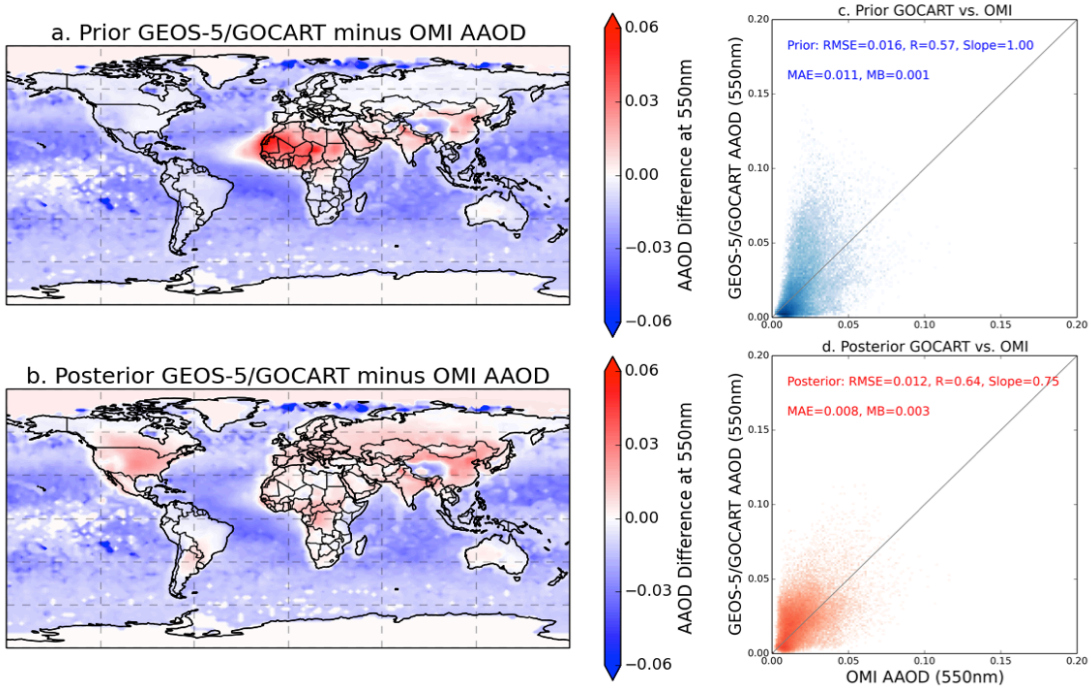

Figure 5.10: Evaluation of prior and posterior GEOS-5/GOCART AAOD at 550nm against AAOD products from OMI (OMAERUV version 1.7.4). (a)) Prior GEOS-5/GOCART minus OMI AAOD; (b) Posterior GEOS-5/GOCART minus OMI AAOD; Scatter plots of prior (c) and posterior (d) GEOS-5/GOCART simulated AAOD at 550nm in comparison with AAOD from OMI. The correlation coefficient (R), root mean square errors (RMSE), slope of linear regression (Slope), mean absolute error (MAE) and mean bias (MB) are provided in the top left of the figures.

5.5 Summary and discussion

The new recent PARASOL long record aerosol products processed with GRASP algorithm provide a potential of constraining the desert dust and primary carbonaceous aerosol emissions simultaneously. In this study, we first develop a global aerosol emission database of desert dust and primary carbonaceous aerosol, using PARASOL/GRASP spectral AOD and AAOD based on GEOS-Chem inverse modeling framework. The utilization of PARASOL/GRASP spectral AOD and AAOD allowed us to tune the model simulation in dimensions of aerosol extinction, absorption and spectrum. The preliminary analysis indicates that posterior GEOS-Chem model simulation using satellite-based aerosol emission database shows a better agreement with independent ground-based AERONET measurements for aerosol properties including AOD, AAOD, SSA and AExp.

Results from satellite-based aerosol emission database are also compared with previous studies using bottom-up and top-down methods. The satellite-based emission database shows lower DD emissions in amount (~-40%), while higher BC and OC emissions in amount (~+250%) than prior GEOS-Chem emissions. Huneeus et al. (2011) reported the model diversity of simulation of DD concentration and DD AOD, and the models overestimate the DD AOD. High biases of DD AOD and AAOD are improved or adjusted in this study by reducing total DD emissions ~40% over globe. However, the overestimation of the prior model DD AOD could also result from the error in particle size distribution, which is shown to biased toward smaller particle sizes compared to the observations in the atmosphere (Kok et al., 2017). Meanwhile, the satellite-based emission database increases the model annual carbonaceous aerosol emission by about 2.5 times. This value is close to the recommendation given in Bond et al. (2013) that increasing global BC absorption by a factor of 3 to fit the observation of columnar AAOD. It is also important to realize that BC from emission sources contains not only element and organic fractions but also brown carbon that have s significant absorbing contribution at short wavelengths (Feng et al., 2013; Lack et al., 2012). Several efforts have been done to include brown carbon in the model simulation (Jo et al., 2016; Wang et al., 2014b), however global brown carbon inventory is still not well developed. Satellite-based aerosol emission database should be improved in future at these points: (i) considering the BC particles absorption enhancement by particle mixing state (Liu et al., 2017); (ii) treating hydrophilic BC as

internal with other soluble hygroscopic aerosol species (Wang et al., 2016); (iii) including the light absorbing brown carbon in the simulation (Wang et al., 2014b); (iv) implementing the more realistic fine mode dust in the forward simulation (Kok et al., 2017).

Overall, the version 1.0 satellite-based aerosol emission database has been developed and tested in GEOS-5/GOCART model simulation. The posterior GEOS-5/GOCART aerosol simulation shows improved agreement with independent measurements from MODIS, MISR and OMI. Further assessments of this emission database are still needed. Also, further model studies by refining the atmospheric process, aerosol chemical composition, microphysical properties, aging scheme and particle mixing state are crucial to improve the aerosol emission database representation.

Acknowledgements

I thank the entire AERONET team, and especially the principal investigators and site mangers of the 462 AERONET stations that we acquired data from. I am also grateful for the MODIS, MISR and OMI aerosol team (O. Torres and H. Jethva) for providing the data used in this investigation, and Mian Chin, Huisheng Bian and Tom Kucsera for incorporating the PARASOL/GRASP emissions into the GEOS-5 model and provide the GEOS-5/GOCART simulation results.

Supplement

A. Illustrations for implementation of satellite-based DD, BC and OC aerosol emission in GEOS-5/GOCART model

While implementation of satellite-based aerosol emission database in GEOS-5/GOCART, some adjustments are done for DD emissions. The retrieval is initialized by "prior model" emissions with a uniform background over land (except snow/ice coverer regions). The retrieval with this initialization could detect new sources and perform satisfactorily even when *a priori* knowledge of aerosol emission is not fully consistent with the assumed emissions (see discussion in section 3.3.1). However, this strategy may result in DD emission occurrences in grid boxes where the prior model DD emissions are zero. Thus, the satellite-based DD emission is adapted to scale of prior GEOS-5/GOCART DD emissions on monthly and regional base. The regional DD emission ratios Posterior/Prior is shown in Figure S5.1. Meanwhile, satellite-based daily total gridded BC (including anthropogenic and biomass burning) and OC (including anthropogenic, biomass burning and biogenic) emissions are directly used as input for posterior GEOS-5/GOCART simulation. Figure S5.2 and S5.3 show the comparison of Prior and Posterior GEOS-5/GOCART monthly AOD and AAOD (January, April, July and October) in 2008, respectively.

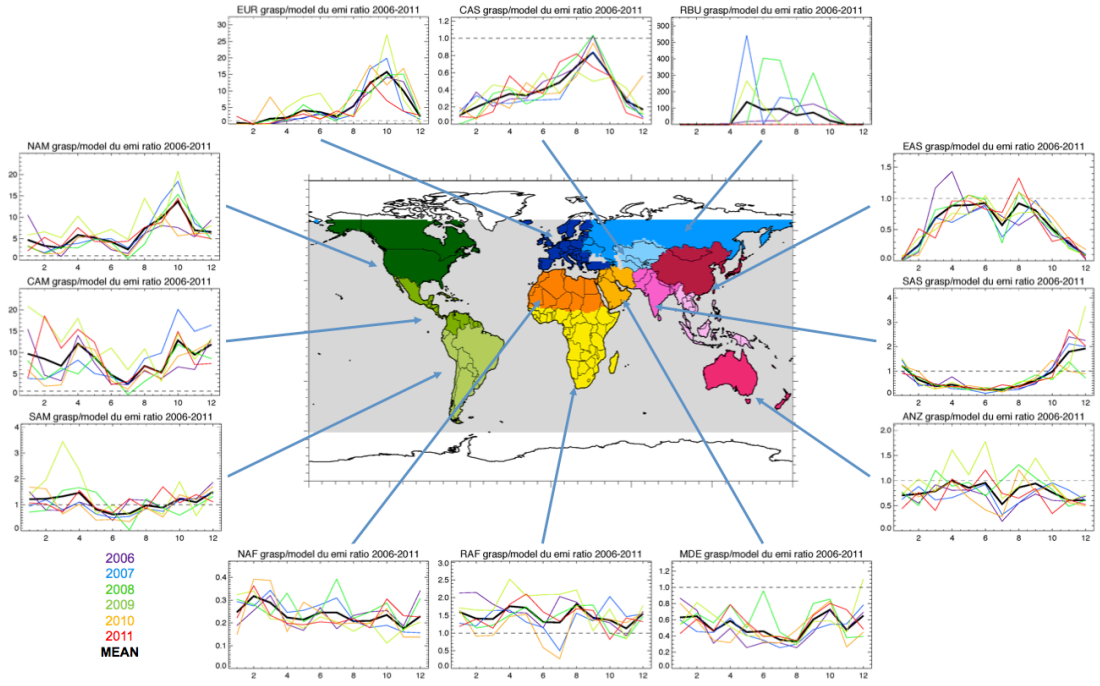

Figure S5.1: The regional DD emission ratios between satellite-based emission database and prior GEOS-5/GOCART DD emission model (adapted from Mian Chin)

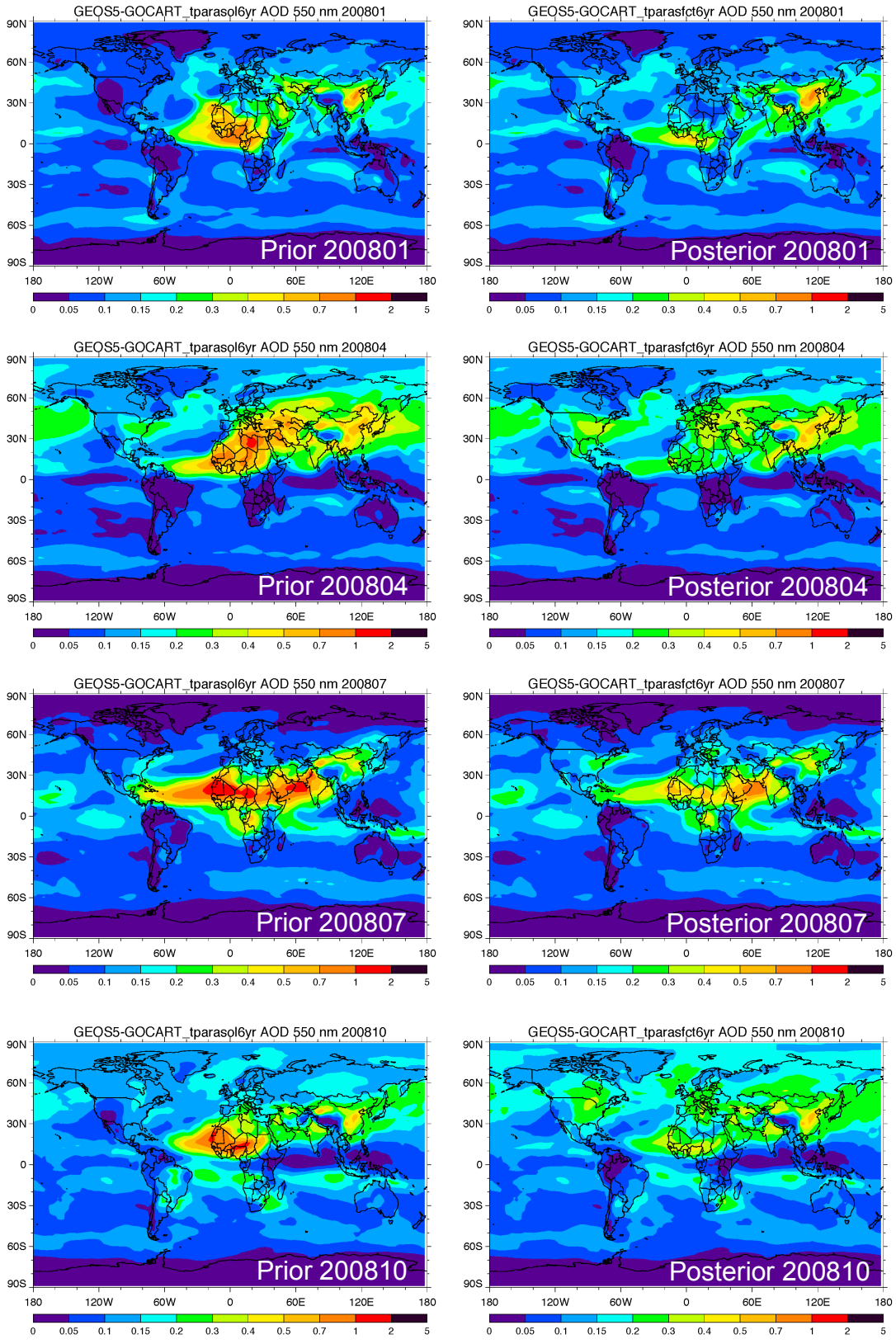

Figure S5.2: Comparison of Prior and Posterior GEOS-5/GOCART simulated monthly AOD (January, April, July and October) in 2008 (adapted from Mian Chin)

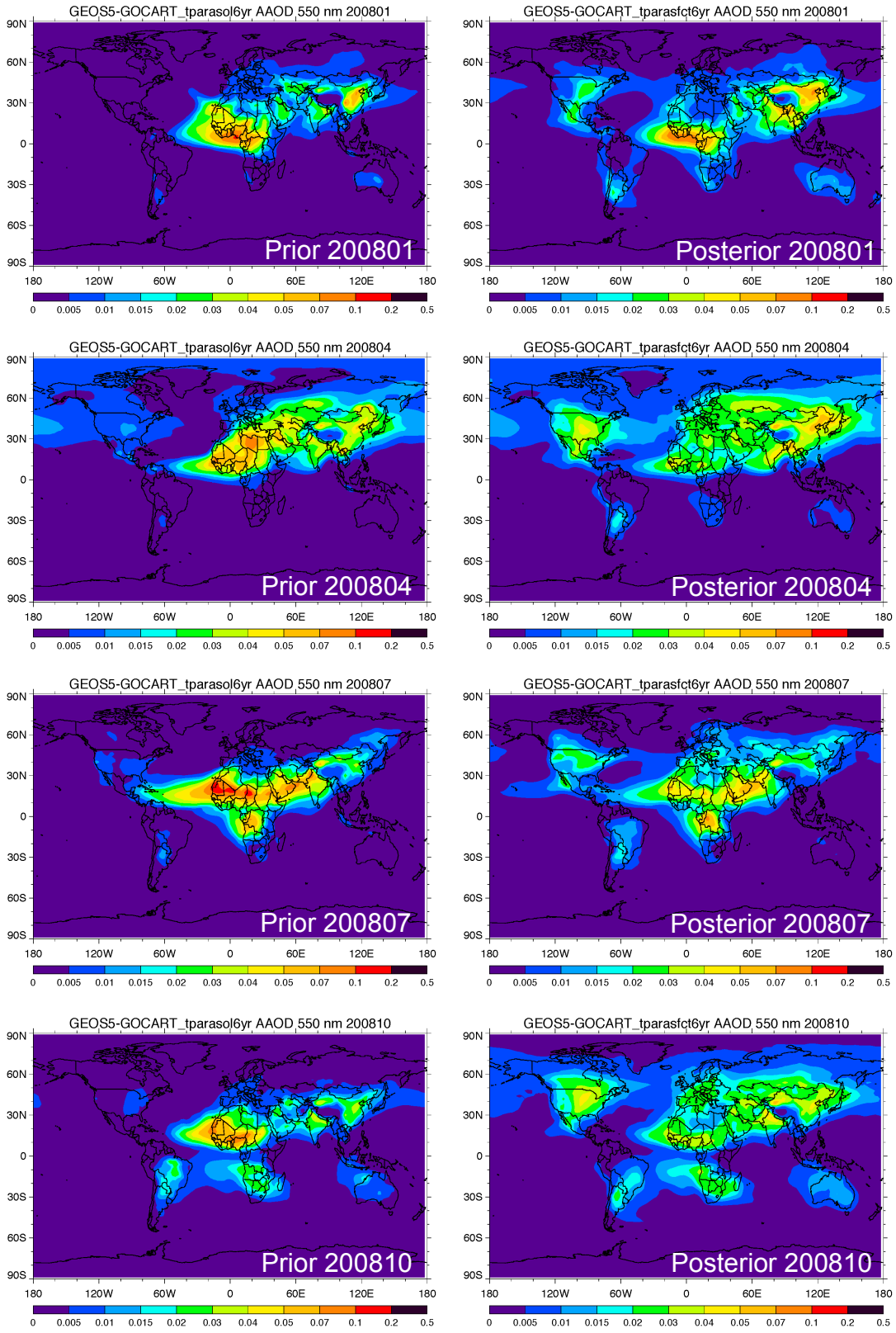

Figure S5.3: Comparison of Prior and Posterior GEOS-5/GOCART monthly AAOD (January, April, July and October) in 2008 (adapted from Mian Chin)

The prior/posterior GEOS-5/GOCART simulation of aerosol properties (AOD, AAOD, SSA, AExp) are further evaluated with ground-based AERONET monthly dataset in Figure S5.4. Overall, the most obvious improvements by using satellite-based emissions are the AExp, reflecting the decrease of coarse mode DD emissions and the increase of fine mode BC and OC emissions. In addition, the agreement of AAOD between model and AERONET retrieval is also slightly improved. However, the posterior AOD over North America is systematically higher than AERONET (green circles), which is likely associated with the high PARASOL/GRASP retrieval uncertainties there resulting from relative low absolute values. This overestimation needs to be investigated in the future by using the latest slow version of PARASOL/GRASP aerosol products.

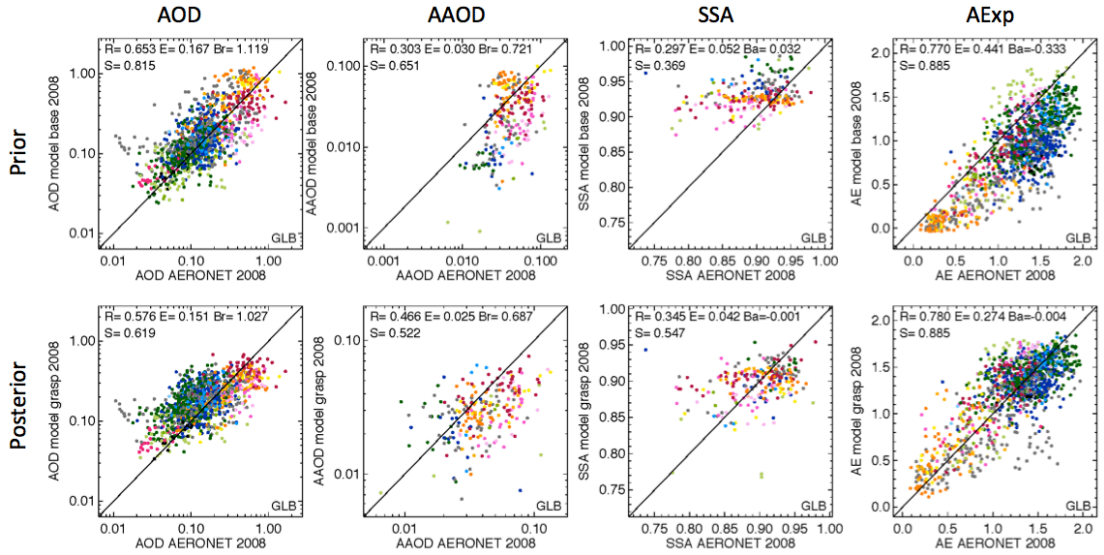

Figure S5.4. Scatter plots of prior/posterior GEOS-5/GOCART monthly mean AOD, AAOD, SSA and AExp in comparison with that from AERONET, color-coded with the predefined regions referred to Figure S5.1. (Adapted from Mian Chin)

Chapter 6

Conclusions and outlook

> Finally, in conclusion, let me say just this.
>
> Peter Sellers

6.1 Conclusion

Atmospheric aerosols remain the largest source of uncertainty in global climate forcing evaluation. Understanding the role atmospheric aerosols play in the earth-atmosphere system is limited by uncertainties in the knowledge of their distribution, composition and sources. Space-borne satellites offer a direct measure of the amount of light scattering or even polarized light through the integrated atmospheric column modifying the diffuse and direct solar radiation by the presence of atmospheric aerosols. However, the satellite observations alone are not sufficient for fully studying emission, transportation, removal and distribution of aerosols. Despite satellite observations having ability to provide extensive spatial coverage aerosol products with a high accuracy, the drawbacks of them are the lack of information on the chemical composition, the relatively large time span (usually more than 24 hours for polar orbiting satellites) between two successive overpasses over an area. There are no such limitations for chemical transport models (CTMs) that are driven by modeling the physical and chemistry processes of atmospheric aerosols. However, CTMs simulations are limited by uncertainties in knowledge of aerosol emission

source characteristics, knowledge of atmospheric processes and the meteorological data used. As a result, even the most recent models are found to capture only the principal global features of aerosol. For example, among different models, quantitative estimates of average regional aerosol properties often disagree by amounts exceeding the uncertainty of remote sensing of aerosol observations (Chin et al., 2002, 2014, Kinne et al., 2003, 2006; Textor et al., 2006). Therefore, combination of aerosol satellite remote sensing and aerosol model simulation is crucial to harmonize and improve aerosol modeling.

In this study, we have developed the adjoint GEOS-Chem model for retrieving DD, BC and OC aerosol emission sources simultaneously from satellite observed spectral AOD and AAOD based on the PARASOL/GRASP retrievals. Previous studies (Dubovik et al., 2008; Escribano et al., 2016, 2017; Huneeus et al., 2012; Meland et al., 2013; Zhang et al., 2015) of constraining aerosol emission in chemical transport model are limited by the information content from the space-borne aerosol products (AOD or AAOD at one wavelength). PARASOL/GRASP spectral (VIS-NIR) AOD and AAOD show sensitivity for optimizing DD, BC and OC sources simultaneously. For the inverse modeling, we use optimal spectral weighting factors for the PARASOL 6 wavelengths are $[1,1,1,1,1,1]^T$ for AOD and $[5,10,15,20,25,30]^T$ for AAOD, and we adopt "prior model" emissions with a uniform background for initial guess, and the emission corrections are assumed daily constant for DD and 4 days constant for BC and OC. These strategies are designed to fit PARASOL/GRASP spectral AOD and AAOD, and determine the spatial distribution and temporal variation of DD, BC and OC aerosol emission simultaneously. In addition, BC refractive index is sensitive to BC emission retrieval, which could produce an additional about 1.8 times differences for total BC emission.

The method was validated in series of numerical tests conducted with synthetic PARASOL-like data. The test results show that the approach allows for retrieval of the distribution and strength of aerosol emissions. The maximum uncertainty of sensitivity test for daily total emission is 25.8% for DD, 5.9% for BC and 26.9% for OC over Africa. Then the method was applied to one-year (December 2007 to November 2008) of data over the African and Arabian Peninsula region – the largest dust source and biomass burning region of the globe. The analysis of resulting retrieved emission sources (701 Tg/yr) indicates 1.8 times overestimation of the prior model DD emission obtained from online dust entrainment and mobilization module.

Some other studies also show similar dust emission flux over Africa (Werner et al., 2002; Miller et al., 2004; Escribano et al., 2016, 2017). For total BC and OC the retrieved emissions show a significant increase of 209.9%~271.8% in comparison to prior GEOS-Chem inventory of carbonaceous aerosol emissions. Our results are close the recommendation given in Bond et al. (2013) that increasing global BC absorption by a factor of 3 to fit the observation of columnar aerosol absorption. The model posterior simulation with retrieved emission sources shows good agreement both with fitted AOD and AAOD PARASOL/GRASP products. The fidelity of the results was evaluated by comparison of posterior simulations with measurements from AERONET that are completely independent and more temporally frequent than PARASOL observations. To further test the robustness of our posterior emissions constrained using PARASOL/GRASP, the posterior emissions are implemented in the GEOS-5/GOCART model and the consistency of simulated AOD (prior: R=0.77, RMSE=0.14, MAE=0.09; posterior: R=0.81, RMSE=0.10, MAE=0.06) and AAOD (prior: R=0.65, RMSE=0.019, MAE=0.014; posterior: R=0.69, RMSE=0.015, MAE=0.011) with other independent measurements (MODIS and OMI) demonstrates promises in applying this database for modeling studies.

The method was applied to global observations. Our analysis showed that the accuracy of SU aerosol emission could affect on the retrieval of OC emission in the industry area (e.g. North America and East China). Therefore, we slightly modified the inversion method by using a sequential approach by dividing the retrieval into two steps. Specifically, we used the fact that carbonaceous is usually fine mode dominant and BC particles are absorbing more ubiquitously from UV to near infrared wavelengths. The DD aerosol is usually coarse mode dominant and is also a major component contributed to aerosol absorption, while the DD particles absorb most strongly in the UV and short wave visible channels. The sensitivity test showed that the mean absolute difference for retrieved daily global DD emission is 6.7%, and the maximum absolute difference is 48%, and mean absolute difference for BC is 3.5%, maximum to 18.3%, and mean absolute difference for BC is 11.0%, maximum to 60.7%. Then, a satellite-based global DD and primary BC and OC aerosol emission database (version 1.0) is developed. Results from satellite-based aerosol emission database are compared with previous studies using bottom-up and top-down methods. The satellite-based emission database showed lower DD emissions by ~-40%, while higher BC and OC emissions by ~+250% than prior GEOS-Chem emissions. The

version 1.0 satellite-based aerosol emission database was used in GEOS-5/GOCART model simulation. The preliminary analysis showed GEOS-5/GOCART aerosol simulation obtained using the posterior emissions has a better agreement with independent measurements from MODIS, MISR and OMI, which indicates the possibility to use this emission database for improving global aerosol modeling results. Further assessments of satellite-based aerosol emission database are still desirable.

6.2 Outlook and future work

Below, I list some specific directions that could be useful for improving our satellite-based aerosol emission database.

✓ Improve the CTMs simulation of aerosol absorption

Brown carbon is one of the factors that cannot be ignored in the model simulation of aerosol absorption. Several efforts have been done to include brown carbon in the model simulation (Jo et al., 2016; Wang et al., 2014b). However, global brown carbon inventory is still not well developed. Zhang et al. (2015) simply performed an experiment by removing 30% of total absorption from observations since model does not include brown carbon. The optimized BC emissions are lower up to 30% compared to the standard results. Thus, to better characterize the BC aerosol emission, we should better characterize the brown carbon in the aerosol simulation.

✓ More representative dust particle size distribution

Recent study by Kok et al. (2017) indicated that the dust found in the atmosphere is substantially coarser than represented in current global climate models. They report that the fine mode dust aerosol (radius: 0.1-1.0μm) accounts for 3.5%-5.7% of the total emitted mass (radius: 0.1-20.0μm). In GEOS-Chem dust simulation (Fairlie et al., 2007), there are four dust size bins (0.1-1.0μm; 1.0-1.8μm; 1.8-3.0μm; 3.0-6.0μm). The contribution of fine dust (0.1-1.0μm) to total dust emission (0.1-6.0μm) is fixed at 12.23% (Fairlie et al., 2007). We perform an experiment by reducing the GEOS-Chem fine mode dust fraction to 6.0%. The GEOS-Chem global mean DD AOD decreases 22.2% compared to the standard results. Hence, the overestimation of the prior model dust emission could also partially result from the error in particle size

distribution. In future study, the more representative dust particle size distribution should be adopted in the dust simulation.

Last but not the least, the continuous efforts on improving CTMs simulation, inverse modeling framework, as well as, using more comprehensive observational data for data assimilation are crucial to characterize the atmospheric aerosols and their roles on climate change and regional air pollution.

Abbreviations and Acronyms

AAOD	Aerosol Absorption Optical Depth
AEROCOM	Aerosol Comparisons between Observations and Models
AERONET	AErosol RObotic NETwork
AExp	Ångström exponent
AOD	Aerosol Optical Depth
ASTER	Advanced Spaceborne Thermal Emission and Reflection Radiometer
ATB	Algorithm Theoretical Basis
AVHRR	Advanced Very High Resolution Radiometer
BC	Black Carbon
BrC	Brown Carbon
CTM	Chemical Transport Model
DB	Deep Blue
DD	Desert Dust
DEAD	Dust Entrainment And Deposition
DJF	December-January-February
DT	Dark Target
FEER	Fire Energetics and Emission Research
GCM	Global Circulation Model
GEOS	Goddard Earth Observing System
GFED	Global Fire Emissions Database
GOCART	Goddard Global Ozone Chemistry Aerosol Radiation and Transport model
GRASP	General Retrieval of Atmosphere and Surface Properties
HTAP	Hemispheric Transport of Atmospheric Pollution
IPCC	Intergovernmental Panel on Climate Change
JJA	June-July-August
MAE	Mean Absolute Error
MAIAC	MultiAngle Implementation of Atmospheric Correction
MAM	Match-April-May
MISR	Multi-angle Imaging SpectroRadiometer
MODIS	Moderate Resolution Imaging Spectroradiometer

MOPITT	Measurements Of Pollution In The Troposphere sensor
NASA	National Aeronautics and Space Administration
NMB	Normalized Mean Bias
OC	Organic Carbon
OM	Organic Matter
OMI	Ozone Monitoring Instrument
OPAC	Optical Properties of Aerosols and Clouds
PARASOL	Polarization & Anisotropy of Reflectances for Atmospheric Sciences coupled with Observations from a Lidar
PBL	Planetary Boundary Layer
PM	Particulate Matter
PSD	Particle Size Distribution
POLDER	POLarization and Directionality of the Earth's Reflectances
RF	Radiative Forcing
RH	Relative Humidity
RMSE	Root Mean Square Error
SON	September-October-November
SS	Sea Salt
SSA	Single Scattering Albedo
SU	Sulfate
TES	Tropospheric Emission Spectrometer
TOA	Top of Atmosphere
UV	Ultraviolet
WHO	World Health Organization

References

Acarreta, J. R., De Haan, J. F. and Stammes, P.: Cloud pressure retrieval using the O2 -O2 absorption band at 477 nm, J. Geophys. Res., 109(D5), D05204, doi:10.1029/2003JD003915, 2004.

Ahn, C., Torres, O. and Bhartia, P. K.: Comparison of Ozone Monitoring Instrument UV Aerosol Products with Aqua/Moderate Resolution Imaging Spectroradiometer and Multiangle Imaging Spectroradiometer observations in 2006, J. Geophys. Res., 113(D16), D16S27, doi:10.1029/2007JD008832, 2008.

Ahn, C., Torres, O. and Jethva, H.: Assessment of OMI near-UV aerosol optical depth over land, J. Geophys. Res. Atmos., 119(5), 2457–2473, doi:10.1002/2013JD020188, 2014.

Albrecht, B. A.: Aerosols, Cloud Microphysics, and Fractional Cloudiness, Science (80-.)., 245(4923), 1989.

Alexander, B., Park, R. J., Jacob, D. J., Li, Q. B., Yantosca, R. M., Savarino, J., Lee, C. C. W. and Thiemens, M. H.: Sulfate formation in sea-salt aerosols: Constraints from oxygen isotopes, J. Geophys. Res., 110(D10), D10307, doi:10.1029/2004JD005659, 2005.

Andres, R. J. and Kasgnoc, A. D.: A time-averaged inventory of subaerial volcanic sulfur emissions, J. Geophys. Res. Atmos., 103(D19), 25251–25261, doi:10.1029/98JD02091, 1998.

Ångström, A.: On the Atmospheric Transmission of Sun Radiation and on Dust in the Air, Geogr. Ann., 11, 156, doi:10.2307/519399, 1929.

Arola, A., Schuster, G., Myhre, G., Kazadzis, S., Dey, S. and Tripathi, S. N.: Inferring absorbing organic carbon content from AERONET data, Atmos. Chem. Phys., 11(1), 215–225, doi:10.5194/acp-11-215-2011, 2011.

Bellouin, N., Boucher, O., Haywood, J. and Reddy, M. S.: Global estimate of aerosol direct radiative forcing from satellite measurements, Nature, 438(7071), 1138–1141, doi:10.1038/nature04348, 2005.

Bey, I., Jacob, D. J., Yantosca, R. M., Logan, J. A., Field, B. D., Fiore, A. M., Li, Q., Liu, H. Y., Mickley, L. J. and Schultz, M. G.: Global modeling of tropospheric chemistry with assimilated meteorology: Model description and evaluation, J. Geophys. Res. Atmos., 106(D19), 23073–23095, doi:10.1029/2001JD000807, 2001.

Blanchard, D. C.: The oceanic production of atmospheric sea salt, J. Geophys. Res., 90(C1), 961, doi:10.1029/JC090iC01p00961, 1985.

Bond, T. C. and Bergstrom, R. W.: Light Absorption by Carbonaceous Particles: An Investigative Review, Aerosol Sci. Technol., 40(1), 27–67, doi:10.1080/02786820500421521, 2006.

Bond, T. C., Streets, D. G., Yarber, K. F., Nelson, S. M., Woo, J. and Klimont, Z.: A technology-based global inventory of black and organic carbon emissions from combustion, J. Geophys. Res., 109(D14), D14203, doi:10.1029/2003JD003697, 2004.

Bond, T. C., Bhardwaj, E., Dong, R., Jogani, R., Jung, S., Roden, C., Streets, D. G. and Trautmann, N. M.: Historical emissions of black and organic carbon aerosol from energy-related combustion, 1850-2000, Global Biogeochem. Cycles, 21(2), GB2018, doi:10.1029/2006GB002840, 2007.

Bond, T. C., Doherty, S. J., Fahey, D. W., Forster, P. M., Berntsen, T., DeAngelo, B. J., Flanner, M. G., Ghan, S., Kärcher, B., Koch, D., Kinne, S., Kondo, Y., Quinn, P. K., Sarofim, M. C., Schultz, M. G., Schulz, M., Venkataraman, C., Zhang, H., Zhang, S., Bellouin, N., Guttikunda, S. K., Hopke, P. K., Jacobson, M. Z., Kaiser, J. W., Klimont, Z., Lohmann, U., Schwarz, J. P., Shindell, D., Storelvmo, T., Warren, S. G. and Zender, C. S.: Bounding the role of black carbon in the climate system: A scientific assessment, J. Geophys. Res. Atmos., 118(11), 5380–5552, doi:10.1002/jgrd.50171, 2013.

Boucher, O.: Air traffic may increase cirrus cloudiness, Nature, 397(6714), 30, doi:10.1038/16169, 1999.

Bouwman, A. F., Lee, D. S., Asman, W. A. H., Dentener, F. J., Van Der Hoek, K. W. and Olivier, J. G. J.: A global high-resolution emission inventory for ammonia, Global Biogeochem. Cycles, 11(4), 561–587, doi:10.1029/97GB02266, 1997.

Brasseur, G. and Jacob, D. J.: Modeling of atmospheric chemistry, Cambridge University Press., 2017.

Brasseur, G. P., Orlando, J. J. and Tyndall, G. S.: Atmospheric Chemistry and Global Change, Oxford University Press, Oxford., 1999.

Bréon, F.-M., Vermeulen, A. and Descloitres, J.: An evaluation of satellite aerosol products against sunphotometer measurements, Remote Sens. Environ., 115(12), 3102–3111, doi:10.1016/J.RSE.2011.06.017, 2011.

Byrd, R. H., Lu, P., Nocedal, J. and Zhu, C.: A Limited Memory Algorithm for Bound Constrained Optimization, SIAM J. Sci. Comput., 16(5), 1190–1208, doi:10.1137/0916069, 1995.

Carn, S. A., Yang, K., Prata, A. J. and Krotkov, N. A.: Extending the long-term record of volcanic SO2 emissions with the Ozone Mapping and Profiler Suite nadir mapper, Geophys. Res. Lett., 42(3), 925–932, doi:10.1002/2014GL062437, 2015.

Chin, M., Rood, R. B., Lin, S.-J., Müller, J.-F. and Thompson, A. M.: Atmospheric sulfur cycle simulated in the global model GOCART: Model description and global properties, J. Geophys. Res. Atmos., 105(D20), 24671–24687, doi:10.1029/2000JD900384, 2000.

Chin, M., Ginoux, P., Kinne, S., Torres, O., Holben, B. N., Duncan, B. N., Martin, R. V., Logan, J. A., Higurashi, A. and Nakajima, T.: Tropospheric Aerosol Optical Thickness from the GOCART Model and Comparisons with Satellite and Sun Photometer Measurements, J. Atmos. Sci., 59(3), 461–483, doi:10.1175/1520-0469(2002)059<0461:TAOTFT>2.0.CO;2, 2002.

Chin, M., Diehl, T., Ginoux, P. and Malm, W.: Intercontinental transport of pollution and dust aerosols: implications for regional air quality, Atmos. Chem. Phys., 7(21), 5501–5517, doi:10.5194/acp-7-5501-2007, 2007.

Chin, M., Diehl, T., Dubovik, O., Eck, T. F., Holben, B. N., Sinyuk, A. and Streets, D. G.: Light absorption by pollution, dust, and biomass burning aerosols: a global model study and evaluation with AERONET measurements, Ann. Geophys., 27(9), 3439–3464, doi:10.5194/angeo-27-3439-2009, 2009.

Chin, M., Diehl, T., Tan, Q., Prospero, J. M., Kahn, R. A., Remer, L. A., Yu, H., Sayer, A. M., Bian, H., Geogdzhayev, I. V., Holben, B. N., Howell, S. G., Huebert, B. J., Hsu, N. C., Kim, D., Kucsera, T. L., Levy, R. C., Mishchenko, M. I., Pan, X., Quinn, P. K., Schuster, G. L., Streets, D. G., Strode, S. A., Torres, O. and Zhao, X.-P.: Multi-decadal aerosol variations from 1980 to 2009: a perspective from observations and a global model, Atmos. Chem. Phys., 14(7), 3657–3690, doi:10.5194/acp-14-3657-2014, 2014.

Chu, D. A., Kaufman, Y. J., Ichoku, C., Remer, L. A., Tanré, D. and Holben, B. N.: Validation of MODIS aerosol optical depth retrieval over land, Geophys. Res. Lett., 29(12), doi:10.1029/2001GL013205, 2002.

Chung, C. E., Ramanathan, V. and Decremer, D.: Observationally constrained estimates of carbonaceous aerosol radiative forcing., Proc. Natl. Acad. Sci. U. S. A., 109(29), 11624–9, doi:10.1073/pnas.1203707109, 2012.

Cohen, J. B. and Wang, C.: Estimating global black carbon emissions using a top-down Kalman Filter approach, J. Geophys. Res. Atmos., 119(1), 307–323, doi:10.1002/2013JD019912, 2014.

Colarco, P., da Silva, A., Chin, M. and Diehl, T.: Online simulations of global aerosol distributions in the NASA GEOS-4 model and comparisons to satellite and ground-based aerosol optical depth, J. Geophys. Res., 115(D14), D14207, doi:10.1029/2009JD012820, 2010.

Cooke, W. F. and Wilson, J. J. N.: A global black carbon aerosol model, J. Geophys. Res. Atmos., 101(D14), 19395–19409, doi:10.1029/96JD00671, 1996.

Dabberdt, W. F., Carroll, M. A., Baumgardner, D., Carmichael, G., Cohen, R., Dye, T., Ellis, J., Grell, G., Grimmond, S., Hanna, S., Irwin, J., Lamb, B., Madronich,

S., McQueen, J., Meagher, J., Odman, T., Pleim, J., Schmid, H. P. and Westphal, D. L.: Meteorological Research Needs for Improved Air Quality Forecasting: Report of the 11th Prospectus Development Team of the U.S. Weather Research Program, Bull. Am. Meteorol. Soc., 85(4), 563–586, doi:10.1175/BAMS-85-4-563, 2004.

Derimian, Y., Dubovik, O., Huang, X., Lapyonok, T., Litvinov, P., Kostinski, A. B., Dubuisson, P. and Ducos, F.: Comprehensive tool for calculation of radiative fluxes: illustration of shortwave aerosol radiative effect sensitivities to the details in aerosol and underlying surface characteristics, Atmos. Chem. Phys., 16(9), 5763–5780, doi:10.5194/acp-16-5763-2016, 2016.

Deshler, T., Johnson, B. J. and Rozier, W. R.: Balloonborne measurements of Pinatubo aerosol during 1991 and 1992 at 41°N: Vertical profiles, size distribution, and volatility, Geophys. Res. Lett., 20(14), 1435–1438, doi:10.1029/93GL01337, 1993.

Deuzé, J. L., Herman, M., Goloub, P., Tanré, D. and Marchand, A.: Characterization of aerosols over ocean from POLDER/ADEOS-1, Geophys. Res. Lett., 26(10), 1421–1424, doi:10.1029/1999GL900168, 1999.

Deuzé, J. L., Bréon, F. M., Devaux, C., Goloub, P., Herman, M., Lafrance, B., Maignan, F., Marchand, A., Nadal, F., Perry, G. and Tanré, D.: Remote sensing of aerosols over land surfaces from POLDER-ADEOS-1 polarized measurements, J. Geophys. Res. Atmos., 106(D5), 4913–4926, doi:10.1029/2000JD900364, 2001.

Le Dimet, F. and Talagrand, O.: Variational algorithms for analysis and assimilation of meteorological observations: theoretical aspects, Tellus A, 38A(2), 97–110, doi:10.1111/j.1600-0870.1986.tb00459.x, 1986.

Diner, D. J., Beckert, J. C., Reilly, T. H., Bruegge, C. J., Conel, J. E., Kahn, R. A., Martonchik, J. V., Ackerman, T. P., Davies, R., Gerstl, S. A. W., Gordon, H. R., Muller, J., Myneni, R. B., Sellers, P. J., Pinty, B. and Verstraete, M. M.: Multi-angle Imaging SpectroRadiometer (MISR) instrument description and experiment overview, IEEE Trans. Geosci. Remote Sens., 36(4), 1072–1087, doi:10.1109/36.700992, 1998.

Diner, D. J., Beckert, J. C., Bothwell, G. W. and Rodriguez, J. I.: Performance of the MISR instrument during its first 20 months in Earth orbit, IEEE Trans. Geosci. Remote Sens., 40(7), 1449–1466, doi:10.1109/TGRS.2002.801584, 2002.

Diner, D. J., Braswell, B. H., Davies, R., Gobron, N., Hu, J., Jin, Y., Kahn, R. A., Knyazikhin, Y., Loeb, N., Muller, J.-P., Nolin, A. W., Pinty, B., Schaaf, C. B., Seiz, G. and Stroeve, J.: The value of multiangle measurements for retrieving structurally and radiatively consistent properties of clouds, aerosols, and surfaces, Remote Sens. Environ., 97(4), 495–518, doi:10.1016/J.RSE.2005.06.006, 2005.

Drury, E., Jacob, D. J., Spurr, R. J. D., Wang, J., Shinozuka, Y., Anderson, B. E., Clarke, A. D., Dibb, J., McNaughton, C. and Weber, R.: Synthesis of satellite (MODIS), aircraft (ICARTT), and surface (IMPROVE, EPA-AQS, AERONET) aerosol observations over eastern North America to improve MODIS aerosol retrievals and constrain surface aerosol concentrations and sources, J. Geophys. Res., 115(D14), D14204, doi:10.1029/2009JD012629, 2010.

Dubovik, O.: Optimization of Numerical Inversion in Photopolarimetric Remote Sensing, in Photopolarimetry in Remote Sensing, pp. 65–106, Kluwer Academic Publishers, Dordrecht., 2004.

Dubovik, O. and King, M. D.: A flexible inversion algorithm for retrieval of aerosol optical properties from Sun and sky radiance measurements, J. Geophys. Res. Atmos., 105(D16), 20673–20696, doi:10.1029/2000JD900282, 2000.

Dubovik, O., Smirnov, A., Holben, B. N., King, M. D., Kaufman, Y. J., Eck, T. F. and Slutsker, I.: Accuracy assessments of aerosol optical properties retrieved from Aerosol Robotic Network (AERONET) Sun and sky radiance measurements, J. Geophys. Res. Atmos., 105(D8), 9791–9806, doi:10.1029/2000JD900040, 2000.

Dubovik, O., Holben, B. N., Lapyonok, T., Sinyuk, A., Mishchenko, M. I., Yang, P. and Slutsker, I.: Non-spherical aerosol retrieval method employing light scattering by spheroids, Geophys. Res. Lett., 29(10), 54-1-54–4, doi:10.1029/2001GL014506, 2002a.

Dubovik, O., Holben, B., Eck, T. F., Smirnov, A., Kaufman, Y. J., King, M. D., Tanré, D. and Slutsker, I.: Variability of Absorption and Optical Properties of Key Aerosol Types Observed in Worldwide Locations, J. Atmos. Sci., 59(3), 590–608, doi:10.1175/1520-0469(2002)059<0590:VOAAOP>2.0.CO;2, 2002b.

Dubovik, O., Sinyuk, A., Lapyonok, T., Holben, B. N., Mishchenko, M., Yang, P., Eck, T. F., Volten, H., Muñoz, O., Veihelmann, B., van der Zande, W. J., Leon, J.-F., Sorokin, M. and Slutsker, I.: Application of spheroid models to account for aerosol particle nonsphericity in remote sensing of desert dust, J. Geophys. Res., 111(D11), D11208, doi:10.1029/2005JD006619, 2006.

Dubovik, O., Lapyonok, T., Kaufman, Y. J., Chin, M., Ginoux, P., Kahn, R. A. and Sinyuk, A.: Retrieving global aerosol sources from satellites using inverse modeling, Atmos. Chem. Phys., 8(2), 209–250, doi:10.5194/acp-8-209-2008, 2008.

Dubovik, O., Herman, M., Holdak, A., Lapyonok, T., Tanré, D., Deuzé, J. L., Ducos, F., Sinyuk, A. and Lopatin, A.: Statistically optimized inversion algorithm for enhanced retrieval of aerosol properties from spectral multi-angle polarimetric satellite observations, Atmos. Meas. Tech., 4(5), 975–1018, doi:10.5194/amt-4-975-2011, 2011.

Dubovik, O., Lapyonok, T., Litvinov, P., Herman, M., Fuertes, D., Ducos, F., Torres, B., Derimian, Y., Huang, X., Lopatin, A., Chaikovsky, A., Aspetsberger, M. and

Federspiel, C.: GRASP: a versatile algorithm for characterizing the atmosphere, SPIE Newsroom, doi:10.1117/2.1201408.005558, 2014.

Duncan, B. N., Martin, R. V., Staudt, A. C., Yevich, R. and Logan, J. A.: Interannual and seasonal variability of biomass burning emissions constrained by satellite observations, J. Geophys. Res., 108(D2), 4100, doi:10.1029/2002JD002378, 2003.

Ealo, M., Alastuey, A., Ripoll, A., Pérez, N., Cruz Minguillón, M., Querol, X. and Pandolfi, M.: Detection of Saharan dust and biomass burning events using near-real-time intensive aerosol optical properties in the north-western Mediterranean, Atmos. Chem. Phys, 16, 12567–12586, doi:10.5194/acp-16-12567-2016, 2016.

Eck, T. F., Holben, B. N., Reid, J. S., Dubovik, O., Smirnov, A., O'Neill, N. T., Slutsker, I. and Kinne, S.: Wavelength dependence of the optical depth of biomass burning, urban, and desert dust aerosols, J. Geophys. Res. Atmos., 104(D24), 31333–31349, doi:10.1029/1999JD900923, 1999.

Elbern, H. and Schmidt, H.: Ozone episode analysis by four-dimensional variational chemistry data assimilation, J. Geophys. Res. Atmos., 106(D4), 3569–3590, doi:10.1029/2000JD900448, 2001.

Elbern, H., Schmidt, H. and Ebel, A.: Variational data assimilation for tropospheric chemistry modeling, J. Geophys. Res. Atmos., 102(D13), 15967–15985, doi:10.1029/97JD01213, 1997.

Elbern, H., Schmidt, H., Talagrand, O. and Ebel, A.: 4D-variational data assimilation with an adjoint air quality model for emission analysis, Environ. Model. Softw., 15(6), 539–548, doi:10.1016/S1364-8152(00)00049-9, 2000.

Engelstaedter, S., Tegen, I. and Washington, R.: North African dust emissions and transport, Earth-Science Rev., 79(1), 73–100, doi:10.1016/j.earscirev.2006.06.004, 2006.

Enting, I. G.: Inverse Problems in Atmospheric Constituent Transport, Cambridge University Press., 2002.

Errico, R. M.: What Is an Adjoint Model?, Bull. Am. Meteorol. Soc., 78(11), 2577–2591, doi:10.1175/1520-0477(1997)078<2577:WIAAM>2.0.CO;2, 1997.

Escribano, J., Boucher, O., Chevallier, F. and Huneeus, N.: Subregional inversion of North African dust sources, J. Geophys. Res. Atmos., 121(14), 8549–8566, doi:10.1002/2016JD025020, 2016.

Escribano, J., Boucher, O., Chevallier, F. and Huneeus, N.: Impact of the choice of the satellite aerosol optical depth product in a sub-regional dust emission inversion, Atmos. Chem. Phys., 17(11), 7111–7126, doi:10.5194/acp-17-7111-2017, 2017.

Fairlie, T. D., Jacob, D. J. and Park, R. J.: The impact of transpacific transport of mineral dust in the United States, Atmos. Environ., 41(6), 1251–1266, doi:10.1016/j.atmosenv.2006.09.048, 2007.

Fedarenka, A., Dubovik, O., Goloub, P., Li, Z., Lapyonok, T., Litvinov, P., Barel, L., Gonzalez, L., Podvin, T. and Crozel, D.: Utilization of AERONET polarimetric measurements for improving retrieval of aerosol microphysics: GSFC, Beijing and Dakar data analysis, J. Quant. Spectrosc. Radiat. Transf., 179, 72–97, doi:10.1016/J.JQSRT.2016.03.021, 2016.

Feng, Y., Ramanathan, V. and Kotamarthi, V. R.: Brown carbon: a significant atmospheric absorber of solar radiation?, Atmos. Chem. Phys., 13(17), 8607–8621, doi:10.5194/acp-13-8607-2013, 2013.

Fisher, M. and Lary, D. J.: Lagrangian four-dimensional variational data assimilation of chemical species, Q. J. R. Meteorol. Soc., 121(527), 1681–1704, doi:10.1002/qj.49712152709, 1995.

Geogdzhayev, I. V., Mishchenko, M. I., Rossow, W. B., Cairns, B. and Lacis, A. A.: Global Two-Channel AVHRR Retrievals of Aerosol Properties over the Ocean for the Period of NOAA-9 Observations and Preliminary Retrievals Using NOAA-7 and NOAA-11 Data, J. Atmos. Sci., 59(3), 262–278, doi:10.1175/1520-0469(2002)059<0262:GTCARO>2.0.CO;2, 2002.

Ghan, S. J. and Schwartz, S. E.: Aerosol Properties and Processes: A Path from Field and Laboratory Measurements to Global Climate Models, Bull. Am. Meteorol. Soc., 88(7), 1059–1083, doi:10.1175/BAMS-88-7-1059, 2007.

Ginoux, P., Chin, M., Tegen, I., Prospero, J. M., Holben, B., Dubovik, O. and Lin, S.-J.: Sources and distributions of dust aerosols simulated with the GOCART model, J. Geophys. Res. Atmos., 106(D17), 20255–20273, doi:10.1029/2000JD000053, 2001.

Ginoux, P., Prospero, J. M., Gill, T. E., Hsu, N. C. and Zhao, M.: Global-scale attribution of anthropogenic and natural dust sources and their emission rates based on MODIS Deep Blue aerosol products, Rev. Geophys., 50(3), RG3005, doi:10.1029/2012RG000388, 2012.

Goloub, P., Tanré, D., Deuzé, J. L., Herman, M., Marchand, A. and Breon, F.-M.: Validation of the first algorithm applied for deriving the aerosol properties over the ocean using the POLDER/ADEOS measurements, IEEE Trans. Geosci. Remote Sens., 37(3), 1586–1596, doi:10.1109/36.763270, 1999.

Gong, S. L.: A parameterization of sea-salt aerosol source function for sub- and super-micron particles, Global Biogeochem. Cycles, 17(4), doi:10.1029/2003GB002079, 2003.

Hakami, A., Henze, D. K., Seinfeld, J. H., Chai, T., Tang, Y., Carmichael, G. R. and Sandu, A.: Adjoint inverse modeling of black carbon during the Asian Pacific

Regional Aerosol Characterization Experiment, J. Geophys. Res. Atmos., 110(D14), doi:10.1029/2004JD005671, 2005.

Hakami, A., Henze, D. K., Seinfeld, J. H., Singh, K., Sandu, A., Kim, S., Byun, D. and Li, Q.: The Adjoint of CMAQ, Environ. Sci. Technol., 41(22), 7807–7817, doi:10.1021/ES070944P, 2007.

Haywood, J. and Boucher, O.: Estimates of the direct and indirect radiative forcing due to tropospheric aerosols: A review, Rev. Geophys., 38(4), 513–543, doi:10.1029/1999RG000078, 2000.

He, C., Li, Q., Liou, K.-N., Qi, L., Tao, S. and Schwarz, J. P.: Microphysics-based black carbon aging in a global CTM: constraints from HIPPO observations and implications for global black carbon budget, Atmos. Chem. Phys., 16(5), 3077–3098, doi:10.5194/acp-16-3077-2016, 2016.

Henze, D. K., Hakami, A. and Seinfeld, J. H.: Development of the adjoint of GEOS-Chem, Atmos. Chem. Phys., 7(9), 2413–2433, doi:10.5194/acp-7-2413-2007, 2007.

Henze, D. K., Seinfeld, J. H. and Shindell, D. T.: Inverse modeling and mapping US air quality influences of inorganic PM2.5 precursor emissions using the adjoint of GEOS-Chem, Atmos. Chem. Phys., 9(16), 5877–5903, doi:10.5194/acp-9-5877-2009, 2009.

Herman, M., Deuzé, J. L., Devaux, C., Goloub, P., Bréon, F. M. and Tanré, D.: Remote sensing of aerosols over land surfaces including polarization measurements and application to POLDER measurements, J. Geophys. Res. Atmos., 102(D14), 17039–17049, doi:10.1029/96JD02109, 1997.

Herman, M., Deuzé, J. □L., Marchand, A., Roger, B. and Lallart, P.: Aerosol remote sensing from POLDER/ADEOS over the ocean: Improved retrieval using a nonspherical particle model, J. Geophys. Res., 110(D10), D10S02, doi:10.1029/2004JD004798, 2005.

Hess, M., Koepke, P. and Schult, I.: Optical Properties of Aerosols and Clouds: The Software Package OPAC, Bull. Am. Meteorol. Soc., 79(5), 831–844, doi:10.1175/1520-0477(1998)079<0831:OPOAAC>2.0.CO;2, 1998.

Highwood, E. J., Haywood, J. M., Silverstone, M. D., Newman, S. M. and Taylor, J. P.: Radiative properties and direct effect of Saharan dust measured by the C-130 aircraft during Saharan Dust Experiment (SHADE): 2. Terrestrial spectrum, J. Geophys. Res., 108(D18), 8578, doi:10.1029/2002JD002552, 2003.

Higurashi, A., Nakajima, T., Higurashi, A. and Nakajima, T.: Development of a Two-Channel Aerosol Retrieval Algorithm on a Global Scale Using NOAA AVHRR, J. Atmos. Sci., 56(7), 924–941, doi:10.1175/1520-0469(1999)056<0924:DOATCA>2.0.CO;2, 1999.

Holben, B. N., Eck, T. F., Slutsker, I., Tanré, D., Buis, J. P., Setzer, A., Vermote, E., Reagan, J. A., Kaufman, Y. J., Nakajima, T., Lavenu, F., Jankowiak, I. and Smirnov, A.: AERONET—A Federated Instrument Network and Data Archive for Aerosol Characterization, Remote Sens. Environ., 66(1), 1–16, doi:10.1016/S0034-4257(98)00031-5, 1998.

Holben, B. N., Eck, T. F., Slutsker, I., Smirnov, A., Sinyuk, A., Schafer, J., Giles, D. and Dubovik, O.: Aeronet's Version 2.0 quality assurance criteria, vol. 6408, edited by S.-C. Tsay, T. Nakajima, R. P. Singh, and R. Sridharan, p. 64080Q, International Society for Optics and Photonics., 2006.

Hsu, N. C., Tsay, S.-C., King, M. D. and Herman, J. R.: Aerosol Properties Over Bright-Reflecting Source Regions, IEEE Trans. Geosci. Remote Sens., 42(3), 557–569, doi:10.1109/TGRS.2004.824067, 2004.

Hsu, N. C., Tsay, S.-C., King, M. D. and Herman, J. R.: Deep Blue Retrievals of Asian Aerosol Properties During ACE-Asia, IEEE Trans. Geosci. Remote Sens., 44(11), 3180–3195, doi:10.1109/TGRS.2006.879540, 2006.

Huneeus, N., Boucher, O. and Chevallier, F.: Simplified aerosol modeling for variational data assimilation, Geosci. Model Dev., 2(2), 213–229, doi:10.5194/gmd-2-213-2009, 2009.

Huneeus, N., Schulz, M., Balkanski, Y., Griesfeller, J., Prospero, J., Kinne, S., Bauer, S., Boucher, O., Chin, M., Dentener, F., Diehl, T., Easter, R., Fillmore, D., Ghan, S., Ginoux, P., Grini, A., Horowitz, L., Koch, D., Krol, M. C., Landing, W., Liu, X., Mahowald, N., Miller, R., Morcrette, J. J., Myhre, G., Penner, J., Perlwitz, J., Stier, P., Takemura, T. and Zender, C. S.: Global dust model intercomparison in AeroCom phase i, Atmos. Chem. Phys., 11(15), 7781–7816, doi:10.5194/acp-11-7781-2011, 2011.

Huneeus, N., Chevallier, F. and Boucher, O.: Estimating aerosol emissions by assimilating observed aerosol optical depth in a global aerosol model, Atmos. Chem. Phys., 12(10), 4585–4606, doi:10.5194/acp-12-4585-2012, 2012.

Huneeus, N., Boucher, O. and Chevallier, F.: Atmospheric inversion of SO2 and primary aerosol emissions for the year 2010, Atmos. Chem. Phys., 13(13), 6555–6573, doi:10.5194/acp-13-6555-2013, 2013.

Husar, R. B., Prospero, J. M. and Stowe, L. L.: Characterization of tropospheric aerosols over the oceans with the NOAA advanced very high resolution radiometer optical thickness operational product, J. Geophys. Res. Atmos., 102(D14), 16889–16909, doi:10.1029/96JD04009, 1997.

Ichoku, C. and Ellison, L.: Global top-down smoke-aerosol emissions estimation using satellite fire radiative power measurements, Atmos. Chem. Phys., 14(13), 6643–6667, doi:10.5194/acp-14-6643-2014, 2014.

Ignatov, A., Stowe, L., Ignatov, A. and Stowe, L.: Physical Basis, Premises, and Self-Consistency Checks of Aerosol Retrievals from TRMM VIRS, J. Appl.

Meteorol., 39(12), 2259–2277, doi:10.1175/1520-0450(2001)040<2259:PBPASC>2.0.CO;2, 2000.

Intergovernmental Panel on Climate Change (IPCC), C. C. 2013: IPCC, Cambridge Univ. Press, Cambridge., 2013.

Jacob, D. J.: Introduction to Atmospheric Chemistry, Princeton University Press., 1999.

Jaeglé, L., Quinn, P. K., Bates, T. S., Alexander, B. and Lin, J.-T.: Global distribution of sea salt aerosols: new constraints from in situ and remote sensing observations, Atmos. Chem. Phys., 11(7), 3137–3157, doi:10.5194/acp-11-3137-2011, 2011.

Jäger, H. and Hofmann, D.: Midlatitude lidar backscatter to mass, area, and extinction conversion model based on in situ aerosol measurements from 1980 to 1987, Appl. Opt., 30(1), 127, doi:10.1364/AO.30.000127, 1991.

Jethva, H., Torres, O. and Ahn, C.: Global assessment of OMI aerosol single-scattering albedo using ground-based AERONET inversion, J. Geophys. Res. Atmos., 119(14), 9020–9040, doi:10.1002/2014JD021672, 2014.

Jo, D. S., Park, R. J., Lee, S., Kim, S.-W. and Zhang, X.: A global simulation of brown carbon: implications for photochemistry and direct radiative effect, Atmos. Chem. Phys., 16(5), 3413–3432, doi:10.5194/acp-16-3413-2016, 2016.

Johnson, B. T., Haywood, J. M., Langridge, J. M., Darbyshire, E., Morgan, W. T., Szpek, K., Brooke, J. K., Marenco, F., Coe, H., Artaxo, P., Longo, K. M., Mulcahy, J. P., Mann, G. W., Dalvi, M. and Bellouin, N.: Evaluation of biomass burning aerosols in the HadGEM3 climate model with observations from the SAMBBA field campaign, Atmos. Chem. Phys., 16(22), 14657–14685, doi:10.5194/acp-16-14657-2016, 2016.

Johnson, M. S., Meskhidze, N. and Praju Kiliyanpilakkil, V.: A global comparison of GEOS-Chem-predicted and remotely-sensed mineral dust aerosol optical depth and extinction profiles, J. Adv. Model. Earth Syst., 4(3), M07001, doi:10.1029/2011MS000109, 2012.

Kahn, R., Banerjee, P. and McDonald, D.: Sensitivity of multiangle imaging to natural mixtures of aerosols over ocean, J. Geophys. Res. Atmos., 106(D16), 18219–18238, doi:10.1029/2000JD900497, 2001.

Kahn, R. A., Gaitley, B. J., Martonchik, J. V., Diner, D. J., Crean, K. A. and Holben, B.: Multiangle Imaging Spectroradiometer (MISR) global aerosol optical depth validation based on 2 years of coincident Aerosol Robotic Network (AERONET) observations, J. Geophys. Res., 110(D10), D10S04, doi:10.1029/2004JD004706, 2005.

Kahn, R. A., Nelson, D. L., Garay, M. J., Levy, R. C., Bull, M. A., Diner, D. J., Martonchik, J. V., Paradise, S. R., Hansen, E. G. and Remer, L. A.: MISR

Aerosol Product Attributes and Statistical Comparisons With MODIS, IEEE Trans. Geosci. Remote Sens., 47(12), 4095–4114, doi:10.1109/TGRS.2009.2023115, 2009.

Kahn, R. A., Gaitley, B. J., Garay, M. J., Diner, D. J., Eck, T. F., Smirnov, A. and Holben, B. N.: Multiangle Imaging SpectroRadiometer global aerosol product assessment by comparison with the Aerosol Robotic Network, J. Geophys. Res., 115(D23), D23209, doi:10.1029/2010JD014601, 2010.

Kalashnikova, O. V. and Kahn, R.: Ability of multiangle remote sensing observations to identify and distinguish mineral dust types: 2. Sensitivity over dark water, J. Geophys. Res., 111(D11), D11207, doi:10.1029/2005JD006756, 2006.

Kalashnikova, O. V. and Kahn, R. A.: Mineral dust plume evolution over the Atlantic from MISR and MODIS aerosol retrievals, J. Geophys. Res., 113(D24), D24204, doi:10.1029/2008JD010083, 2008.

Kasten, F. and Young, A. T.: Revised optical air mass tables and approximation formula, Appl. Opt., 28(22), 4735, doi:10.1364/AO.28.004735, 1989.

Kaufman, Y. J., Tanré, D., Remer, L. A., Vermote, E. F., Chu, A. and Holben, B. N.: Operational remote sensing of tropospheric aerosol over land from EOS moderate resolution imaging spectroradiometer, doi.org, 102(D14), 17051–17067, doi:10.1029/96jd03988, 1997.

Kaufman, Y. J., Tanré, D. and Boucher, O.: A satellite view of aerosols in the climate system, Nature, 419(6903), 215–223, doi:10.1038/nature01091, 2002.

Kettle, A. J., Andreae, M. O., Amouroux, D., Andreae, T. W., Bates, T. S., Berresheim, H., Bingemer, H., Boniforti, R., Curran, M. A. J., DiTullio, G. R., Helas, G., Jones, G. B., Keller, M. D., Kiene, R. P., Leck, C., Levasseur, M., Malin, G., Maspero, M., Matrai, P., McTaggart, A. R., Mihalopoulos, N., Nguyen, B. C., Novo, A., Putaud, J. P., Rapsomanikis, S., Roberts, G., Schebeske, G., Sharma, S., Simó, R., Staubes, R., Turner, S. and Uher, G.: A global database of sea surface dimethylsulfide (DMS) measurements and a procedure to predict sea surface DMS as a function of latitude, longitude, and month, Global Biogeochem. Cycles, 13(2), 399–444, doi:10.1029/1999GB900004, 1999.

Kim, D., Wang, C., Ekman, A. M. L., Barth, M. C. and Rasch, P. J.: Distribution and direct radiative forcing of carbonaceous and sulfate aerosols in an interactive size-resolving aerosol–climate model, J. Geophys. Res., 113(D16), D16309, doi:10.1029/2007JD009756, 2008.

King, M. D., Kaufman, Y. J., Tanré, D. and Nakajima, T.: Remote Sensing of Tropospheric Aerosols from Space: Past, Present, and Future, Bull. Am. Meteorol. Soc., 80(11), 2229–2259, doi:10.1175/1520-0477(1999)080<2229:RSOTAF>2.0.CO;2, 1999.

Kinne, S., Lohmann, U., Feichter, J., Schulz, M., Timmreck, C., Ghan, S., Easter, R., Chin, M., Ginoux, P., Takemura, T., Tegen, I., Koch, D., Herzog, M., Penner, J., Pitari, G., Holben, B., Eck, T., Smirnov, A., Dubovik, O., Slutsker, I., Tanré, D., Torres, O., Mishchenko, M., Geogdzhayev, I., Chu, D. A. and Kaufman, Y.: Monthly averages of aerosol properties: A global comparison among models, satellite data, and AERONET ground data, J. Geophys. Res., 108(D20), 4634, doi:10.1029/2001JD001253, 2003.

Kinne, S., Schulz, M., Textor, C., Guibert, S., Balkanski, Y., Bauer, S. E., Berntsen, T., Berglen, T. F., Boucher, O., Chin, M., Collins, W., Dentener, F., Diehl, T., Easter, R., Feichter, J., Fillmore, D., Ghan, S., Ginoux, P., Gong, S., Grini, A., Hendricks, J., Herzog, M., Horowitz, L., Isaksen, I., Iversen, T., Kirkevåg, A., Kloster, S., Koch, D., Kristjansson, J. E., Krol, M., Lauer, A., Lamarque, J. F., Lesins, G., Liu, X., Lohmann, U., Montanaro, V., Myhre, G., Penner, J., Pitari, G., Reddy, S., Seland, O., Stier, P., Takemura, T. and Tie, X.: An AeroCom initial assessment – optical properties in aerosol component modules of global models, Atmos. Chem. Phys., 6(7), 1815–1834, doi:10.5194/acp-6-1815-2006, 2006.

Kleidman, R. G., O'Neill, N. T., Remer, L. A., Kaufman, Y. J., Eck, T. F., Tanré, D., Dubovik, O. and Holben, B. N.: Comparison of Moderate Resolution Imaging Spectroradiometer (MODIS) and Aerosol Robotic Network (AERONET) remote-sensing retrievals of aerosol fine mode fraction over ocean, J. Geophys. Res., 110(D22), D22205, doi:10.1029/2005JD005760, 2005.

Koch, D.: Transport and direct radiative forcing of carbonaceous and sulfate aerosols in the GISS GCM, J. Geophys. Res. Atmos., 106(D17), 20311–20332, doi:10.1029/2001JD900038, 2001.

Koch, D., Jacob, D., Tegen, I., Rind, D. and Chin, M.: Tropospheric sulfur simulation and sulfate direct radiative forcing in the Goddard Institute for Space Studies general circulation model, J. Geophys. Res. Atmos., 104(D19), 23799–23822, doi:10.1029/1999JD900248, 1999.

Koch, D., Schulz, M., Kinne, S., McNaughton, C., Spackman, J. R., Balkanski, Y., Bauer, S., Berntsen, T., Bond, T. C., Boucher, O., Chin, M., Clarke, A., De Luca, N., Dentener, F., Diehl, T., Dubovik, O., Easter, R., Fahey, D. W., Feichter, J., Fillmore, D., Freitag, S., Ghan, S., Ginoux, P., Gong, S., Horowitz, L., Iversen, T., Kirkevåg, A., Klimont, Z., Kondo, Y., Krol, M., Liu, X., Miller, R., Montanaro, V., Moteki, N., Myhre, G., Penner, J. E., Perlwitz, J., Pitari, G., Reddy, S., Sahu, L., Sakamoto, H., Schuster, G., Schwarz, J. P., Seland, Ø., Stier, P., Takegawa, N., Takemura, T., Textor, C., van Aardenne, J. A. and Zhao, Y.: Evaluation of black carbon estimations in global aerosol models, Atmos. Chem. Phys., 9(22), 9001–9026, doi:10.5194/acp-9-9001-2009, 2009.

Kok, J. F., Ridley, D. A., Zhou, Q., Miller, R. L., Zhao, C., Heald, C. L., Ward, D. S., Albani, S. and Haustein, K.: Smaller desert dust cooling effect estimated from analysis of dust size and abundance, Nat. Geosci., 10(4), 274–278, doi:10.1038/ngeo2912, 2017.

Kokhanovsky, A. A., Davis, A. B., Cairns, B., Dubovik, O., Hasekamp, O. P., Sano, I., Mukai, S., Rozanov, V. V., Litvinov, P., Lapyonok, T., Kolomiets, I. S., Oberemok, Y. A., Savenkov, S., Martin, W., Wasilewski, A., Di Noia, A., Stap, F. A., Rietjens, J., Xu, F., Natraj, V., Duan, M., Cheng, T. and Munro, R.: Space-based remote sensing of atmospheric aerosols: The multi-angle spectro-polarimetric frontier, Earth-Science Rev., 145, 85–116, doi:10.1016/j.earscirev.2015.01.012, 2015.

Kopacz, M., Jacob, D. J., Henze, D. K., Heald, C. L., Streets, D. G. and Zhang, Q.: Comparison of adjoint and analytical Bayesian inversion methods for constraining Asian sources of carbon monoxide using satellite (MOPITT) measurements of CO columns, J. Geophys. Res., 114(D4), D04305, doi:10.1029/2007JD009264, 2009.

Koepke P., Hess M., Schult I., and Shettle E. P.: Global aerosol dataset, Report N 243, Max-Plank-Institut für Meteorologie, Hamburg, 44 pp., September 1997.

Lack, D. A., Langridge, J. M., Bahreini, R., Cappa, C. D., Middlebrook, A. M. and Schwarz, J. P.: Brown carbon and internal mixing in biomass burning particles., Proc. Natl. Acad. Sci. U. S. A., 109(37), 14802–7, doi:10.1073/pnas.1206575109, 2012.

Lenoble, J., Remer, L. and Tanré, D.: Aerosol Remote Sensing, edited by J. Lenoble, L. Remer, and D. Tanré, Springer Berlin Heidelberg, Berlin, Heidelberg., 2013.

Levy, R. C., Remer, L. A., Mattoo, S., Vermote, E. F. and Kaufman, Y. J.: Second-generation operational algorithm: Retrieval of aerosol properties over land from inversion of Moderate Resolution Imaging Spectroradiometer spectral reflectance, J. Geophys. Res. Atmos., 112(D13), doi:10.1029/2006JD007811, 2007.

Levy, R. C., Remer, L. A., Kleidman, R. G., Mattoo, S., Ichoku, C., Kahn, R. and Eck, T. F.: Global evaluation of the Collection 5 MODIS dark-target aerosol products over land, Atmos. Chem. Phys., 10(21), 10399–10420, doi:10.5194/acp-10-10399-2010, 2010.

Levy, R. C., Mattoo, S., Munchak, L. A., Remer, L. A., Sayer, A. M., Patadia, F. and Hsu, N. C.: The Collection 6 MODIS aerosol products over land and ocean, Atmos. Meas. Tech., 6(11), 2989–3034, doi:10.5194/amt-6-2989-2013, 2013.

Li, J., Carlson, B. E. and Lacis, A. A.: A study on the temporal and spatial variability of absorbing aerosols using Total Ozone Mapping Spectrometer and Ozone Monitoring Instrument Aerosol Index data, J. Geophys. Res., 114(D9), D09213, doi:10.1029/2008JD011278, 2009a.

Li, R.-R., Remer, L., Kaufman, Y. J., Mattoo, S., Gao, B.-C. and Vermote, E.: Snow and Ice Mask for the MODIS Aerosol Products, IEEE Geosci. Remote Sens. Lett., 2(3), 306–310, doi:10.1109/LGRS.2005.847755, 2005.

Li, Z., Goloub, P., Dubovik, O., Blarel, L., Zhang, W., Podvin, T., Sinyuk, A., Sorokin, M., Chen, H., Holben, B., Tanré, D., Canini, M. and Buis, J.-P.: Improvements for ground-based remote sensing of atmospheric aerosol properties by additional polarimetric measurements, J. Quant. Spectrosc. Radiat. Transf., 110(17), 1954–1961, doi:10.1016/J.JQSRT.2009.04.009, 2009b.

Li, Z., Niu, F., Fan, J., Liu, Y., Rosenfeld, D. and Ding, Y.: Long-term impacts of aerosols on the vertical development of clouds and precipitation, Nat. Geosci., 4(12), 888–894, doi:10.1038/ngeo1313, 2011.

Li, Z., Gu, X., Wang, L., Li, D., Xie, Y., Li, K., Dubovik, O., Schuster, G., Goloub, P., Zhang, Y., Li, L., Ma, Y. and Xu, H.: Aerosol physical and chemical properties retrieved from ground-based remote sensing measurements during heavy haze days in Beijing winter, Atmos. Chem. Phys., 13(20), 10171–10183, doi:10.5194/acp-13-10171-2013, 2013.

Lin, J.-T. and McElroy, M. B.: Impacts of boundary layer mixing on pollutant vertical profiles in the lower troposphere: Implications to satellite remote sensing, Atmos. Environ., 44(14), 1726–1739, doi:10.1016/J.ATMOSENV.2010.02.009, 2010.

Lions, J.-L. (Jacques-L.: Optimal control of systems governed by partial differential equations, Springer-Verlag., 1971.

Liousse, C., Penner, J. E., Chuang, C., Walton, J. J., Eddleman, H. and Cachier, H.: A global three-dimensional model study of carbonaceous aerosols, J. Geophys. Res. Atmos., 101(D14), 19411–19432, doi:10.1029/95JD03426, 1996.

Liousse, C., Guillaume, B., Grégoire, J. M., Mallet, M., Galy, C., Pont, V., Akpo, A., Bedou, M., Castéra, P., Dungall, L., Gardrat, E., Granier, C., Konaré, A., Malavelle, F., Mariscal, A., Mieville, A., Rosset, R., Serça, D., Solmon, F., Tummon, F., Assamoi, E., Yoboué, V. and Van Velthoven, P.: Updated African biomass burning emission inventories in the framework of the AMMA-IDAF program, with an evaluation of combustion aerosols, Atmos. Chem. Phys., 10(19), 9631–9646, doi:10.5194/acp-10-9631-2010, 2010.

Liu, D., Whitehead, J., Alfarra, M. R., Reyes-Villegas, E., Spracklen, D. V., Reddington, C. L., Kong, S., Williams, P. I., Ting, Y.-C., Haslett, S., Taylor, J. W., Flynn, M. J., Morgan, W. T., McFiggans, G., Coe, H. and Allan, J. D.: Black-carbon absorption enhancement in the atmosphere determined by particle mixing state, Nat. Geosci., 10(3), 184–188, doi:10.1038/ngeo2901, 2017.

Liu, H., Jacob, D. J., Bey, I. and Yantosca, R. M.: Constraints from 210 Pb and 7 Be on wet deposition and transport in a global three-dimensional chemical tracer model driven by assimilated meteorological fields, J. Geophys. Res. Atmos., 106(D11), 12109–12128, doi:10.1029/2000JD900839, 2001.

Lopatin, A., Dubovik, O., Chaikovsky, A., Goloub, P., Lapyonok, T., Tanré, D. and Litvinov, P.: Enhancement of aerosol characterization using synergy of lidar and

sun-photometer coincident observations: the GARRLiC algorithm, Atmos. Meas. Tech., 6(8), 2065–2088, doi:10.5194/amt-6-2065-2013, 2013.

Lyapustin, A., Wang, Y., Laszlo, I., Kahn, R., Korkin, S., Remer, L., Levy, R. and Reid, J. S.: Multiangle implementation of atmospheric correction (MAIAC): 2. Aerosol algorithm, J. Geophys. Res., 116(D3), D03211, doi:10.1029/2010JD014986, 2011a.

Lyapustin, A. I., Martonchik, J. V., Wang, Y., Laszlo, I. and Korkin, S.: Multiangle implementation of atmospheric correction (MAIAC): 1. Radiative transfer basis and look-up tables, J. Geophys. Res., 116(D3), D03210, doi:10.1029/2010JD014985, 2011b.

Lyapustin, A. I., Wang, Y., Laszlo, I., Hilker, T., Hall, F. G., Seller, P. J., Tucker, C. J. and Korin, S. V.: Multi-angle implementation of atmospheric correction for MODIS (MAIAC): 3. Atmospheric correction, Remote Sens. Environ., 127, 385–393, doi:10.1016/J.RSE.2012.09.002, 2012.

Marchuk, G.: Numerical solution of the problems of the dynamics of the atmosphere and the ocean (In Russian), Gidrometeoizdat., 1974.

Martien, P. T., Harley, R. A. and Cacuci, D. G.: Adjoint Sensitivity Analysis for a Three-Dimensional Photochemical Model: Implementation and Method Comparison, Environ. Sci. Technol., 40(8), 2663–2670, doi:10.1021/ES0510257, 2006.

Martin, R. V., Chance, K., Jacob, D. J., Kurosu, T. P., Spurr, R. J. D., Bucsela, E., Gleason, J. F., Palmer, P. I., Bey, I., Fiore, A. M., Li, Q., Yantosca, R. M. and Koelemeijer, R. B. A.: An improved retrieval of tropospheric nitrogen dioxide from GOME, J. Geophys. Res., 107(D20), 4437, doi:10.1029/2001JD001027, 2002.

Martin, R. V., Jacob, D. J., Yantosca, R. M., Chin, M. and Ginoux, P.: Global and regional decreases in tropospheric oxidants from photochemical effects of aerosols, J. Geophys. Res. Atmos., 108(D3), 4097, doi:10.1029/2002JD002622, 2003.

Martins, J. V., Tanré, D., Remer, L., Kaufman, Y., Mattoo, S. and Levy, R.: MODIS Cloud screening for remote sensing of aerosols over oceans using spatial variability, Geophys. Res. Lett., 29(12), 8009, doi:10.1029/2001GL013252, 2002.

Martonchik, J. V., Diner, D. J., Kahn, R. A., Ackerman, T. P., Verstraete, M. M., Pinty, B. and Gordon, H. R.: Techniques for the retrieval of aerosol properties over land and ocean using multiangle imaging, IEEE Trans. Geosci. Remote Sens., 36(4), 1212–1227, doi:10.1109/36.701027, 1998.

Martonchik, J. V., Diner, D. J., Crean, K. A. and Bull, M. A.: Regional aerosol retrieval results from MISR, IEEE Trans. Geosci. Remote Sens., 40(7), 1520–1531, doi:10.1109/TGRS.2002.801142, 2002.

Meland, B. S., Xu, X., Henze, D. K. and Wang, J.: Assessing remote polarimetric measurement sensitivities to aerosol emissions using the geos-chem adjoint model, Atmos. Meas. Tech., 6(12), 3441–3457, doi:10.5194/amt-6-3441-2013, 2013.

Menut, L.: Adjoint modeling for atmospheric pollution process sensitivity at regional scale, J. Geophys. Res., 108(D17), 8562, doi:10.1029/2002JD002549, 2003.

Miller, R. L., Tegen, I. and Perlwitz, J.: Surface radiative forcing by soil dust aerosols and the hydrologic cycle, J. Geophys. Res. Atmos., 109(D4), doi:10.1029/2003JD004085, 2004.

Mishchenko, M. I., Geogdzhayev, I. V., Cairns, B., Rossow, W. B. and Lacis, A. A.: Aerosol retrievals over the ocean by use of channels 1 and 2 AVHRR data: sensitivity analysis and preliminary results, Appl. Opt., 38(36), 7325, doi:10.1364/AO.38.007325, 1999.

Mishchenko, M. I., Cairns, B., Hansen, J. E., Travis, L. D., Kopp, G., Schueler, C. F., Fafaul, B. A., Hooker, R. J., Maring, H. B., Itchkawich, T., Mishchenko, M. I., Cairns, B., Hansen, J. E., Travis, L. D., Kopp, G., Schueler, C. F., Fafaul, B. A., Hooker, R. J., Maring, H. B. and Itchkawich, T.: Accurate Monitoring of Terrestrial Aerosols and Total Solar Irradiance: Introducing the Glory Mission, Bull. Am. Meteorol. Soc., 88(5), 677–691, doi:10.1175/BAMS-88-5-677, 2007.

Monahan, E. C., Spiel, D. E. and Davidson, K. L.: A Model of Marine Aerosol Generation Via Whitecaps and Wave Disruption, pp. 167–174, Springer, Dordrecht., 1986.

Monks, P. S., Granier, C., Fuzzi, S., Stohl, A., Williams, M. L., Akimoto, H., Amann, M., Baklanov, A., Baltensperger, U., Bey, I., Blake, N., Blake, R. S., Carslaw, K., Cooper, O. R., Dentener, F., Fowler, D., Fragkou, E., Frost, G. J., Generoso, S., Ginoux, P., Grewe, V., Guenther, A., Hansson, H. C., Henne, S., Hjorth, J., Hofzumahaus, A., Huntrieser, H., Isaksen, I. S. A., Jenkin, M. E., Kaiser, J., Kanakidou, M., Klimont, Z., Kulmala, M., Laj, P., Lawrence, M. G., Lee, J. D., Liousse, C., Maione, M., McFiggans, G., Metzger, A., Mieville, A., Moussiopoulos, N., Orlando, J. J., O'Dowd, C. D., Palmer, P. I., Parrish, D. D., Petzold, A., Platt, U., Pöschl, U., Prévôt, A. S. H., Reeves, C. E., Reimann, S., Rudich, Y., Sellegri, K., Steinbrecher, R., Simpson, D., ten Brink, H., Theloke, J., van der Werf, G. R., Vautard, R., Vestreng, V., Vlachokostas, C. and von Glasow, R.: Atmospheric composition change – global and regional air quality, Atmos. Environ., 43(33), 5268–5350, doi:10.1016/j.atmosenv.2009.08.021, 2009.

Moulin, C. and Chiapello, I.: Evidence of the control of summer atmospheric transport of African dust over the Atlantic by Sahel sources from TOMS satellites (1979-2000), Geophys. Res. Lett., 31(2), doi:10.1029/2003GL018931, 2004.

Müller, J.-F. and Stavrakou, T.: Inversion of CO and NOx emissions using the adjoint of the IMAGES model, Atmos. Chem. Phys., 5(5), 1157–1186, doi:10.5194/acp-5-1157-2005, 2005.

Myhre, G., Shindell, D., Bréon, F.-M., Collins, W., Fuglestvedt, J., Huang, J., Koch, D., Lamarque, J.-F., Lee, D., Mendoza, B., Nakajima, T., Robock, A., Stephens, G., Takemura, T. and Zhang, H.: Anthropogenic and Natural Radiative Forcing, in Contribution of Working Group I to the Fifth Assessment Report of the Intergovernmental Panel on Climate Change [Stocker, T.F., D. Qin, G.-K. Plattner, M. Tignor, S.K. Allen, J. Boschung, A. Nauels, Y. Xia, V. Bex and P.M. Midgley (eds.)], Cambridge University Press, Cambridge, United Kindom and New York, NY, USA. [online] Available from: https://www.ipcc.ch/pdf/assessment-report/ar5/wg1/WG1AR5_Chapter08_FINAL.pdf, 2013.

Nester, K. and Panitz, H.-J.: Sensitivity analysis by the adjoint chemistry transport model DRAISfor an episode in the Berlin Ozone (BERLIOZ) experiment, Atmos. Chem. Phys., 6(8), 2091–2106, doi:10.5194/acp-6-2091-2006, 2006.

Park, R. J., Jacob, D. J., Chin, M. and Martin, R. V.: Sources of carbonaceous aerosols over the United States and implications for natural visibility, J. Geophys. Res., 108(D12), 4355, doi:10.1029/2002JD003190, 2003.

Park, R. J., Jacob, D. J., Field, B. D., Yantosca, R. M. and Chin, M.: Natural and transboundary pollution influences on sulfate-nitrate-ammonium aerosols in the United States: Implications for policy, J. Geophys. Res., 109(D15), D15204, doi:10.1029/2003JD004473, 2004.

Penner, J. E., Eddleman, H. and Novakov, T.: Towards the development of a global inventory for black carbon emissions, Atmos. Environ., 27(8), 1277–1295, doi:10.1016/0960-1686(93)90255-W, 1993.

Penning de Vries, M. J. M., Beirle, S., Hörmann, C., Kaiser, J. W., Stammes, P., Tilstra, L. G., Tuinder, O. N. E. and Wagner, T.: A global aerosol classification algorithm incorporating multiple satellite data sets of aerosol and trace gas abundances, Atmos. Chem. Phys., 15(18), 10597–10618, doi:10.5194/acp-15-10597-2015, 2015.

Philip T. Martien, P. T. and Harley, R. A.: Adjoint Sensitivity Analysis for a Three-Dimensional Photochemical Model: Application to Southern California, Environ. Sci. Technol., 40(13), 4200–4210, doi:10.1021/ES051026Z, 2006.

Popp, T., de Leeuw, G., Bingen, C., Brühl, C., Capelle, V., Chedin, A., Clarisse, L., Dubovik, O., Grainger, R., Griesfeller, J., Heckel, A., Kinne, S., Klüser, L., Kosmale, M., Kolmonen, P., Lelli, L., Litvinov, P., Mei, L., North, P., Pinnock, S., Povey, A., Robert, C., Schulz, M., Sogacheva, L., Stebel, K., Stein Zweers, D., Thomas, G., Tilstra, L., Vandenbussche, S., Veefkind, P., Vountas, M. and Xue, Y.: Development, Production and Evaluation of Aerosol Climate Data Records from European Satellite Observations (Aerosol_cci), Remote Sens., 8(5), 421, doi:10.3390/rs8050421, 2016.

Prospero, J. M. and Lamb, P. J.: African Droughts and Dust Transport to the Caribbean: Climate Change Implications, Science (80-.)., 302(5647), 1024–1027, 2003.

Pye, H. O. T., Liao, H., Wu, S., Mickley, L. J., Jacob, D. J., Henze, D. K. and Seinfeld, J. H.: Effect of changes in climate and emissions on future sulfate-nitrate-ammonium aerosol levels in the United States, J. Geophys. Res., 114(D1), D01205, doi:10.1029/2008JD010701, 2009.

Quélo, D., Mallet, V. and Sportisse, B.: Inverse modeling of NOx emissions at regional scale over northern France: Preliminary investigation of the second-order sensitivity, J. Geophys. Res., 110(D24), D24310, doi:10.1029/2005JD006151, 2005.

Ramanathan, V., Crutzen, P. J., Kiehl, J. T. and Rosenfeld, D.: Aerosols, Climate, and the Hydrological Cycle, Science (80-.)., 294(5549), 2001.

Randerson, J. T., van der Werf, G. R., L. Giglio, Collatz, G. J. and Kasibhatla, P. S.: Global Fire Emissions Database, Version 3.1, , doi:doi:10.3334/ORNLDAAC/1191, 2013.

Remer, L. A., Tanré, D., Kaufman, Y. J., Ichoku, C., Mattoo, S., Levy, R., Chu, D. A., Holben, B., Dubovik, O., Smirnov, A., Martins, J. V., Li, R. □R. and Ahmad, Z.: Validation of MODIS aerosol retrieval over ocean, Geophys. Res. Lett., 29(12), 8008, doi:10.1029/2001GL013204, 2002.

Remer, L. A., Kaufman, Y. J., Tanré, D., Mattoo, S., Chu, D. A., Martins, J. V., Li, R.-R., Ichoku, C., Levy, R. C., Kleidman, R. G., Eck, T. F., Vermote, E., Holben, B. N., Remer, L. A., Kaufman, Y. J., Tanré, D., Mattoo, S., Chu, D. A., Martins, J. V., Li, R.-R., Ichoku, C., Levy, R. C., Kleidman, R. G., Eck, T. F., Vermote, E. and Holben, B. N.: The MODIS Aerosol Algorithm, Products, and Validation, J. Atmos. Sci., 62(4), 947–973, doi:10.1175/JAS3385.1, 2005.

Ridley, D. A., Heald, C. L. and Ford, B.: North African dust export and deposition: A satellite and model perspective, J. Geophys. Res. Atmos., 117(D2), doi:10.1029/2011JD016794, 2012.

Ridley, D. A., Heald, C. L., Kok, J. F. and Zhao, C.: An observationally constrained estimate of global dust aerosol optical depth, Atmos. Chem. Phys., 16(23), 15097–15117, doi:10.5194/acp-16-15097-2016, 2016.

Roeckner, E., Arpe, K., Bengtsson, L., Christoph, M., Claussen, M., Duemenil, L., Esch, M., Giorgetta, M., Schlese, U. and Schulzweida, U.: The atmospheric general circulation model ECHAM-4: Model description and simulation of present-day climate, Hamburg, Germany., 1996.

Roeckner, E., Bäuml, G. and Kirchner, I.: The atmospheric general circulation model ECHAM-5: Model description, Hamburg, Germany., 2003.

Sandu, A., Liao, W., Carmichael, G. R., Henze, D. K. and Seinfeld, J. H.: Inverse Modeling of Aerosol Dynamics Using Adjoints: Theoretical and Numerical Considerations, Aerosol Sci. Technol., 39(8), 677–694, doi:10.1080/02786820500182289, 2005.

Sato, M., Hansen, J., Koch, D., Lacis, A., Ruedy, R., Dubovik, O., Holben, B., Chin, M. and Novakov, T.: Global atmospheric black carbon inferred from AERONET., Proc. Natl. Acad. Sci. U. S. A., 100(11), 6319–6324, doi:10.1073/pnas.0731897100, 2003.

Schuster, G. L., Dubovik, O., Holben, B. N. and Clothiaux, E. E.: Inferring black carbon content and specific absorption from Aerosol Robotic Network (AERONET) aerosol retrievals, J. Geophys. Res., 110(D10), D10S17, doi:10.1029/2004JD004548, 2005.

Schuster, G. L., Dubovik, O. and Holben, B. N.: Angstrom exponent and bimodal aerosol size distributions, J. Geophys. Res., 111(D7), D07207, doi:10.1029/2005JD006328, 2006.

Seinfeld, J. H. and Pandis, S. N.: Atmospheric chemistry and physics : from air pollution to climate change, edited by John Wiley & Sons., 2016.

Smirnov, A., Holben, B. N., Eck, T. F., Dubovik, O. and Slutsker, I.: Cloud-Screening and Quality Control Algorithms for the AERONET Database, Remote Sens. Environ., 73(3), 337–349, doi:10.1016/S0034-4257(00)00109-7, 2000.

Smirnov, A., Holben, B. N., Giles, D. M., Slutsker, I., O 'neill, N. T., Eck, T. F., Macke, A. and Croot, P.: Maritime aerosol network as a component of AERONET – first results and comparison with global aerosol models and satellite retrievals, Atmos. Meas. Tech, 4, 583–597, doi:10.5194/amt-4-583-2011, 2011.

Stevens, B., Giorgetta, M., Esch, M., Mauritsen, T., Crueger, T., Rast, S., Salzmann, M., Schmidt, H., Bader, J., Block, K., Brokopf, R., Fast, I., Kinne, S., Kornblueh, L., Lohmann, U., Pincus, R., Reichler, T. and Roeckner, E.: Atmospheric component of the MPI□M Earth System Model: ECHAM6, J. Adv. Model. Earth Syst., 5(2), 146–172, doi:10.1002/JAME.20015, 2013.

Streets, D. G., Bond, T. C., Carmichael, G. R., Fernandes, S. D., Fu, Q., He, D., Klimont, Z., Nelson, S. M., Tsai, N. Y., Wang, M. Q., Woo, J.-H. and Yarber, K. F.: An inventory of gaseous and primary aerosol emissions in Asia in the year 2000, J. Geophys. Res. Atmos., 108(D21), doi:10.1029/2002JD003093, 2003.

Streets, D. G., Zhang, Q., Wang, L., He, K., Hao, J., Wu, Y., Tang, Y. and Carmichael, G. R.: Revisiting China's CO emissions after the Transport and Chemical Evolution over the Pacific (TRACE-P) mission: Synthesis of inventories, atmospheric modeling, and observations, J. Geophys. Res., 111(D14), D14306, doi:10.1029/2006JD007118, 2006.

Takemura, T., Nozawa, T., Emori, S., Nakajima, T. Y. and Nakajima, T.: Simulation of climate response to aerosol direct and indirect effects with aerosol transport-radiation model, J. Geophys. Res., 110(D2), D02202, doi:10.1029/2004JD005029, 2005.

Talagrand, O. and Courtier, P.: Variational Assimilation of Meteorological Observations With the Adjoint Vorticity Equation. I: Theory, Q. J. R. Meteorol. Soc., 113(478), 1311–1328, doi:10.1002/qj.49711347812, 1987.

Tanré, D., Bréon, F. M., Deuzé, J. L., Dubovik, O., Ducos, F., François, P., Goloub, P., Herman, M., Lifermann, A. and Waquet, F.: Remote sensing of aerosols by using polarized, directional and spectral measurements within the A-Train: the PARASOL mission, Atmos. Meas. Tech., 4(7), 1383–1395, doi:10.5194/amt-4-1383-2011, 2011.

Tegen, I. and Lacis, A. A.: Modeling of particle size distribution and its influence on the radiative properties of mineral dust aerosol, J. Geophys. Res. Atmos., 101(D14), 19237–19244, doi:10.1029/95JD03610, 1996.

Tegen, I., Koch, D., Lacis, A. A. and Sato, M.: Trends in tropospheric aerosol loads and corresponding impact on direct radiative forcing between 1950 and 1990: A model study, J. Geophys. Res. Atmos., 105(D22), 26971–26989, doi:10.1029/2000JD900280, 2000.

Textor, C., Schulz, M., Guibert, S., Kinne, S., Balkanski, Y., Bauer, S., Berntsen, T., Berglen, T., Boucher, O., Chin, M., Dentener, F., Diehl, T., Easter, R., Feichter, H., Fillmore, D., Ghan, S., Ginoux, P., Gong, S., Grini, A., Hendricks, J., Horowitz, L., Huang, P., Isaksen, I., Iversen, I., Kloster, S., Koch, D., Kirkevåg, A., Kristjansson, J. E., Krol, M., Lauer, A., Lamarque, J. F., Liu, X., Montanaro, V., Myhre, G., Penner, J., Pitari, G., Reddy, S., Seland, Ø., Stier, P., Takemura, T. and Tie, X.: Analysis and quantification of the diversities of aerosol life cycles within AeroCom, Atmos. Chem. Phys., 6(7), 1777–1813, doi:10.5194/acp-6-1777-2006, 2006.

Toledano, C., Cachorro, V. E., Berjon, A., de Frutos, A. M., Sorribas, M., de la Morena, B. A. and Goloub, P.: Aerosol optical depth and Ångström exponent climatology at El Arenosillo AERONET site (Huelva, Spain), Q. J. R. Meteorol. Soc., 133(624), 795–807, doi:10.1002/qj.54, 2007.

Torres, O., Bhartia, P. K., Herman, J. R., Ahmad, Z. and Gleason, J.: Derivation of aerosol properties from satellite measurements of backscattered ultraviolet radiation: Theoretical basis, J. Geophys. Res. Atmos., 103(D14), 17099–17110, doi:10.1029/98JD00900, 1998.

Torres, O., Bhartia, P. K., Herman, J. R., Sinyuk, A., Ginoux, P., Holben, B., Torres, O., Bhartia, P. K., Herman, J. R., Sinyuk, A., Ginoux, P. and Holben, B.: A Long-Term Record of Aerosol Optical Depth from TOMS Observations and Comparison to AERONET Measurements, J. Atmos. Sci., 59(3), 398–413, doi:10.1175/1520-0469(2002)059<0398:ALTROA>2.0.CO;2, 2002.

Torres, O., Tanskanen, A., Veihelmann, B., Ahn, C., Braak, R., Bhartia, P. K., Veefkind, P. and Levelt, P.: Aerosols and surface UV products from Ozone Monitoring Instrument observations: An overview, J. Geophys. Res., 112(D24), D24S47, doi:10.1029/2007JD008809, 2007.

Torres, O., Ahn, C. and Chen, Z.: Improvements to the OMI near-UV aerosol algorithm using A-train CALIOP and AIRS observations, Atmos. Meas. Tech., 6(11), 3257–3270, doi:10.5194/AMT-6-3257-2013, 2013.

Twomey, S.: Pollution and the planetary albedo, Atmos. Environ., 8(12), 1251–1256, doi:10.1016/0004-6981(74)90004-3, 1974.

Twomey, S.: The Influence of Pollution on the Shortwave Albedo of Clouds, J. Atmos. Sci., doi:10.1175/1520-0469(1977)034<1149:TIOPOT>2.0.CO;2, 1977.

Vautard, R., Beekmann, M. and Menut, L.: Applications of adjoint modelling in atmospheric chemistry: sensitivity and inverse modelling, Environ. Model. Softw., 15(6–7), 703–709, doi:10.1016/S1364-8152(00)00058-X, 2000.

Veihelmann, B., Levelt, P. F., Stammes, P. and Veefkind, J. P.: Simulation study of the aerosol information content in OMI spectral reflectance measurements, Atmos. Chem. Phys., 7(12), 3115–3127, doi:10.5194/acp-7-3115-2007, 2007.

Vukićević, T. and Hess, P.: Analysis of tropospheric transport in the Pacific Basin using the adjoint technique, J. Geophys. Res. Atmos., 105(D6), 7213–7230, doi:10.1029/1999JD901110, 2000.

Wang, J., Cubison, M. J., Aiken, A. C., Jimenez, J. L. and Collins, D. R.: The importance of aerosol mixing state and size-resolved composition on CCN concentration and the variation of the importance with atmospheric aging of aerosols, Atmos. Chem. Phys., 10(15), 7267–7283, doi:10.5194/acp-10-7267-2010, 2010.

Wang, J., Xu, X., Henze, D. K., Zeng, J., Ji, Q., Tsay, S.-C. and Huang, J.: Top-down estimate of dust emissions through integration of MODIS and MISR aerosol retrievals with the GEOS-Chem adjoint model, Geophys. Res. Lett., 39(8), L08802, doi:10.1029/2012GL051136, 2012.

Wang, Q., Jacob, D. J., Fisher, J. A., Mao, J., Leibensperger, E. M., Carouge, C. C., Le Sager, P., Kondo, Y., Jimenez, J. L., Cubison, M. J. and Doherty, S. J.: Sources of carbonaceous aerosols and deposited black carbon in the Arctic in winter-spring: implications for radiative forcing, Atmos. Chem. Phys., 11(23), 12453–12473, doi:10.5194/acp-11-12453-2011, 2011.

Wang, R., Tao, S., Balkanski, Y., Ciais, P., Boucher, O., Liu, J., Piao, S., Shen, H., Vuolo, M. R., Valari, M., Chen, H., Chen, Y., Cozic, A., Huang, Y., Li, B., Li, W., Shen, G., Wang, B. and Zhang, Y.: Exposure to ambient black carbon derived from a unique inventory and high-resolution model., Proc. Natl. Acad. Sci. U. S. A., 111(7), 2459–63, doi:10.1073/pnas.1318763111, 2014a.

Wang, R., Balkanski, Y., Boucher, O., Ciais, P., Schuster, G. L., Chevallier, F., Samset, B. H., Liu, J., Piao, S., Valari, M. and Tao, S.: Estimation of global black carbon direct radiative forcing and its uncertainty constrained by observations, J. Geophys. Res. Atmos., 121(10), 5948–5971, doi:10.1002/2015JD024326, 2016.

Wang, X., Heald, C. L., Ridley, D. A., Schwarz, J. P., Spackman, J. R., Perring, A. E., Coe, H., Liu, D. and Clarke, A. D.: Exploiting simultaneous observational constraints on mass and absorption to estimate the global direct radiative forcing of black carbon and brown carbon, Atmos. Chem. Phys., 14(20), 10989–11010, doi:10.5194/acp-14-10989-2014, 2014b.

Wang, Y., Jacob, D. J. and Logan, J. A.: Global simulation of tropospheric O3-NOx hydrocarbon chemistry: 3. Origin of tropospheric ozone and effects of nonmethane hydrocarbons, J. Geophys. Res. Atmos., 103(D9), 10757–10767, doi:10.1029/98JD00156, 1998.

Watson, J. G., Zhu, T., Chow, J. C., Engelbrecht, J., Fujita, E. M. and Wilson, W. E.: Receptor modeling application framework for particle source apportionment, Chemosphere, 49(9), 1093–1136, doi:10.1016/S0045-6535(02)00243-6, 2002.

van der Werf, G. R., Randerson, J. T., Giglio, L., Collatz, G. J., Kasibhatla, P. S. and Arellano, A. F.: Interannual variability in global biomass burning emissions from 1997 to 2004, Atmos. Chem. Phys., 6(11), 3423–3441, doi:10.5194/acp-6-3423-2006, 2006.

van der Werf, G. R., Randerson, J. T., Giglio, L., Collatz, G. J., Mu, M., Kasibhatla, P. S., Morton, D. C., DeFries, R. S., Jin, Y. and van Leeuwen, T. T.: Global fire emissions and the contribution of deforestation, savanna, forest, agricultural, and peat fires (1997–2009), Atmos. Chem. Phys., 10(23), 11707–11735, doi:10.5194/acp-10-11707-2010, 2010.

Werner, M., Tegen, I., Harrison, S. P., Kohfeld, K. E., Prentice, I. C., Balkanski, Y., Rodhe, H. and Roelandt, C.: Seasonal and interannual variability of the mineral dust cycle under present and glacial climate conditions, J. Geophys. Res., 107(D24), 4744, doi:10.1029/2002JD002365, 2002.

Wesely, M. L.: Parameterization of surface resistances to gaseous dry deposition in regional-scale numerical models, Atmos. Environ., 23(6), 1293–1304, doi:10.1016/0004-6981(89)90153-4, 1989.

WHO: Ambient air pollution - A global assessment of exposure and burden of disease, World Health Organization, Geneva, Switzerland. [online] Available from: http://who.int/phe/publications/air-pollution-global-assessment/en/, 2016.

Xu, X. and Wang, J.: Retrieval of aerosol microphysical properties from AERONET photopolarimetric measurements: 1. Information content analysis, J. Geophys. Res. Atmos., 120(14), 7059–7078, doi:10.1002/2015JD023108, 2015.

Xu, X., Wang, J., Henze, D. K., Qu, W. and Kopacz, M.: Constraints on aerosol sources using GEOS-Chem adjoint and MODIS radiances, and evaluation with multisensor (OMI, MISR) data, J. Geophys. Res. Atmos., 118(12), 6396–6413, doi:10.1002/jgrd.50515, 2013.

Xu, X., Wang, J., Zeng, J., Spurr, R., Liu, X., Dubovik, O., Li, L., Li, Z., Mishchenko, M. I., Siniuk, A. and Holben, B. N.: Retrieval of aerosol microphysical properties from AERONET photopolarimetric measurements: 2. A new research algorithm and case demonstration, J. Geophys. Res. Atmos., 120(14), 7079–7098, doi:10.1002/2015JD023113, 2015.

Yu, H., Zhang, Y., Chin, M., Liu, Z., Omar, A., Remer, L. A., Yang, Y., Yuan, T. and Zhang, J.: An integrated analysis of aerosol above clouds from A-Train multi-sensor measurements, Remote Sens. Environ., 121, 125–131, doi:10.1016/J.RSE.2012.01.011, 2012.

Yu, H., Remer, L. A., Kahn, R. A., Chin, M. and Zhang, Y.: Satellite perspective of aerosol intercontinental transport: From qualitative tracking to quantitative characterization, Atmos. Res., 124, 73–100, doi:10.1016/J.ATMOSRES.2012.12.013, 2013.

Zender, C. S., Bian, H. and Newman, D.: Mineral Dust Entrainment and Deposition (DEAD) model: Description and 1990s dust climatology, J. Geophys. Res., 108(D14), 4416, doi:10.1029/2002JD002775, 2003.

Zhang, L., Gong, S., Padro, J. and Barrie, L.: A size-segregated particle dry deposition scheme for an atmospheric aerosol module, Atmos. Environ., 35(3), 549–560, doi:10.1016/S1352-2310(00)00326-5, 2001.

Zhang, L., Jacob, D. J., Kopacz, M., Henze, D. K., Singh, K. and Jaffe, D. A.: Intercontinental source attribution of ozone pollution at western U.S. sites using an adjoint method, Geophys. Res. Lett., 36(11), L11810, doi:10.1029/2009GL037950, 2009.

Zhang, L., Kok, J. F., Henze, D. K., Li, Q. and Zhao, C.: Improving simulations of fine dust surface concentrations over the western United States by optimizing the particle size distribution, Geophys. Res. Lett., 40(12), 3270–3275, doi:10.1002/grl.50591, 2013.

Zhang, L., Henze, D. K., Grell, G. A., Carmichael, G. R., Bousserez, N., Zhang, Q., Torres, O., Ahn, C., Lu, Z., Cao, J. and Mao, Y.: Constraining black carbon aerosol over Asia using OMI aerosol absorption optical depth and the adjoint of GEOS-Chem, Atmos. Chem. Phys., 15(18), 10281–10308, doi:10.5194/acp-15-10281-2015, 2015.

Zhang, Q., Jiang, X., Tong, D., Davis, S. J., Zhao, H., Geng, G., Feng, T., Zheng, B., Lu, Z., Streets, D. G., Ni, R., Brauer, M., van Donkelaar, A., Martin, R. V., Huo, H., Liu, Z., Pan, D., Kan, H., Yan, Y., Lin, J., He, K. and Guan, D.: Transboundary health impacts of transported global air pollution and international trade, Nature, 543(7647), 705–709, doi:10.1038/nature21712, 2017.

Zhao, C., Liu, X., Leung, L. R., Johnson, B., McFarlane, S. A., Gustafson, W. I., Fast, J. D. and Easter, R.: The spatial distribution of mineral dust and its shortwave radiative forcing over North Africa: modeling sensitivities to dust emissions and aerosol size treatments, Atmos. Chem. Phys., 10(18), 8821–8838, doi:10.5194/acp-10-8821-2010, 2010.

Zhu, C., Byrd, R. H., Lu, P. and Nocedal, J.: Algorithm 778: L-BFGS-B: Fortran subroutines for large-scale bound-constrained optimization, ACM Trans. Math. Softw., 23(4), 550–560, doi:10.1145/279232.279236, 1997.

Zhu, L., Henze, D. K., Cady-Pereira, K. E., Shephard, M. W., Luo, M., Pinder, R. W., Bash, J. O. and Jeong, G.-R.: Constraining U.S. ammonia emissions using TES remote sensing observations and the GEOS-Chem adjoint model, J. Geophys. Res. Atmos., 118(8), 3355–3368, doi:10.1002/jgrd.50166, 2013.